NEAR SURFACE WEAR STRUCTURE OF CERAMIC COMPONENTS

by

Bing-Hwai Hwang

Dissertation submitted to the Faculty of the

Virginia Polytechnic Institute and State University

in partial fulfillment of the requirements for the degree of

Doctor of Philosophy

in

Materials Engineering Science

APPROVED:

Charles R. Houska

Jack L. Lytton

Charles W. Smith

Norman S. Eiss

Raymond E. Dessy

May, 1987

Blacksburg, Virginia

NEAR SURFACE WEAR STRUCTURE OF CERAMIC COMPONENTS

by

Bing-Hwai Hwang

Charles R. Houska

Materials Engineering Science

(ABSTRACT)

X-ray techniques were used extensively in this work to examine ceramic samples. The well known techniques including :(1) identification of phases and chemical species, (2) peak separation, (3) quantitative phase analysis, (4) intensity band simulation, and (5) line shape analysis, were applied to ceramic materials of silicon nitride, zirconia toughened alumina, fully and partially stabilized zirconia. A theoretical derivation of the x-ray intensity from a rough sample based on a statistical roughness model was carried out. The statistical model was then combined with the intensity band simulation technique to simulate the intensity band from a rough sample. The modified technique for intensity band simulation was used to determine the strain profile in the near surface regions of a flat and a rough fully stabilized zirconia samples. The results show that a compressive zone is present in the near surface region of each sample. A partially stabilized zirconia disk was examined using symmetrical and asymmetrical diffraction optics after a prolonged pin on disk wear test. The different diffraction optics provided different probe depths and revealed a depth gradient of the phase distribution. A general picture of the wearing process of ceramic components is described based on the examinations carried out in this work.

Acknowledgements

The author would like to express his sincere thanks to Dr. C. R. Houska who provided the patient guidance and instruction required to complete this work. Thanks are also due to Drs. J. L. Lytton, C. W. Smith, N. S. Eiss and R. E. Dessy, who unselfishly devoted their time and knowledge while participating as members of my committee. A special thanks goes to Dr. N. S. Eiss who provided the instrument and assistance needed in the profilometer measurement.

Grateful appreciation is due to Mr. Harry C. Dudley for his technical and nontechnical assistance during my residence in Blacksburg. Thanks also go to the following colleagues and friends, who are ranked in chronological sequence of my association with them: Lawrence Macdonald, Dr. Satish Rao, Richard Neiser, Tawei Sun and Paul Wolf.

The author wishes to express his thanks to his parents, who misssed their youngest son for about four years at the later stage of their lives.

Table of Contents

List of Illustrations

List of Tables

Chapter 1

INTRODUCTION

As ceramic materials find more and more applications as machine parts in recent years, the characterization of the near surface wear structure also becomes more and more important. Adequate characterization can provide the information on phase transformation, porosity, residual stress, failure mechanisms, thermal expansion ...etc.. Proper adjustments in synthesis, fabrication or manufacturing can be taken accordingly to improve the characteristics of the final product. Among the many surface examination techniques, x-ray diffraction and fluorescence are the most versitile and powerful because the following advantages: (1) nondestructive examination; (2) capability of identifying both constitute elements and the crystal structures; (3) capability of changing probe depth; (4) directly applicable to both conductor and nonconductor; (5) availability of quantitative analyses of diffraction data; (6) availability of huge x-ray data bank; (7) no need for vacuum condition.

If the x-ray probe is to be used as a quantitative tool, one must consider the influence of the surface roughness on intensity and control of probe depth over a large range. Although it is very desirable to vary the probe depth within a sample for a near surface examination, traditional x-ray users have only limited control over the probe depth. In this work, two techniques are used to vary

the probe depth within a sample. This requires either a change in wavelength or asymmetrical beam paths. The asymmetric beam paths are obtaind from an asymmetric optics where the incident and signal angles are not equal. Although the asymmetrical optics can be obtained in some conventional diffractometers by tilting the sample normal away from the regular position of symmetrical optics, the intrinsic divergence in the incident beam makes it impractical to attain glancing angles less than 6°. Also, only a few discrete wavelengths are commercially available. Beamlines at the National Synchrotron Light Source (NSLS) have the advantage of offering symmetrical or asymmetrical optics and continuously tunable wavelenths. A highly parallel incident beam allows one to work well below 6°. Although no sample is ideally flat, theoretical calculations of x-ray intensity have been based on the assumption of flat surface. The effect of roughness on the x-ray intensity becomes more significant with decreasing probe depths. A first treatment for the roughness effect from real surfaces is made in this work which uses a generally accepted statistical model to describe surface asperities[1]. This statistical model assumes that the heights of the surface profile are normally distributed with standard deviation σ. An exponentially decayed autocorrelation function with correlation distance τ_c is also used to describe the smoothness of spatial fluctuations.

Harrison and Paskin[2] presented some general considerations for symmetrical diffraction optics which are used to provide insights on how the statistical model must influence x-ray intensities. An extended version covering asymmetric beam paths and diffraction or fluorescence signal was developed by Houska[3] and presented here for the first time. According to these theories, the intensity correction relative to the case of a flat sample is always negative except at two extreme cases where incident and signal rays are completely correlated or uncorrelated. These two extreme cases give no intensity correction and provide convenient checks for the statistical model. Also, an exact intensity calculation was carried out by Borie for a sample with a one dimensional but highly ideallized sawtooth surface[4] This provides a useful limiting comparison with the results obtained from the statistical model. It will be shown that two samples with the same σ and τ_c values have the same maximum intensity correction even though their surfaces have very different forms, i.e. a sawtooth or Gaussian. Of course, the shape of the intensity correction differs considerably. The

simulation results based on the statistical model are confirmed by the experimental data from a rough fully stabilized zirconia sample over a θ range extending from $\sim$ 15° to 90°. At very low incident angles, the absorption consideration becomes very complicated due to multiple intersections between the x-ray beams and free surfaces. This requires an extension of the present model.

A Siemens x-ray diffractometer and spectrometer as well as the Oak Ridge National Laboratory (ORNL) beamline at the NSLS were used to examine several ceramic materials and subsequent analyses were carried out. These include: peak separation using Pearson-VII function; quantitative phase analyses for homogeneous samples; a determination of lattice parameters; simulation of intensity bands using depth profiles of d-spacings; determination of phase distribution using two probe depths. The previously developed theoretical background needed for these analyses are reviewed in Chapter 2. Other needed theories are developed in this work and presented in the following chapters. Harrison and Paskin's work is reviewed and elucidated in Chapter 3 along with Borie's work. Chapter 4 introduces the concept of stochastic processes to which the surface roughness belongs. The theoretical derivation and experimental verification of the statistical roughness model are presented in Chapter 5 along with the comparison with Harrison, Paskin and Borie's results. In Chapter 6, the theory of intensity band simulation previously developed[5] and reviewed in Chapter 2 is combined with the roughness model developed in Chapter 5 to simulate the intensity band from a rough sample. An example of applying this theory to two fully stabilized zirconia samples to determine the residual strain profiles is presented in Chapter 7. Some routine examinations and analyses for three high performance ceramic materials using the techniques reviewed in Chapter 2 are presented in Chapter 8. The theory and an example of the determination of phase distributions in a partially stabilized zirconia (PSZ) disk are presented in Chapter 9. The PSZ disk was subjected to a pin on disk wear test at Advanced Mechanical Technology, Inc. in Newton, Massachusetts before the x-ray examination. A picture of the wear process for ceramics is described and a complete procedure of wear structure study is suggested in Chapter 10 as concluding marks.

Chapter 2

THEORETICAL REVIEW OF X-RAY TECHNIQUES EMPLOYED IN THIS WORK

2.1 An Overview of X-Ray Theory of Value to This Research

Figure 1 is a schematic diagram showing some general geometrical aspects for the present study. The following quantities appear in this figure and are used throughout this work:

I_0 = incident intensity

A_0 = cross section area of incident beam

Z = height measured from the flat sample surface

θ_i = incident angle

θ_s = signal angle

$2\theta = \theta_i + \theta_s$ = the angle between incident and signal beams

—NEAR SURFACE CHARACTERIZATION
BY
X-RAY DIFFRACTION/FLUORESCENCE—

FOR A HOMOGENEOUS, FLAT SAMPLE WITHOUT TEXTURE:

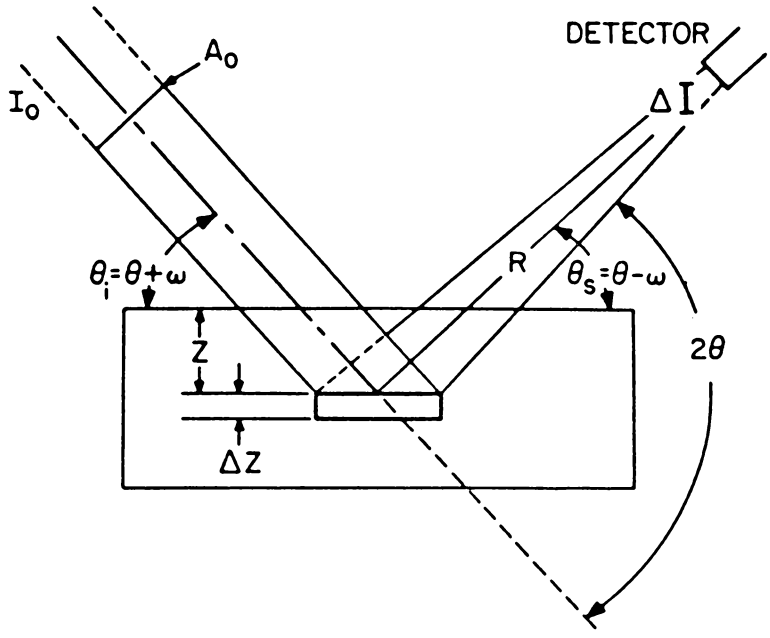

Figure 1. A schematic diagram showing the geometry of x-ray measurement.

ω = tilt angle

For a monochromatic incident beam, the fluorescence signal can be detected at any 2θ position, while for a diffraction peak, Bragg's law must be satisfied and the structure factor must not be 0. Bragg's law is used in the following form:

$$\lambda = 2d \sin\theta \qquad (2-1)$$

where

λ = wavelength of the incident beam

d = lattice spacing of the reflecting planes

θ = Bragg angle

The signal generated by a small layer (see Fig. 1) of volume $\Delta V = A_0 \Delta Z / \sin(\theta + \omega)$ from a non-textured, homogeneously dispersed, multiphase, flat sample is[5,6]:

$$\Delta I = I_0 \left\{ \begin{matrix} Q_f \\ H_\alpha Q_d \end{matrix} \right\} e^{-[<\mu_i> |Z| / \sin(\theta+\omega) + <\mu_s> |Z| / \sin(\theta-\omega)]} \qquad (2-2)$$

The exponential term is the exponential absorption attenuation factor with

$<\mu_i>$ = average linear absorption coefficient for the incident ray impinging upon a planar element at depth Z.

$<\mu_s>$ = average linear absorption coefficient for the signal ray coming from the same element

$Z/\sin(\theta+\omega)$ = absorption length for the incident ray

$Z/\sin(\theta-\omega)$ = absorption length for the signal ray

The factor Q_f is used for the fluorescence signal from a sample of effective volume of unity and one unit of incident intensity. $H_\alpha Q_d$ is the corresponding quantity for the integrated diffracted intensity from the α phase. More specifically, it is the integrated diffracted intensity from unit intensity and effective volume. In each case, the effective volume includes the absorption term.

For a specific kind of atom, the fluorescence factor contains the following terms[5]:

$$Q_f = Q_{fi} = N_i \left(\frac{D_i}{4\pi R_2}\right) \qquad (2-3)$$

where

N_i = number of i atoms per volume

σ_i = atomic cross section of atom i for producing fluorescence of one type

D_i = dimensionless absorption factor for fluorescence radiation in the path from sample surface to detecor times the detector efficiency

R = sample to detector distance

For a specific phase[6] diffracting according to the Bragg's law,

$$H_\alpha Q_d = \text{constant} \times H_\alpha \times \frac{\lambda^3}{v_c^2} \times \frac{1 + \cos^2 2\theta \cos^2 2\theta'}{\sin\theta \sin 2\theta} \times pF^2 \qquad (2-4)$$

where

H_α = volume fraction of α phase

Q_d = reflectivity of the concerned reflection

λ = wavelength of the incident beam

v_c = volume of the unit cell

2θ = Bragg angle for the concerned reflection

2θ′ = Bragg angle for the diffracted-beam monochromator

p = multiplicity

F = structure factor

Because the wavelength of a fluorescence radiation emitted by the sample may be different from that of the incident ray, $<\mu_i>$, $<\mu_s>$ are not equal in general for the fluorescence signal while $<\mu_i> = <\mu_s> = <\mu>$ for the diffraction signal.

When the tilt angle ω is 0, the incident and signal rays are symmetrical with respect to the sample normal. In an aligned commercial x-ray diffractometer, the optics is typically symmetrical although asymmetric optics can be obtained with some diffractometers by intentionally tilting the sample normal away from the symmetrical position.

From Eqs. (2-2) and (2-3), it is clear that the concentration of each kind of atom can be monitored by the relative intensity of its fluorescence signal. Similarly, from Eqs. (2-2) and (2-4), the volume fraction of a specific phase can be monitored by the relative intensity of its diffraction signal.

2.2 Calculation of Lattice Parameters:

A computer program called "lattice" was developed by the Argonne National Laboratory[7] to obtain lattice parameters and the cell axes angles for a specific sample from its x-ray diffraction (XRD) pattern. The needed input data are: the Miller indices of various reflections, their 2θ peak positions in the XRD pattern, the crystal system (e.g. cubic, etc.) and the x-ray wavelength. The calculations are based on the method of least squares. If desired, a weighting factor may be used for each reflection, which may involve constant, a trigonometric function or both. This program is used repeatedly with equal weighting factors in Chapter 8 for various samples.

2.3 *Computer Simulation of X-ray Diffraction Pattern*

A computer program named "powder" was previously developed at VPI[8] to simulate x-ray diffraction patterns. The needed data include: the identity of the atomic species; their positions within the unit cell; the lattice parameters; the crystal system, the angles between unit cell axes, and the x-ray wavelength. The simulation not only calculates the Bragg angle , but also the relative intensity according to Eq. (2-4), the structure factor and the Q_d for each reflection. This program is used frequently in this work and many examples can be found in Chapter 8.

2.4 *Peak Separation Using Pearson-VII Function*

A computer program named "Pearson" was previously developed to unscramble the overlapping diffraction peaks using a function named Pearson-VII. Pearson-VII function[9], as shown below,

$$Y = Y_0[1 + \frac{(2\theta - 2\theta_0)^2}{ma^2}]^{-m} \qquad (2-5)$$

uses two parameters Y , $2\theta_0$ to indicate the intensity and the position of the peak, and the other two parameters a, m describe the peak shape and width.

The full width at half maximum (FWHM) can be shown to be

$$W = 2a[m(2^{1/m} - 1)]^{1/2} \qquad (2-6)$$

When m = 1, 2 and ∞ the Pearson-VII becomes a Cauchy, modified Lorentzian , and Gaussian, respectively. A value of m = 20 is sufficient to represent a Gaussian shape. The "m" parameter is best defined as shape parameter and "a" is a width parameter. Both, of course, are required to obtain W. This computer program first takes the second derivative of the overlapped profile to find out the number and locations of the overlapped peaks. Then, the values of the parameters for each peak can be guessed by the user. By comparing the experimental profile and the simulated profile based upon the previous guesses, the parameters can be adjusted consecutively until the profiles are within the experimental error. Finally, the program can search the optimum value of each parameter based upon minimizing the squares error. The whole program, including the plotting, can be run interactively. Therefore, it is very convenient for peak separations when using a graphics terminal.

2.5 *Quantitative Phase Analysis*

According to Eqs. (2-2) and (2-4), the intensity ratio between reflection *i* of the α phase and reflection j of the β phase for a homogeneous two phase sample is

$$\frac{I_{i,\alpha}}{I_{j,\beta}} = \frac{H_\alpha Q_{i,\alpha}}{H_\beta Q_{j,\beta}} \qquad (2-7)$$

combining Eq. (2-7) and

$$H_\alpha + H_\beta = 1 \qquad (2-8)$$

the volume fractions H_α and H_β can be obtained because $I_{i,\alpha}$, $I_{j,\beta}$ can be measured and $Q_{i,\alpha}$, $Q_{j,\beta}$ can be calculated. Note that the measurements of $I_{i,\alpha}$ and $I_{j,\beta}$ are more accurate when the two reflections are well separated than when they are overlapped. To determine the intensities of individual reflections from overlapping peaks, requires a computer separation (see Section **2.4**) which introduces additional error. For samples with more than two phases, additional relations can be used to obtain the volume fractions for each phase. A more detailed discussion of this analysis can be found in fundamental x-ray diffraction textbooks.[10]. Some results of the quantitative phase analyses for homogeneous samples are given in Chapter 8.

2.6 Simulation of Intensity Band

If a continuous range in d-spacing exists, a diffraction peak appears as an intensity band covering an extended range of 2θ. This often happens in a sample after diffusion of a deposited material into the substrate. Due to the depth gradient of the concentration of the deposited material, the d-spacing of the reflecting planes also change continuously as a function of depth. The continuous variation of the d-spacing subsequently causes the intensity from the sample to spread over a 2θ range according to the Bragg law. In addition to this, the peak is further broadened by the instrumental and sample broadenings to form the observed intensity band. A previously developed computer program[11] was used to fit the measured intensity band and obtain the concentration profile of the deposited material. A Pearson-VII function is used again in the program to account for instrumental and particle size broadening. Because a similar d-spacing change in the near surface region can also be caused by a stress and chemical gradients, the computer program is slightly modified in this work to give d-spacing profile instead of the concentration profile. Another modification is also made to accomodate the asymmetrical diffraction optics by using different absorption lengths for incident and signal rays.

The program first divides the sample to many fine layers along the depth direction. The d-spacing in each layer is treated as a constant and the corresponding intensity is calculated. The calculated intensity is then redistributed around each corresponding 2θ position according to the Pearson-VII function. Different sets of parameters for Pearson-VII functions can be used to distinguish between those layers in the highly strained near surface zone and those layers in the deeper substrate because the deformation broadening is likely to be different in these two regions. Figure 2 illustrates the relation between the d-spacing profile and the intensity band. By trial and error, a correct d-spacing profile can be obtained to fit the observed intensity band. An apparent strain profile can then be calculated from the d-spacing profile. Further modifications have incorporated sample roughness and asymmetrical diffraction geometry. This will be described in detail in Chapter 6 after the roughness theory is presented. Examples of using the modified program are shown in Chapter 7 where both flat and rough zirconia samples are examined symmetrically and asymmetrically to reveal their strain profiles in the near surface regions.

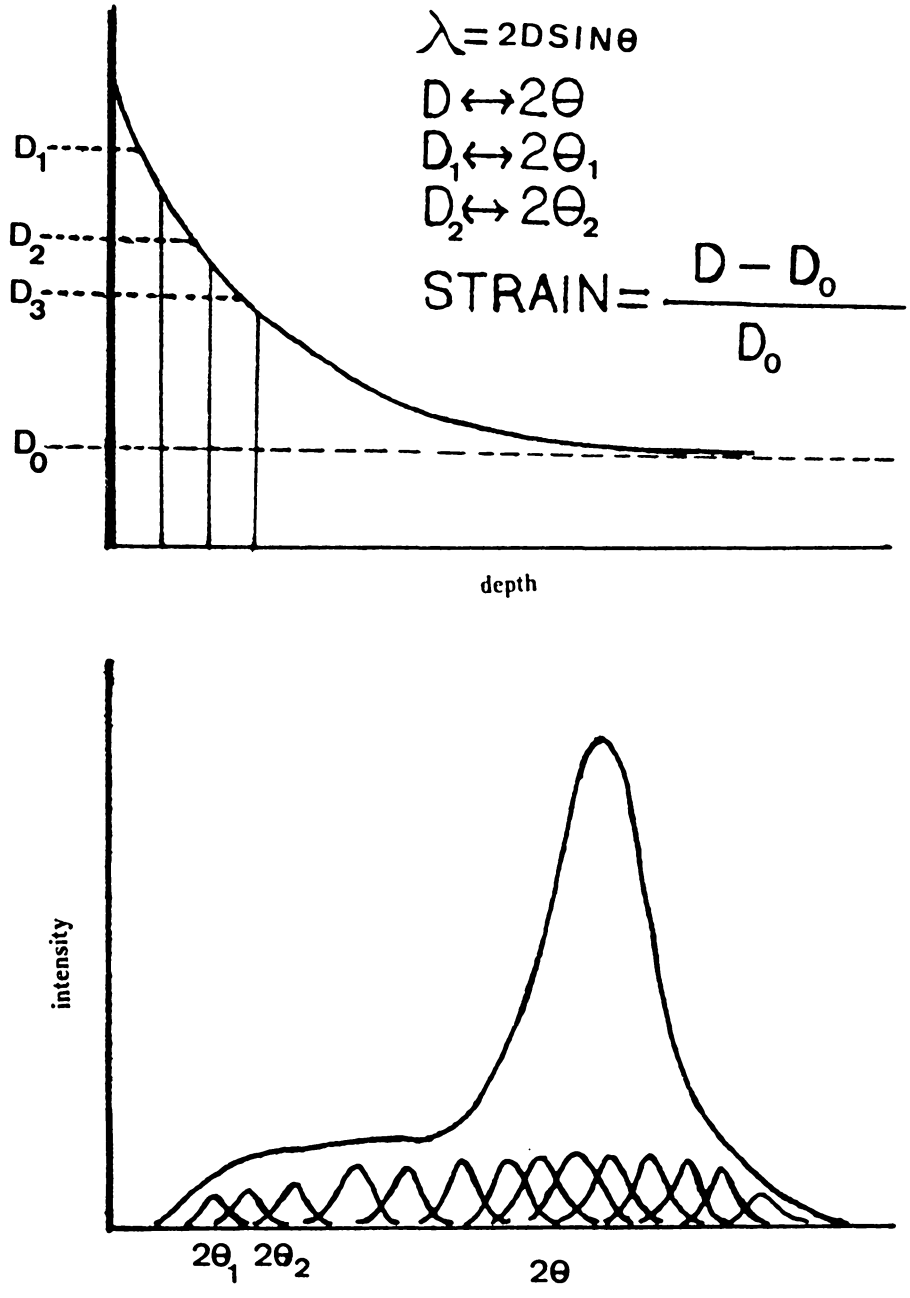

Figure 2. A schematic diagram showing the relation between an intensity band and a d-spacing depth profile.

Chapter 3

REVIEW OF X-RAY INTENSITY CALCULATIONS RELATED TO THE PRESENT STATISTICAL ROUGHNESS MODEL

A new theory is developed in this work to calculate the x-ray intensity from a rough sample based on a statistical roughness model. Before presenting this statistical model, two works previously carried out by (1) Harrison and Paskin[2] and (2) Borie[4] are reviewed in this chapter as they related to the statistical model.

3.1 Harrison and Paskin's Theory

Harrison and Paskin's theory deals with the granularity effect on the diffracted x-ray intensity in powders. The granularity in the powder samples inevitably introduces porosity. The absorption length associated with a signal generating element is changed from the corresponding value of a dense sample due to the presence of pores. Statistical variations in the absorption lengths results in an intensity correction relative to a theoretically dense sample. Similarly, for a rough sample, the absorption length is disturbed by the surface roughness which results in an intensity correction relative to the flat sample. Therefore, the granularity and roughness effects are similar in the sense that both are caused by the irregular spatial distribution of material within a sample. In fact, the general principles concluded by Harrison and Paskin can be applied to both roughness and granularity cases. This will become clear as the discussion proceeds.

The granularity effect on diffracted x-ray intensity treated by Harrison and Paskin is depicted in Figure 3. For any arbitrary point (X,Z) within the sample exposed to the incident beam, we consider an incident ray and an associated signal ray. One such pair of rays are shown in Figure 3. Because of porosity, the true absorption lengths experienced by the incident and signal rays are less than the lengths of the rays and denoted as $L_{ai}(X,Z)$ and $L_{as}(X,Z)$ respectively. The most important result of Harrison and Paskin's work is that they are able to explictly separate the intensity correction relative to an ideally dense sample from the intensity of a powder sample. This is given by (refer to Figure 3):

$$I_{\text{correction}} = I_{\text{powder}} - I_{\text{dense sample}} = I_0 Q \frac{A_0}{2(X_B - X_A)\tan\theta} \times \int_{-\infty}^{0} \int_{X_A - Z\cot\theta}^{X_B - Z\cot\theta} e^{-\mu(L_{ai} + L_{as})} \left[\left(\frac{\partial L_{ai}}{\partial X}\right)_Z - \left(\frac{\partial L_{as}}{\partial X}\right)_Z \right] dX dZ \qquad (3-1)$$

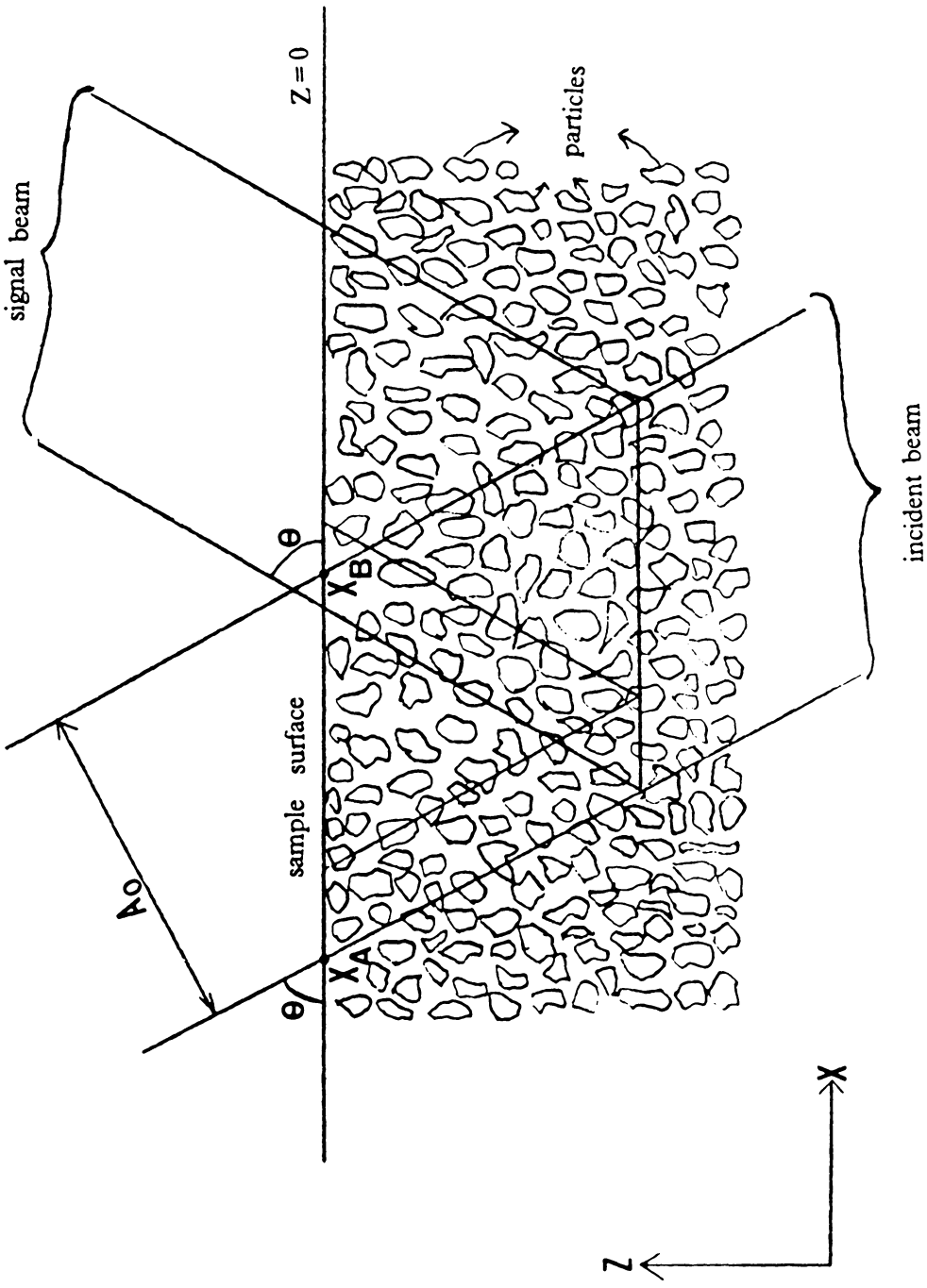

Figure 3. The x-ray diffraction optics with a powder sample.

such that $I_{correction} \leq 0$ and

I_0 = incident intensity

Q = reflectivity

A_0 = cross section area of incident beam

Z = vertical coordinate with Z = 0 for the upmost layer occupied by the material

X = horizontal coordinate

X_A, X_B = two horizontal extremes illuminated by the incident beam at Z = 0

$L_{ai}(X,Z)$ = true absorption length of an incident ray associated with a point at (X,Z)

$L_{as}(X,Z)$ = true absorption length of a signal ray associated with a point at (X,Z)

The result has been generalized by Houska[3] to incorporate the fluorescence signal and asymmetrical x-ray optics as follows:

$$I_{correction} = I_{powder} - I_{dense\ sample} = I_0 Q \frac{A_0}{(X_B - X_A)(\mu_i + \mu_s \frac{\sin\theta_i}{\sin\theta_s})} \times$$
$$\int_{-\infty}^{0} \int_{X_A - Z\cot\theta_i}^{X_B - Z\cot\theta_i} e^{-(\mu_i L_{ai} + \mu_s L_{as})} \left[\frac{\mu_i}{\tan\theta_i} (\frac{\partial L_{ai}}{\partial X})_Z - \frac{\mu_s}{\tan\theta_s} (\frac{\partial L_{as}}{\partial X})_Z \right] dX dZ \qquad (3-2)$$

When $\theta_i = \theta_s$, Eq.(3-2) degenerates to Eq. (3-1).

It is clear from Eqs. (3-1) and (3-2) that the intensity correction is due solely to the variation of absorption lengths along the horizontal direction at each fixed depth. For an ideally flat dense sample, $(\frac{\partial L_{ai}}{\partial X})_Z = (\frac{\partial L_{as}}{\partial X})_Z = 0$ and the correction vanishes. Because the intensity correction depends on the variation of the absorption lengths but not on what causes the variation, Eqs. (3-1) and (3-2) are equally applicable for both granularity and surface roughness. In other words, both granularity and roughness can cause variation of absorption lengths which results in an intensity correction. A rough sample can be viewed as a special case with pores located above the free surface as shown in Figure 4.

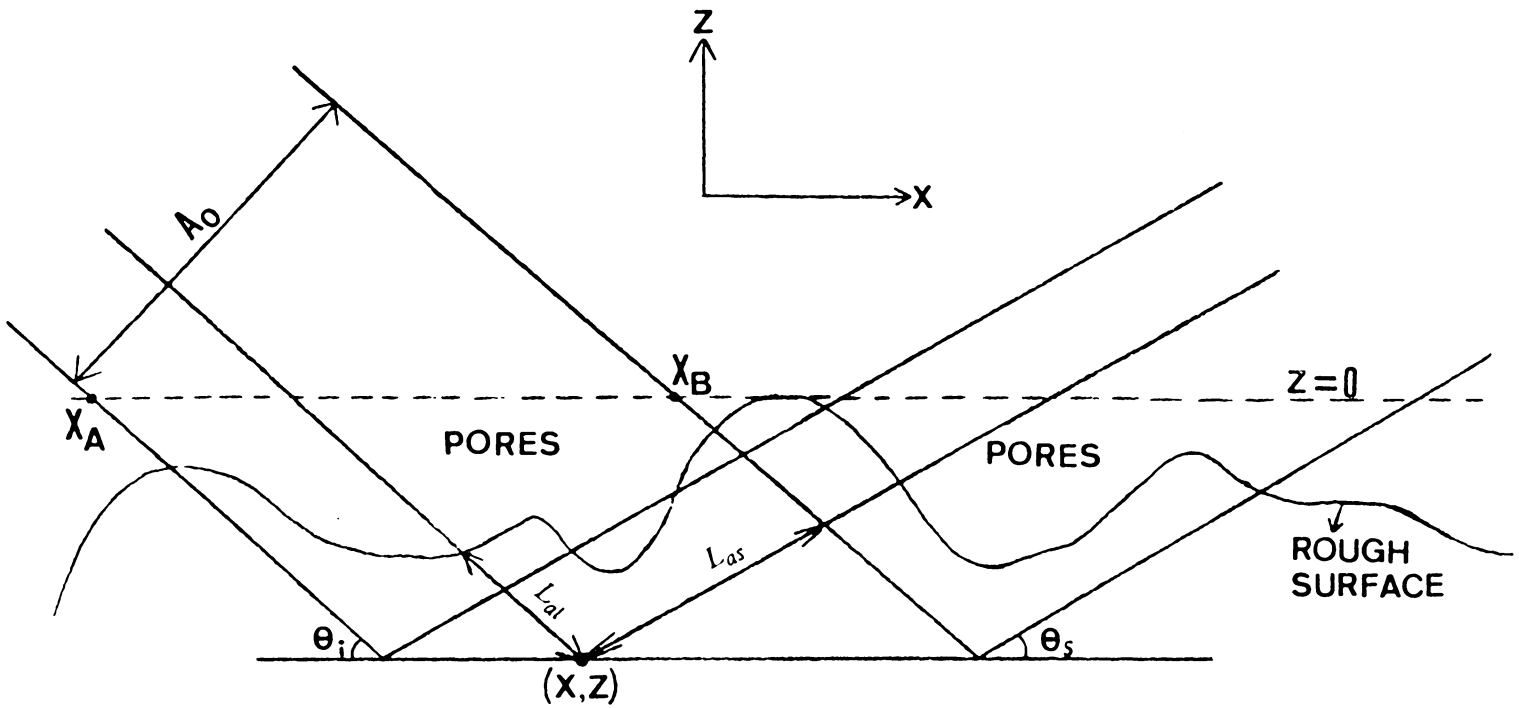

Figure 4. The x-ray diffraction or fluorescence optics with a rough sample.

Although the double integral in Eqs. (3-1) and (3-2) can not be carried out unless the spatial distribution of particles (for powder sample) or the specific surface profile (for rough dense sample) is known, they bear the following important physical insights:

As indicated by Harrison and Paskin, for powder diffraction samples and symmetrical optics, the average (over X) values of $(\frac{\partial L_{ai}}{\partial X})_Z$ and $(\frac{\partial L_{as}}{\partial X})_Z$ are zero, because negative and positive contributions are equiprobable. The reason that the integral of each of these terms is not zero is because the absorption factor is generally different for negative and positive fluctuations. If the paths in and out are completely uncorrelated throughout, one expects the two terms to give the same integrated values and hence the correction is zero. This was mathematically proved by Harrison and Paskin. If the paths in and out are completely correlated, i.e. $(\frac{\partial L_{ai}}{\partial X})_Z = (\frac{\partial L_{as}}{\partial X})_Z$, again the intensity correction is zero.

For the more general case involving a fluorescence signal and asymmetrical x-ray optics, the two extreme cases still give zero intensity correction. To see this, we use the arguments of Harrison and Paskin. Let's compare the intensity correction contributed by a horizontal layer of thickness dZ with the integrated intensity from a thick flat sample, $I_{\text{flat sample}}$. The former is given by the inner integral of Eq. (3-2) along with the pre-integral term while the latter is well known and described by Eq.(5-8). Dividing the former by $I_{\text{flat sample}}$ ($= \frac{I_0 Q A_0}{\mu_i + \mu_s \frac{\sin\theta_i}{\sin\theta_s}}$, see Eq. (5-8)), one obtains

$$\frac{1}{(X_B - X_A)} \int_{X_A - Z\cot\theta_i}^{X_B - Z\cot\theta_i} e^{-(\mu_i L_{ai} + \mu_s L_{as})} \left[\frac{\mu_i}{\tan\theta_i} (\frac{\partial L_{ai}}{\partial X})_Z - \frac{\mu_s}{\tan\theta_s} (\frac{\partial L_{as}}{\partial X})_Z \right] dX dZ \qquad (3-3)$$

This can be written as

$$\frac{1}{(X_B - X_A)} \int_{X=X_A - Z\cot\theta_i}^{X=X_B - Z\cot\theta_i} e^{-(\mu_i L_{ai} + \mu_s L_{as})} \left[\frac{\mu_i}{\tan\theta_i} dL_{ai} - \frac{\mu_s}{\tan\theta_s} dL_{as} \right] dZ \qquad (3-4)$$

$$= \frac{1}{(X_B - X_A)} \int_{X=X_A - Z\cot\theta_i}^{X=X_B - Z\cot\theta_i} \left\{ \frac{1}{\tan\theta_i} e^{-(\mu_i L_{ai} + \mu_s L_{as})} d(\mu_i L_{ai}) - \frac{1}{\tan\theta_s} e^{-(\mu_i L_{ai} + \mu_s L_{as})} d(\mu_s L_{as}) \right\} dZ$$

For completely uncorrelated incident and signal paths, L_{ai} and L_{as} are independent of each other. Therefore, one can replace $e^{-\mu_i L_{ai}}$ by its average value in the integral over $d(\mu_s L_{as})$ and likewise replace $e^{-\mu_s L_{as}}$ by its average value in the integral over $d(\mu_i L_{ai})$. Then Eq. (3-4) becomes

$$\frac{1}{(X_B - X_A)} \int_{X = X_A - Z\cot\theta_i}^{X = X_B - Z\cot\theta_i} \left\{ \frac{-1}{\tan\theta_i} < e^{-\mu_s L_{as}} > d(e^{-\mu_i L_{ai}}) + \frac{1}{\tan\theta_s} < e^{-\mu_i L_{ai}} > d(e^{-\mu_s L_{as}}) \right\} dZ$$

$$= \frac{dZ}{X_B - X_A} \left\{ \frac{< e^{-\mu_i L_{ai}} >}{\tan\theta_s} e^{-\mu_s L_{as}} \Big|_{X = X_A - Z\cot\theta_i}^{X = X_B - Z\cot\tan\theta_i} - \frac{< e^{-\mu_s L_{as}} >}{\tan\theta_i} e^{-\mu_i L_{ai}} \Big|_{X = X_A - Z\cot\theta_i}^{X = X_B - Z\cot\theta_i} \right\}$$

(3 − 5)

Because $L_{ai}, L_{as} \geq 0$ at any point (X,Z), $e^{-\mu_s L_{as}}$ and $e^{-\mu_i L_{ai}}$ are positive and normally less than 1 when evaluated at $X = X_A - Z\cot\theta_i, X = X_B - Z\cot\theta_i$ for any Z. Also, $< e^{-\mu_i L_{ai}} >$ and $< e^{-\mu_s L_{as}} >$ are positive and less than 1. Therefore, the absolute numerical magnitude of the exponential products inside the brace of last Eq. is normally less than 1. When θ_i or θ_s decreases, the incident or signal ray is closer to a horizontal ray and the corresponding true absorption length L_{ai} or L_{as} increases. This causes a very rapid decrease in the value of $e^{-\mu_i L_{ai}}$ or $e^{-\mu_s L_{as}}$ and hence the numerical value of the formula in the brace is even closer to 0. Therefore, the absolute numerical magnitude of Eq. (3-5) is at most around $dZ/(X_B - X_A)$. For common x-ray measurements, $X_B - X_A$, the width of incident beam at the sample surface, is in the order of cm. Because the intensity from the material beyond a few μm deep is trivially small due to absorption, the total intensity correction relative to the integrated intensity from the flat sample, $\frac{\Sigma dZ}{X_B - X_A}$ (ΣdZ is the total thickness of the signal generating zone), is in the order of μm/cm = 10^{-4}. This is smaller than the experimental error and hence the intensity correction is essentially 0 in the case of complete uncorrelation.

When the incident and signal paths are completely correlated, $L_{ai} = L_{as}$ and $(\frac{\partial L_{ai}}{\partial X})_Z = (\frac{\partial L_{as}}{\partial X})_Z = (\frac{\partial L_a}{\partial X})_Z$ everywhere. Eq. (3-3) can be written as,

$$\frac{1}{X_B - X_A}\int_{X_A - Z\cot\theta_i}^{X_B - Z\cot\theta_i} e^{-(\mu_i + \mu_s)L_a}\left(\frac{\mu_i}{\tan\theta_i} - \frac{\mu_s}{\tan\theta_s}\right)\left(\frac{\partial L_a}{\partial X}\right)_Z dX dZ$$

$$= \frac{dZ}{X_B - X_A}\left(\frac{\mu_i}{\tan\theta_i} - \frac{\mu_s}{\tan\theta_s}\right)\int_{X = X_A - Z\cot\theta_i}^{X = X_B - Z\cot\theta_i} e^{-(\mu_i + \mu_s)L_a}\, dL_a$$

$$= \frac{dZ}{X_B - X_A}\left(\frac{\mu_i}{\tan\theta_i} - \frac{\mu_s}{\tan\theta_s}\right)\frac{1}{\mu_i + \mu_s}\int_{X = X_A - Z\cot\theta_i}^{X = X_B - Z\cot\theta_s} e^{-(\mu_i + \mu_s)L_a} d[(\mu_i + \mu_s)L_a] \qquad (3-6)$$

$$= -\frac{dZ}{X_B - X_A}\left(\frac{\mu_i}{\tan\theta_i} - \frac{\mu_s}{\tan\theta_s}\right)\frac{1}{\mu_i + \mu_s} e^{-(\mu_i + \mu_s)L_a}\Big|_{X = X_A - Z\cot\theta_i}^{X = X_B - Z\cot\theta_i}$$

$$= \frac{dZ}{X_B - X_A}\left\{\left[\frac{1}{(1 + \frac{\mu_i}{\mu_s})\tan\theta_s} - \frac{1}{(1 + \frac{\mu_s}{\mu_i})\tan\theta_i}\right] e^{-(\mu_i + \mu_s)L_a}\Big|_{X = X_A - Z\cot\theta_i}^{X = X_B - Z\cot\theta_i}\right\}$$

Because the numerical values of $1/(1 + \frac{\mu_s}{\mu_i})$ and $1/(1 + \frac{\mu_i}{\mu_s})$ are in the order of 1, the absolute numerical magnitude of Eq. (3-5) is again at most around $dZ/(X_B - X_A)$ by the same reason given in the complete random case. This consequently results in a total intensity correction of $\frac{\Sigma dZ}{X_B - X_A}$ which has been shown to vanish.

Besides the two extreme cases just considered, in most cases the paths in and out are partially correlated and the intensity correction does not vanish. The degree of correlation depends on the distribution of the intergranular pores along the incident and signal paths. By considering the correlation arising specifically when the incoming and outgoing rays are associated with a cubic particle, Harrison and Paskin were able to show that $(L_{ai} + L_{as})$ are larger when $\left[\left(\frac{\partial L_{ai}}{\partial X}\right)_Z - \left(\frac{\partial L_{as}}{\partial X}\right)_Z\right]$ is positive and smaller when $\left[\left(\frac{\partial L_{ai}}{\partial X}\right)_Z - \left(\frac{\partial L_{as}}{\partial X}\right)_Z\right]$ is negative. This mechanism results in a negative correction. A serious reader should carefully examine the variation of $(L_{ai} + L_{as})$ and $\left[\left(\frac{\partial L_{ai}}{\partial X}\right)_Z - \left(\frac{\partial l_{as}}{\partial X}\right)_Z\right]$ shown in the Figure 2 of the original article to fully appreciate this mechanism.

For the roughness case, the correlation between L_{ai} and L_{as} are determined by the surface excursion instead of intergranular pores. For completely uncorrelated excursions, the excursion height

at each location is independent of the excursion height at any other location. This results in the completely uncorrelated absorption lengths L_{ai} and L_{as} and hence the zero intensity correction. However, it should be noted that no excursions are completely uncorrelated unless they are infinitely far apart. Because the incident and signal rays associated with a same signal generating element are usually not infinitely far apart, so do their intersections with the surface profile. Therefore, the extreme case of complete uncorrelation does not happen usually. For the complete correlation case, $(\frac{\partial L_{ai}}{\partial X})_Z = (\frac{\partial L_{as}}{\partial X})_Z = (\frac{\partial L_a}{\partial c_X})_Z$ everywhere again even though the surface is rough and the intensity correction vanishes. Besides the two extreme cases, we can see that L_{ai} and L_{as} can be partially correlated. In the statistical model, this correlation is established through the excursion height above the signal generating element which is related to L_{ai} and L_{as}. This point will become clear in Chapter 5 when the statistical model is used to calculate the distribution of absorption lengths.

3.2 *Borie's Calculation*[4]

An exact absorption calculation for a rough sample with 45° sawtooth surface was carried out by Borie. Although the sawtooth surface is artificial, it provides a maximum intensity correction and the calculation is exact. It thereby gives a useful comparison and limiting boundary for the present statistical approach.

It should be noted that the surface excursions described in the statistical model as compared with the periodic sawtooth variation have intrinsic differences. A Gaussian surface, as described in the statistical model, has normal probability density for its excursion heights, while a sawtooth surface, due to its linear shape, has constant probability density. This is shown in Figure 5 where the height of sawtooth is "a". The probability density of the surface height is constant (= 1/a) in the range (-a/2, a/2) and zero elsewhere. This distribution is very different from the normal distribution and results in a big difference in the distribution of absorption lengths for the two surfaces. Con-

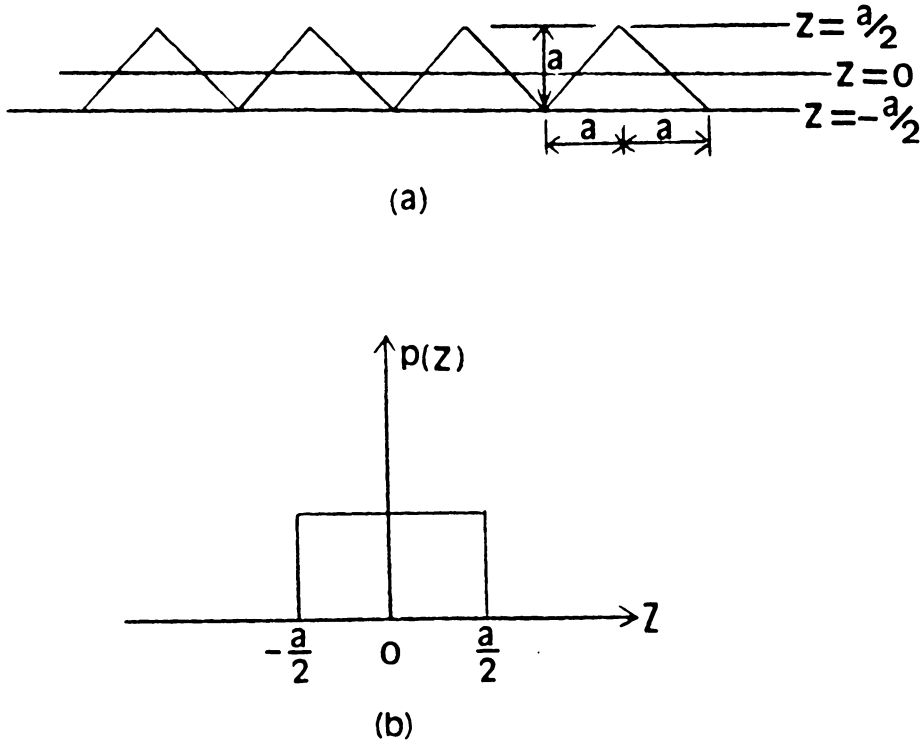

Figure 5. (a) A sawtooth surface and (b) The distribution of the surface height.

sequently, a modification is made in the statistical model to make the comparison more meaningful. This point will become clear later after the absorption calculation based on the statistical model is introduced.

Chapter 4

THE STATISTICAL MODEL OF SURFACE ROUGHNESS

4.1 Roughness as A Stochastic Process[1,2]

There are many examples of random (stochastic) processes in nature,[12,13] some of which are meteorological phenomena, thermal noise in electric circuits, Brownian motion of particles, vibration phenomena, and certain economic fluctuations. The common nature is an indeterminacy in expected behavior of any single record, coupled with strong statistical features for large collections of records. Knowledge of the past behavior of a single random record by itself does not give any precise indication of its future action. Any random single input is an accident, never likely to occur again. The best one can do is to make a particular measurement of interest over large collections of records, then average these individual results in different desired ways so as to determine some of the apparent statistical variations. Figure 6 illustrates an example of random process. A collect of all possible sample functions is defined as a random or stochastic process.

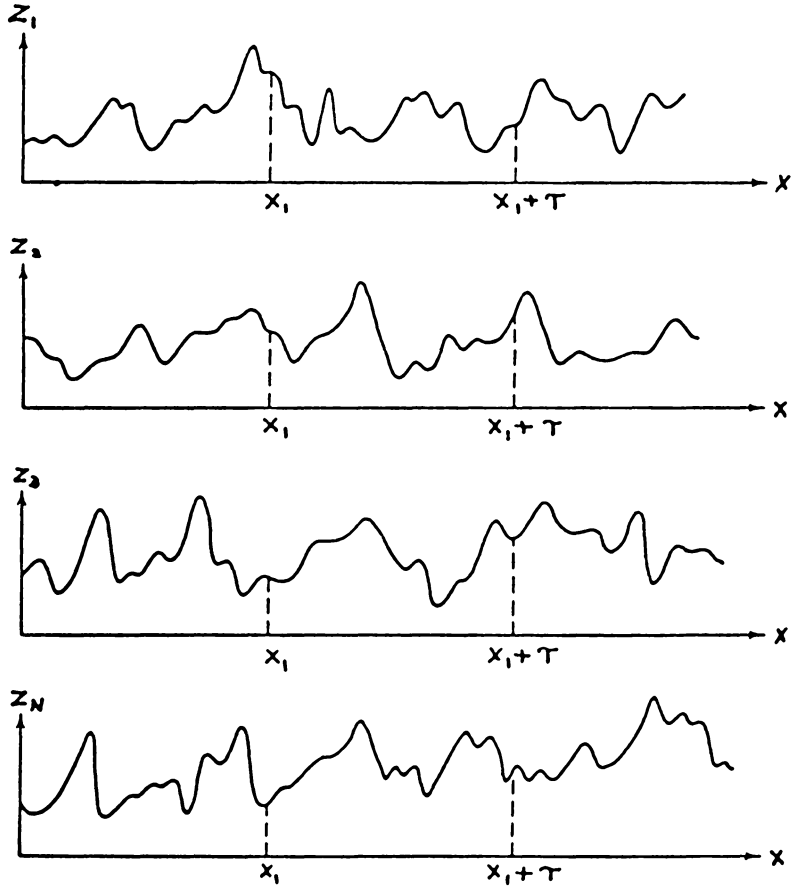

Figure 6. Ensemble of four sample functions forming random process.

The excursion fluctuation along any direction of a rough surface is random and can not be predicted from its previous fluctuation. Therefore, surface roughness is also a stochastic process. The traces formed by the intersections of planes perpendicular to the rough surface provide displays of surface roughness and serve as statistical samples.

Random processes are classified as stationary and nonstationary processes. The meaning of the term stationary may be understood by examining a collection of sample functions or an ensemble. The mean value of the first moment of the random process at some position, X_1 can be computed by taking the value of each sample function of the ensemble at X_1, summing the values, and dividing by the number of sample functions (see Fig. 6). In a similar manner, a correlation or joint moment between the values of the random process at two different positions (called the autocorrelation function) can be computed by taking the ensemble average of the product of instantaneous values at two positions, X_1 and $X_1 + \tau$. That is, for the random process where the symbol { } is used to denote an ensemble of sample functions, the mean value $\mu_Z(X_1)$ and the autocorrelation function $R_Z(X_1, X_1 + \tau)$ are given by:

$$\mu_Z(X_1) = \lim_{N \to \infty} \frac{1}{N} \sum_{k=1}^{N} Z_k(X_1) \qquad (4 - 1a)$$

$$R_Z(X_1, X_1 + \tau) = \lim_{N \to \infty} \frac{1}{N} \sum_{k=1}^{N} Z_k(X_1) Z_k(X_1 + \tau) \qquad (4 - 1b)$$

where the final summation assumes each sample function is equiprobable. For the special case where $\mu_Z(X_1)$ and $R_Z(X_1, X_1 + \tau)$ do not vary as X_1 varies, the random process {Z(X)} is said to be stationary. For stationary random processes, the mean value is a constant and the autocorrelation function is dependent only upon the displacement. That is, $\mu_Z(X_1) = \mu_Z$ and $R_Z(X_1, X_1 + \tau) = R_Z(\tau)$. Note that for a rough surface, μ_Z is usually set to 0 to account for the mean plane and surface fluctuation is measured relative to the mean plane.

Stationary processes are further classified as ergodic and nonergodic processes. What does "ergodic" mean? In most cases, it is also possible to describe the properties of a stationary random process by computing averages over specific sample functions in the ensemble. For example, consider the kth sample function for the random process, the mean value $\mu_Z(k)$ and the autocorrelation function $R_Z(\tau,k)$ for the kth sample function are given by:

$$\mu_Z(k) = \lim_{L\to\infty} \frac{1}{L}\int_0^L Z_k(X)dX \qquad (4-2a)$$

$$R_Z(\tau,k) = \lim_{L\to\infty} \frac{1}{L}\int_0^L Z_k(X)Z_k(X+\tau)dX \qquad (4-2b)$$

If the random process {Z(X)} is stationary, and $\mu_Z(k)$ and $R_Z(\tau,k)$ as defined in Eqs. (4-2a) and (4-2b) do not differ when computed over different sample functions, the random process is said to be ergodic. For ergodic random process, the distance averaged mean value and autocorrelation function as well as all other distance averaged properties are equal to the corresponding ensemble averaged time value. That is, $\mu_Z(k) = \mu_Z$ and $R_Z(\tau,k) = R_Z(\tau)$. Only stationary random processes can be ergodic. Ergodic random processes are an important class of random processes since all properties of ergodic random processes can be determined by performing averages over a single sample function.

The general rough surfaces, as indicated by Saley et. al.[14], are not stationary. The nonstationarity is due to the different features in different areas of a general rough surface. This is best understood by imagining an ensemble composed of many geographical "traces". If all traces start at points in the middle west region of the North American Continent and end at points in the Rocky Mountain region, the ensemble average of the altitude at the starting point is certainly not equal to the corresponding average at the final point. Consequently, the requirement of stationarity is not fulfilled and the topography of North American Continent can not be treated as a stationary random process. Fortunately, for general machined surfaces, the local feature changes form one place to the other very mildly and such differences between "Rockey Mountain" and "Middle West"

does not happen. Therefore, a sample of length L, will have statistical properties very similar to any other surface length L taken form any part of the same surface. This is termed "stationary within an interval"[13] and implies that, similar to the ergodic process, all statistical properties can be extracted from a single sample function instead of from the whole ensemble. Although the change of the local feature on a machined surface is very mild, it may not be trivial. Consequently, a longer sampling length will accommodate more local difference than a shorter sampling length and all statistical properties are functions of sampling length. The dependence of the statistical properties on the sampling length can be further understood by considering the following example. Shown in Figure 7 is a trace from a rough surface and its mean plane ($Z = 0$), the corresponding sampling length is $l = 2l'$. If the sampling length is reduced to l', then the original trace consists of two sampling lengths. In each sampling length, an independent mean plane is established and shown as $Z' = 0$. Obviously, the standard deviation of the excursion height (i.e. σ, a statistical parameter) relative to $Z = 0$ plane is much larger than that relative to the $Z' = 0$ plane. Because the dependence of the statistical properties on the sampling length, statistical parameters measured by different techniques are comparable only when a same sampling length is used. This point will be examined later when comparing the x-ray and profilometer measurements.

4.2 The Statistical Model of Surface Roughness

The most commonly used description of the probability density of the excursion heights of a trace obtained from a real surface is described by the Gaussian or normal distribution. The Gaussian density distribution of excursions from the mean surface plane is given by the symmetrical function

$$p(Z) = \frac{1}{\sqrt{2\pi}\,\sigma} e^{-\frac{Z^2}{2\sigma^2}} \qquad (4-3)$$

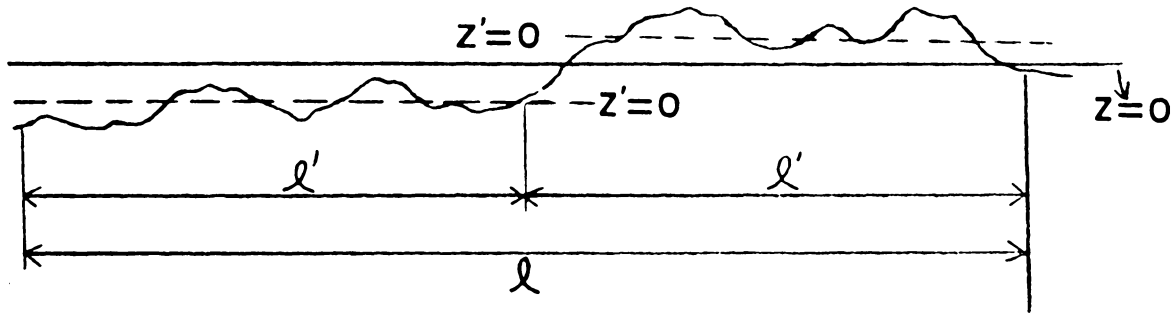

Figure 7. A rough surface with different sampling lengths.

where

Z = height of excursion (for mean plane, Z = 0)

σ = standard deviation of height

The fraction of excursions between Z and Z + dZ is given by the product $p(Z)dZ$. Although surfaces produced by many machining processes (e.g. grinding, spark eroding, sand blasting) have excursion height distribution very close to normal (see Figure 8), other machining processes and wear tend to remove the material located at higher positions and leave the deep excursion relatively unchanged. This is called "running in" and can be clearly demonstrated by the cumulative probability function. The cumulative probability function for a specific probability density function $p(Z)$ is defined as:

$$P(Z) = \int_{-\infty}^{Z} p(Z')dZ' \qquad (4-4)$$

For a Gaussian surface

$$P(Z) = \frac{1}{\sqrt{2\pi}\,\sigma}\int_{-\infty}^{Z} e^{-\frac{Z'^2}{2\sigma^2}}dZ' = \frac{1}{2}\{1 + erf\frac{Z}{\sqrt{2}\,\sigma}\} \qquad (4-5)$$

As shown in Figure 9, a horizontal line located at height Z only partially occupied by material. The fraction of occupation A_f is the cumulative probability from Z = Z to Z = ∞. That is,

$$A_f(Z) = \int_{Z}^{\infty} p(Z)dZ = 1 - \int_{-\infty}^{Z} p(Z)dZ = 1 - P(Z) \qquad (4-6)$$

For a Gaussian surface,

$$A_f(Z) = 1 - \frac{1}{2}\{1 + erf\frac{Z}{\sqrt{2}\,\sigma}\} = \frac{1}{2}erfc\frac{Z}{\sqrt{2}\,\sigma} \qquad (4-7)$$

This behaves as expected yielding

$$A_f(Z \to \infty) \to 0, \text{ well above surface}$$

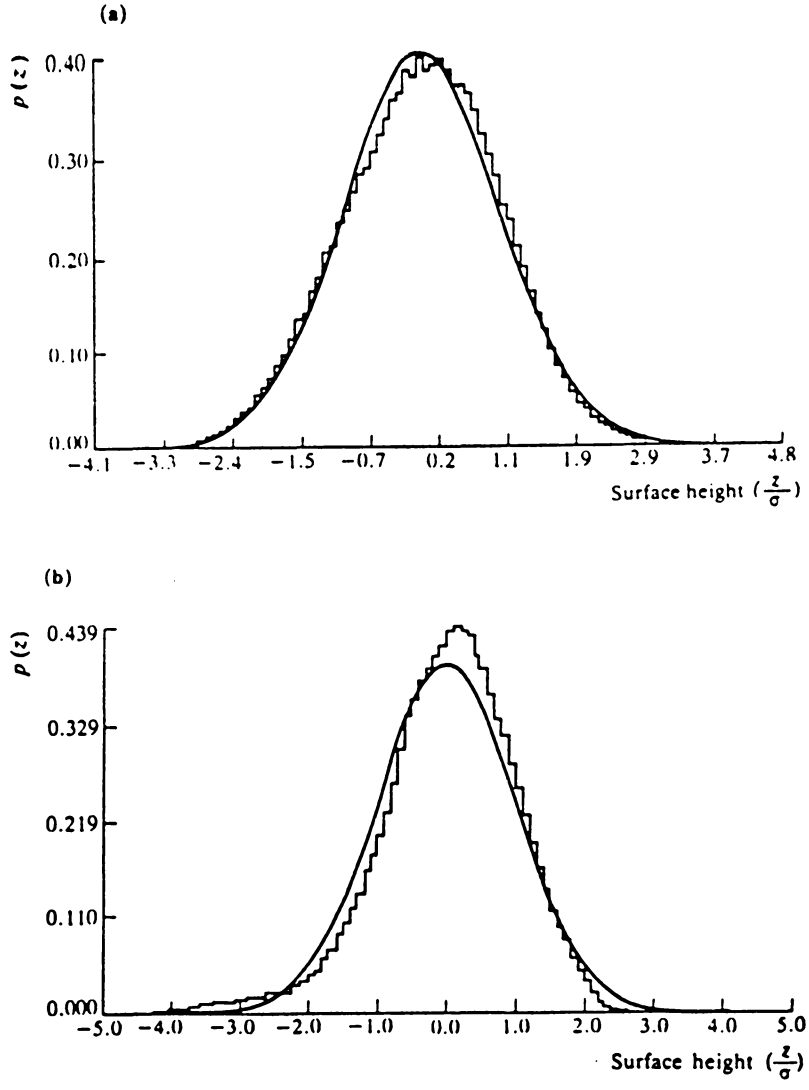

Figure 8. Normalized histograms of heights compared with Gaussian distributions of the same standard deviation.: (a) 282,309 heights from 8mm * 5mm of a spark-eroded surface, $\sigma = 3.13$ μm. (b) 403,200 heights from 5mm * 7.5mm of a ground surface, $\sigma = 2.35$ μm (Sayles and Thomas,[15] 1979).

Figure 9. A rough surface.

$$A_f(Z \to -\infty) \to 1, \text{ well below surface}$$

$$A_f(Z = 0) = \frac{1}{2}, \text{ at mean surface} \qquad (4-8)$$

A common and useful way of representing the shape of a surface is to display the cumulative probability density function (Eq. (4-4)) on a probabilty graph paper. This plotting procedure is scaled in such a way that the cumulative form of the Gaussian function becomes a straight line. Consequently, it is easy to see whether a surface is Gaussian. Moreover, the "running in" effect can be clearly seen if the cumulative probability density functions at various wear stages are plotted in the same probability graph paper. Figure 10 shows such an example where cumulative probability density functions of the initial and seven progressive stages are plotted.

In developing the x-ray calculation, it will be necessary to specify the depth of a volume element and examine the material traversed by rays entering and leaving the element. It is essential to know how much material is being traversed in order to determine beam absorption. This requires pairs of points to be compared at various distances which is accmplished with a conditional probability density function $p(Z_2/Z_1)$. With this notation, Z_1 is specified while the distribution of Z_2 at a distance τ is given by the resultant density function $p(Z_2/Z_1)$. The statistical model begins with the two dimensional joint probability function based on a Gaussian distribution

$$p(Z_1, Z_2, \tau) = \frac{1}{2\pi\sigma^2\sqrt{1-\rho^2(\tau)}} e^{-\frac{Z_1^2 - 2\rho(\tau)Z_1Z_2 + Z_2^2}{2\sigma^2(1-\rho^2(\tau))}} \qquad (4-9)$$

where σ is the standard deviation of the excursion height relative to the mean plane. This function describes the probability density function of excursion heights at two locations separated by a horizontal distance τ on a trace. The autocorrelation function defined as follows,

$$\rho(\tau) = \frac{R(\tau)}{\sigma^2} \qquad (4-10)$$

Cumulative height distributions showing effect of pressing an initially rough surface (●) against a very hard flat. The seven non-Gaussian distributions (O) represent, from right to left, progressive stages in the flattening process. Profiles for three of the distributions are shown in the lower diagram (Williamson et al. 1969).[16]

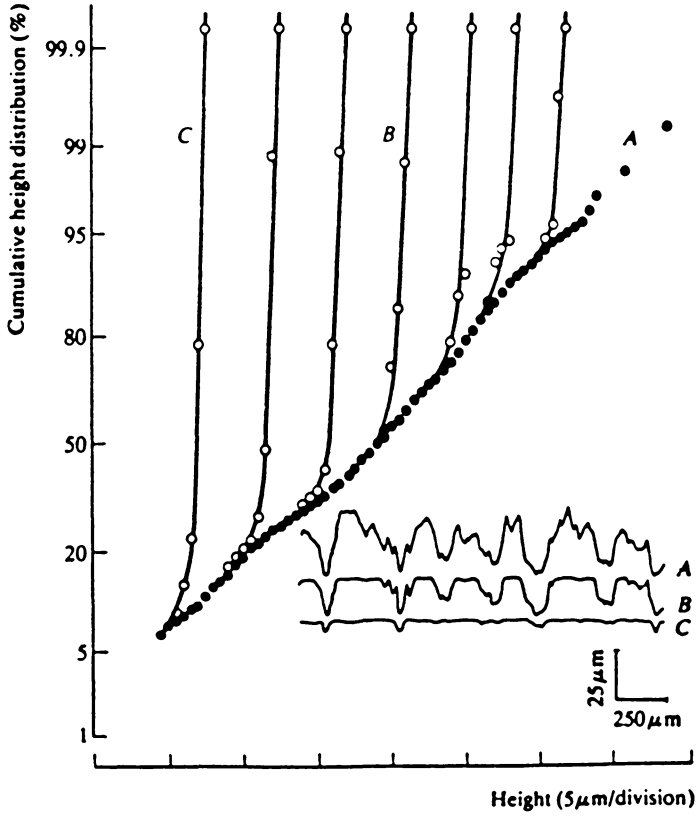

Figure 10. Cumulative height distributions of a surface with changing roughness.

with

$$R(\tau) = \lim_{L\to\infty} \frac{1}{2L} \int_{-L}^{L} Z(X)Z(X+\tau)dX \qquad (4-11)$$

indicates how closely the excursion at the two locations are related.

By statistical definition, $R(0) = \sigma^2$ and $\rho(0) = 1$. Physically, this means the two locations merge together and their excursion heights are completely correlated. As $\tau \to \infty$, the two locations are well separated and their correlation vanishes. In other words, $R(\infty) = \rho(\infty) = 0$. Between these two extremes, the excursion heights at the two locations are partially correlated, i.e. $0 < \rho(\tau) < 1$. The empirical function given below has been found to be a good representation of many phenomena[1] and will be used in the statistical model:

$$\rho(\tau) = e^{-\frac{|\tau|}{\tau_c}} \qquad (4-12)$$

τ_c is called correlation distance and defined as the separation corresponding to $\rho = \frac{1}{e}$. The desired conditional probability density is given by

$$p(Z_2/Z_1) = \frac{p(Z_1,Z_2)}{p(Z_1)} \qquad (4-13)$$

Here, Z_1 is specified to lie between Z_1 and $Z_1 + dZ_1$ and the probability of finding Z_2 between Z_2 and $Z_2 + dZ_2$ is to be determined. For the present distribution with correlation,

$$p(Z_2/Z_1,\tau) = \frac{1}{\sqrt{2\pi}\,\sigma[1-\rho^2(\tau)]^2} e^{-\frac{[Z_2-\rho(\tau)Z_1]^2}{2\sigma^2(1-\rho^2(\tau))}} \qquad (4-14)$$

The final distribution that is required is defined as a joint cumulative conditional distribution function (JCCD) which is not a density function. This is given by integrating over the range $-\infty$ to Z_2, i.e.

$$P(Z_2' \leq Z_2/Z_1) = \int_{-\infty}^{Z_2} p(Z_2'/Z_1)\, dZ_2' \qquad (4-15)$$

This is analogous to Eq. (4-4) as it is not a density function and is cumulative. It differs in that Z_1 is specified in Eq. (4-14) but not in Eq. (4-4).

Eq. (4-15) can be based upon Gaussian distribution, i.e. Eq. (4-14). By integrating

$$P(Z_2' \leq Z_2/Z_1,\tau) = \frac{1}{\sqrt{2\pi}\,\sigma[1-\rho^2(\tau)]^{1/2}} \int_{-\infty}^{Z_2} e^{-\frac{[Z_2' - \rho(\tau)Z_1]^2}{2\sigma^2(1-\rho^2(\tau))}} dZ_2'$$

Let

$$t = \frac{Z_2' - \rho Z_1}{\sqrt{2}\,\sigma(1-\rho^2)^{1/2}}, \quad dt = \frac{dZ_2'}{\sqrt{2}\,\sigma(1-\rho^2)^{1/2}}$$

Then

$$P(Z_2' \leq Z_2/Z_1,\tau) = \frac{1}{2}\left(1 + erf\frac{Z_2 - \rho Z_1}{\sqrt{2}\,\sigma(1-\rho^2)^{1/2}}\right) \qquad (4-16)$$

or

$$A_f(Z_2/Z_1,\tau) = 1 - P(Z_2/Z_1,\tau) = \frac{1}{2} erfc\frac{Z_2 - \rho Z_1}{\sqrt{2}\,\sigma(1-\rho^2)^{1/2}} \qquad (4-17)$$

This is analogous to the fraction of occupation given in Eq. (4-7) with the only difference that Z_1 is specified in Eq. (4-17). In other words, $A_f(Z_2/Z_1,\tau)$ is the chance of finding material at Z_2 when the concerned excursion is known to pass through Z_1 . This is dependent on how close the location of Z_1 is relatve to the location of Z_2 and hence $\rho(\tau)$. Figure 11 shows $A_f(Z_2/Z_1,\tau)$ for various values of $\rho(\tau)$ and a fixed $Z_1(=\sqrt{2}\,\sigma)$. It is clear that when $\rho = 0$, $A_f(Z_2/Z_1,\tau)$ degenerates to the complementary error function given in Eq. (4-7). On the other hand, as $\rho \to 1$, $A_f(Z_2/Z_1,\tau) \to 1$ or 0,

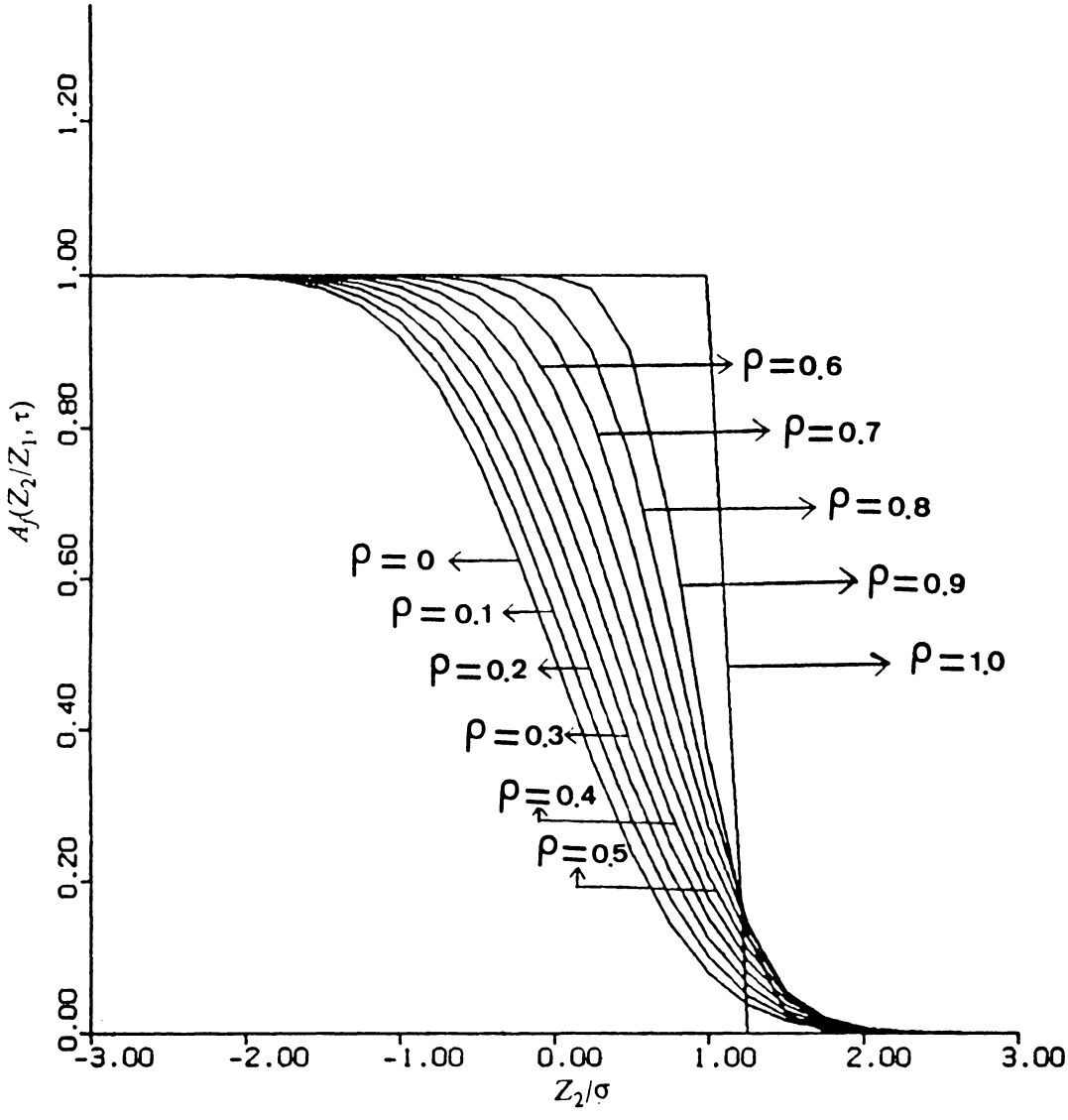

Figure 11. The conditional probability of occupation at Z_2 when Z_1 is fixed at $\sqrt{2}\sigma$.

depending on Z_2 is below or above Z_1. This function is, as will be seen later, useful in determining the distribution of absorption lengths and average absorption length which are affected by roughness in the near surface region. The statistical descriptions mentioned above will be used in the next chapter to calculate the x-ray intensity from a rough sample.

Another useful parameter of a rough surface is the average absolute slope $\overline{|s|}$. If the probability density of the slope is Gaussian with mean 0 and standard deviation σ_{slope}, then

$$\begin{aligned}\overline{|s|} &= \int_{-\infty}^{\infty} \overline{|s|}\, p(s)ds = \frac{1}{\sqrt{2\pi}\,\sigma_{slope}} \int_{-\infty}^{\infty} \overline{|s|}\, e^{-\frac{s^2}{2\sigma_{slope}^2}} ds \\ &= \sqrt{\frac{2}{\pi}}\,\sigma_{slope} = 0.8\sigma_{slope}\end{aligned} \qquad (4-18)$$

σ_{slope} can be calculated from the autocorrelation function $R(\tau)$ as follows:

$$\begin{aligned}R(\tau) &= \lim_{2L\to\infty} \frac{1}{2L} \int_{-L}^{L} Z(X)Z(X+\tau)\, dX \\ -R''(0) &= \lim_{2L\to\infty} \frac{1}{2L} \int_{-L}^{L} Z(X)\ddot{Z}(X)\, dX \quad (\text{differentiate } R(\tau) \text{ twice}) \\ &= \lim_{2L\to\infty} \frac{1}{2L} \int_{-L}^{L} \dot{Z}(X)\dot{Z}(X)\, dX \quad (\text{integrate by parts}) \\ &= \text{Expectation}(\dot{Z}\,\dot{Z}) \\ &= \sigma_{slope}^2\end{aligned} \qquad (4-19)$$

Combine Eqs. (4-18) and (4-19),

$$\overline{|s|} = 0.8\sigma_{slope} = 0.8\sqrt{-R''(0)} \qquad (4-20)$$

It should be noticed that the empirical function $R(\tau) = \sigma^2\rho(\tau) = \sigma^2 e^{-\frac{|\tau|}{\tau_c}}$ can not be used to calculate $R''(0)$ because it is not reliable around the origin. The failure of the empirical function at origin is commented by Thomas[1] as follws: " ... The model has created much controversy between the theoreticians and experimentalists, mainly because of its discontinuity at the origin,....

$$\rho'(0) = -\frac{1}{\tau_c} \text{ as } \tau \to 0^+ \quad \text{(from above)}$$

$$\rho'(0) = +\frac{1}{\tau_c} \text{ as } \tau \to 0^- \quad \text{(from below)}$$

Obviously $\rho'(0)$ is undefined at $\tau = 0$, and further derivatives are invalid,....".

Another way of calculating average absolute slope may be obtained directly from the digitized surface profile. The absolute slope is calculated for each pair of adjacent points and then the arithmetic average of the absolute slopes is taken. However, this method suffers from the uncertainty caused by the intrinsic discontinuity of a digitized profile. Because the excursion between any two adjacent digitized points is continuous and the slope along it varies continuously. This varing slope is replaced by the slope determined from the two digitized points in above method. Therefore, the average absolute slope depends on the spacing used for digitization. An average absolute slope calculated from the digitized profile should not be considered as absolutely accurate.

For sample surfaces produced by general maching processes, the surface fluctuation is very mild and the slope is rarely over $10°$[1]. Therefore, a surface profile is highly unlikely to cross an incoming or outgoing x-ray more than once unless the ray makes a very small angle with the horizontal plane. In the statistical model, single intersection between the surface profile and the incident or signal ray is assumed based on this fact. This assumption, as will be seen later, enables the model to calculate the distribution of the absorption lengths which are affected by the surface roughness.

Chapter 5

THEORETICAL CALCULATION OF X-RAY INTENSITY BASED ON THE STATISTICAL MODEL

As the penetration depth of x-ray beam becomes smaller and smaller, the roughness effect becomes more and more significant, and the fundamntal calculation of x-ray intensity based on the assumption of flat sample becomes more and more inadequate. To illustrate the x-ray penetration, it is convenient to begin with a monochromatic x-ray beam and a flat sample (see Figure 12). Although this ideal situation is never reallized, it provides a convenient reference point. Because the intensity of an x-ray beam within a sample is only attenuated exponentially as the path length increases but never reaches 0, it is convenient to define an effective penetration depth. As shown in Fig. 12, the effective penetration depth is defined in terms of $\delta_{1/e}$, or the depth where the combination of incident and signal paths produces an intensity reduction of e^{-1}, i.e.

$$e^{-\left(\mu_f \frac{\delta_{1/e}}{\sin(\theta+\omega)} + \mu_s \frac{\delta_{1/e}}{\sin(\theta-\omega)}\right)} = e^{-1} \qquad (5-1)$$

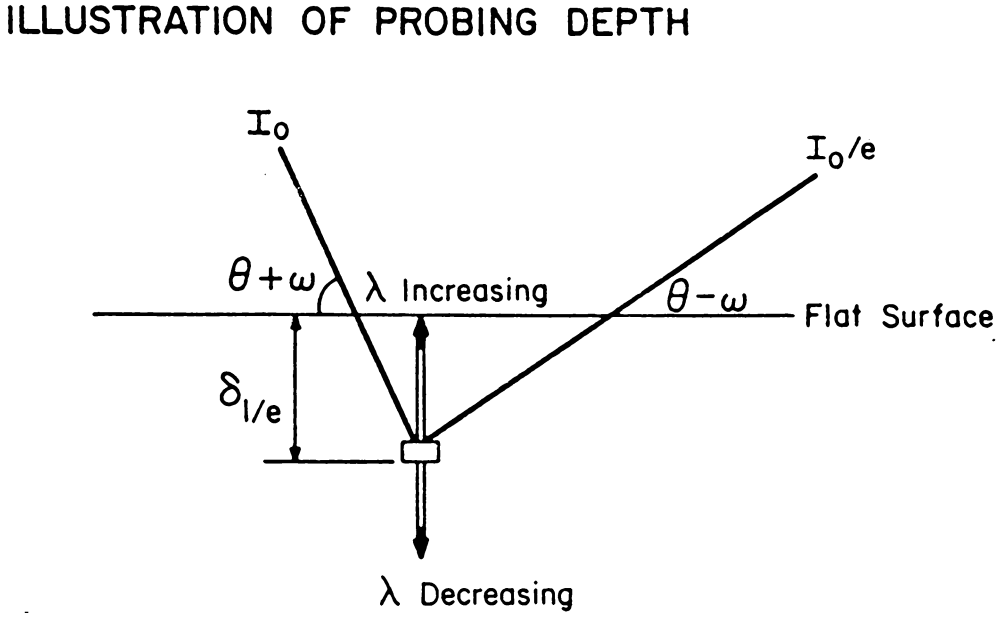

Figure 12. A shematic diagram showing the effective penetration depth.

Therefore,

$$\delta_{1/e} = \frac{1}{\frac{\mu_i}{\sin(\theta + \omega)} + \frac{\mu_s}{\sin(\theta - \omega)}} \qquad (5-2)$$

Because $\delta_{1/e}$ is a function of absorption (hence wavelength λ) and tilt angle ω, it can be altered by either changing the x-ray wavelength or using asymmetrical geometry. The dependence of $\delta_{1/e}$ on absorption coefficient (hence λ) and tilt angle ω are illustrated in Figures 13, 14, 15 and 16.

In Fig 13, $\delta_{1/e}$ is plotted as a function of ω for the (400) reflection of a flat zirconia sample. For this particular reflection, Bragg angle $\theta = 64.2°$ and 37.3° for Cr $K\alpha$ and Cu $K\alpha$ radiations respectively according to the Bragg's law. For Cr $K\alpha$ radiation, the linear absorption coeeficient $\mu =$ 1850 cm^{-1} and $\delta_{1/e}$ decreases from 2.43 μm to 0.07 μm as ω changes from 0 ° to ± 63.5°. For Cu $K\alpha$ radiation, the linear absorption coefficient $\mu = 630$ cm^{-1} and $\delta_{1/e}$ decreases from 4.81 μm to 0.22 μm as ω changes from 0° to ± 36.5°. In Fig. 14, similar curves are plotted for (111) reflection. The Bragg angles are $\theta = 15.2°$, 22.9°, and 42.9° respectively for Cu Kα radiation, Cr Kα radiation and the synchrotron radiation of 4 Å. For Cu Kα radiation, $\delta_{1/e}$ decreases from 2.08 μm to 0.19 μm as ω changes from 0 to ± 14.5°; For Cr Kα radiation, $\delta_{1/e}$ decreases from 1.05 μm to 0.083 μm as ω changes from 0° to ± 22°; For 4 Å radiation, the linear absorption coefficient $\mu =$ 8070 cm^{-1} and $\delta_{1/e}$ decreases from 0.42 μm to 0.02 μm as ω changes from 0 ° to ± 42°. Note in Figs. 13 and 14, evervy curve is symmetrical with respect to the $\omega = 0°$ line. Also, for any radiation, the tilt angle is restricted to the range $-\theta \leq \omega \leq \theta$. An ω value beyond these ranges corresponds to back reflection where the signal from a bulk sample is not readily accesssible. In Fig. 15, $\delta_{1/e}$ is plotted as a function of λ for the (111) reflection of a flat zorconia sample. The lower curve is for the symmetrical diffraction ($\omega = 0°$) condition while the upper is for the asymmetrical condition with $\omega = \omega_{max.} = \pm (\theta - 0.5°)$. Note that the Bragg angle θ increases as λ increases, thereby $|\omega_{max.}|$ also increases as λ increases. Similar curves are drawn in Fig. 16 for the (400) reflection where the longest suitable wavelength is around 2.5 Å according to the Bragg's law. The plots in Figs. 15 and 16

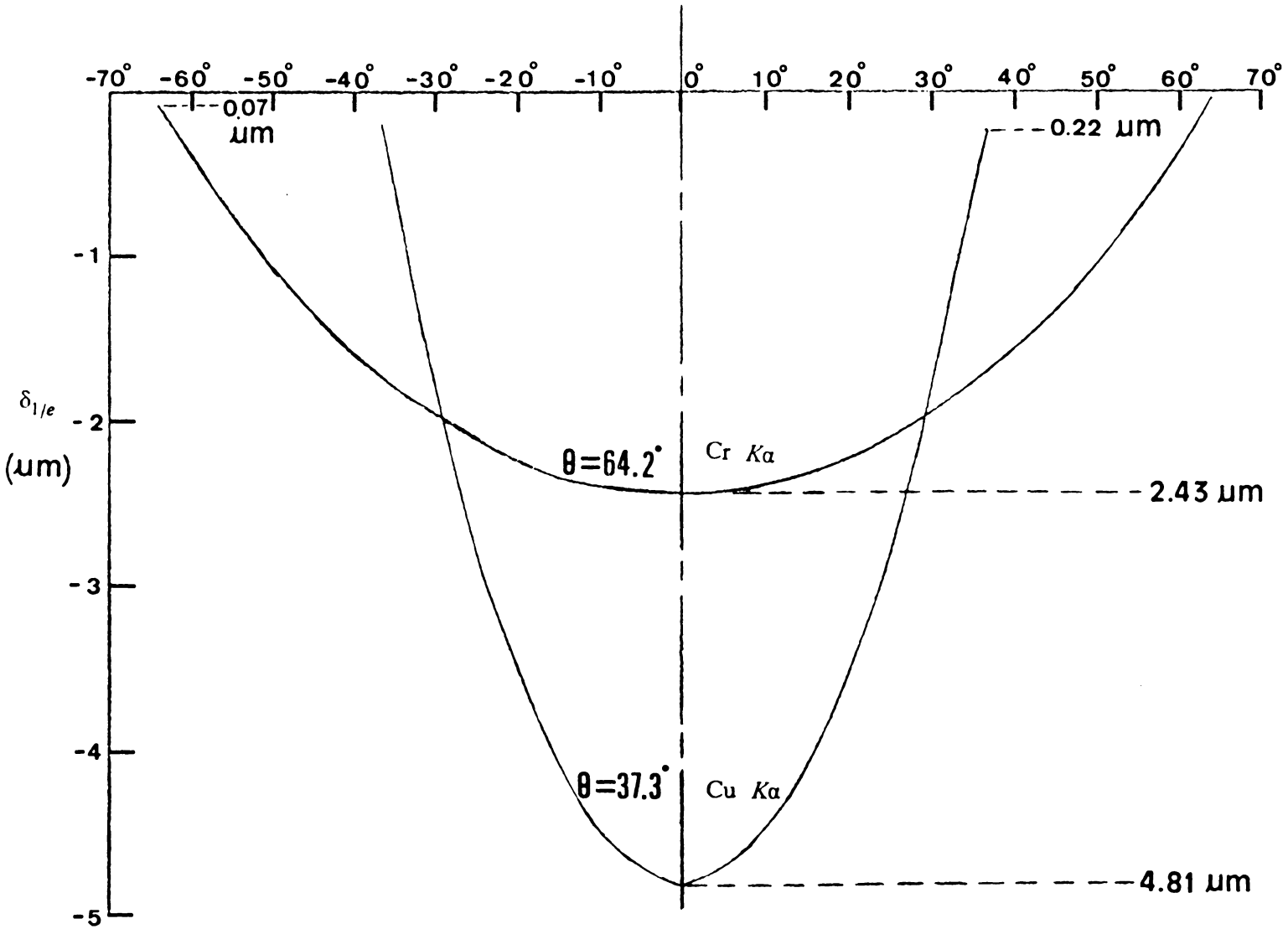

Figure 13. Effective penetration depths as functions of tilt angles for (400) reflection of PSZ

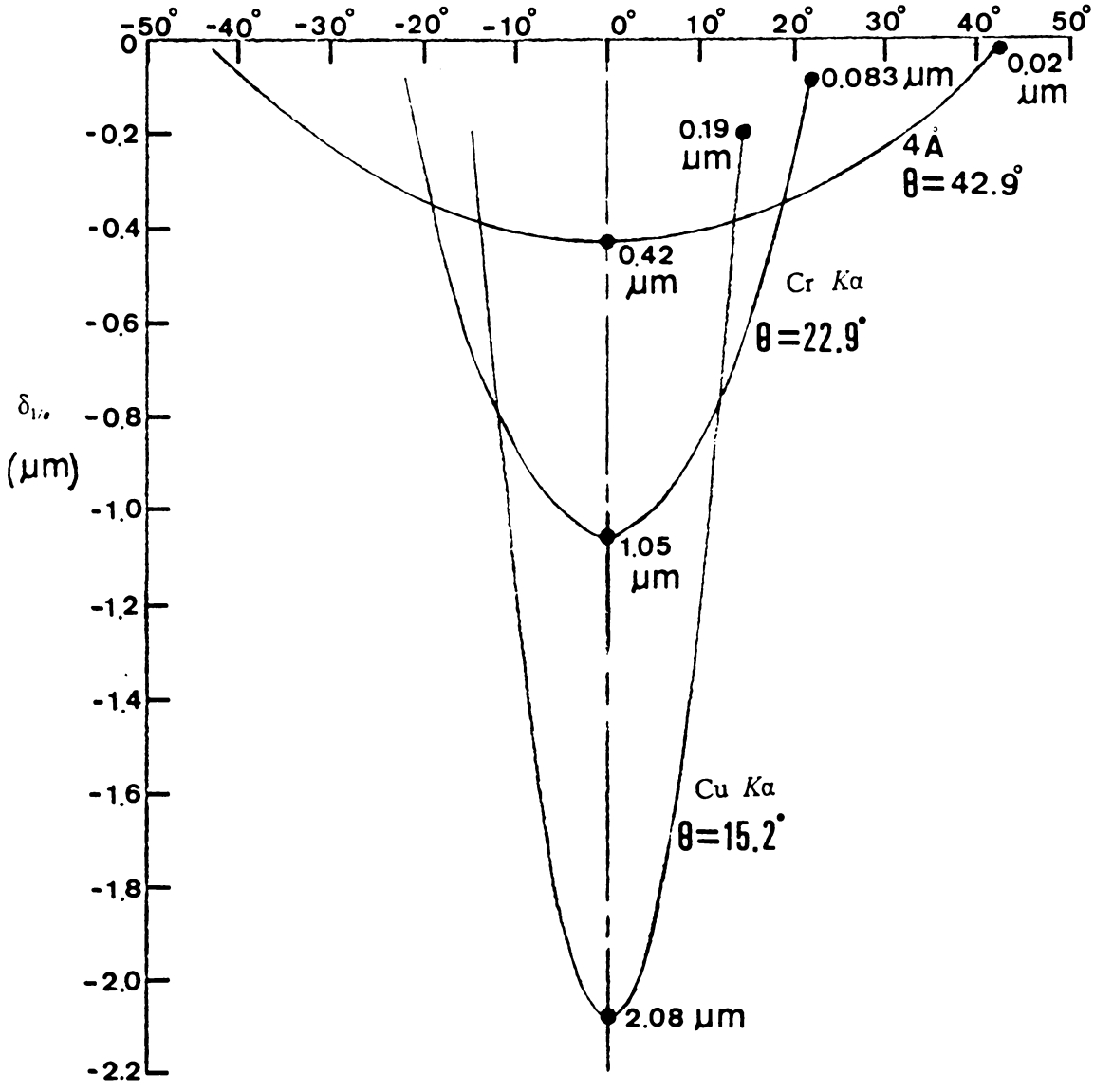

Figure 14. Effective penetration depths as functions of tilt angles for (111) rflection of PSZ

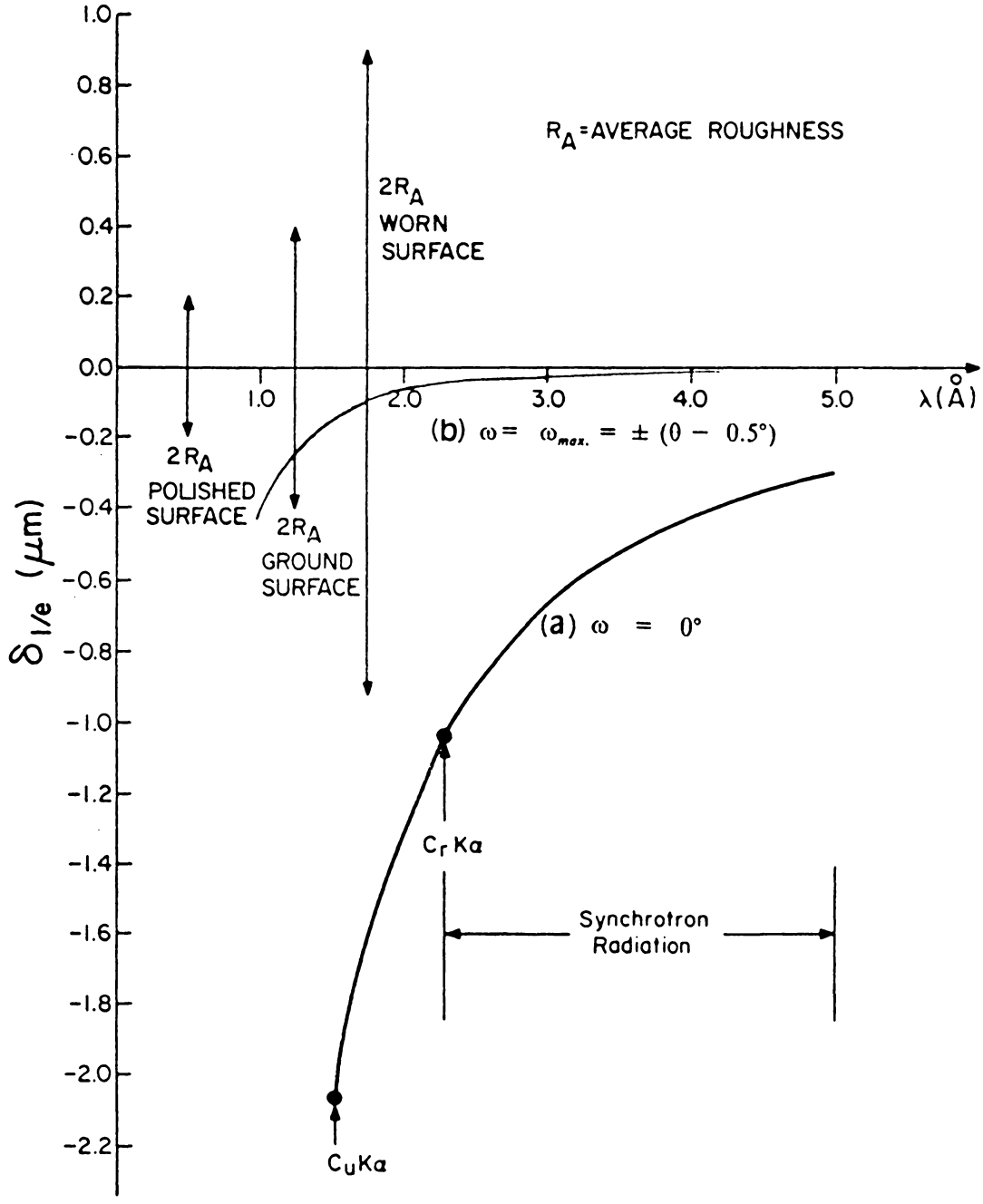

Figure 15. The effective penetration depth as a function of wavelength for (111) reflection of PSZ: (a) Symmetrical diffraction optics (b) Asymmetrical diffraction optics with a maximum tilt angle.

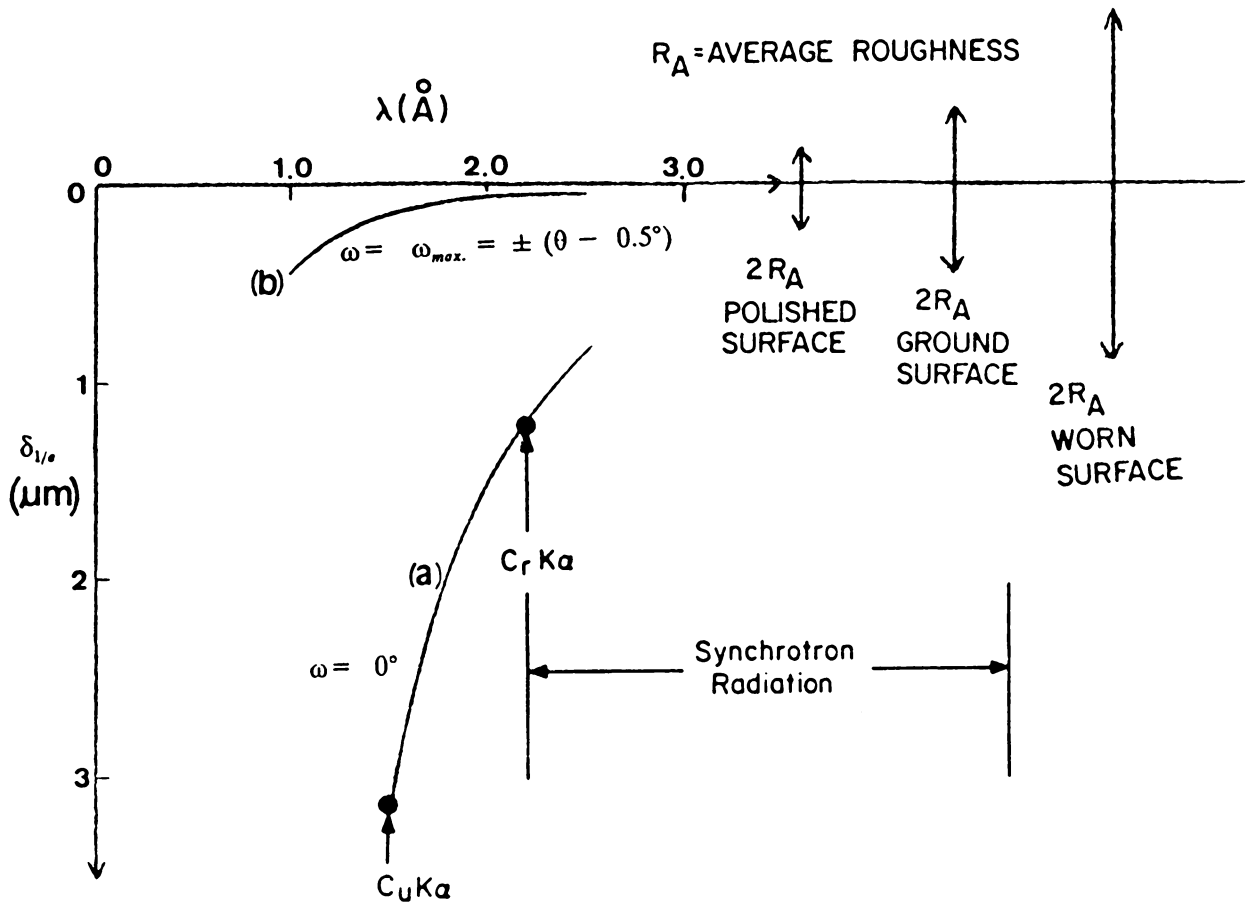

Figure 16. The effective penetration depth as a function of wavelength for (400) reflection of PSZ: (a) Symmetrical diffraction optics (b) Asymmetrical diffraction optics with a maximum tilt angle.

show that the effective penetration depth is much smaller when maximum tilt angle is used comparing to no tilt situation. Also shown in Figs. 15 and 16 are the average roughnesses produced by some machining processes. The average roughness, commonly used by tribologists, is defined as the average of absolute excursion height from the mean plane. From Figs. 15 and 16, it is clear that the average roughness could be close to or even larger than the effective penetration depth, depending on the wavelength and the tilt angle used. The magnitude of intensity correction due to surface roughness is treated in the following section using the statistical model presented in last chapter.

5.1 Theoretical Derivation of X-ray Intensity Using Statistical Roughness Model

For the ease of manupulation, the "length" or "height" terms in the statistical model are often scaled by $\sqrt{2}\sigma$. For example, $Z_s = Z/\sqrt{2}\sigma$, $dZ_s = dZ/\sqrt{2}\sigma$, $Z_{1s} = Z_1/\sqrt{2}\sigma$. The scaled forms of one dimensional and two dimensional joint normal distribution functions are:

$$p(Z_s) = \frac{1}{\sqrt{2\pi}\,\sigma} e^{-Z_s^2} \qquad (5-3)$$

$$p(Z_{1s}, Z_{2s}, \tau) = \frac{1}{2\pi\sigma^2\sqrt{1-\rho(\tau)^2}} e^{-\frac{Z_{1s}^2 - 2\rho Z_{1s}Z_{2s} + Z_{2s}^2}{1-\rho(\tau)^2}} \qquad (5-4)$$

The scaled forms of the conditional probability density function based on normal distribution and the empirical autocorrelation coefficient are:

$$p(Z_{2s}/Z_{1s}, \tau) = \frac{1}{\sqrt{2\pi}\,\sigma[1-\rho^2(\tau)]^2} e^{-\frac{[Z_{2s} - \rho(\tau)Z_{1s}]^2}{(1-\rho^2(\tau))}} \qquad (5-5)$$

$$\rho(\tau) = e^{-\frac{|\tau_s|}{\tau_{cs}}} \qquad (5-6)$$

The scaled form of the fraction of occupation given in Eq. (4-17) is,

$$A_f(Z_{2s}/Z_{1s}, \tau) = \frac{1}{2} erfc \frac{Z_{2s} - \rho Z_{1s}}{(1-\rho^2)^{1/2}} \qquad (5-7)$$

Note all scaling in above equations happens in the exponential term or in the argument of the complementary error function which must be dimensionless.

Before considering the effect of roughness on intensity, it is instructive to calculate the integrated intensity from a single phase flat sample. This is easily done by integrating Eq. (2-2) through all signal generating layers to get the total intensity:

$$I_{integrated} = \int_0^\infty \frac{I_0 Q A_0}{\sin\theta_i} e^{-(\mu_i \frac{Z}{\sin\theta_i} + \mu_s \frac{Z}{\sin\theta_s})} dZ = \frac{I_0 Q A_0}{\sin\theta_i} \frac{1}{\frac{\mu_i}{\sin\theta_i} + \frac{\mu_s}{\sin\theta_s}} \qquad (5-8)$$

The simplicity of Eq. (5-8) is largely due to the fact that all material in the same horizontal layer experiences the same absorption length. This is no longer true for a rough sample. As shown in Figure 17, the absorption lengths are different for different volume "elements" even if they are in the same layer. This fluctuation of absorption lengths is determined by the distribution of material in space and results in a deviation of the total intensity from that of the flat sample. For a rough sample, the fluctuation of absorption lengths is only significant in the near surface region. Below this region, the material associates with long absorption lengths and the surface perturbation is relatively uinimportant. Therefore, in the following calculation, the roughness effect is localized for the material to a depth of $3\sqrt{2}\sigma$, while beyond this depth, the flat sample calculation becomes adequate. The intensity contribution from this deep region can be calculated by the following equation based on the flat surface assumption.

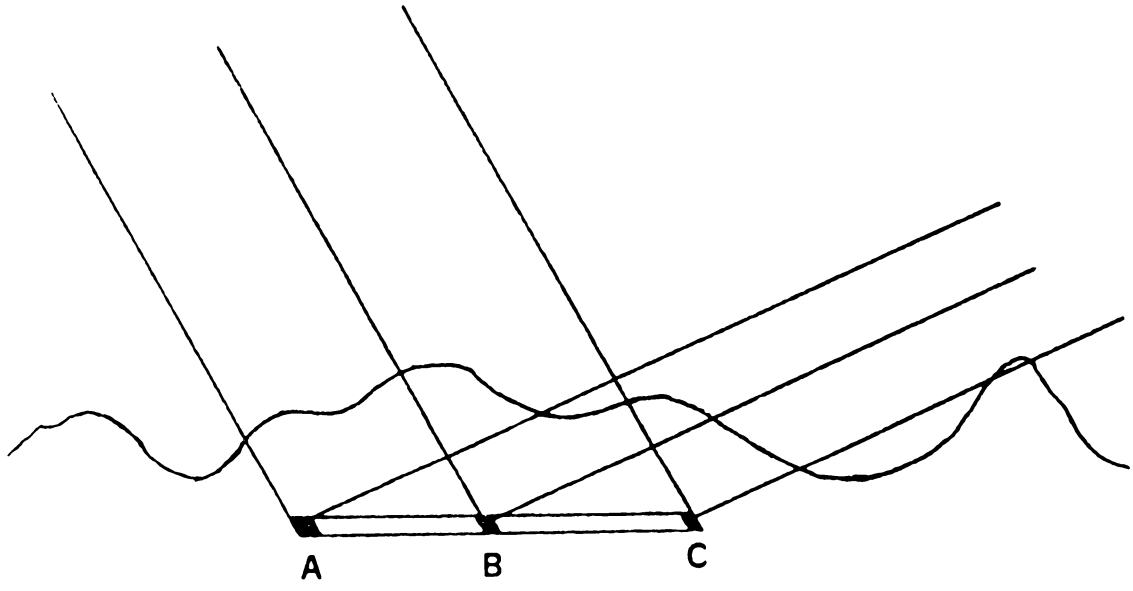

Figure 17. A schematic diagram showing different absorption lengths for different volume elements in a same layer of a rough sample.

$$I_{\text{deep region}} = \frac{I_0 Q A_0}{\sin\theta_i}\int_{-\infty}^{-3\sqrt{2}\sigma} e^{(\frac{\mu_i}{\sin\theta_i}+\frac{\mu_s}{\sin\theta_s})Z} dZ$$

$$= \frac{I_0 Q A_0}{\sin\theta_i}\frac{1}{(\frac{\mu_i}{\sin\theta_i}+\frac{\mu_s}{\sin\theta_s})} \times e^{-3\sqrt{2}\sigma(\frac{\mu_i}{\sin\theta_i}+\frac{\mu_s}{\sin\theta_s})} \qquad (5-9)$$

In the near surface region, the material located above $Z = -3\sqrt{2}\sigma$ is treated with the statistical model. The total intensity from a rough sample is the summation of the intensities calculated by the statistical model and the intensity given in Eq. (5-9). This can be expressed as:

$$I_{\text{rough sample}} = I_{\text{surface region}} + I_{\text{deep region}} \qquad (5-10)$$

with $I_{\text{surface region}}$ representing the intensity calculated from the statistical model.

The intensity from the surface region of a rough sample is the summation of intensities contributed by each volume element in this region. For each volume element, an incident and a signal rays are associated with it. As shown in Figure 18, the volume elements within a same layer are divided to many groups. Each group corresponds to a specific excursion height. For example, volume elements A,B,C,D shown in Figure 18 belong to the same group because the excursion heights are the same. This group is called group (Z_s, Z_{0s}). The intensity contributed by a group can be calculated from the following absorption consideration.

A signal ray coming out from an element of the (Z_s, Z_{0s}) group makes an angle of θ_s with the horizontal plane (see Figure 19). When excursions corresponding to all "elements" in this group are drawn in the same figure, many intersections between the excursions and the signal ray appear along the signal ray. If each excursion only intersects the signal ray once, then the signal ray is completely occupied by material below the intersection and completely empty beyond the intersection. Therefore, the distribution of the intersections along the signal ray also determines the distribution of its absorption lengths. By restricting this development to one intersection as dis-

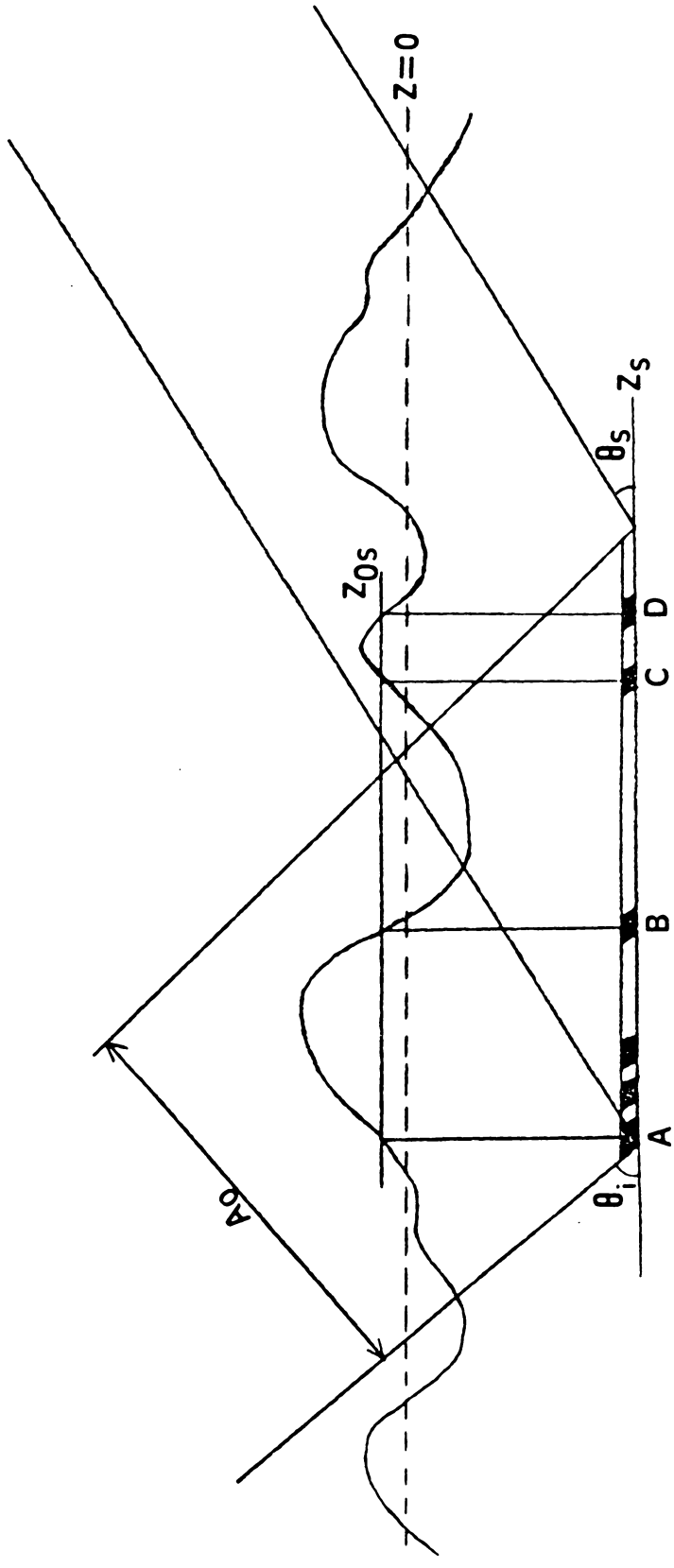

Figure 18. A schematic diagram showing the signal generating elements of a group in a rough sample.

cussed in Chapter 3, the distribution of the intersections along the signal ray for the (Z_s, Z_{0s}) group can be determined rather simply from a two-dimensional model.

In Figure 20, a point absorber on the signal ray is shown located at a scaled height of $Z_{1s} = Z_1/\sqrt{2}\,\sigma$ and separated by a scaled horizontal distance $\tau_s = \tau/\sqrt{2}\,\sigma$ from the signal generating element. A vertical line passing through this point is also shown as an absorption line. On the other hand, the vertical line passing through the signal generating element is called a signal line. Suppose the distribution of excursion heights at the signal and absorption lines can be described by a correlated two-dimensional normal distribution function $p(Z_{1s}, Z_{0s}, \tau_s)$, then the distribution of scaled excursion heights at the absorption line for (Z_s, Z_{0s}) group is given by the conditional probability density function $p(Z_{1s}/Z_{0s}, \tau)$. Every excursion of the (Z_s, Z_{0s}) group crosses the absorption line once. Among these crossings, the fraction of crossings located at or above Z_{1s} is the cumulative probability function of $p(Z_{1s}/Z_{0s}, \tau_s)$ from Z_{1s} to ∞. This function is given by Eq. (5-7),

$$A_f(Z_{1s}/Z_{0s}, \tau) = \frac{1}{2} erfc \frac{Z_{1s} - \rho Z_{0s}}{(1 - \rho^2)^{1/2}} \qquad (5-7)$$

where ρ is the autocorrelation coefficient function given in Eq. (5-6).

Because the point absorber on the signal ray is arbitrarily chosen, Eq. (5-7) is valid for any point along the signal ray. In other words, the scaled height Z_{1s} can be any value in the range of Z_s to ∞ and the function $A_f(Z_{1s}/Z_{0s}, \tau)$ given in Eq. (5-7) represents the relative probability of finding crossings in an arbitrary absorption line above the signal ray.

As shown in Figure 21, two closely spaced absorption lines intersect the signal ray at heights of Z_{1s} and $Z_{1s} + dZ_{1s}$ respectively. If the total number of signal generating elements in the (Z_s, Z_s) group is N, then the total excursions starting from the signal line is also N. $NA_f(Z_{1s}/Z_{0s}, \tau_s)$ and $NA_f(Z_{1s} + dZ_{1s}/Z_{0s}, \tau_s + d\tau_s)$ excursions are located above signal ray in the two absorption lines respectively. The difference $n = NA_f(Z1_s/Z0_s, \tau) - NA_f(Z1_s + dZ1_s/Z0_s, \tau_s + d\tau_s)$

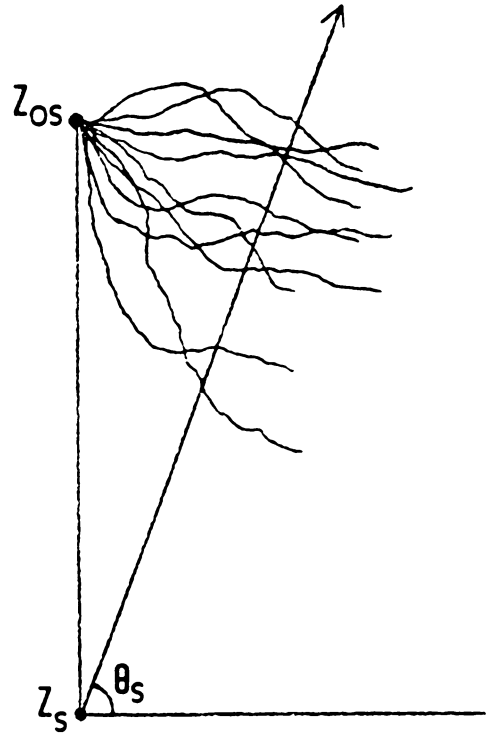

Figure 19. A shematic diagram showing the intersections between the signal ray and the surface profiles for a signal generating group.

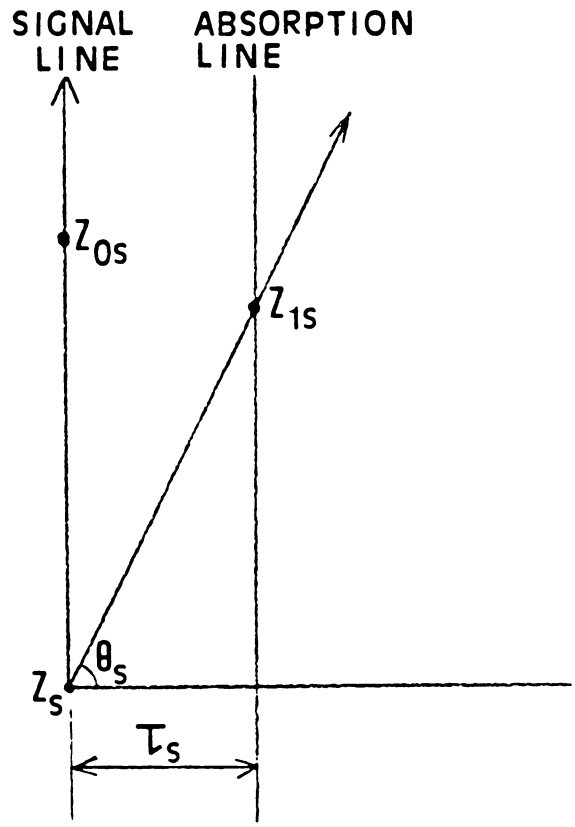

Figure 20. A schematic diagram showing the signal line and the absorption line.

gives the number of excursions passing through the signal ray in the differential spacing between the two absorption lines. Because the total number of intersections between the excursions and the signal ray is also N, n out of N intersections give a absorption length of $l_s = \sqrt{2}\,\sigma(Z_{1s} - Z_s)/\tan\theta_s$. Consequently, the probability density function $p(l_s)$ for absorption length distribution is

$$p(l_s)dl_s = \frac{n}{N} = \frac{-N[A_f(Z_{1s} + dZ_{1s}/Z_{0s,}\tau_s + d\tau_s) - A_f(Z_{1s}/Z_{0s,}\tau_s)]}{N} \qquad (5-11)$$

$$= -[A_f(Z_{1s} + dZ_{1s}/Z_{0s,}\tau_s + d\tau_s) - A_f(Z_s/Z_{0s,}\tau_s)]$$

Note that the subscript s in l_s stands for the signal ray, not scaling.

Because $A_f(Z_{1s} + dZ_{1s}/Z_{0s,}\tau_s + d\tau_s) \cong A_f(Z_{1s}/Z_{0s,}\tau_s) + A_f'(Z_{1s}/Z_{0s,}\tau_s)dZ_{1s}$,

$$p(l_s)dl_s = -A_f'(Z_{1s}/Z_{0s,}\tau_s)dZ_{1s} \qquad (5-12)$$

The derivative of $A_f(Z1_s/Z0_{s,}\tau_s)$ with respect to Z_{1s} gives the required probability density for absorption paths of length l_s.

Start from Eq. (5-7),

$$A_f'(Z_{1s}/Z_{0s,}\tau) = \frac{d}{dZ_{1s}}[A_f(Z_{1s}/Z_{0s,}\tau)] = \frac{d}{dZ_{1s}}\left[\frac{1}{2}erfc\,\frac{Z_{1s} - \rho Z_{0s}}{(1-\rho^2)^{1/2}}\right]$$

let $t = \frac{Z_{1s} - \rho Z_{os}}{(1-\rho^2)^{1/2}}$, then

$$A_f'(Z_{1s}/Z_{0s,}\tau) = \frac{d}{dZ_{1s}}\left[\frac{1}{2}erfc\,(t)\right] = \frac{d\left[\frac{1}{2}erfc\,(t)\right]}{dt}\frac{dt}{dZ_{1s}} \qquad (5-13)$$

$$= -\frac{1}{\sqrt{\pi}}e^{-t^2} \times \frac{dt}{dZ_{1s}} = -\frac{1}{\sqrt{\pi}}e^{-\frac{(Z_{1s} - \rho Z_{0s})^2}{1-\rho^2}} \times \frac{dt}{dZ_{1s}}$$

where

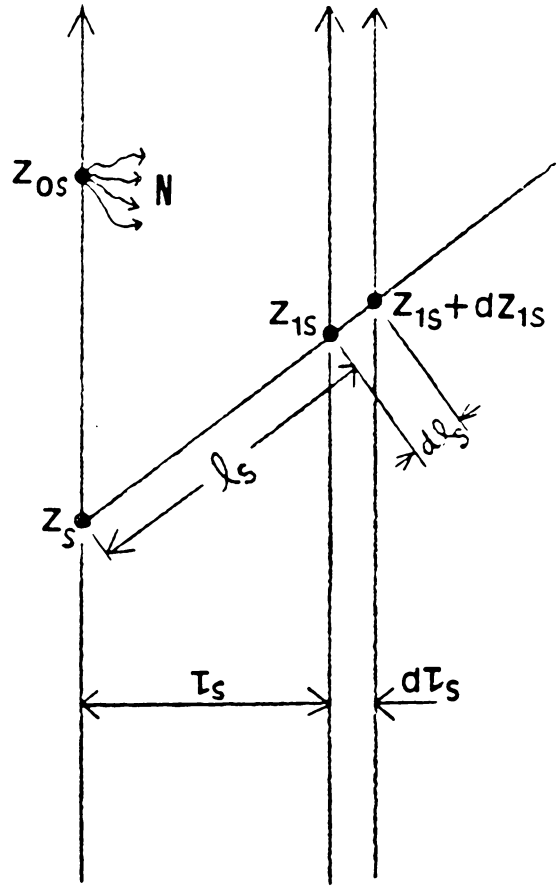

Figure 21. A shematic diagram illutrating a small section on the signal ray for the surface profiles to cross.

$$\frac{dt}{dZ_{1s}} = \frac{1}{(1-\rho^2)^{1/2}}\frac{d(Z_{1s}-\rho Z_{0s})}{dZ_{1s}} + (Z_{1s}-\rho Z_{0s})\,d\frac{[(1-\rho^2)^{-1/2}]}{dZ_{1s}}$$

$$= \frac{1}{(1-\rho^2)^{1/2}}(1 - Z_{0s}\frac{d\rho}{dZ_{1s}}) + \frac{\rho(Z_{1s}-\rho Z_{0s})}{(1-\rho^2)^{2/3}}\frac{d\rho}{dZ_{1s}} \qquad (5-14)$$

Note that $\rho = e^{-\tau_s/\tau_{cs}}$ and $\tau_s = \frac{Z_{1s}-Z_s}{\tan\theta_s}$, thereby,

$$\frac{d\rho}{dZ_{1s}} = \frac{d\rho}{d\tau_s}\frac{d\tau_s}{dZ_{1s}} = -\frac{\rho}{\tau_{cs}}(\frac{1}{\tan\theta_s}) = -\frac{\rho}{\tau_{cs}\tan\theta_s} \qquad (5-15)$$

Combine Eqs. (5-12), (5-13), (5-14) and (5-15),

$$p(l_s)dl_s = \frac{1}{\sqrt{\pi}}e^{-\frac{(Z_{1s}-\rho Z_{0s})^2}{1-\rho^2}} \times \left\{\frac{1}{\sqrt{1-\rho^2}} - \frac{\rho^2 Z_{1s}-\rho Z_{0s}}{\tau_{cs}\tan\theta_s(1-\rho^2)^{3/2}}\right\}dZ_{1s} \qquad (5-16)$$

Knowing this distribution of absorption lengths, the average absorption attenuation experienced by the signal rays of the group (Z_s, Z_{0s}) can be calculated:

$$<e^{-\mu_s l_s}> = \int_0^\infty e^{-\mu_s l_s}p(l_s)dl_s$$

$$= \frac{1}{\sqrt{\pi}}\int_{Z_s}^4 e^{-\frac{\sqrt{2}\,\sigma\mu_s(Z_{1s}-Z_s)}{\sin\theta_s}}e^{-\frac{(Z_{1s}-\rho Z_{0s})^2}{1-\rho^2}} \times \left\{\frac{1}{\sqrt{1-\rho^2}} - \frac{\rho^2 Z_{1s}-\rho Z_{0s}}{\tau_{cs}\tan\theta_s(1-\rho^2)^{3/2}}\right\}dZ_{1s} \qquad (5-17)$$

Note that the upper limit of integration is trancated at 4 since less than 0.01% of absorber can be located above $Z = 4\sqrt{2}\,\sigma$.

Eqs. (5-16) and (5-17) can be used for rays inclined at any fixed angle. Therefore, by replacing θ_s with θ_i (the incident angle) in Eqs. (5-16) and (5-17), the absorption length distribution $p(l_i)$ and average absorption attenuation factor $<e^{-\mu_i l_i}>$ for incident rays can be calculated. That is,

$$p(l_i)dl_i = \frac{1}{\sqrt{\pi}}e^{-\frac{(Z_{1s}-\rho Z_{0s})^2}{1-\rho^2}} \times \left\{\frac{1}{\sqrt{1-\rho^2}} - \frac{\rho^2 Z_{1s}-\rho Z_{0s}}{\tau_{cs}\tan\theta_i(1-\rho^2)^{3/2}}\right\}dZ_{1s} \qquad (5-18)$$

$$< e^{-\mu_i l_i} > = \int_0^\infty e^{-\mu_i l_i} p(l_i) dl_i$$

$$= \frac{1}{\sqrt{\pi}} \int_{Z_s}^{4} e^{-\frac{\sqrt{2}\,\sigma\mu_i (Z_{1s} - Z_s)}{\sin\theta_i}} e^{-\frac{(Z_{1s} - \rho Z_{0s})^2}{1-\rho^2}} \times \left\{ \frac{1}{\sqrt{1-\rho^2}} - \frac{\rho^2 Z_{1s} - \rho Z_{0s}}{\tau_{cs} \tan\theta_i (1-\rho^2)^{3/2}} \right\} dZ_{1s} \qquad (5-19)$$

The average absorption attenuation factor the group (Z_s, Z_{0s}) is:

$$A(Z_s, Z_{0s}) = < e^{-(\mu_i l_i + \mu_s l_s)} > = \int_0^\infty \int_0^\infty p(l_i, l_s)\, e^{-(\mu_i l_i + \mu_s l_s)} dl_i dl_s \qquad (5-20)$$

where $p(l_i, l_s)$ is the probability density of the signal generating elements having absorption lengths l_i and l_s in incident and signal paths. $p(l_i, l_s)$ is determined by the correlation between the intersections of (1) the excursions and the incident rays and (2) the excursions and the signal rays. This correlation can only be obtained when the specific surface profile is known. In this statistical model, this correlation is built through the common dependence of both intersections on the excursion height above the intermediate signal generating point. In other words, the distribution of the intersections in either side depends only on the excursion height on the intermediate signal line but not on the distribution of the intersections in the other side. This approximation gives

$$A(Z_s, Z_{0s}) = < e^{-(\mu_i l_i + \mu_s l_s)} > \cong \int_0^\infty \int_0^\infty p(l_i)\, p(l_s) e^{-(\mu_i l_i + \mu_s l_s)} dl_i dl_s$$

$$= \int_0^\infty p(l_i)\, e^{-\mu_i l_i} dl_i \int_0^\infty p(l_s)\, e^{-\mu_s l_s} dl_s = < e^{-\mu_i l_i} > < e^{-\mu_s l_s} > \qquad (5-21)$$

Note that for the symmetrical case of $\theta_i = \theta_s$, $p(l_i) = p(l_s)$. This implies a statistical symmetry in the sense that excursions 1 and 2 (see Figure 22) are equally probable.

When incident and signal rays are on the same side of the sample normal, the signal line does not serve adequately as a bridge for relating the intersections on the incident and signal rays because it is no more intermediate. Therefore, this model is restricted to the range of 0° to 90° for both θ_i and θ_s.

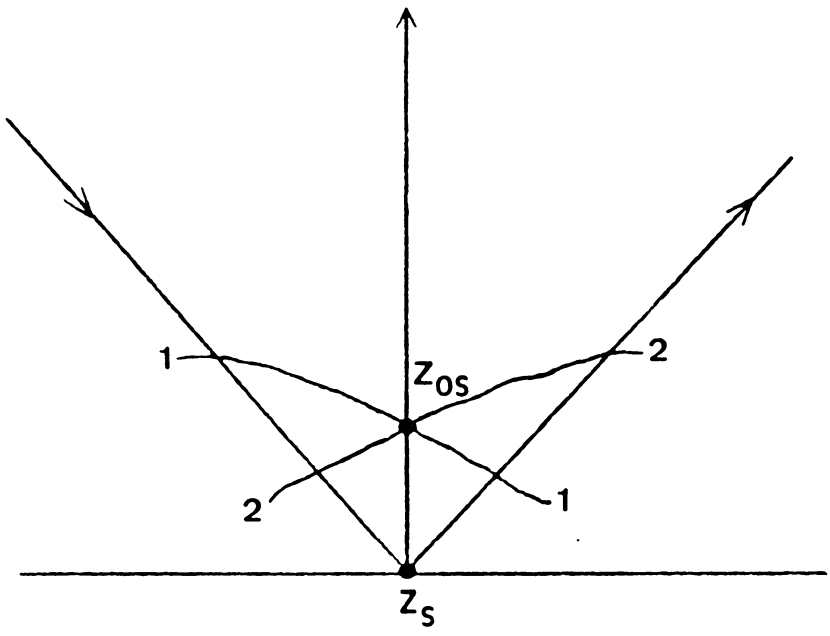

Figure 22. A schematic diagram showing two equiprobable surface profiles in a signal generating group.

According to the fundamental x-ray theory, the intensity contributed by a specific group (Z_s, Z_{0s}) is

$$I_{\text{group}(Z_s, Z_{0s})} = I_0 Q \Delta V_{\text{group}(Z_s, Z_{0s})} \times A(Z_s, Z_{0s}) \qquad (5-22)$$

where $\Delta V_{\text{group}(Z_s, Z_{0s})}$ is the total volume of all elements in group (Z_s, Z_{0s}). Because the height distribution of excursion is normal (see Fig. 18),

$$\begin{aligned} \Delta V_{\text{group}(Z_s, Z_{0s})} &= \Delta V_{\text{layer}(Z_s)} \times (\text{volume fraction of group } (Z_s, Z_{0s}) \text{ in layer}(Z_s)) \\ &= \Delta V_{\text{layer}(Z_s)} \times \sqrt{2}\,\sigma p(Z_{0s}) dZ_{0s} \end{aligned} \qquad (5-23)$$

where $p(Z_{0s})$ is the normalized probability density function given in Eq. (5-3) and $\Delta V_{\text{layer}(Z_s)}$ is: (see Figure 18)

$$\Delta V_{\text{layer}(Z_s)} = \frac{\sqrt{2}\,\sigma A_0}{\sin\theta_i} dZ_s \qquad (5-24)$$

Combine Eqs. (5-3), (5-22), (5-23), (5-24),

$$I_{\text{group}(Z_s, Z_{0s})} = \frac{\sqrt{2}\,\sigma I_0 Q A_0}{\sqrt{\pi}\,\sin\theta_i} \times e^{-Z_{0s}^2} A(Z_s, Z_{0s}) dZ_{0s} dZ_s \qquad (5-25)$$

The intensity contributed by layer(Z_s) is simply the summation of the intensities contributed by all groups in this layer. It can be obtained by integrating Eq. (5-25) through all possible Z_{0s} :

$$I_{\text{layer}(Z_s)} = \frac{\sqrt{2}\,\sigma I_0 Q A_0}{\sqrt{\pi}\,\sin\theta_i} \times \int_{Z_s}^{3} e^{-Z_{0s}^2} A(Z_s, Z_{0s}) dZ_{0s} dZ_s \qquad (5-26)$$

Note that Z_{0s} ranges from Z_s to 3. For $Z_{0s} < Z_s$, the corresponding groups have empty elements (see Fig. 18) which contribute no intensity. For $Z_{0s} > 3$, the corresponding groups have little ma-

terial and are neglected as mentioned earilier. Because the total intensity from the near surface region is the summation of the intensities contributed by each layer in this region, it can be obtained by integrating Eq. (5-26) through all possible Z_s :

$$I_{\text{surface region}} = \frac{\sqrt{2}\,\sigma I_0 Q A_0}{\sqrt{\pi}\,\sin\theta_i} \times \int_{-3}^{3}\int_{Z_s}^{3} e^{-Z_{0s}^2} A(Z_s, Z_{0s})\, dZ_{0s}\, dZ_s \qquad (5-27)$$

Note that Z_s ranges from -3 to 3, the near surface region. Both Eqs. (5-17), (5-19), and (5-27) have no closed form and need to be integrated numerically. Combine Eqs. (5-9), (5-10), and (5-27),

$$\begin{aligned} I_{\text{rough sample}} = {} & \frac{\sqrt{2}\,\sigma I_0 Q A_0}{\sqrt{\pi}\,\sin\theta_i} \times \int_{-3}^{3}\int_{Z_s}^{3} e^{-Z_{0s}^2} A(Z_s, Z_{0s})\, dZ_{0s}\, dZ_s \\ & + \frac{I_0 Q A_0}{\sin\theta_i} \frac{1}{\dfrac{\mu_i}{\sin\theta_i} + \dfrac{\mu_s}{\sin\theta_s}} \times e^{-3\sqrt{2}\,\sigma\left(\frac{\mu_i}{\sin\theta_i} + \frac{\mu_s}{\sin\theta_s}\right)} \end{aligned} \qquad (5-28)$$

The intensity given in Eq. (5-28) is usually divided by the corresponding intensity from a flat sample given in Eq. (5-8) to give the intensity ratio R:

$$\begin{aligned} R = \frac{I_{\text{rough sample}}}{I_{\text{flat sample}}} = {} & \sqrt{2/\pi}\,\sigma\left(\frac{\mu_i}{\sin\theta_i} + \frac{\mu_s}{\sin\theta_s}\right) \times \int_{-3}^{3}\int_{Z_s}^{3} e^{-Z_{0s}^2} A(Z_s, Z_{0s})\, dZ_{0s}\, dZ_s \\ & + e^{-3\sqrt{2}\,\sigma\left(\frac{\mu_i}{\sin\theta_i} + \frac{\mu_s}{\sin\theta_s}\right)} \end{aligned} \qquad (5-29)$$

A computer program with repeated use of 12 points Gaussian-Legendre guadrature formula is written to carry out the integral in Eq. (5-29). This program is well documented and shown in Appendix A.

5.2 *Experimental Verification of The Statistical Model*

The statistical model is verified by measuring the intensities from two real samples. The samples are fully stablized zirconia (FSZ) with 8 mol% Y_2O_3 as stabilizer. One sample is well polished to serve as a flat standard. The other is intentionally roughened by severe griding. Both samples have the final shape of a circular disk with diameter of 7/8 inch and thickness of 2.5 mm.

The values of σ and τ_c needed in the simulation are obtained by profilometer measurement. Three traces on each sample were measured by a Talysurf 4 profilometer along with a personal computer for recording. While the stylus travels along the traces at a speed of 91.4 mm/min., one digitized height was recorded by the computer every two miliseconds without electronic or digital filtering. The horizontal interval between two successive points is $\Delta X = 3.046\,\mu m$. The total length of each trace is 1.52 mm which consists of 499 digitized points. One trace of each sample is plotted using the digitized points and shown in Figures 23 and 24. Also shown in Fig. 23 and 24 are the corresponding autocorrelation coefficient function. The autocorrelation coefficient function is calculated directly from the digitized data as follows,

$$\rho(n\Delta X) = \frac{1}{\sigma^2}\frac{1}{N}\sum_{N} Z(X)Z(X + n\Delta X) \qquad (5-30)$$

where n is integer and $n\Delta X$ is the distance between two locations whose correlation are calculated. N is the number of pairs of locations averaged in Eq. (5-30). Note N = 499-n because only 499 digitized points are available. The variance σ^2 is calculated by

$$\sigma^2 = \frac{1}{499}\sum_{n=0}^{498} Z(n\Delta X)Z(n\Delta X) \qquad (5-31)$$

As shown in Fig. 23 and 24, the autocorrelation coefficient starts at 1, decays first, then followed by some irregular fluctuation. The abscissa where the autocorrelation coefficient drops to 1/e is

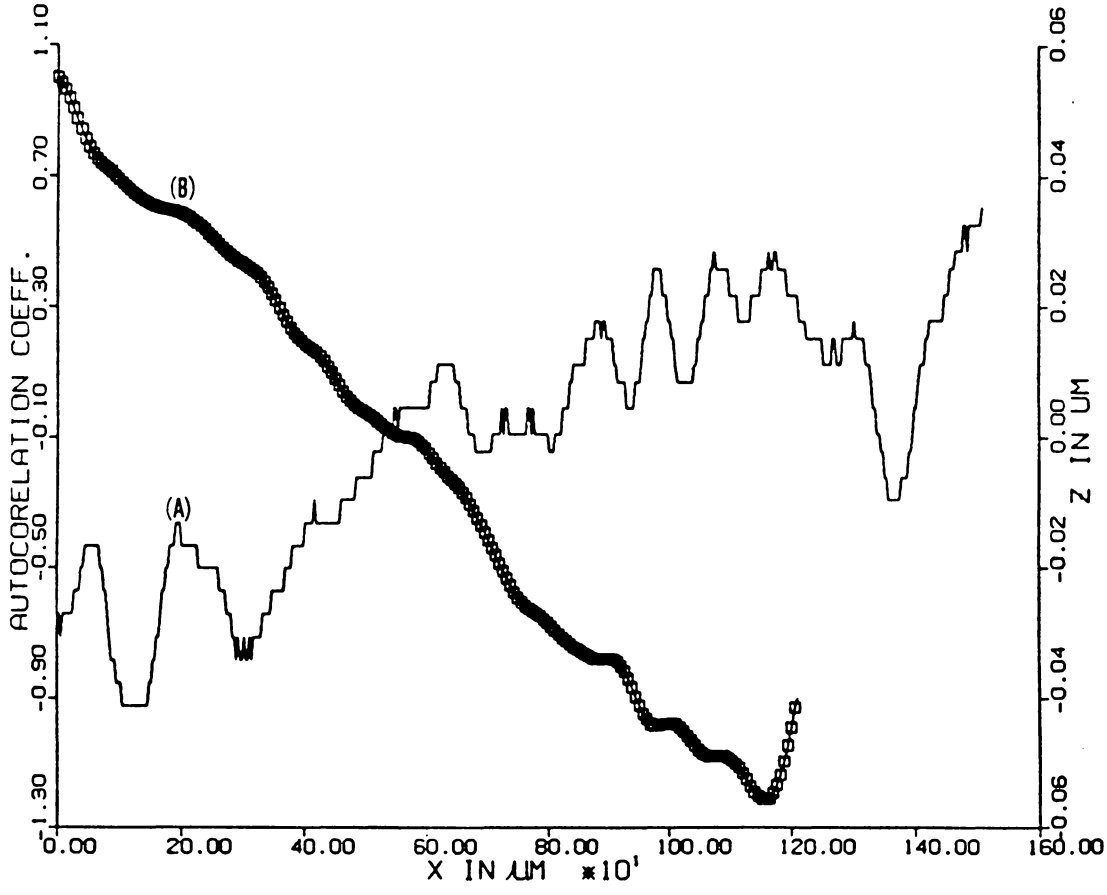

Figure 23. **The surface profile and autocorrelation function of the polished FSZ sample:** (A) Surface profile (B) Autocorrelation function

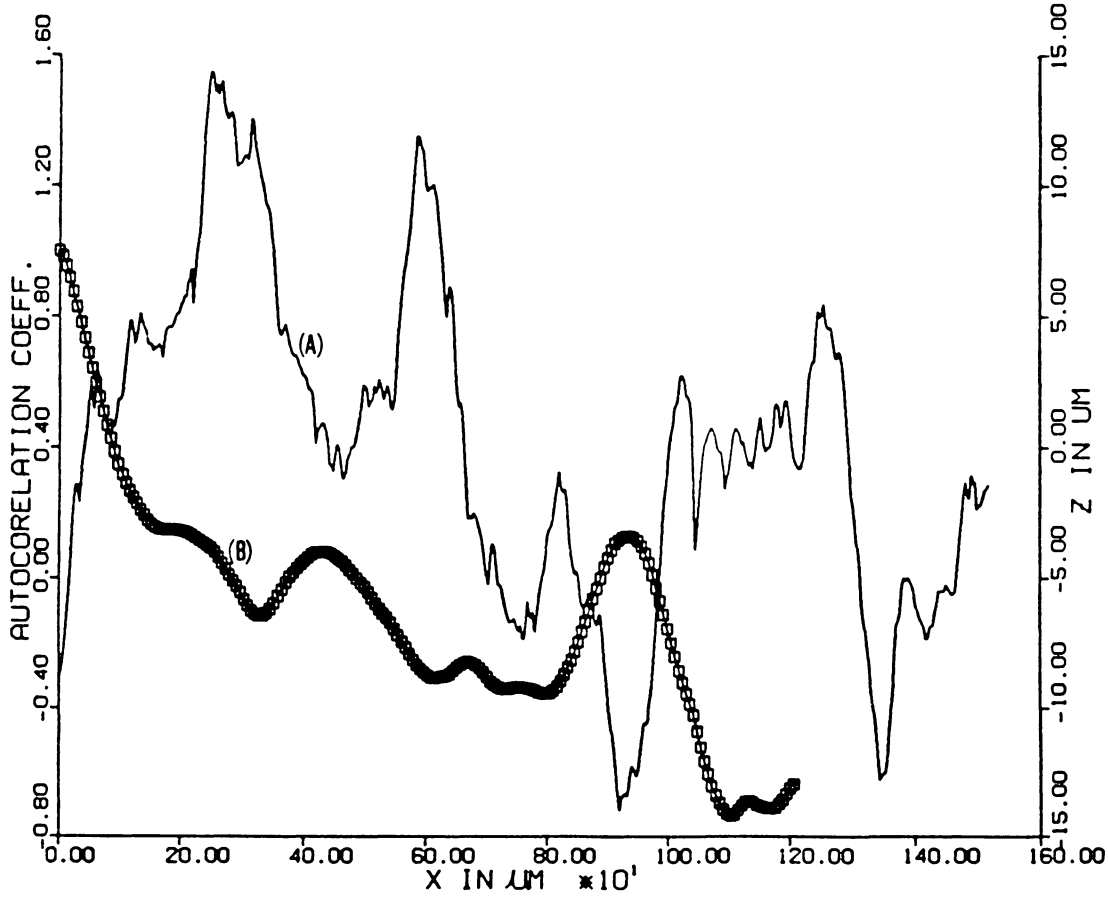

Figure 24. **The surface profile and autocorrelation function of the ground PSZ sample:** (A) Surface profile (B) Autocorrelation function

taken as τ_c, the correlation distance. The σ and τ_c values obtained from different traces of the two samples are listed in Tables 1 and 2. The values averaged over all traces are $\sigma = 6.2$ μm, $\tau_c = 82$ μm for the rough sample and $\sigma = 0.027$ μm, $\tau_c = 200$ μm for the flat sample. As expected, these values indicate that the polished sample has much smaller surface fluctuation and much smaller fluctuation rate comparing to the ground sample.

The intensity ratio given in Eq. (5-29) is simulated using the averaged σ and τ_c values of the rough sample for symmetrical diffraction and Cu $K\alpha_1$ radiation. The linear absorption coefficient of FSZ for this radiation is 650 cm^{-1}. The result is shown in Figure 25. The dashed line in Fig. 25 represents a region influenced by multiple intersection which will be discussed in Section **5.4**. Also shown in Fig. 25 is the ratios of intensities measured from the flat and rough samples. The measurements were carried out on a Siemens diffractometer with Cu tube and a diffracted beam quartz monochromator. The tube was operated at an accerating voltage of 50 kV and a tube current of 20 mA. The quartz monochromator was used to eliminate the $K\alpha_2$ component from the Cu $k\alpha$ radiation. The incident and receving slits are 1° and 0.05° respectively. Two overlapping slow scans (0.1°/min.) were made over a total of 12 peaks for each sample under symmetrical diffraction geometry. The peak areas corrected for background are then measured by a planimeter. The ratio of the areas from the same reflection of the two samples was then taken as intensity ratio.

As shown in Fig. 25, the theoretical simulation based on the statistical model is close to the experimental data except in the very low angle region where no experimental data is available and the theory becomes inappropriate because of multiple intersections. The slight difference between the results of simulation and experiments is due to the simplification of the correlation made in Eq. (5-21). The influence of the multiple intersections will be further discussed in Section **5.4**.

Due to the nonstationarity of a rough sample mentioned in Chapter 2, the sampling length of x-ray measurement is ideally to be kept at the same value used by the profilometer. However, this sampling length, essentially the width of the sample illuminated by the incident beam, changes from

Table 1. The σ and τ Values of the Polished FSZ Sample.

	trace #1	trace #2	trace #3
σ (μm)	0.0197	0.0191	0.0411
τ_c (μm)	66	338	192

Table 2. The σ and τ Values of the Ground FSZ Sample.

	trace #1	trace #2	trace #3
σ (μm)	5.371	7.096	6.197
τ_c (μm)	63	58	94

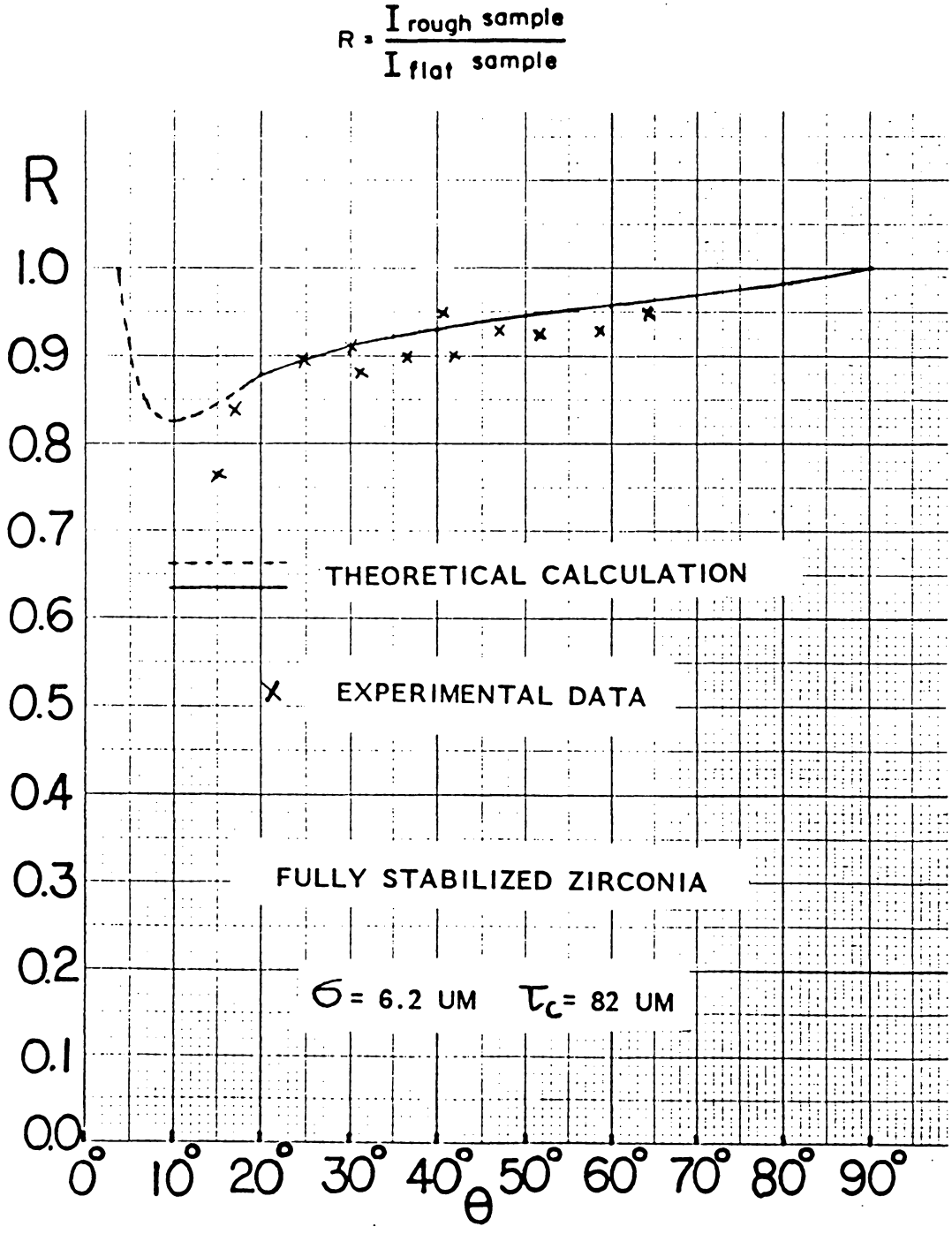

Figure 25. The calculated and experimental intensity corrections for the ground FSZ sample.

one reflection to the other when a fixed incident slit is used. In the measurements of x-ray intensities from the FSZ samples, the illuminated widths ranges from 3.65 mm (corresponding to (111) reflection) to 1.04 mm (corresponding to (600) reflection) with most of them concentrate around 1.52 mm, the sampling length used by the profilometer. This compromise in measurement, as shown in Figure 25, still yields good agreement between the theoretical predictions and experimental data. This agreement implies that τ_c and σ are not strong functions of the sampling length.

5.3 Comparison with Borie's Calculation

As indicated in Section **5.2**, the probability density of excursion heights for a sawtooth surface is very different from that of a Gaussian surface. This is shown in Fig. 5 and results in a big difference in the distribution of absorption lengths. This difference can be seen in Figure 26 where signal generating elements A, B, A′, B′... all belong to the (Z_s, Z_{0s}) group of a sample with a sawtooth surface. The absorption length associated with element A is equal to that associated with element A′ and the absorption length associated with element B is equal to that of element B′ due to the periodic repeatition of the identical geometrical environment. In fact, there are only two different absorption lengths associated with each group. This is very different from the Gaussian surface where the members in a same group may experience many different absorption lengths. To make the intensity comparison between these two surfaces more meaningful, the statistical model is modified in such a way that an average absorption length is used for all signal generating elements in the same group. This average absorption length is obtained as follows.

In Figure 27, a signal generating element belonging to the (Z_s, Z_{0s}) group is shown along with its signal ray. An arbitrary point with scaled height Z_{1s} is chosen on the signal ray. This point may be empty for some signal generating elements and occupied by material for the other signal generating elements in the same group. Imagine an absorption line running through the chosen point

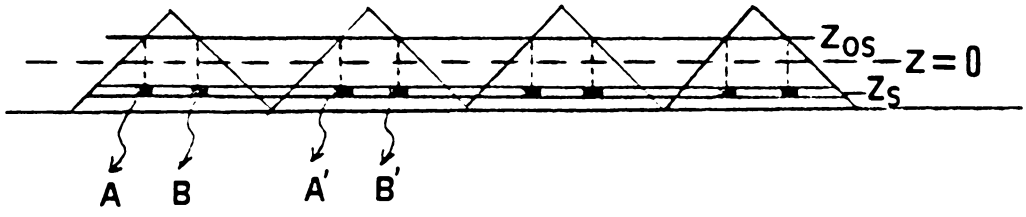

Figure 26. A shematic diagram showing the signal generating elements of a same group in a sample with sawtooth surface.

again, if the excursion intersects this line at a position higher than Z_{1s} , then the chosen point is occupied by material, otherwise, it is empty. Therefore, the possibility for this point to be occupied is

$$A_f(Z1_s/Z_{0s},\tau) = \sqrt{2}\,\sigma\int_{Z_{1s}}^{\infty} p(Z_{1s}'/Z_{0s},\ \tau_s)dZ_{1s}'$$

This was shown previously and given in Eq. (5-7), i.e.

$$A_f(Z_{1s}/Z_{0s},\tau) = \frac{1}{2}\mathrm{erfc}\frac{Z_{1s} - \rho Z_{0s}}{\sqrt{1-\rho^2}} \qquad (5-7)$$

Because the point on the signal ray is arbitrary chosen, it can be any point on the signal ray and Eq. (5-7) gives the possibility of occupation for any point along the signal ray. As shown in Figure 27, the incremental length of the signal ray at the height of Z_{1s} is

$$dl_s = d\left[\frac{\sqrt{2}\,\sigma(Z_{1s} - Z_s)}{\sin\theta_s}\right] \qquad (5-32)$$

Therefore, the average absorption length for signal rays of the (Z_{1s}, Z_{0s}) group is

$$\begin{aligned} <l_s> &= \int_0^{\infty} A_f(Z_{1s}/Z_{0s},\tau)\,dl = \int_0^{\infty} A_f(Z_{1s}/Z_{0s},\tau)\,d\left[\frac{\sqrt{2}\,\sigma(Z_{1s} - Z_s)}{\sin\theta_s}\right] \\ &= \frac{\sqrt{2}\,\sigma}{\sin\theta_s}\int_{Z_s}^{\infty} A_f(Z_{1s}/Z_{0s},\tau)\,dZ_{1s} \end{aligned} \qquad (5-33)$$

Similarly, the average absorption length for incident rays of (Z_s, Z_{0s}) group is

$$<l_i> = \frac{\sqrt{2}\,\sigma}{\sin\theta_i}\int_{Z_s}^{\infty} A_f(Z_{1s}/Z_{0s},\tau)\,dZ_{1s} \qquad (5-34)$$

and the fictitious absorption factor for the (Z_s, Z_{0s}) group is

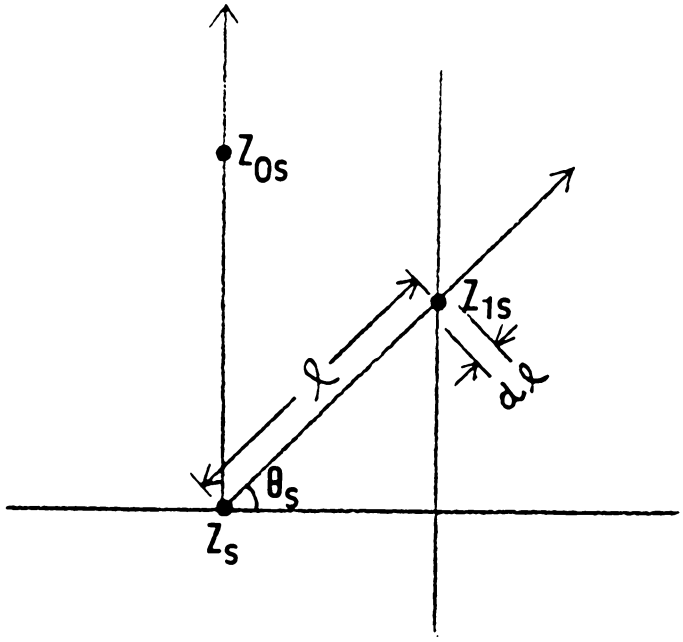

Figure 27. A schematic diagram showing a signal generating element and the signal ray.

$$\overline{A}(Z_s, Z_{0s}) = e^{-\{\mu_i < l_i > + \mu_s < l_s >\}} \qquad (5-35)$$

By replacing $A(Z_s, Z_{0s})$ in Eq. (5-21) by $\overline{A}(Z_s, Z_{0s})$ in Eq. (5-35), and let $\mu_i = \mu_s = \mu$ and $< l_i > = < l_s >$ for symmetrical diffraction, the intensity ratios given in Eq. (5-29) are calculated and the result is shown in Figure 28 along with Borie's exact calculation for a sawtooth surface. Note that σ, τ_c and absorption coefficient are chosen to be the same for both samples. The chosen value of linear absorption coefficient corresponds to the Cr $K\alpha$ radiation for the FSZ sample. Although the height distributions of the two surfaces are very different, the result in Figure 28 still shows striking simularities:

1. Both curves of intensity ratio converge to unity at $\theta = 0°$ and $\theta = 90°$. These agree with Harrison and Paskin's theory because $\theta = 0°$ corresponds to the case where the signal and incident rays are completely uncorrelated and $\theta = 90°$ corresponds to the completely correlated case.

2. Both curves of intensity ratio go down as θ deviates from the two extremes. The minimum intensity ratios shown by both curves are amazingly close.

The maximum correction for the sawtooth sample appears at $\theta = 45°$. This is due to the 45° angle in the sawtooth which results in an average absolute slope $\overline{|s|} = 1$. This relationship between the location of maximum correction and the average absolute slope (i.e. $\tan^{-1}\overline{|s|} = \theta_{\text{max. correction}}$) suggests that $\theta_{\text{max. correction}}$ is a function of $\overline{|s|}$. Does the same relation hold for the sample with a Gaussian surface? This point will be discussed in next section where the original statistical model is based without using the fictitious absorption factor.

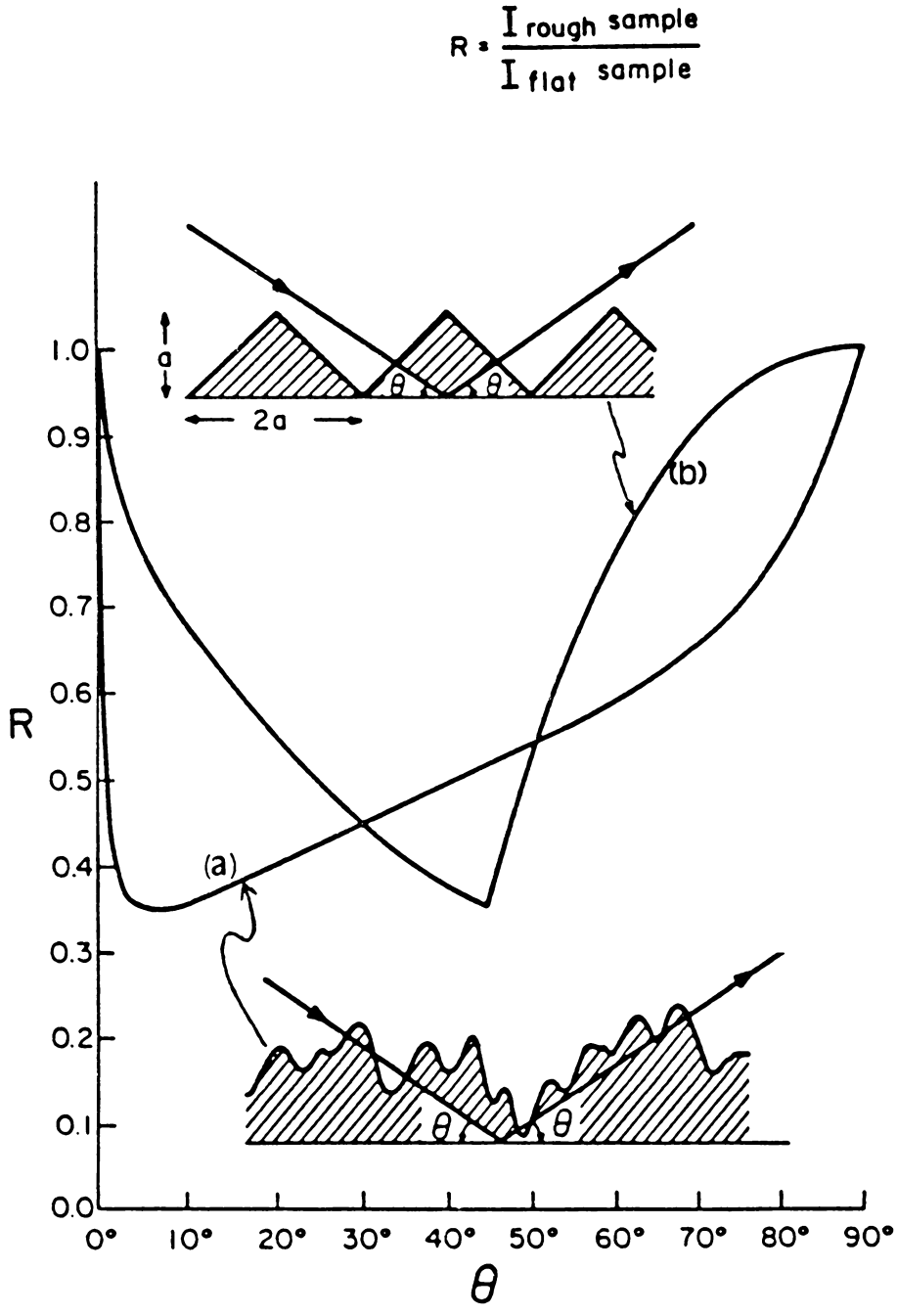

Figure 28. The calculated intensity ratios: (a) statistical model (b) sawtooth model ($\sigma = 6.08$ μm, $\mu = 1900$ cm^{-1})

5.4 *Comparison with Harrison and Paskin's Theory*

Although Harrison and Paskin's theory can be applied to the roughness problem, it does have some differences from the present statistical model. As mentioned in Section **3.1**, except the two extreme cases, Harrison and Paskin's theory only describes the intensity correction qualitatively in terms of the correlation between the incoming and outgoing paths. The quantitative calculation, as shown in Eq. (3-1), can not be carried out unless the specific surface profile is known. On the other hand, quantitative intensity calculation based on the statistical model and Eq. (5-29) can be made as long as the σ and τ_c values are known. One important difference between Harrison and Paskin's theory and the statistical model is implicit in Eqs. (3-1) and (5-29). In Eq. (3-1), the integration of $(\frac{\partial L_{ai}}{\partial X})_Z$ and $(\frac{\partial L_{as}}{\partial X})_Z$ need to be carried out throughout the whole volume illuminated by the incident beam. In other words, this calculation includes the points which are empty as well as those who are occupied by material. On the other hand, by directly calculating the total intensity instead of intensity correction, the statistical model requires each signal generating element to be occupied by material. This is reflected in Eq. (5-29) where Z_{0s}, the scaled excursion height at signal line (see Fig. 20), ranges from Z_s to 3.

Another big difference between Harrison and Paskin's theory and the statistical model lies in their treatments of correlation. To be specific, Eq. (3-1) is determined by the correlation between $(\frac{\partial L_{ai}}{\partial X})_Z$ and $(\frac{\partial L_{as}}{\partial X})_Z$. That is, the correlation between the changing rate of the true absorption lengths in incident and signal paths along the horizontal direction. For the case of granularity effect, this correlation depends on the distribution of intergranular pores within the sample. Both incident and signal rays experience on-off, on-off sequences of absorption as they travel in the sample. As shown in Figure 29(a), the absorption lengths of each "on" or "off" period are not costant because the integranular pores and particles have various sizes. For the roughness case, similar on-off sequence is caused by the multiple intersections between the surface profile and the incident or signal ray. Again the "on" and "off" periods are not contant as shown in Figure 29(b). Due to this irreular

sized on-off sequences, the correlation between the changing rate along the horizontal direction of the true absorption lengths in the incoming and outgoing paths is very complicated. This complexity is avoided in the statistical model by the "single intersection" assumption. With this assumption, the incident or signal ray only intersects the surface profile once and the on-off sequence does not exist. Because the position of intersection determines the absorption length for the concerned ray, the complicated correlation mentioned above is simplified to the correlation between the intersection positions on the incident and signal paths. This simplified correlation is finally established indirectly in the statistical model through (1) the correlation between the intersection in incident path and the excursion height above signal generating element and (2) the correlation between the intersection in the signal path and the excursion height above the signal generating element. As presented in Section **5.1**, the correlation in either (1) or (2) is based on a two-dimensional normal distribution function for the excursion heights with a exponentially decaying autocorrelation coefficient function. The simplification in the statistical model allows a complicated phenomenon to be handled mathematically.

In the low angle cases, the incident and signal rays make very small angles with the horizontal plane and tend to intersect the surface profile more than once. An estimate is needed for the critical angle below which the multiple intersections cause perceptible error in the intensity calculation.

An approach for estimating this critical angle is based on the consideration of the surface slope. If a surface profile is to intersect a signal or incident ray for the second time after the first intersection, the absolute slope of the profile needs to be larger than that of the signal or incident ray for a considerable long interval after the first intersection. For a Gaussian slope distribution with mean 0 and standard deviation σ_{slope}, the total probability of the slope within the range of $(-2\sigma_{slope}, 2\sigma_{slope})$ is 0.96. Because only 4% of the surface profile has absolute slope larger than $2\sigma_{slope}$, a profile is highly unlikely to intersect a signal or incident ray for the second time if the ray has absolute slope larger than $2\sigma_{slope}$. This yields a natural estimate of the critical angle $\theta_c = \tan^{-1}(2\sigma_{slope})$ above which multiple intersection is trivial. Because average absolute slope

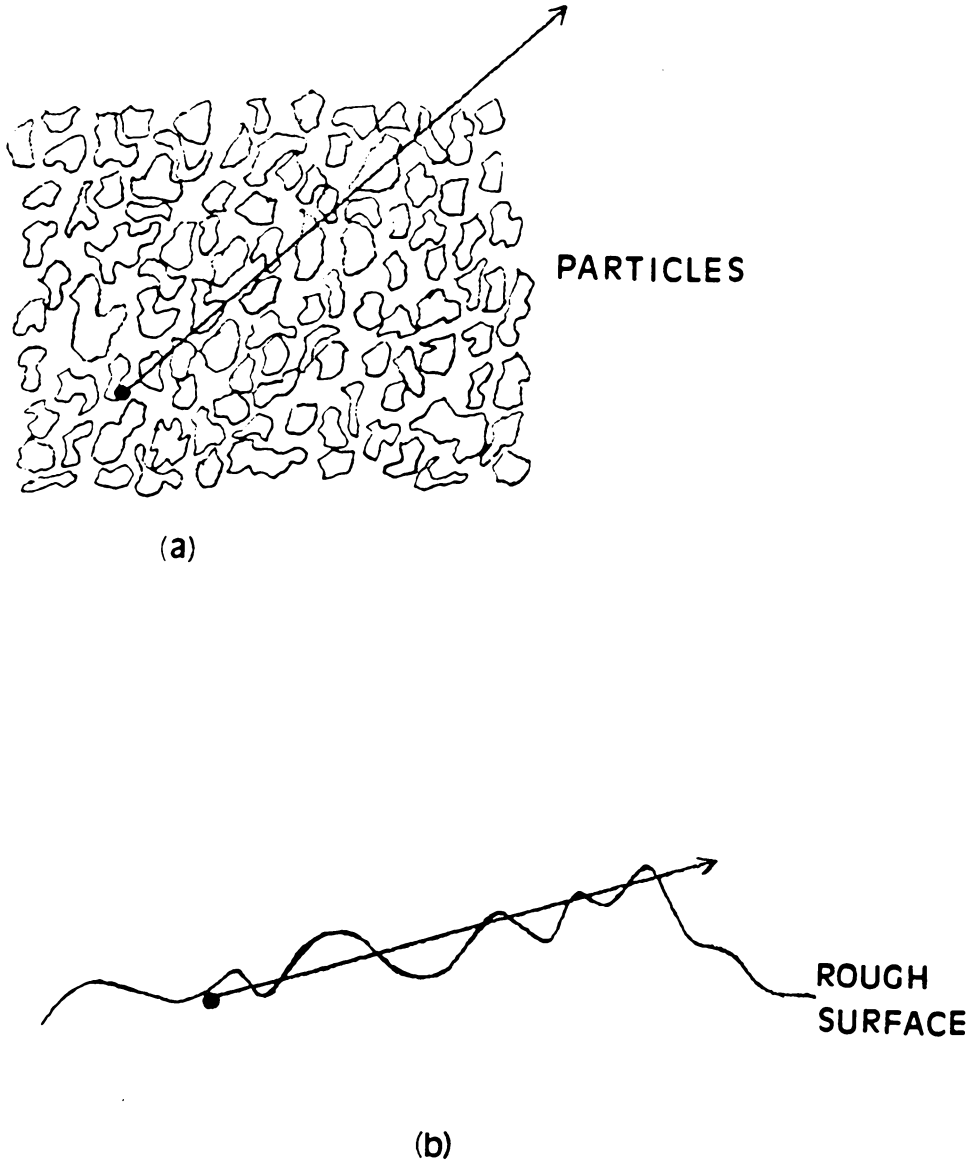

Figure 29. The absorption experienced by an x-ray beam in (a) a powder sample (b) a rough sample.

$\overline{|s|} = 0.8\sigma_{slope}$ for a Gaussian slope distribution (see Eq. (4-20)), the critical angle can be expressed as

$$\theta_c = \tan^{-1}(2\overline{|s|}/0.8) = \tan^{-1}(2.5\overline{|s|}) \qquad (5-36)$$

The critical angle for the rough FSZ sample can be calculated from Eq. (5-36) using the $\overline{|s|}$ values obtained from the profilometer measurement. The $\overline{|s|}$ values of the three traces from the rough FSZ sample are calculated directly from the digitized profiles and shown in Table 3. By using average $\overline{|s|} = 0.16$ in Eq. (5-36), a critical angle of

$$\theta_c = \tan^{-1}(2.5 \times 0.16) = 21.8° \qquad (5-37)$$

is obtained. It is based on this calculation that the simulation curve in Fig. 25 is separated to a dashed section and a solid section. Note that the critical angle is much smaller for general samples because samples produced by general machining processes are much smmother than this intensionally roughened sample and multiple intersections will start at much smaller angles.

Outside the low angle region, when $\theta_i = \theta_s = 90°$, the incident and signal rays are completely correlated (i.e. $\rho = 1$) and the intensity ratio should be unity according to Harrison and Paskin's theory. This provides a good check for the statistical model. As shown in Fig. 25, the intensity ratio approaches to unity as θ ($=\theta_i = \theta_s$) approaches 90°. When $\theta = 90°$, $\rho = 1$ and the computer program is screwed up due to overflow. Fortunately, this limiting case can be calculated analytically as follows:

For any group (Z_s, Z_{0s}), the incident ray, the signal ray and the sample normal coincide when $\theta_i = \theta_s = 90°$. Therefore, the absorption attenuation factor for the group (Z_s, Z_{0s}) is

$$A(Z_s, Z_{0s}) = e^{-\sqrt{2}\sigma\mu_i(Z_{0s} - Z_s) - \sqrt{2}\sigma\mu_s(Z_{0s} - Z_s)} \qquad (5-37)$$

Use Eq. (5-37) in Eq. (5-29) and integrate from $-\infty$ to ∞ as follows:

Table 3. Mean Absolute Slope of the Ground FSZ Sample.

trace #1	trace #2	trace #3
0.1621	0.1678	0.1501

$$R = \sqrt{\frac{2}{\pi}}\,\sigma(\mu_i + \mu_s)\int_{-\infty}^{\infty}\int_{Z_s}^{\infty} e^{-\sqrt{2}\,\sigma(\mu_i + \mu_s)(Z_{0s} - Z_s)} e^{-Z_{0s}^2} dZ_{0s} dZ_s \qquad (5-38)$$

The double integral in Eq. (5-38) can be carried out analytically and the result is R = 1.

The final point of interest of the statistical model is the angle of maximum intensity correction $\theta_{\text{max. correction}}$. Does the relation

$$\tan^{-1}\overline{|s|} = \theta_{\text{max. correction}} \qquad (5-39)$$

hold again as it did for the sawtooth surface? Because $\overline{|s|}$ is 0.16 (see Table 3) for the rough sample, $\tan^{-1}(0.16) = 9.1°$. The $\theta_{\text{max. correction}}$ given by the statistical model is 10° (see Fig. 25). Therefore Eq. (5-39) still holds reasonably well. However, one should note that the $\theta_{\text{max. correction}}$ is located in the multiple intersection region. Therefore, its magnitude of correction may not be accurate. As a matter of fact, the criterion in Eq. (5-36) indicates that the multiple intersection region is $\theta \leq \tan^{-1}(2.5\overline{|s|})$, therefore, the maximum correction angle given in Eq. (5-39) is always located in this region.

Simulation shown in Fig. 25 is repeated with τ_c changes from 82 μm to 40 μm and 160 μm, the results are shown in Figure 30. Note that $\theta_{\text{max. correction}}$ changes as $\frac{\sigma}{\tau_c}$ changes. These simulated $\theta_{\text{max. correction}}$ values based on the statistical model are listed in Table 4 along with the values calculated from Eq. (5-39). The $\overline{|s|}$ values needed in Eq. (5-39) are obtained by assuming $\overline{|s|}$ changes proportionally to σ/τ_c and extrapolating from the $\overline{|s|}$ value measured from the rough sample. The slight mismatch between $\tan^{-1}\overline{|s|}$ and simulated $\theta_{\text{max. correction}}$ in Table 4 is probably due to the effect of multiple intersection.

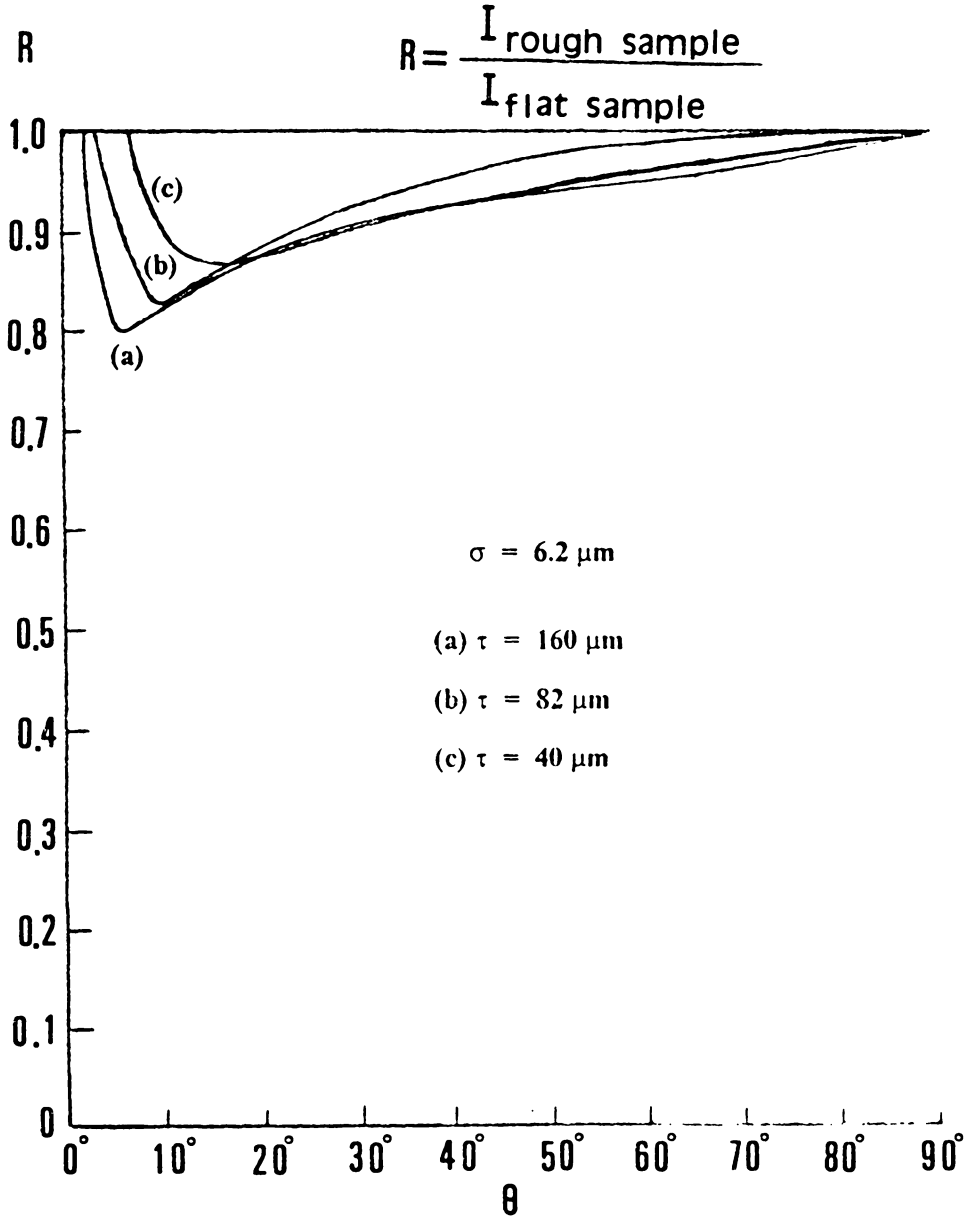

Figure 30. The intensity corrections calculated from the statistical model for three different autocorrelation distances and a same σ.

Table 4. The Positions of Maximum Intensity Correction with Sym. Diff. Optics Calculated from the Statistical Model and the Mean Absolute Slope.

	=40 μm	=82 μm	=160 μm
$\overline{\lvert s \rvert}$	0.328	0.160	0.082
$\tan^{-1}(\overline{\lvert s \rvert})$	18.2°	9.1°	4.7°
simulated $\theta_{max.\ correction}$	15°	10°	6°

Chapter 6

MODIFIED VERSION OF INTENSITY BAND SIMULATION FOR ROUGH SAMPLES

As mentioned in Section **2.5**, if the d-spacing of a flat sample has depth gradient, then the d-spacings of horizontal layers at different depths are different. Consequently, the intensity from the sample will distribute along a 2θ range and form an intensity band. When the sample is rough, the depth gradient of d spacing becomes more complicated. A first question one would ask is what is depth? Is the depth measured from the free surface or from a mean plane? The second question is how does the roughness change the shape and magnitude of an intensity band? This chapter presents a theoretical derivation for the simulation of the intensity band from a rough sample based on the previous statistical roughness model. The depth is measured from the free surface in this derivation. The result will be used in the next chapter to simulate the intensity band for the severely ground FSZ sample. A corresponding simulation without considering the roughness effect will also be given to show the difference.

Shown in Figure 31 is a rough surface with two vertical coordinate systems: (1) Z_s, the scaled height from the mean plane; (2) Y_s, the scaled depth from the free surface. Note that Z_s ranges from

negative infinity to positive infinity while Y_s is always positive. The layer located at a depth Y_s is called layer (Y_s). If the d-spacing is the same everywhere on the sample surface and varies as a function of depth, then the d-spacing is also the same everywhere for layer (Y_s). Theory derived in last section can be modified to acount for the roughness effect and calculate the intensity from each layer(Y_s).

If consecutive layers like the one given in Fig. 31 is counted from the free surface as 1st, 2nd, 3rd...layer, the scaled depth of jth layer can be denoted as Y_s^j and its intensity as I_j. If the thickness of a layer is very small, the d-spacing within the layer can be treated as a constant and denoted as d_j. The corresponding Bragg angle is denoted as $2\theta_j$. Similar to the flat sample case, the intensity from a general layer I_j is broadened according to the following Pearson-VII function to account for the instrumental and grain size broadening:

$$I_j y_0 \left[1 + \frac{(2\theta - 2\theta_j)^2}{ma^2} \right]^{-m} \qquad (6-1)$$

where y_0 is the normalization factor while "a" and "m" are width and shape parameters. Normalization requires

$$y_0 = \frac{1}{a\sqrt{\pi m}} \frac{\Gamma(m)}{\Gamma(m - 1/2)} \qquad (6-2)$$

with $\Gamma(m) = \int_0^\infty x^{m-1} e^{-x}$ and $m > 0$. The intensity due to all layers at each 2θ point is obtained by summing the individual contributions, i.e.

$$P_B(2\theta) = \sum_j I_j y_0 \left[1 + \frac{(2\theta - 2\theta_j)^2}{ma^2} \right]^{-m} \qquad (6-3)$$

while I_j's need to be calculated from the statistical model, "a", "m" and $2\theta_j$'s can be adjusted by trial and error to fit the measured intensity band. Note that $2\theta_j$'s are adjusted through the adjustment

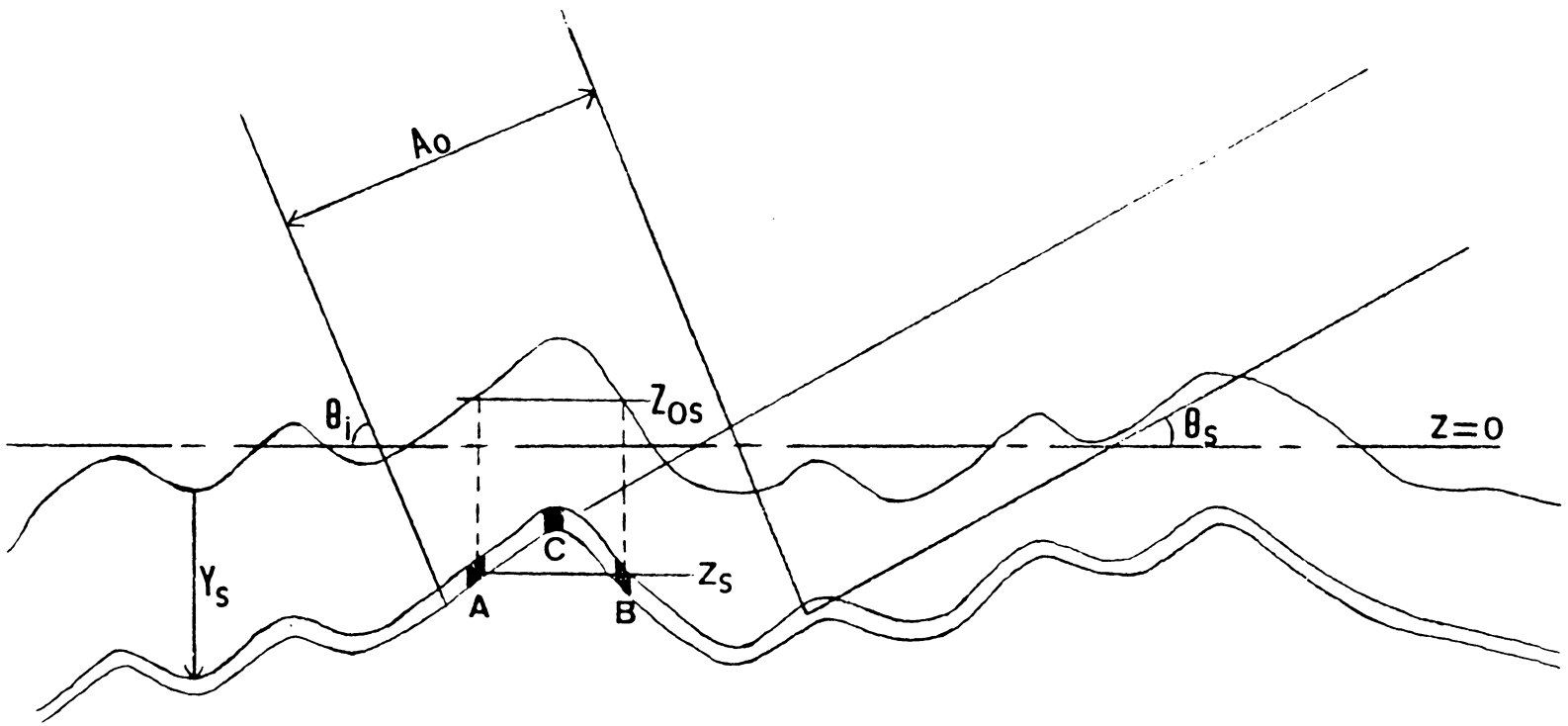

Figure 31. A schematic diagram showing a layer in a rough sample for intensity band simulation.

of the d-spacing profile. The intensity I_j from a general layer (Y_s^j) of a rough sample is calculated as follows:

Layer (Y_s) (see Figure 31) is first divided to many groups, each group consists of signal generating elements which are located at the same height. For example, elements A, B belong to the same group. The group of height Z_s and depth Y_s^j is designated (Z_s, Y_s^j). Because the surface excursion corresponding to the elements of group(Z_s, Y_s^j) is located at $Z_{0s} = Z_s + Y_s^j$, the average absorption factor for group (Z_s, Y_s^j) becomes A(Z_s, Z_{0s}) as given by Eq. (5-18). Again, the volume of the layer of thickness Δt_j is $\Delta V_j = A_0 \Delta t_j \sin\theta_i$ and the volume fraction of group (Z_s, Y_s^j) in layer (Y_s^j) of a sample with Gaussian surface is

$$p(Z_0)dZ_0 = \sqrt{2}\,\sigma p(Z_{0s})dZ_{0s} = \frac{1}{\sqrt{\pi}} e^{-(Z_s + Y_s^j)^2} dZ_s \qquad (6-4)$$

Consequently,

$$\begin{aligned} I_{\text{group}(Z_s,\, Y_s^j)} &= I_0 Q\, p(Z_0)\, dZ_0\, A(Z_s, Z_{0s}) \Delta V_j \\ &= \frac{I_0 Q A_0}{\sin\theta_i} \frac{1}{\sqrt{\pi}} A(Z_s, Z_{0s})\, e^{-(Z_s + Y_s^j)^2} dZ_s \Delta t_j \end{aligned} \qquad (6-5)$$

$$\begin{aligned} I_j &= \Sigma \text{ intensity of each group in layer}(Y_s^j) \\ &= \frac{I_0 Q A_0}{\sin\theta_i} \frac{1}{\sqrt{\pi}} \int_{-\infty}^{\infty} A(Z_s, Z_{0s})\, e^{-(Z_s + Y_s^j)^2} dZ_s\, \Delta t_j \end{aligned} \qquad (6-6)$$

To numerically calculate Eq. (6-6), the upper limit of the integration is trancated at 3 because very little material is located above $Z_s = 3$. The trancated integral is then separated to two parts as follows:

$$\int_{-\infty}^{3} A(Z_s, Z_{0s})\, e^{-(Z_s + Y_s^j)^2} dZ_s = \int_{-3}^{3} A(Z_s, Z_{0s})\, e^{-(Z_s + Y_s^j)^2} dZ_s + \int_{-\infty}^{-3} A(Z_s, Z_{0s})\, e^{-(Z_s + Y_s^j)^2} dZ_s$$

$$(6-7)$$

The last integral in Eq. (6-7) corresponds to the material located below $Z_s = -3$ where the flat sample approach is appropriate. i.e.

$$\int_{-\infty}^{-3} A(Z_s,Z_{0s})\, e^{-(Z_s + Y_s^j)^2} dZ_s = \int_{-\infty}^{-3} e^{\sqrt{2}\,\sigma(\frac{\mu_i}{\sin\theta_i} + \frac{\mu_s}{\sin\theta_s})Z_s} e^{-(Z_s + Y_s^j)^2} dZ_s \quad (6-8)$$

Combine Eqs. (6-6), (6-7), and (6-8):

$$I_j = \frac{I_0 A_0 Q}{\sqrt{\pi}\,\sin\theta_i}\left\{\int_{-\infty}^{-3} e^{\sqrt{2}\,\sigma(\frac{\mu_i}{\sin\theta_i} + \frac{\mu_s}{\sin\theta_s})Z_s} e^{-(Z_s + Y_s^j)^2} dZ_s + \int_{-3}^{3} A(Z_s,Z_{0s})\, e^{-(Z_s + Y_s^j)^2} dZ_s\right\}\Delta t_j$$

$$(6-9)$$

Carry out the first integral in last Eq.:

$$I_j = \frac{\sqrt{\pi}}{2} e^{\sigma^2(\frac{\mu_i}{\sin\theta_i} + \frac{\mu_s}{\sin\theta_s})^2/2 - \sqrt{2}\,\sigma Y_s^j(\frac{\mu_i}{\sin\theta_i} + \frac{\mu_s}{\sin\theta_s})}\{1 + erf[3 + Y_s^j - \sqrt{2}\,\sigma(\frac{\mu_i}{\sin\theta_i} + \frac{\mu_s}{\sin\theta_s})/2]\}\Delta t_j$$

$$(6-10)$$

$$+ \left\{\frac{I_0 A_0 Q}{\sqrt{\pi}\,\sin\theta_i}\int_{-3}^{-3} A(Z_s,Z_{0s})\, e^{-(Z_s + Y_s^j)^2} dZ_s\right\}\Delta t_j$$

Numerical integration is needed for the integral in Eq. (6-10).

The intensity band program previously developed[11] is modified in this work to take into consideration of the roughness effect, i.e. using Eq.(6-10) to build intensity band given by Eq. (6-3). The modified version of the intensity band simulation is used in the next chapter to determine the d-spacing gradient in the severely groung FSZ sample. This is done by first simulating an intensity band based on a guessed d-spacing profile. By comparing the simulated band and the experimental data, successive guesses are then made accordingly until the resultant band matches the experimental curve. The well documented computer program for intensity band simulation is included

in Appendix B. It is easier to describe the d-spacing profile using analytical functions than using a whole set of points. The following functions are found useful in curve fitting the d-spacing profiles.

$$d(Y) = d_0 + \sum_{i=1}^{i=l} a_{1i} erfc\left(\frac{Y - a_{2i}}{a_{3i}}\right) + \sum_{j=1}^{j=m} b_{1j} e^{-\frac{Y - b_{2j}}{b_{3j}}} + \sum_{k=1}^{k=n} c_{1k} e^{-\left(\frac{Y - c_{2k}}{c_{3k}}\right)^2} \quad (6-11)$$

Note Y is the depth and all terms involving a, b, c are adjustable constants with dimension of "length", not lattice parameters. As shown in the next chapter, functions of the type of Eq. (6-11) are used for both the polished and severely groun FSZ samples.

Chapter 7

XPS STUDY AND RESIDUAL STRAIN ANALYSIS FOR FSZ SAMPLES

The FSZ samples reported in Chapter 5 showed considerable asymmetrical broadening of the XRD peaks. Although residual strain caused by plastic deformation appears to adequately explain this broadening, composition depth gradients remain as another possible explanation. This uncertainty is resolved by x-ray photoelectron spectroscopy (XPS) study and the residual study using XRD techniques. The XPS study concludes that the composition depth gradients do not exist. The XRD residual strain study was carried out using Cu $K\alpha_1$ radiation and synchrotron radiation with a wavelength of 2.4797Å. The (111) reflection was used throughout the XRD work because it is the strongest reflection having the most reliable well separated peak profile. A toal of eight XRD scans were made using either symmetrical or asymmetrical diffraction optics. The measured profiles were then fitted with the d-spacing profiles using the modified intensity band program presented in Chapter 6. The resualts of these fittings are also intepreted.

7.1 XPS Study

The FSZ sample contains 8 mol% Y_2O_3 as stabilizer. These FSZ samples are completely cubic phase with some Y atoms replacing Zr atoms to form a solid solution. Some vacancies are also created in the oxygen sites to keep electrical neutrality. Because Y^{+3} ions have much larger sizes than Zr^{+4} ions (1.051Å vs. 0.84Å in radii[17]), a composition gradient of Y^{+3} could produce a lattice parameter gradient and related peak broadening. The following XPS work was carried to reveal this depth gradient, if indeed it exists.

Survey XPS scans from both the polished and the severely ground samples showed the presence of O, Zr, Y, AL and C at the surfaces of both samples. Slow scans and ion milling were then carried out alternatively to reveal the depth profiles of concentrations of above atom species. Each set of scans collected for the above elements was followed by a short period of ion milling. The ion milling was used to sequentially remove surface layers from the sample and expose new material for the subsequent XPS scans. An x-ray tube with Mg target was operated at 13 kV and 20 mA to produce Mg $K\alpha$ radiation for the incident beam. The vacuum was kept at 1.0×10^{-9} torr during the XPS scans. Ar^+ ions were used during the ion milling with ion beam energy of 4.0 kev and Ar pressure at 2.0×10^{-6} torr.

The concentration of each element is plotted as a function of cumulative milling time in Figures 32 and 33 for the polished and the ground samples. The carbon deposition on the sample surfaces was milled away quickly. As the concentration of carbon drops, the concentrations of other elements rise up quickly and reach constant values within a couple of minutes milling. This implies that the samples are homogeneous except in the very small surface regions contaminated by carbon. Because the hydrocarbon compounds in the residual gas of a ultra high vacuum system always deposit on the sample surface due to physisorption, carbon contamination is common and not related

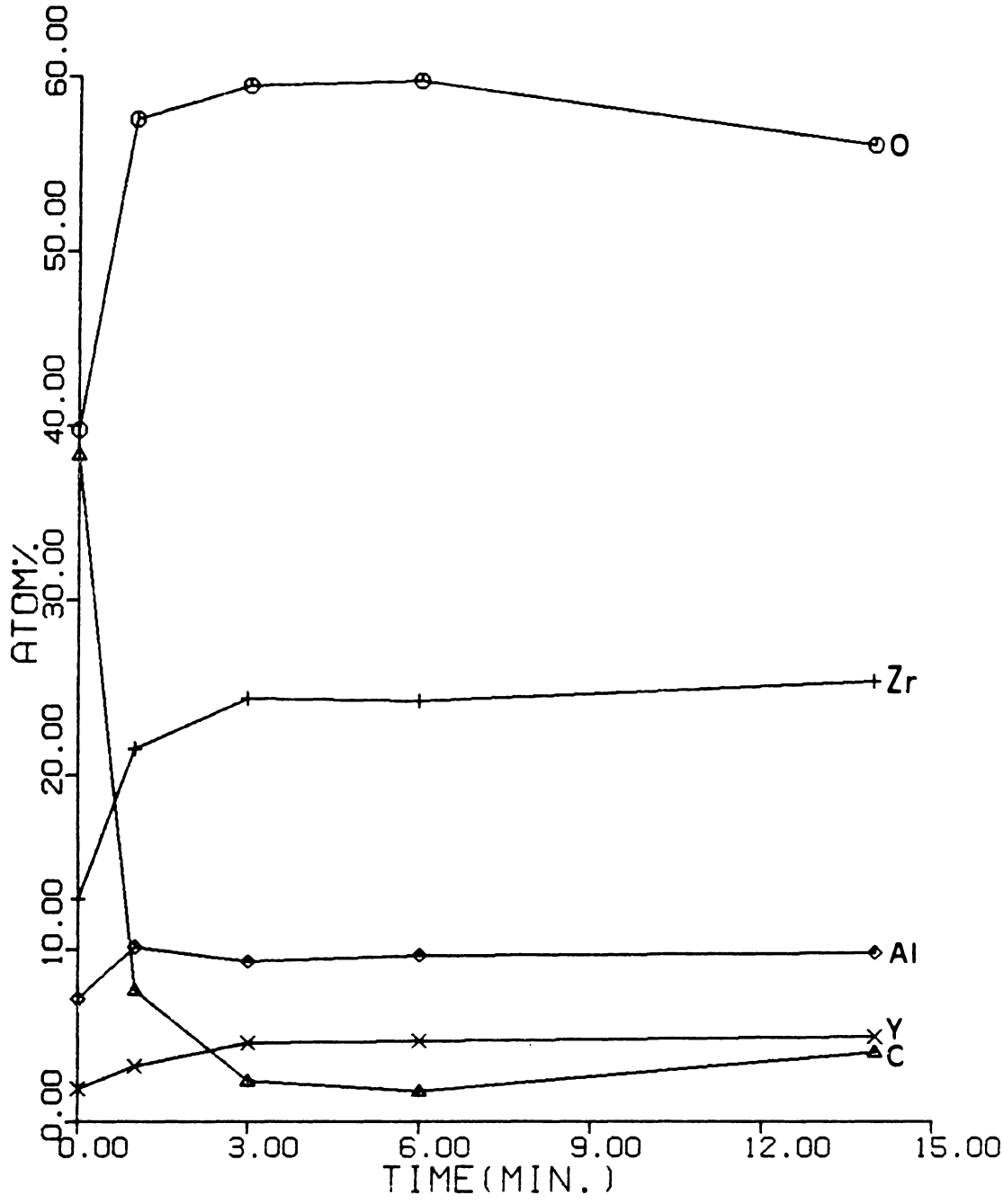

Figure 32. Depth profiles of the atomic concentrations (polished FSZ sample).

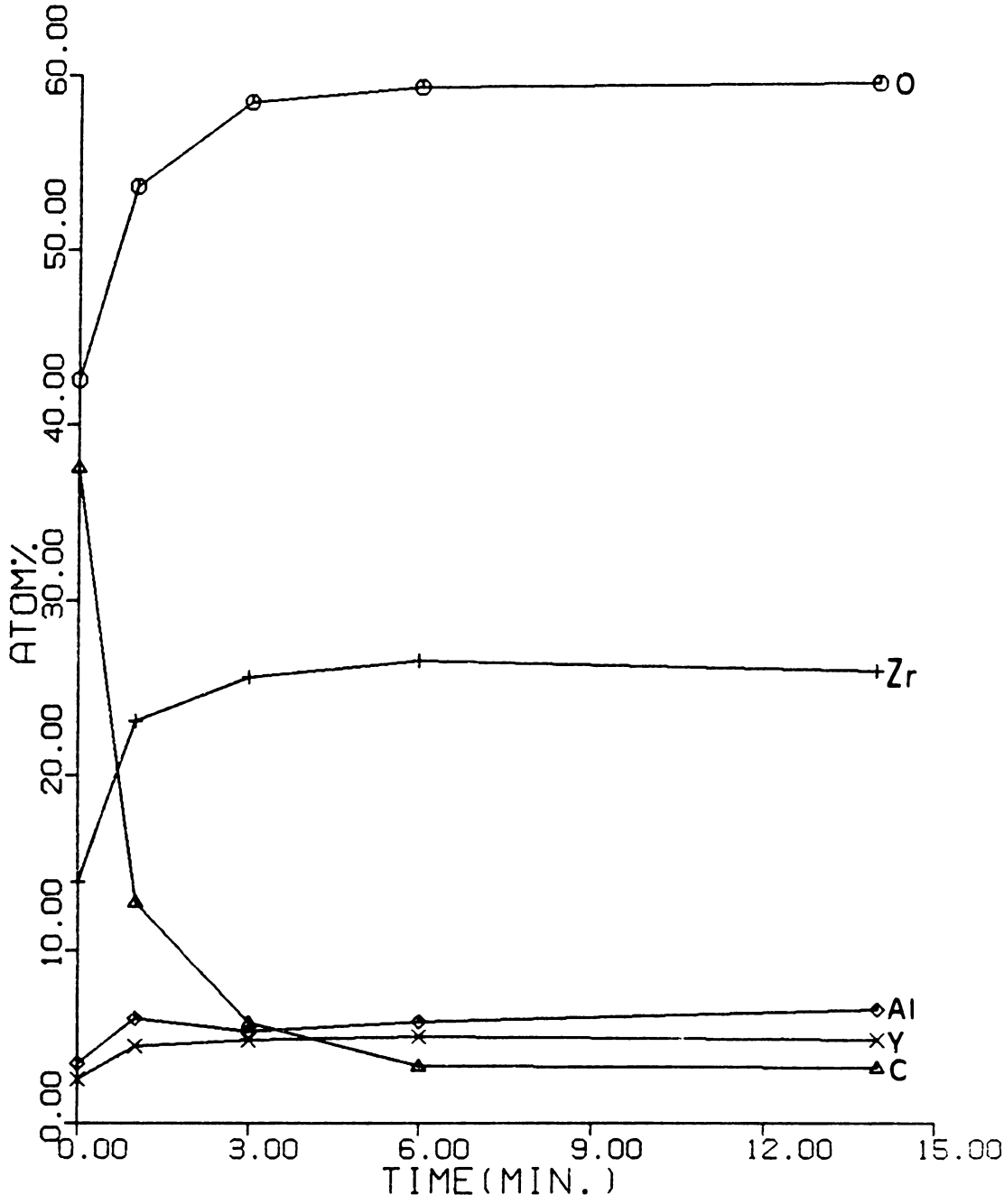

Figure 33. Depth profiles of the atomic concentrations (ground FSZ sample).

to the lattice distortion of the substrate.[18] Therefore, the possibility of the composition depth gradients contributing toward the observed asymmetrical peak broadening is eliminated.

7.2 Residual Strain Study by XRD

7.2.1 Measurements of the (111) profiles of the FSZ samples

The (111) peak profiles of the polished and the ground FSZ samples were point counted using Cu $K\alpha_1$ radiation and symmetrical diffraction optics. The counting at each point was stopped at either 8000 counts or 1000 seconds, whichever was reached first. The Cu $K\alpha_1$ radiation was obtained using a diffracted beam quartz monochromator and a Cu tube operated at 50kV and 20 mA. The incident and receiving slits were 1° and 0.05°, respectively. The results from the polished and ground samples are shown in Figures 34 and 35, respectively. Both profiles show asymmetry. The peak profile from the ground sample shows a peak shift to the low angle side and some broadening relative to that of the polished sample. Both samples were then annealed at 1200°C for one hour and furnace cooled. The same point counting was then repeated for the annealed samples. The peak profiles of both annealed samples are the same and one of them (the polished and annealed) is shown in Figure 36. The peak profile after annealing is sharpened considerably. A peak shift of 0.025° toward the high angle side is also observed relative to the profile of the polished, unannealed sample. However, this shift is due to the different alignments of the diffractometer before and after the annealing. The following procedure confirmed the effect as well as the shift in alignment. The polished and annealed sample was re-polished using alumina powder. The maximum intensity portion of the (111) profile was point counted to locate the peak position imediately before and after the re-polishing with the same diffractometer alignment. No peak shift was observed. A subsequent prolonged point counting was then carried out for the re-polished sample. The result shows

definite broadening comparing to the profile of the annealed state. This leads one to a conclusion that the a polishing introduces a low level intensity band but not shifting of the main peak. On the other hand, the peak shift between the profiles of the ground and polished samples before annealing is real, and due to the extended range of the strain gradient in the severely ground sample. Both were measured with the same alignment.

The (111) profiles of the polished and the ground samples were also measured with synchrotron radiation of 2.4797Å at the ORNL beamline in NSLS before annealing. The profiles measured with the symmetrical diffraction optics are shown in Figures 37 and 38, respectively for the polished and the ground sample. A peak shift and an intensity band are observed again in the profile of the ground sample relative to that of the polished sample. Also, both profiles show some asymmetry. The (111) profiles of both samples were also measured with asymmetrical diffraction optics and shown in Figures 39 and 40. The asymmetric diffraction optics was obtained by tilting the sample normal toward the diffracted beam by an amount such that the incident angle is 3°. The small incident angle results in a shallower pnetration ($\delta_{1/e} = 0.2\,\mu m$ comparing to 0.9 μm of the symmetrical diffraction condition) and expected to influence the peak profile. The peak profile of the polished sample obtained with asymmetrical diffraction optics shows a more extensive band on the low angle side comparing to its counterpart of symmetrical diffraction optics. Surprisingly, no change is observed between the profiles obtained with symmetrical and asymmetrical diffrcation optics for the ground sample. A mechanism is proposed in the final section to explain this unexpected result.

7.2.2 Fitting of the experimental intensity bands

The profile of the annealed sample shown in Fig. 36 is fitted by a Pearson-VII function[9]. The fitted Pearson-VII function is shown in Fig. 36 as a solid line along with the experimental data represented by the symbols. The "a" and "m" values of the fitted Pearson-VII are 0.032 and 1.8, respectively. Because the annealed sample is strain-free, these "a" and "m" values are characteristic

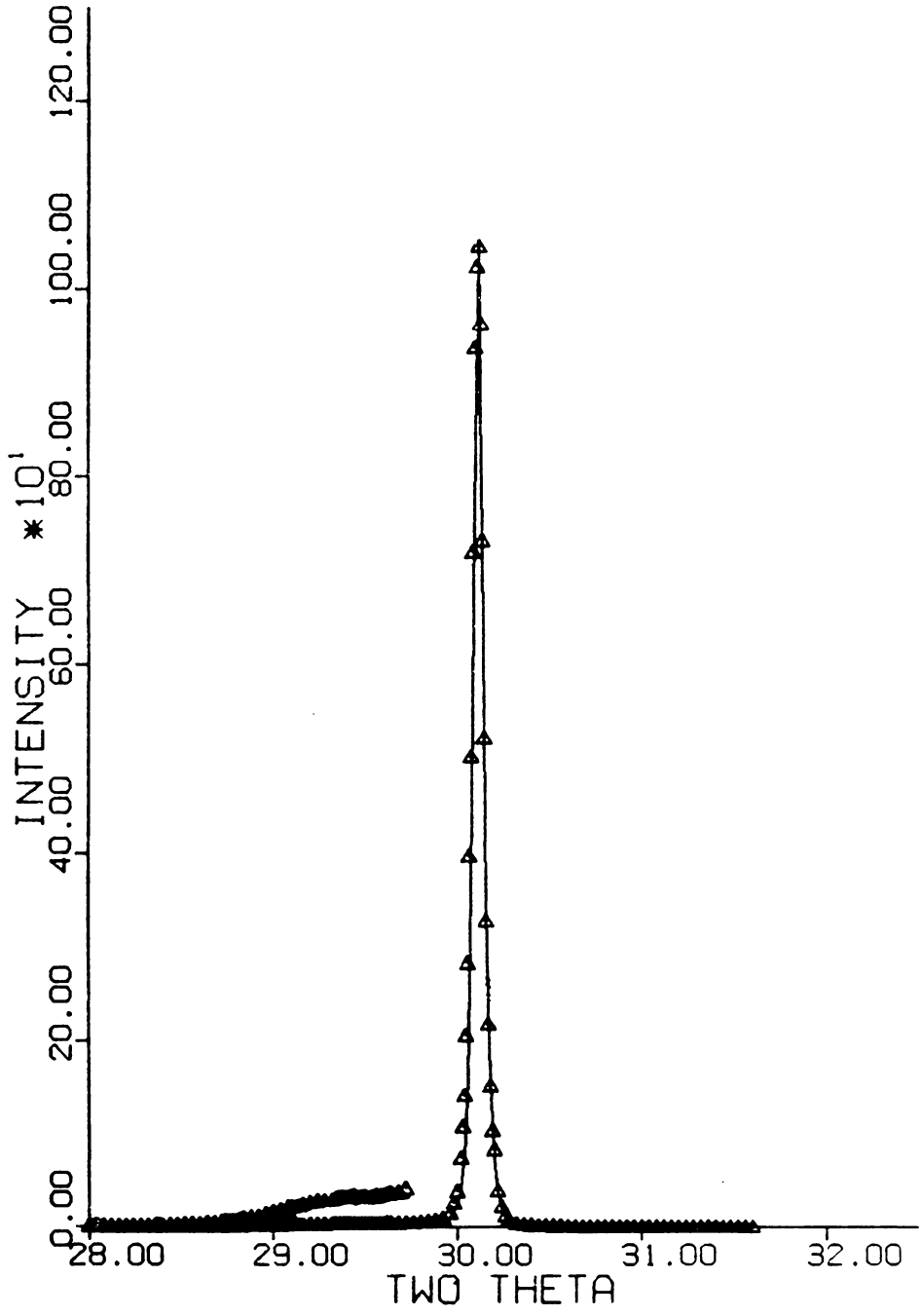

Figure 34. The (111) intensity band of the polished sample (symmetric diffraction optics, Cu kα radiation).: Δ Δ Δ: experimental data; —— : computer simulation.

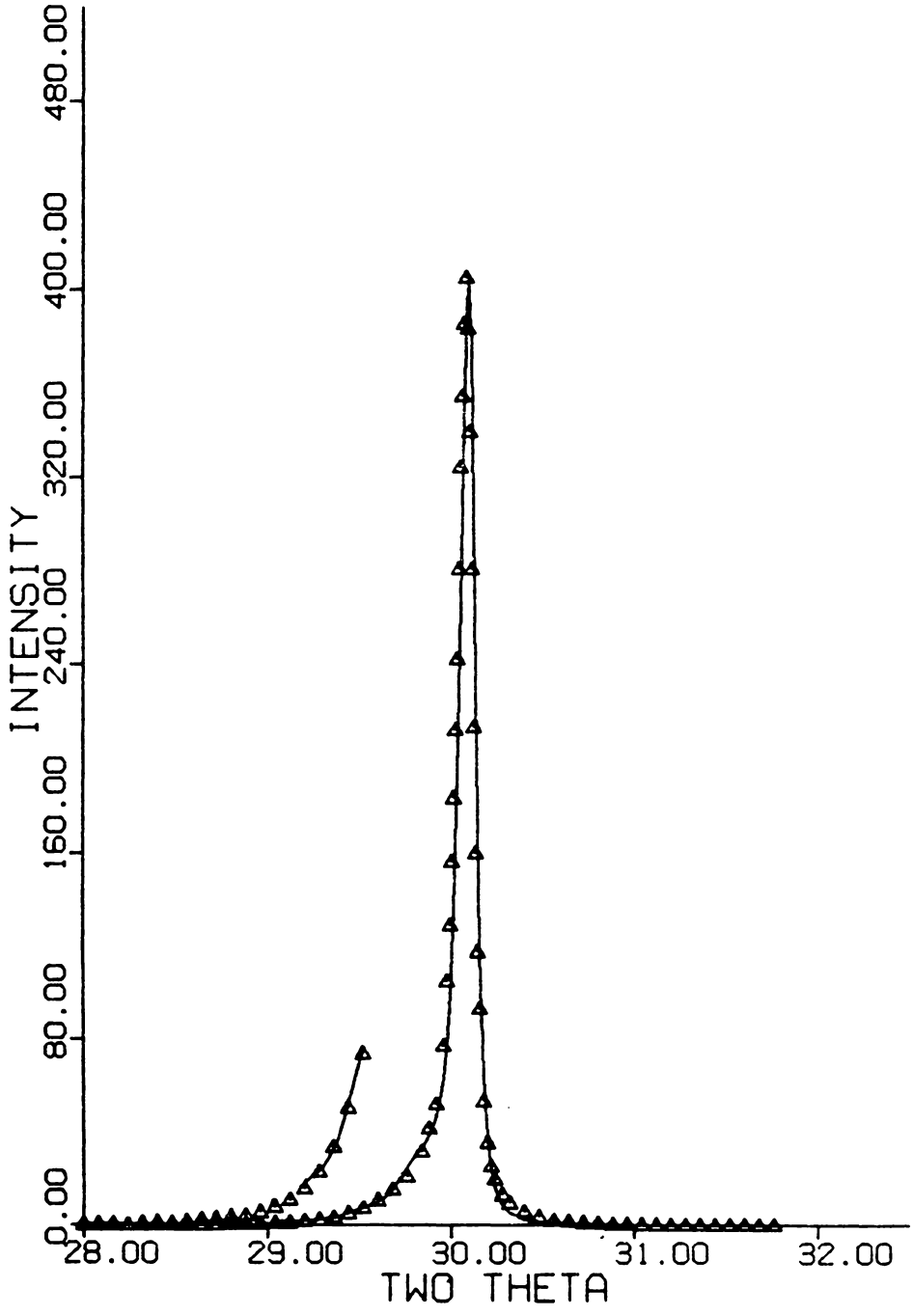

Figure 35. The (111) intensity band of the ground sample (symmetric diffraction optics, Cu Kα radiation).: △ : experimental data; — : computer simulation.

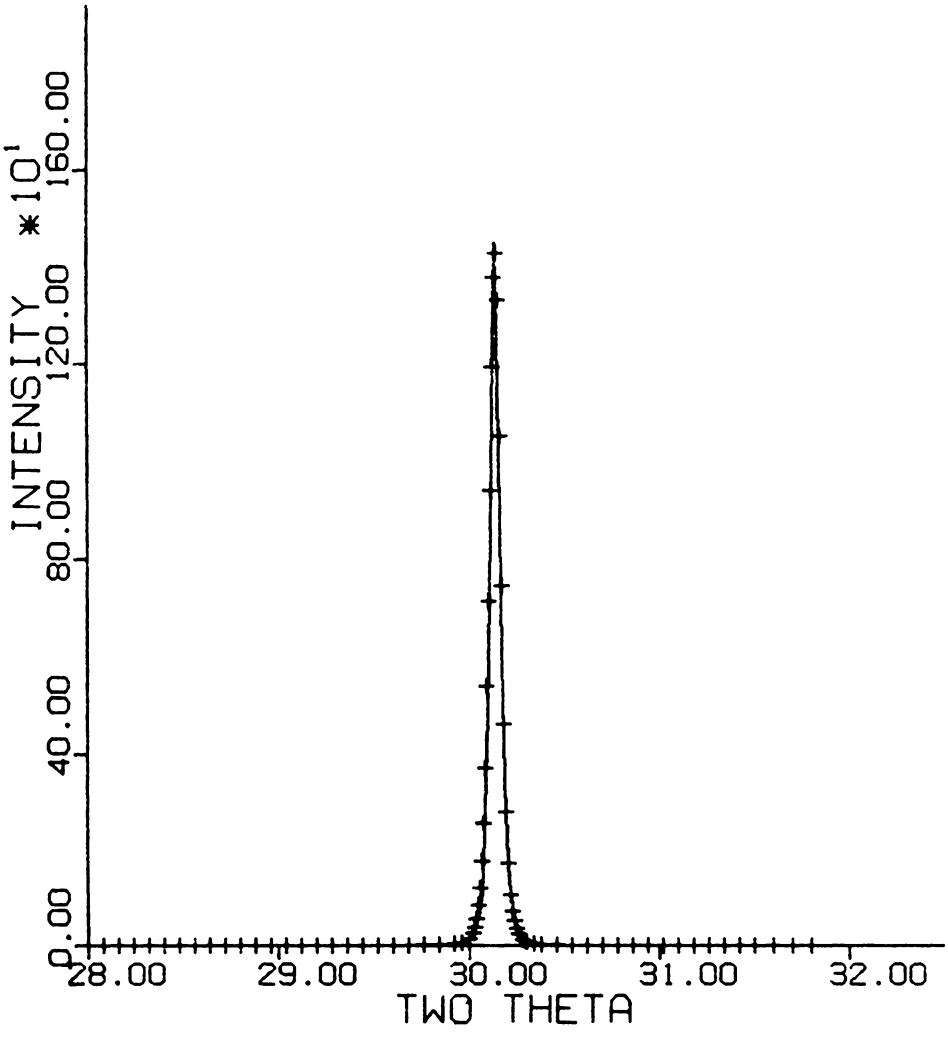

Figure 36. The (111) peak profile of the polished and annealed sample (symmetric diffraction optics, Cu Kα radiation).: + + + : experimental data; — : Pearson-VII function.

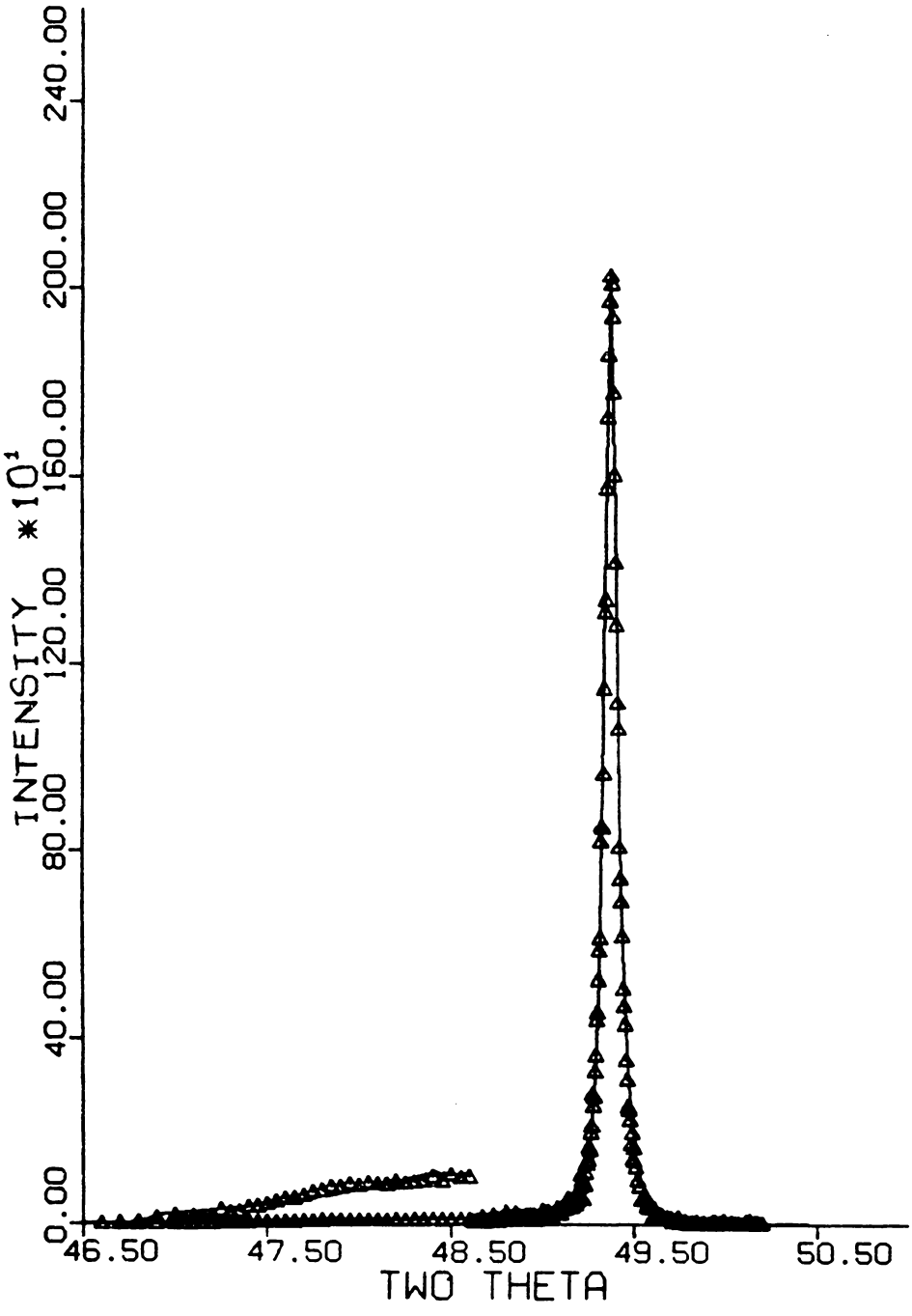

Figure 37. The (111) intensity band of the polished sample (symmetric diffraction optics, $\lambda = 2.4797$ A).: △ : experimental data; —: computer simulation.

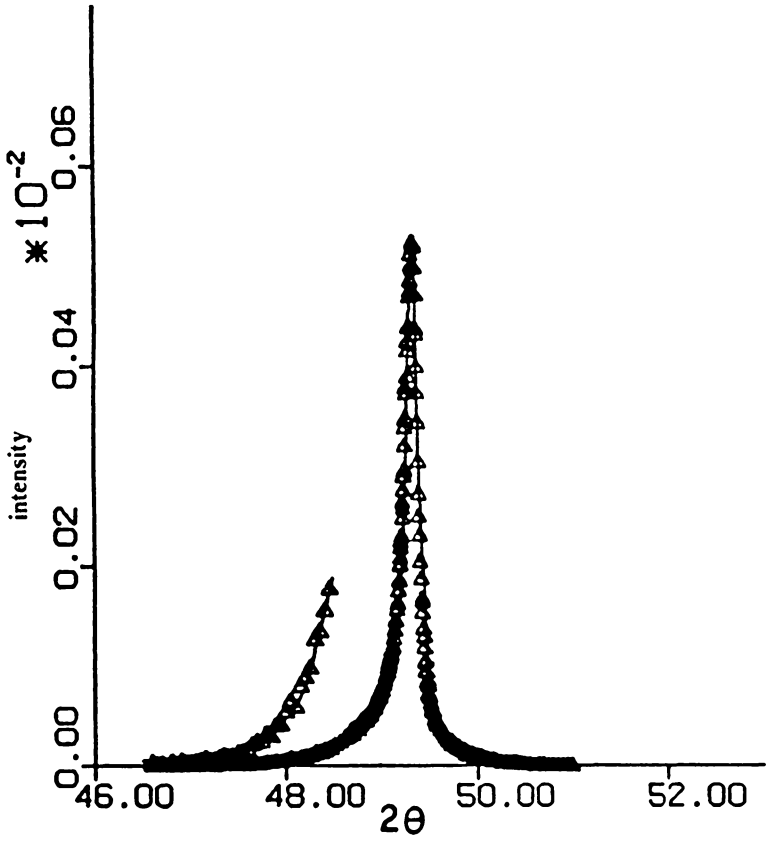

Figure 38. The (111) intensity band of the ground sample (symmetric diffraction optics, $\lambda = 2.4797$ A).: △ : experimental data; — : computer simulation.

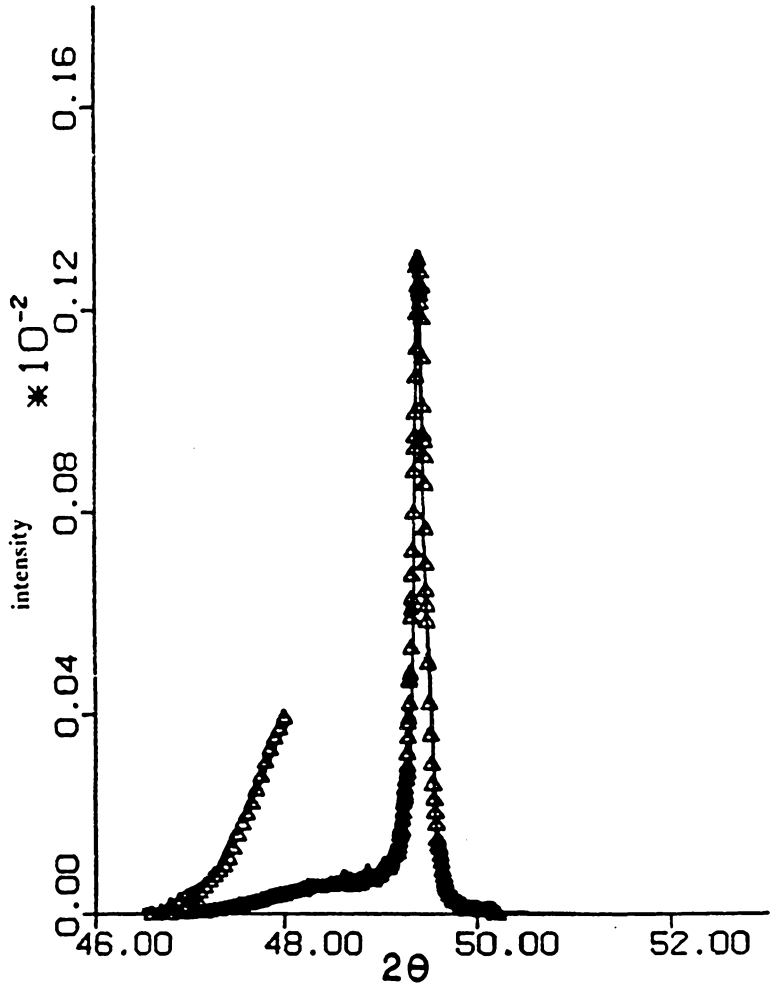

Figure 39. The (111) intensity band of the polished sample (asymmetric diffraction optics, $\lambda = 2.4797$ A).: △ : experimental data; —— : computer simulation.

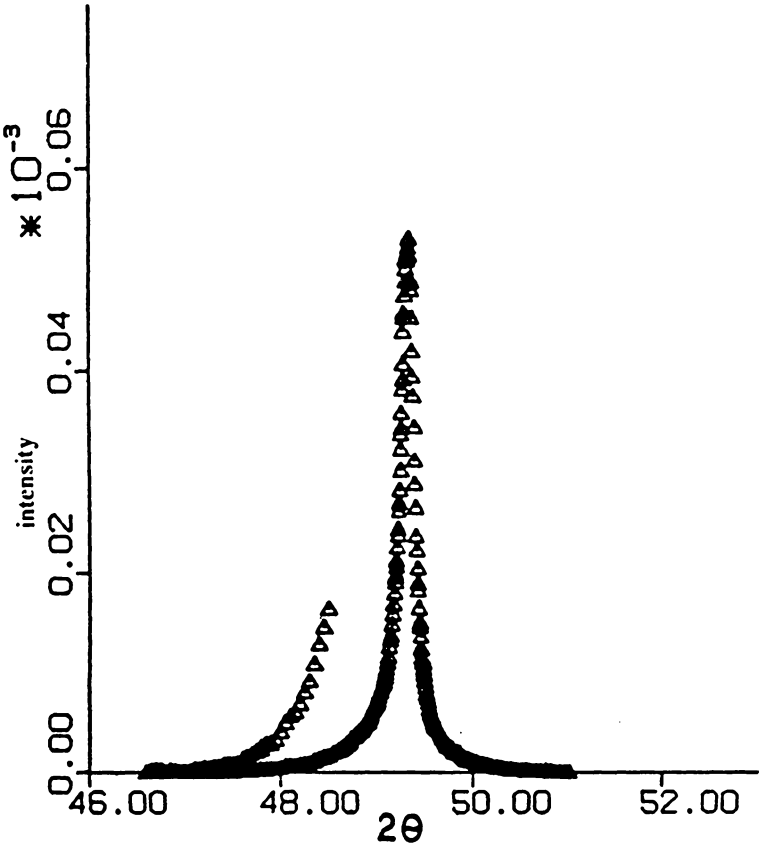

Figure 40. The (111) intensity band of the ground sample (asymmetric diffraction optics, $\lambda = 2.4797$ A).: △ : experimental data.

of the instrumental and particle size broadening and should create the minimum broadening for the ground and the polished samples.

As the peak profiles of the ground and polished sample show clear broadening and asymmetry of the main peak relative to that of the annealed samples, they are treated as intensity bands and fitted with the d-spacing profiles. For each fitting, an initial depth profile of d-spacing is guessed. The depth is measured from the free surface. The sample can be treated as a combination of many thin layers located at different depths. The d-spacing of each layer is treated as a constant and the corresponding intensity is calculated using the theory developed in Chapter 6. Note that the polished sample is flat and the layers are parallel to the sample surface, while the ground sample is rough and the layers have the same fluctuation as the surface profile. The generalized theory developed in Chapter 6 calculates the intensity from each layer considering the absorption attenuation for both the flat and the rough samples under both the symmetrical and asymmetrical diffraction optics. Because the d-spacing changes from one layer to another continuously, the calculated intensities are spread over a 2θ range according to the Bragg's law. These are then redistributed according to a Pearson-VII function around their individual 2θ positions. The distributed intensities are then superimposed to form an intensity band. The simulated intensity band is then compared with the experimental data and the d-spacing profile is adjusted accordingly until the simulation and the experimental data show good agreement. The results of these fittings are shown in Figs. 34, 35, 37, 38 and 39 with the solid lines representing the simulated bands and the symbols representing the experimental data. Note both the measured and simulated profiles are expanded vertically by ten times over a section in the low angle side to better show the details of the final fit. The d-spacing profiles are expressed in the following analytical forms:

(1) Profile shown in Fig. 34, polished sample, symmetrical diffraction, Cu $K\alpha_1$ radiation.

$$d = 0.1\,e^{-\frac{x}{0.035}} + 0.03\,e^{-\frac{x}{0.005}} + 0.02\,e^{-\frac{x}{0.04}} - \begin{cases} 0.018\,e^{-(\frac{x-0.07}{0.02})^2} & x < 0.07 \\ 0.018\,e^{-(\frac{x-0.07}{0.04})^2} & x \geq 0.07 \end{cases} + 2.9646\ \text{Å} \qquad (7-1)$$

(2) Profile shown in Fig. 35, ground sample, symmetrical diffraction optics, Cu $K\alpha_1$ radiation.

$$d = 0.01\, erfc(\frac{x}{2.0}) + 0.03\, erfc(\frac{x}{0.015}) + 0.04\, erfc(\frac{x}{0.4}) + 0.03\, erfc(\frac{x}{0.07}) + 2.9646 \text{ Å} \qquad (7-2)$$

(3) Profile shown in Fig. 37, polished sample, symmetrical diffraction optics, $\lambda = 2.4797$ Å.

$$d = 0.1\, e^{-\frac{x}{0.035}} + 0.03\, e^{-\frac{x}{0.005}} + 0.02\, e^{-\frac{x}{0.04}} - \begin{cases} 0.018\, e^{-(\frac{x-0.07}{0.02})^2} & x < 0.07 \\ 0.018\, e^{-(\frac{x-0.07}{0.04})^2} & x \geq 0.07 \end{cases} + 2.9683 \text{ Å} \qquad (7-3)$$

(4) Profile shown in Fig. 38, ground sample, symmetrical diffraction optics, $\lambda = 2.4797$ Å.

$$d = 0.01\, erfc(\frac{x}{1.5}) + 0.04\, erfc(\frac{x}{0.006}) + 0.03 erfc(\frac{x}{0.3}) + 0.03 erfc(\frac{x}{0.07}) + 2.9683\text{Å} \qquad (7-4)$$

(5) Profile shown in Fig. 39, polished sample, asymmetrical diffraction optics, $\lambda = 2.4797$ Å.

$$d = 0.09\, erfc(\frac{x}{0.04}) + 0.02\, e^{-\frac{x}{0.04}} + 0.02\, erfc(\frac{x}{0.005}) + 0.02 erfc(\frac{x}{0.001}) - \begin{cases} 0.01\, e^{-(\frac{x-0.07}{0.02})^2} & x < 0.07 \\ 0.01\, e^{-(\frac{x-0.07}{0.04})^2} & x \geq 0.07 \end{cases} + 2.9683 \text{ Å} \qquad (7-5)$$

The x in above equations is depth in μm. The "a" and "m" values used in the Pearson-VII functions for these fittings are listed in Table 5. Note that the profile of the ground sample shown in Fig. 40 is not fitted because the roughness model used in Chapter 6 does not apply to the case of a small incident angle.

Table 5. "a" and "m" Values Used in the Pearson-VII Functions for Intensity Band Simulation.

FSZ sample	diffraction optics	radiation	a	m
polished	symmetrical	Cu $K\alpha_1$	0.032	1.80
ground	symmetrical	Cu $K\alpha_1$	0.032	1.30
polished then annealed	symmetrical	Cu $K\alpha_1$	0.032	1.80
polished	symmetrical	synchrotron	0.040	1.20
ground	symmetrical	synchrotron	0.045	1.00
polished	asymmetrical	Cu $K\alpha_1$	0.058	1.05

7.2.3 Discussions

As shown in Table 5, the "a" and "m" values used in fitting the peak profiles of the ground and the polished samples obtained with Cu $K\alpha_1$ radiation are very close to the corresponding values for the annealed sample. This is consistant with the conclusion that all samples have about the same instrumental and particle size broadening. The "a" and "m" values used in fitting the peak profiles of both samples obtained with synchrotron radiation also show good consistancy, although a profile from an annealed sample is not available for comparison.

The d-spacing values given in Eqs. (7-1) to (7-5) all vary in the near surface region but stay constant in the bulk. The d-spacing in the bulk of both the ground and the polished samples are the same, indicating as expected that well below the surface the bulk is undisturbed for both samples. This corresponds to a d-spacing, obtained from the the Cu $K\alpha_1$ profiles, of 2.9646 Å. The corresponding value obtained from the synchrotron profiles is 2.9863 Å. The difference between these two values is believed to be due to problems in the alignment of ORNL diffractometer at the NSLS.

Strain profiles are obtained from the d-spacing profiles using $\varepsilon = \frac{d - d_0}{d_0}$, where ε is strain and d_0 is the d-spacing value in the bulk. The strain profiles obtained from Eqs. (7-1) to (7-5) are plotted in Figures 41 to 45, respectively. The strain profiles of the polished sample shown in Figs. 41, 43 and 45 are very close. This indicates that the peak profiles obtained with different diffraction optics or different radiation yield a consistant d-spacing profile for the polished sample. A same consistancy is observed in the d-spacing profiles shown in Figs. 42 and 44 for the ground sample. The strain profile of the polished sample shows a large compressive strain at the sample surface, which decreases rapidly at greater depths. The near surface compressive zone is follwed by a relatively small zone of tension before the strain-free bulk is reached. The overall strained zone is about 0.1 μm. The strain profiles of the ground sample show a much larger compressive zone of about 1 μm. No zone of tension is observed because the peak profile is not sensitive to a small tension zone

in a relatively deep position. Although the maximum strain of 5% at the polished surface appears to be large, it is compatible with the $<\varepsilon_1^2>^{1/2}$ value of 2.2% found in the wear debris (see Chapter 8) because the latter is a root mean square value of a Gaussian distribution. The maximum strain at the ground surface is only 3%. The top layer of the ground sample had probably reached the same high strain of 5% but broke away as debris leaving a lower strain in the surface. This is reasonable because the grinding wheel has much larger momentum than the polishing powder and tends to knock off the asperities. Also, a much larger amount of debris is produced in a rough grinding process than in a polishing process.

The intensity in the low angle portion of the peak profile of the polished sample is enhanced when the diffraction optics changes from the symetrical to asymmetric condition (see Figs. 37 and 39). This enhancement is due to the emphasis of the surface region by the small incident angle. The corresponding enhancement is not observed in Figs. 38 and 40 for the ground sample. This can be explained qualitatively by the following argument. As shown in Figure 46, a horizontal layer is located at a depth $|Z|$ below the flat surface. A signal generating element E belonging to this layer has an absorption length of $AE + EA'$ when the symmetrical diffraction optics is used. The absorption length is greatly increased to $BE + EB'$ when the asymmetric diffraction optics is used with a flat surface. As shown below, the same increase does not happen in the ground sample. The ground sample was intentionally roughened with a σ value of 6.2 μm. The surface profile appears to consist of mountains and valleys due to the roughness. Because the incident angle is very small (i.e. 3°), the valleys are somewhat hidden in the shadow of the mountains and contribute little intensity. Therefore, let's only consider the intensity from the mountain tops. A layer located at a depth Y is depicted in Figure 47 along with three signal generating elements E,F and G belonging to the layer. The absorption length of element F changes from $AF + FA'$ for the symmetrical diffraction condition to $BF + FB'$ for the asymmetric diffraction condition. Due to the curved shape of the surface profile, these two absorption lengths are close. The corresponding change of the absorption length is from $CG + GC'$ to $DG + GD'$ for element G, and $PE + EP'$ to $QE + EQ'$ for element E. The former change increases the absorption length while the latter decreases. By the same

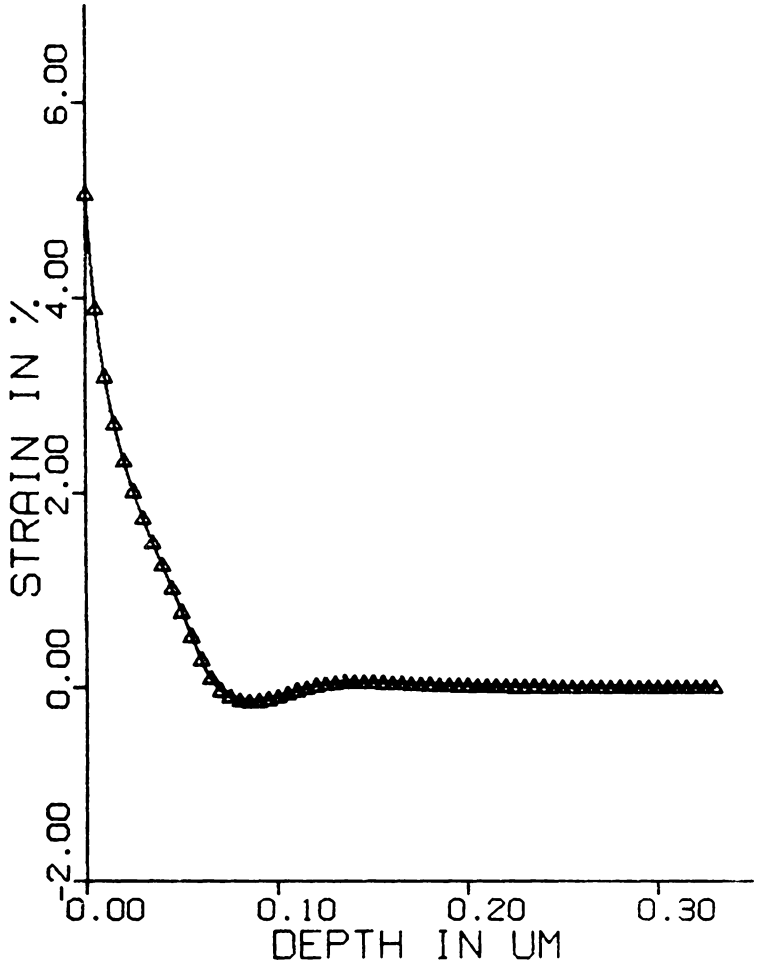

Figure 41. The depth profile of the strain perpendicular to the sample surface. (polished FSZ, symmetric diffraction optics, Cu Kα radiation).

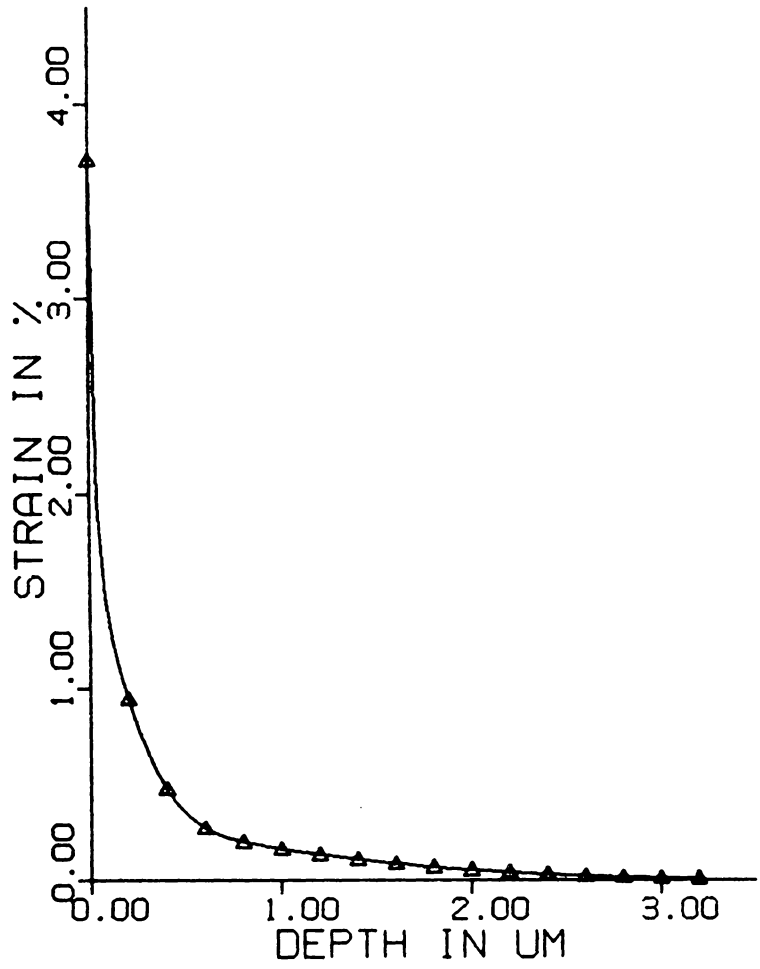

Figure 42. The depth profile of the strain perpendicular to the sample surface (ground FSZ, symmetric diffraction optics, Cu Kα radiation).

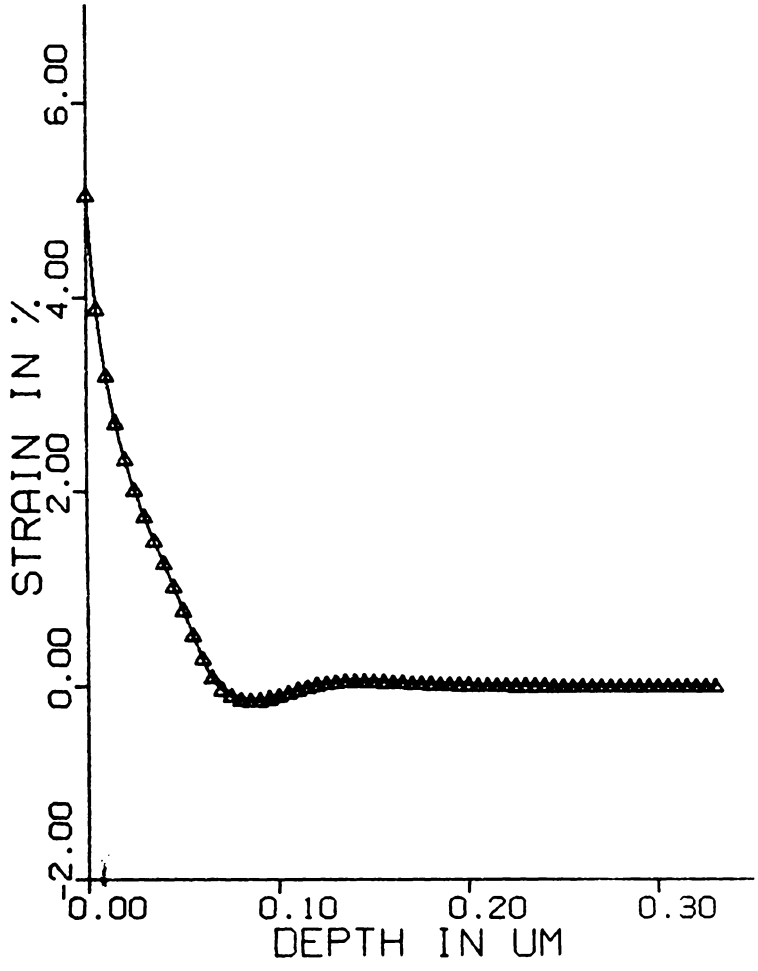

Figure 43. The depth profile of the strain perpendicular to the sample surface (polished FSZ, symmetric diffraction optics, $\lambda = 2.4797$ A).

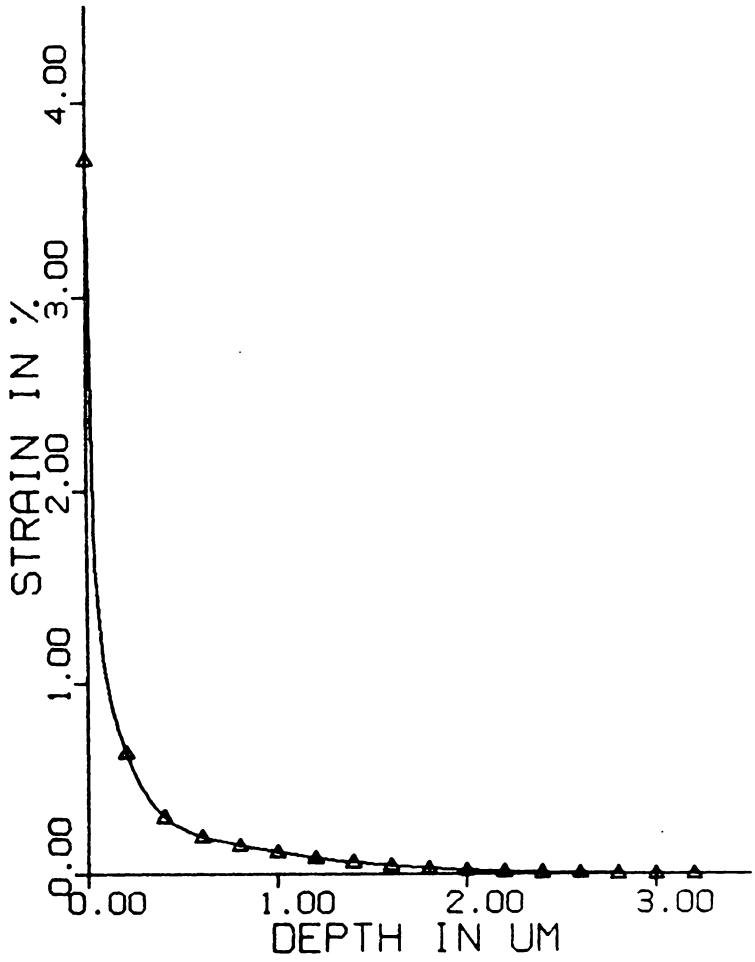

Figure 44. The depth profile of the strain perpendicular to the sample surface (ground FSZ, symmetric diffraction optics, $\lambda = 2.4797$ A).

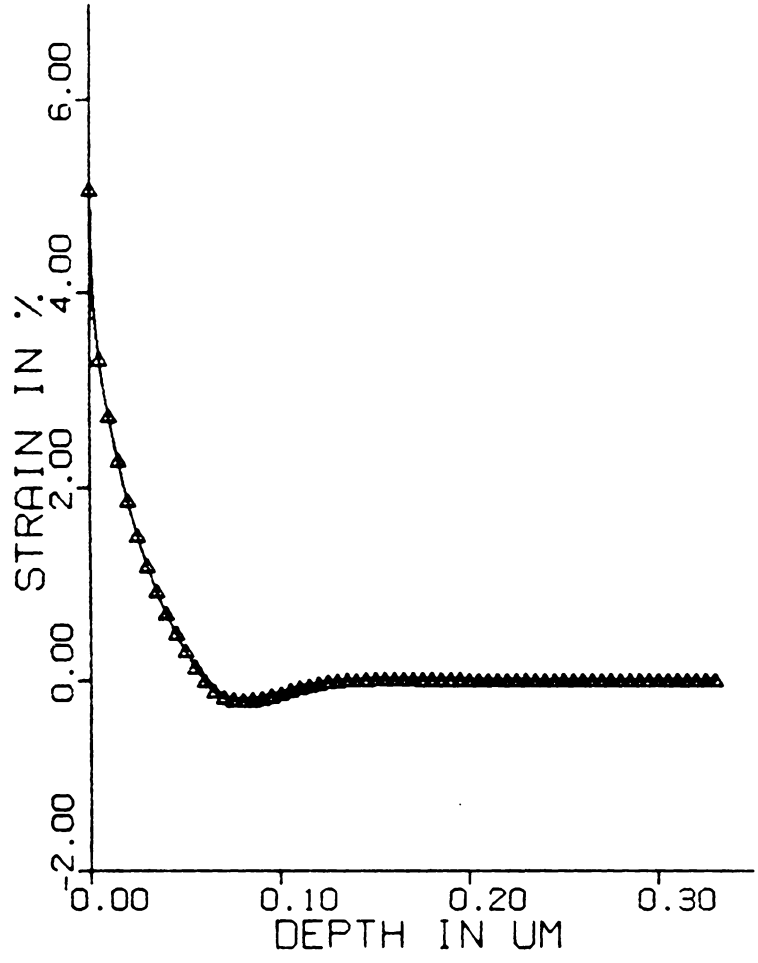

Figure 45. The depth profile of the strain perpendicular to the sample surface (polished FSZ, asymmetric diffraction optics, $\lambda = 2.4797$ A).

token, some signal generating elements in the same layer have increased absorption lengths while the others have decreased ones. Due to this compensation, the total intensity generated by a layer may remain approximately constant for different diffraction optics and the peak profiles as shown in Figs. 38 and 40 are possible.

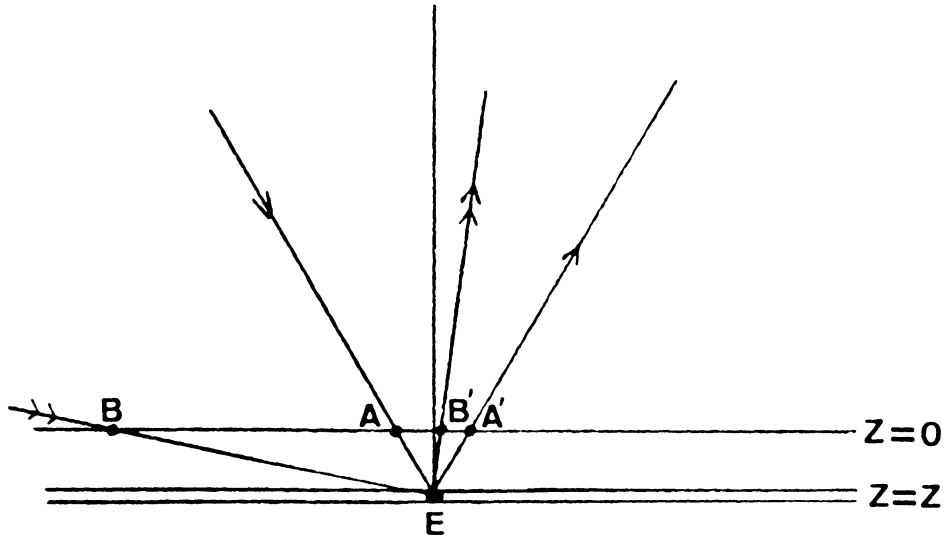

Figure 46. A schematic diagram showing the absorption lengths of the symmetric and asymmetric diffraction optics for a flat sample.

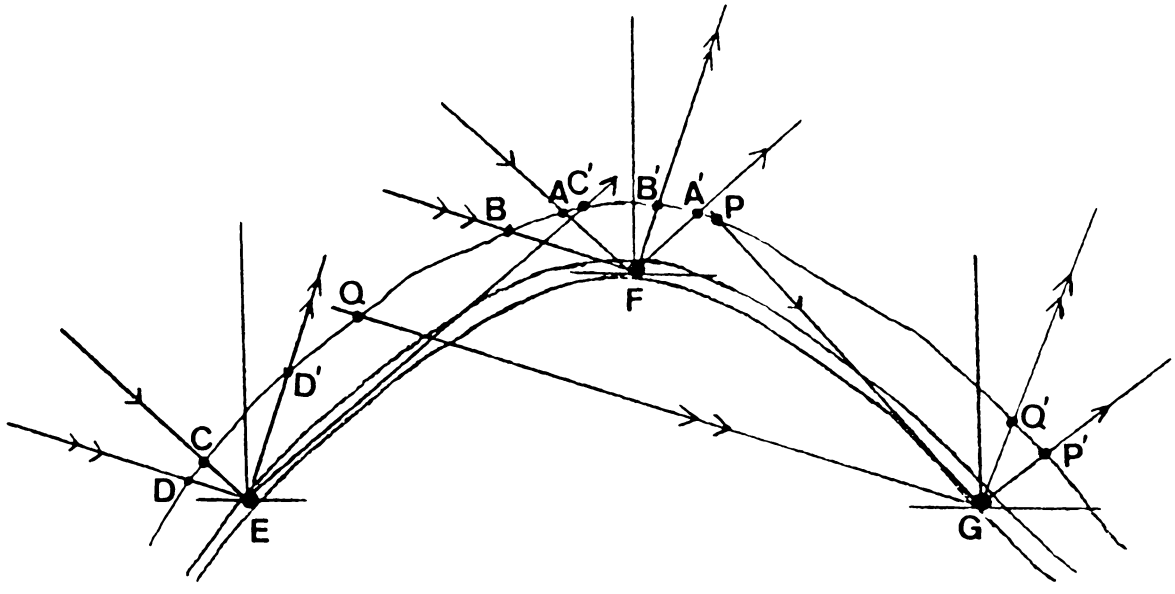

Figure 47. The schematic diagram showing the absorption lengths of the symmetric and asymmetric diffraction optics for a rough sample.

Chapter 8

EXAMINATION OF THREE HIGH PERFORMANCE CERAMIC MATERIALS BY X-RAY DIFFRACTION AND FLUORESCENCE

Except for the fully stabilized zirconia (FSZ) samples described in Chapter 5 and Chapter 7 for the roughness and the residual strain studies, three other ceramic materials are also examined using x-ray diffraction and spectroscopy. The experimental details and the results are presented in this chapter in the following order: (1)zirconia toughened alumina, (2) silicon nitride and (3) partially stabilized zirconia (PSZ). A further investigation of the PSZ samples is presented in the next chapter for the phase distribution study.

8.1 Zirconia Toughened Alumina

An x-ray diffraction (XRD) pattern and spectroscopy scans were obtained from a GE grade 460 zirconia toughened alumina sample. The XRD scans were made on an Ω type Siemens diffractometer with Cu *Kα* radiation and a scintillation counter. The x-ray tube was operated at an accerating voltage of 50 kV and a tube current of 20 mA. Repeated scans were made to record the XRD pattern on the chart for three different full scales. The three full scales are 300 cps (counts per second), 1000 cps and 3000 cps. For each full scale, two overlapping slow scans (0.1°/min.) were made to assure high statistical accuracy. The complete XRD pattern covers a 2θ range of ~ 60° and consists of six scans. This requires a total measurement time of 60 hours and the resultant statistical accuracy represents a limit one can get from commercial diffractometers.

In the spectroscopy work, a tungsten tube was used and operated at 50 kV and 20 mA to provide the incident radiation for the sample. A flow counter with 90% argon and 10% methane was used along with a wide open energy window for counting. Both lithium-fluoride (LiF) and RbAP ($RbHC_8H_4O_4$) crystals were used between the sample and the counter to analyze the radiations coming form the sample. LiF has a precise d-spacing of 2.014 Å while RbAP has a precise d-spacing of 13.0605 Å. A combination of these two provides a wide analyzing range of wavelengths for the radiation emitted from the sample. The air in the chamber containing the analyzer and sample was evacuated by a mechanical pump to reduce the attenuation of the weak fluorescence signal.

The XRD pattern of the zirconia toughened alumina sample is shown in Figure 48. Compared to the XRD patterns of metals, the most salient features of this pattern are the large number of diffraction lines and the various degrees of overlapping of these lines. These are characteristic of all ceramic materials because their crystal structures are in general more complicated than those of metals. The indexed pattern shows the presence of monoclinc, tetragonal and cubic phases of

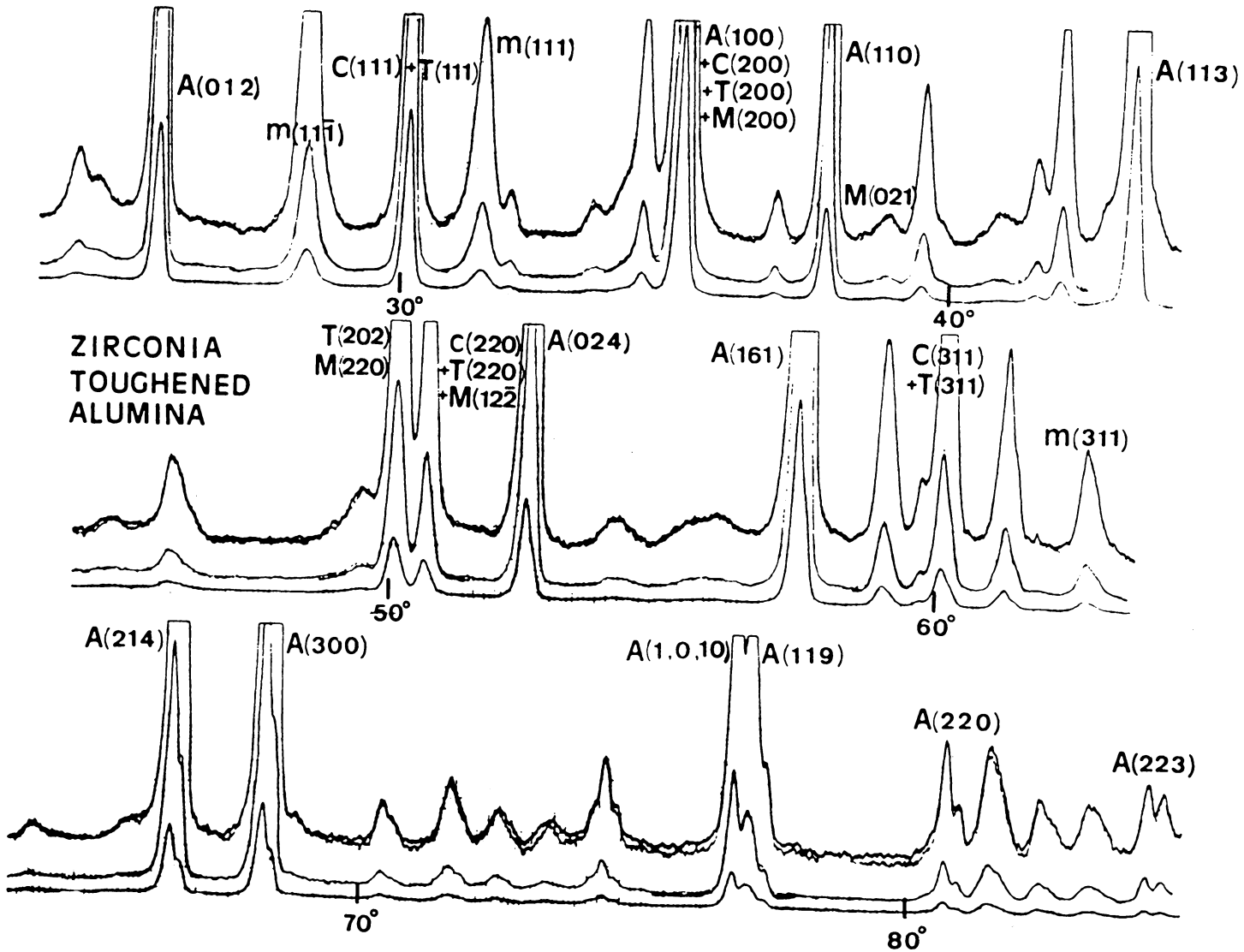

Figure 48. The XRD pattern of the zirconia toughened alumina (Cu Kα radiation).

zirconia and the α-hexagonal phase of alumina. Some unidentified minor peaks are also present in the XRD pattern. This is expected because a commercial product usually has low purity. The impurities often form minor compounds with the main elements to give extra reflection lines. Most of the reflections from these minor compounds are buried in the reflection peaks of the main phases. The unburied reflections are from many minor phases and are not necessarily the strongest three reflections from individual minor phases (even the three strongest reflections may be buried). This complexity makes a complete identification of the minor peaks very time consuming or sometimes even impossible. This difference between a ceramic system and a metalic system can be realizes and fully appreciated by an attempt to completely identify an XRD pattern like the one shown in Fig. 48.

In addition to Al and Zr, Hf and Co are also observed in the fluorescence spectra. As mentioned above, Hf and Co are probably related to the unidentified minor peaks in the diffraction pattern.

Eleven reflection lines and the corresponding 2θ positions of the α alumina are listed in the first two columns of Table 6(a). These were used as input in the "lattice" program mentioned in Section **2.2** to deduce the lattice parameters. $\alpha = \beta = 90°$ and $\gamma = 120°$ are also assigned as input because α alumina is hexagonal. The lattice parameters calculated by the computer program are listed in Table 6(b) along with data from (1) Pearson's[19] and (2) Taylor and Kagle's[20] handbooks. The three sets of lattice parameters in Table 6(b) were then used as input in the "powder" program (see Section **2.3**) to calculate the 2θ positions for the original 11 reflections. The results are listed in the 3rd, 4th and 5th columns of Table 6(a). Note that the 2θ positions of the high angle lines (denoted by **) in Table 6(a) are based on Cu $K\alpha_1$ radiation while the others are based on the Cu $K\alpha$ doublet. For each reflection, the 2θ position calculated from the "powder" program based on the lattice parameters deduced from the XRD pattern is compared with the value observed in the XRD pattern. The differences are very small, as can be seen in the last column of Table 6(a).

Table 6. (a) Peak Positions ($2\theta°$) of the Hexagonal Alumina (Cu Kα radiation).

Plane	Observed on current sample	Calculation based on Pearson	Calculation based on Taylor & Kagle	Calculation based on current lattice parameters*	Deviation from observed values
(012)	25.59	25.60	25.64	25.60	+0.01
(104)	35.16	35.18	35.30	35.18	+0.02
(110)	37.79	37.81	37.82	37.82	+0.03
(113)	43.36	43.39	43.45	43.39	+0.03
(024)	52.57	52.60	52.69	52.55	-0.02
(116)	57.51	57.55	57.73	57.55	+0.04
(214)$	66.54	66.52	66.60	66.53	-0.01
(300)$	68.23	68.21	68.22	68.23	0.00
(220)$	80.73	80.70	80.72	80.72	-0.01
(223)$	84.40	84.36	84.41	84.38	-0.02

*See Table 6(b), $Position for Cu $K\alpha_1$ radiation.

Table 6(b) Lattice Parameters of Hexagonal Alumina (Å)

Lattice Parameters	Data from Pearson	Data from Taylor & Kagle	Values Cauculated from Current Sample
a=b=	4.7589	4.758	4.7576
c=	12.991	12.925	12.9944

8.2 *Silicon Nitride*

A curved section of about 2 cm in length of a ceramic cam was obtained from ORNL. Both the worn and unworn sides were investigated by x-ray diffraction using the same experimental settings as described in Section **8.1**. The XRD patterns of both sides are shown in Figures 49 and 50. The main peaks, as identified in the XRD patterns, are from the β-hexagonal phase of silicon nitride. Some minor peaks caused by impurities are again observed in both patterns. The amorphous phase observed between 28° and 32° of the XRD pattern of the unworn surface is not observed in the XRD pattern of the worn surface. Instead, some additional unknown reflections from the worn surface are observed. This implies a phase transformation introduced by wear.

Again, three sets of lattice parameters and 2θ positions for β silicon nitride are obtained and listed in Tables 7 and 8 by applying the "lattice" and "powder" programs. The values of these three sets show good agreement among one another.

8.3 *Partially Stabilized Zirconia*

8.3.1 Background knowledge

Partially Stabilized Zirconia (PSZ) has attracted a lot of attention recently both in research and in applications[21]. Because it has some unique characteristics, some background knowledge of this material is introduced first before the experimental results.

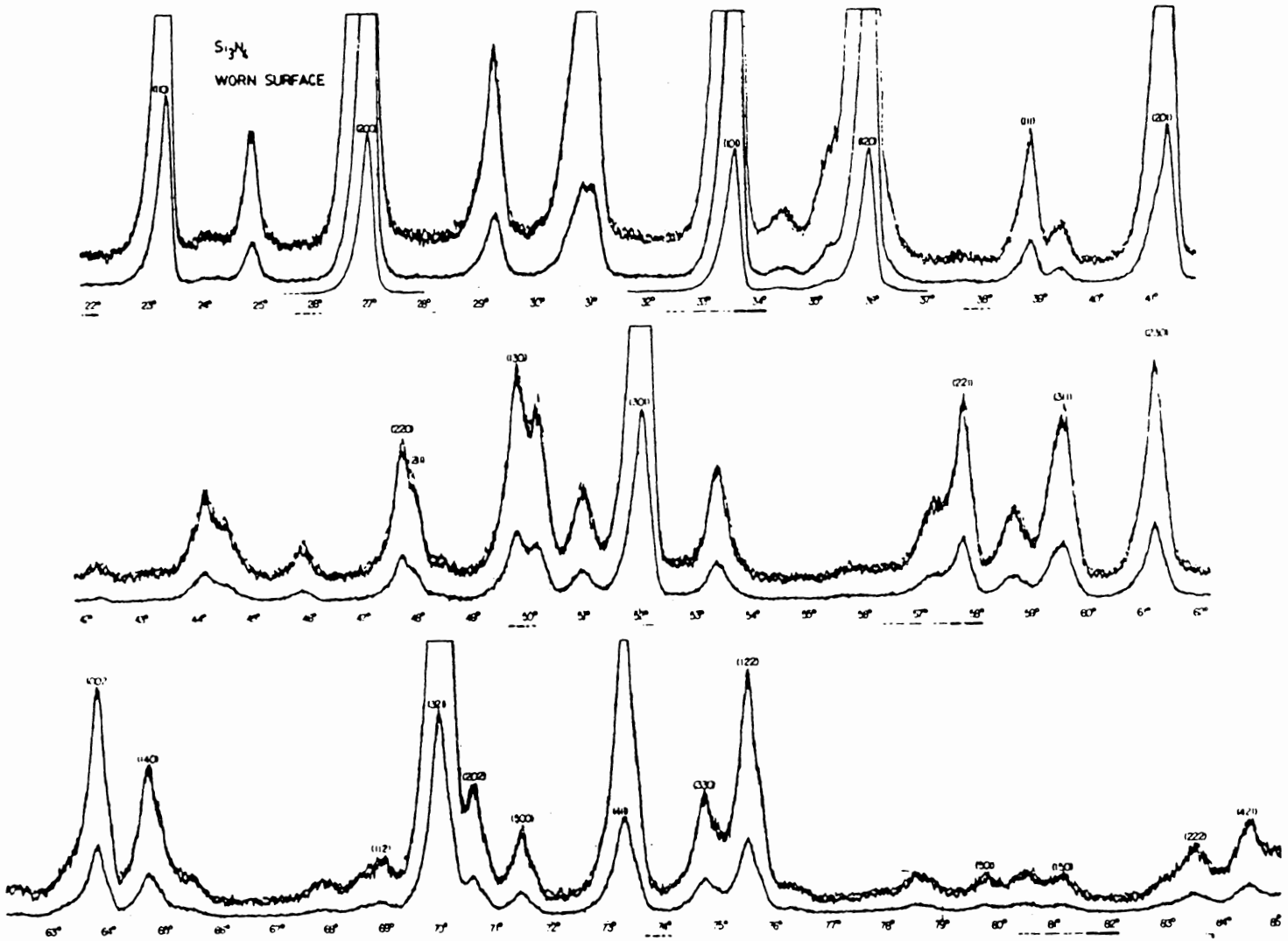

Figure 49. The XRD pattern of the silicon nitride cam (worn surface, Cu Kα radiation).

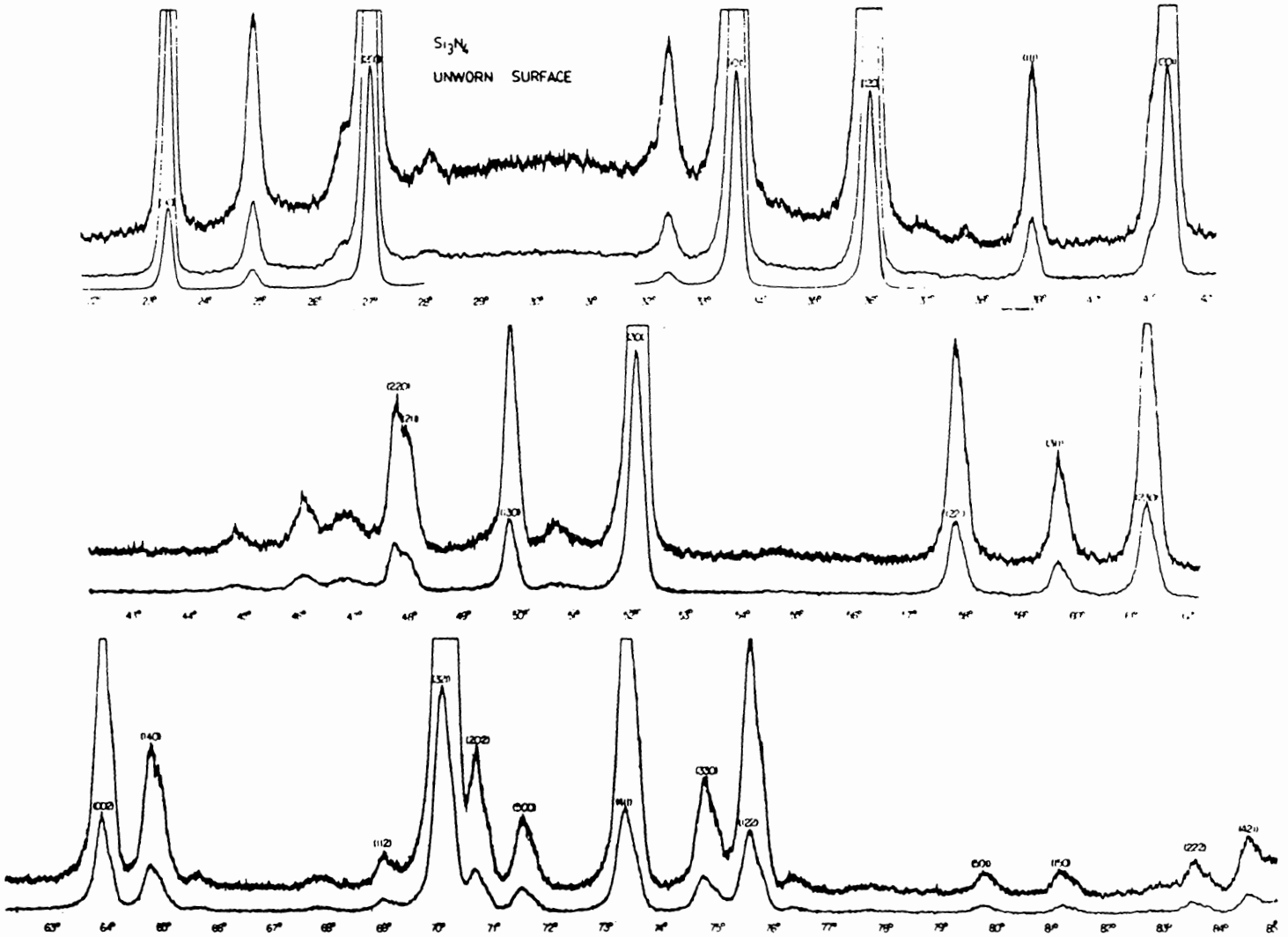

Figure 50. The XRD pattern of the silicon nitride cam (unworn surface, Cu Kα radiation).

Table 7. Peak Positions (2θ°) of β Silicon Nitride (Cu Kα radiation).

Plane	Observed on current sample	Calculation based on Pearson	Calculation based on Taylor & Kagle	Calculation based on current lattice parameters*	Deviation from observed values
(110)	23.38	23.37	23.37	23.36	-0.02
(200)	27.06	27.04	27.05	27.04	-0.02
(101)	33.64	33.63	33.65	33.63	-0.01
(120)	36.04	36.04	36.05	36.03	-0.01
(111)	38.94	38.93	38.95	38.93	-0.01
(300)	41.07	41.06	41.08	41.06	-0.01
(201)	41.36	41.36	41.38	41.35	-0.01
(220)	47.82	47.78	47.79	47.78	-0.04
(211)	47.97	48.04	48.06	48.04	+0.07
(130)	49.86	49.86	49.88	49.86	0.00
(301)	52.12	52.13	52.15	52.12	0.00
(221)	57.87	57.86	57.89	57.86	-0.01
(311)	59.68	59.70	59.72	59.69	+0.01
(230)	61.28	61.27	61.29	61.27	-0.01
(002)	63.91	63.91	63.96	63.91	0.00
(140)	64.79	64.79	64.81	64.78	-0.01
(112)	69.04	69.03	69.08	69.03	-0.01
(321)	70.07	70.09	70.12	70.08	+0.01
(202)	70.70	70.70	70.75	70.70	0.00
(500)	71.50	71.54	71.56	71.53	+0.03
(411)	73.38	73.39	73.42	73.38	0.00
(330)	74.82	74.82	74.84	74.81	-0.01
(122)	75.62	75.61	75.66	75.61	-0.01
(501)	79.82	79.83	79.86	79.82	0.00
(150)	81.22	81.22	81.25	81.21	-0.01
(222)	83.57	83.58	83.63	83.58	+0.01
(421)	84.54	84.57	84.61	84.56	+0.02

*See Table 8.

Table 8. Lattice Parameters of β Silicon Nitride (Å).

Lattice Parameters	Data from Pearson	Data from Taylor & Kagle	Values Cauculated from Current Sample
a	7.608	7.606	7.6088
b	7.608	7.606	7.6088
c	2.911	2.909	2.9109

Pure zirconia has three different forms depending on the temperture[22]. The cubic phase is stable from 2370°C to the melting temperature of (2680 ± 15°C). The tetragonal phase is stable from 1170°C to 2370°C and the monoclinic phase is stable at all temperature below 1170°C. While little is known about the transformation between the cubic and tetragonal phases, the transformation between the tetragonal and monoclinic phases is martensitic[23] with the following characteristics: (1) The high temperature tetragonal phase can not be quenched to room temperature. (2) Pure zirconia undergoes substantial contraction on heating and a corresponding expansion on cooling through the monoclinic-tetragonal transformation[24,25,26] leading to a crumbling of the ceramic.

Early studies on zirconia alloyed with CaO, MgO, Y_2O_3, and rare earth oxides showed that the two transition temperatures (monoclinic-tetragonal and tetragonal-cubic) are lowered with the addition of these alloying substances. This can be seen in the phase diagrams[27] shown in Figures 51, 52 and 53. Moreover, with a suitable amount of alloying dopant and an adequate heat treatment, the high temperature cubic phase can be retained completely or partially at room temperature. The alloying dopants (i.e. MgO, CaO, Y_2O_3... etc.) are called stabilizers. The stabilization of the high temperature phase is achieved through the dissolution of the stabilizer into the matrix of the cubic phase. The cations from the stabilizer replace some of the Zr^{+2} ions in the matrix and form a solid solution. Some vacancies are also created in the O^{-2} sites to maintain electrical neutrality. Because the retained cubic phase at room temperature is a metastable phase, it is not given in the phase diagrams.

In a PSZ sample, the monoclinic phase and tetragonal phases are dispersed in the matrix of the cubic phase. The presence and the amount of the tetragonal phase depends on the identity of the stabilizer and the process of heat treatment. The incorporation of a stabilizer in a PSZ sample not only decreases the transition temperatures, but also decreases the linear thermal expansion coefficient and the volume change associated with the monoclinic-tetragonal phase transformation. The lower linear thermal expansion coefficient of PSZ than that of pure as well as fully stabilized zirconia[24,25,26] contributes to the better thermal shock resistance of the PSZ[28] than that of cubic

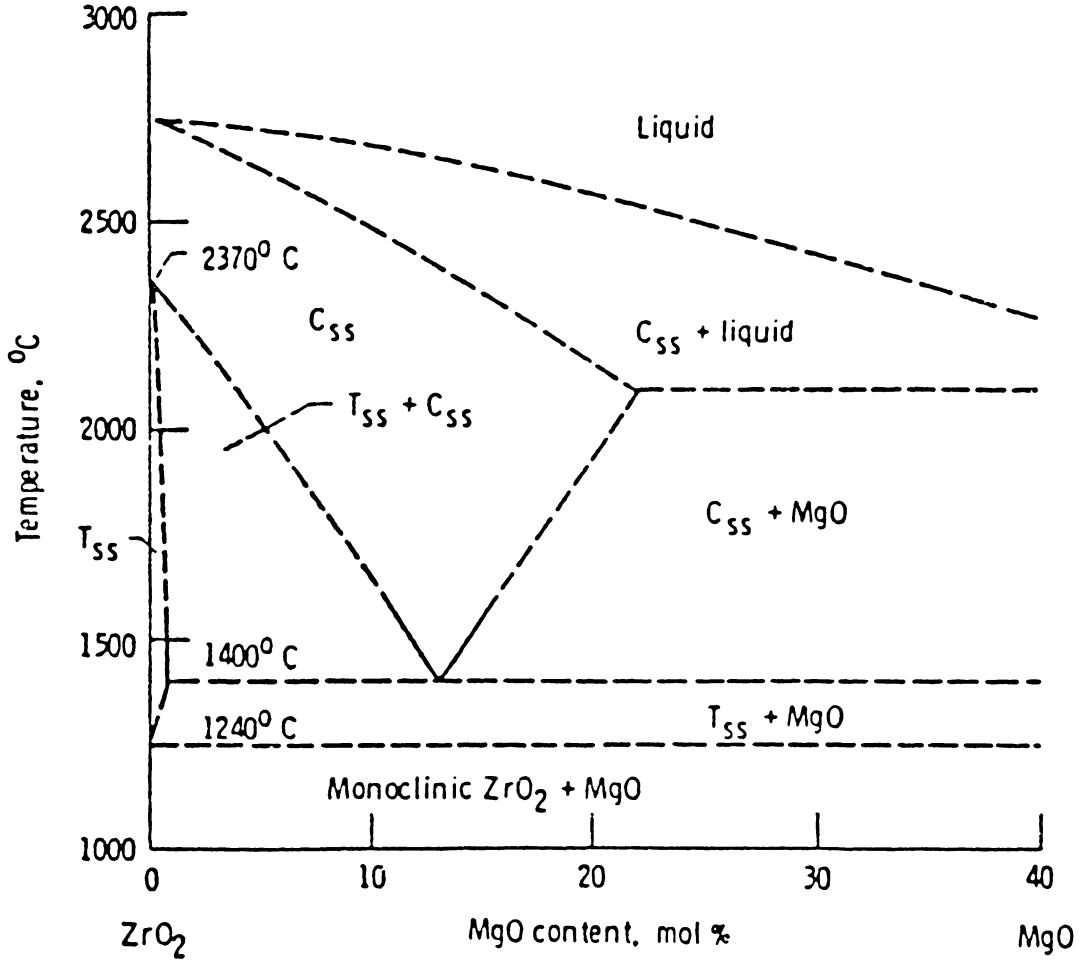

Figure 51. Phase diagram of system ZrO_2-MgO.

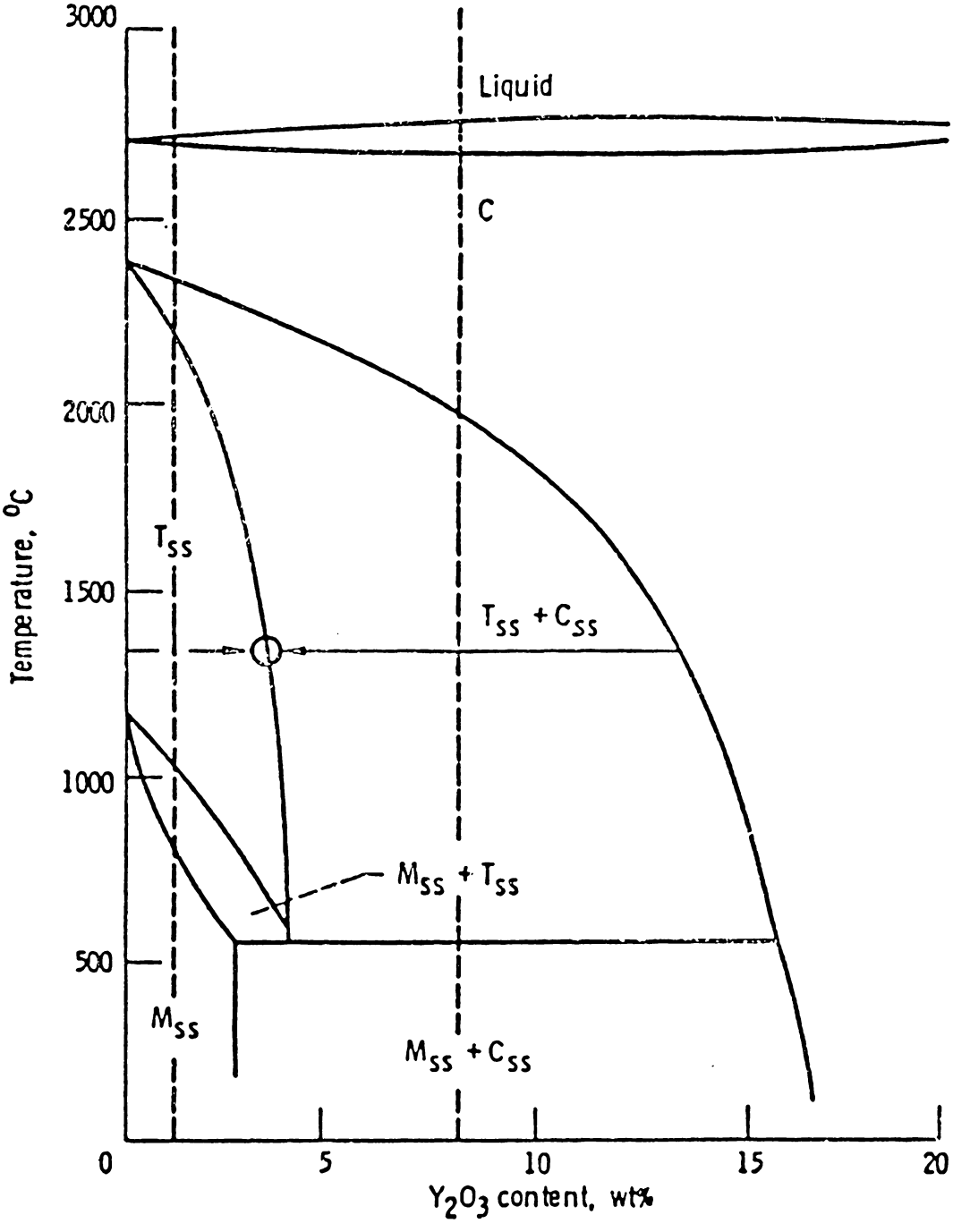

Figure 52. Phase diagram of system ZrO_2-Y_2O_3.

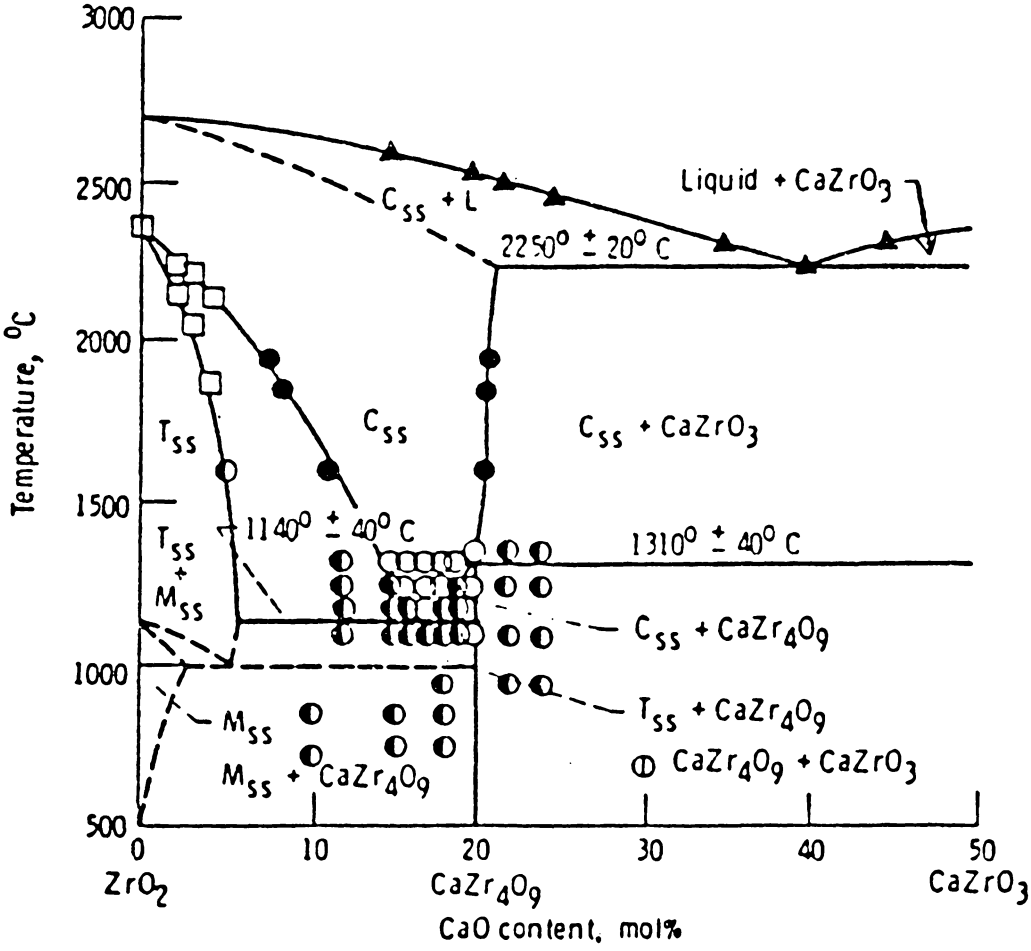

Figure 53. Phase diagram of system ZrO_2-CaO.

(stabilized) and monoclinic (pure) zirconia. Moreover, when the tetragonal phase is present, the stress at the tip of the propagating crack can be relieved by the plastic deformation which accompanies the transformation from the tetragonal to the monoclinic phase. This mechanism greatly increases the toughness of PSZ and makes it a unusual material with both strength and toughness.

Some controversy over the identity of the strongest reflection of the tetragonal phase has been raised. The strongest reflection is called (111) in some literature and (101) in other literature. This is because two closely related crystal structures were proposed for the tetragonal phase of ZrO_2 . The first structure was proposed by Ruff and Ebert in 1929[29]. It is similar to CaF_2 (fluorite) with Zr and O atoms located in the following equivalent positions within the unit cell:

Zr	0.0 0.0 0.0 0.0 0.5 0.5 0.5 0.0 0.5 0.5 0.5 0.0
O	0.25 0.25 0.25 0.75 0.75 0.25 0.75 0.25 0.75 0.25 0.75 0.75 0.75 0.75 0.75 0.25 0.25 0.75 0.25 0.75 0.25 0.75 0.25 0.25

The only difference from the cubic fluorite structure is that one edge ($c \cong 5.18$Å) of the unit cell is slightly longer than the other two edges ($a \cong 5.09$Å) instead of being equal, as in the case of cubic fluorite.

Another tetragonal structure was proposed by Taufer[30] in 1962 which has $a \cong 3.6$Å and $c \cong 5.18$Å. The equivalent positions for Zr and O atoms are as follows:

Zr	0.0 0.0 0.0 0.5 0.5 0.5

$$O \quad \begin{matrix} 0.0 & 0.5 & 0.185 \\ 0.5 & 0.5 & -0.185 \\ 0.0 & 0.5 & 0.685 \\ 0.5 & 0.0 & 0.315 \end{matrix}$$

This structure is modified by Taufer with respect to the first structure by:

1. Choosing the unit cell in the lattice in such a way that the c edge remains parallel to the c edge of the first structure while the other two edges are rotated 45° with respect to the corresponding edges of the first structure.

2. Moving oxygen atoms along the the c edge direction away from the original 1/4 and 3/4 positions in the first structure.

A computer simulation of XRD patterns with Cu $K\alpha$ radiation is presented in Table 9. It is noted that Taufer's structure gives some extra weak lines in addition to those predicted by the fluorite structure. Also, the predicted 2θ and intensity values from corresponding reflecting planes differ slightly with each other in the two structures. With these subtle small differences, the superiority and inferiority of these two structures cannot be judged unless an experimental XRD pattern of a pure tetragonal sample is available. While the strongest reflection is called the (101) according to Taufer's structure, it is called the (111) according to fluorite structure. Because they are really the same reflection and the latter is more widely used, (111) is used in this work.

8.3.2 X-ray examination of PSZ samples

Several PSZ samples from the Nilsen company have been investigated. These samples are classified as TS or MS grade depending on the heat treatmant. This results in different fractions of

Table 9. Simulated XRD Patterns of Zirconia (Tetragonal Phase, Cu Kα radiation).

Fluorite Structure				Teufer's Structure		
Normalized Intensity	Reflection Plane (hkl)	2θ (°)	D spacing (Å)	2θ (°)	Reflection Plane (hkl)	Normalized Intensity
100.00	111	30.206	2.956	30.232	101	100.00
6.93	002	34.588	2.591	34.617	002	9.73
13.26	200	35.233	2.545	35.263	110	13.25
-	-	-	2.103	43.011	012	2.45
42.82	202	50.203	1.816	50.248	112	36.49
20.78	220	50.682	1.800	50.727	200	20.79
14.89	113	59.287	1.557	59.341	103	14.90
28.53	311	60.143	1.537	60.198	211	28.55
6.32	222	62.817	1.478	62.872	202	8.05
-	-	-	1.367	68.640	122	0.81
3.30	004	72.960	1.296	73.031	004	1.98
6.22	400	74.500	1.273	74.572	220	6.23
-	-	-	1.219	78.457	014	0.46
12.35	313	81.700	1.178	81.782	213	12.37
6.05	331	82.446	1.169	82.529	301	6.06

cubic, teragonal and monoclinic phases at room temperature. Samples of both grades are partially stabilized by 2.8-4.0 wt% MgO. These samples include:

(1) A ground and lapped cube (TS grade)

(2) An as-received plate of TS grade and an as-received plate of MS grade

(3) A used cam

(4) Debris collected from a pin on disk test (TS grade)

The same operation conditions described in Section **8.1** are employed for the diffraction and spectroscopy measurements on PSZ. In addition to the Cu $K\alpha$ radiation, Cr $K\alpha$ and Cu $K\alpha_1$ radiations are also used. While the Cu tube was operated at 50 kV and 20 mA, the Cr tube was operated at 35 kV and 28 mA. Cr $K\alpha$ radiation is used to provide information from regions closer to the surface because its penetration depth is only $\sim$ 1/3 of that of Cu $K\alpha$ radiation in PSZ. The Cu $K\alpha_1$ radiation is obtained by a diffracted beam quartz monochromator which eliminates the $K\alpha_2$ component from the $K\alpha$ doublet. Also, point counting is used with $K\alpha_1$ radiation to obtain peak profiles of high statistical accuracy. At each point, the counting is terminated at either 1000 seconds or 8000 counts, whichever is reached first. While scans with Cu $K\alpha$ radiation cover a wide range of 2θ to give the general features of the XRD patterns, those with Cr $K\alpha$ or Cu $K\alpha_1$ radiation only cover the overlapping (111) reflections for the quantitative phase analysis or peak shape analysis. The results are given as follows:

(1) The ground and lapped cube (TS grade)

The fluorescence spectrum from the ground and lapped sample shows that Sr, Hf and Zr are present. Although some MgO was added by the supplier as a stablizer, Mg is not observed. This abscence is probably due to the low concentration of Mg and the high absorption of its characteristic radiations in both the sample and the spectrometer windows. The XRD pattern of Cu $K\alpha$ radiation is shown in Figure 54. The 2θ positions of various reflections from the monoclinic phase

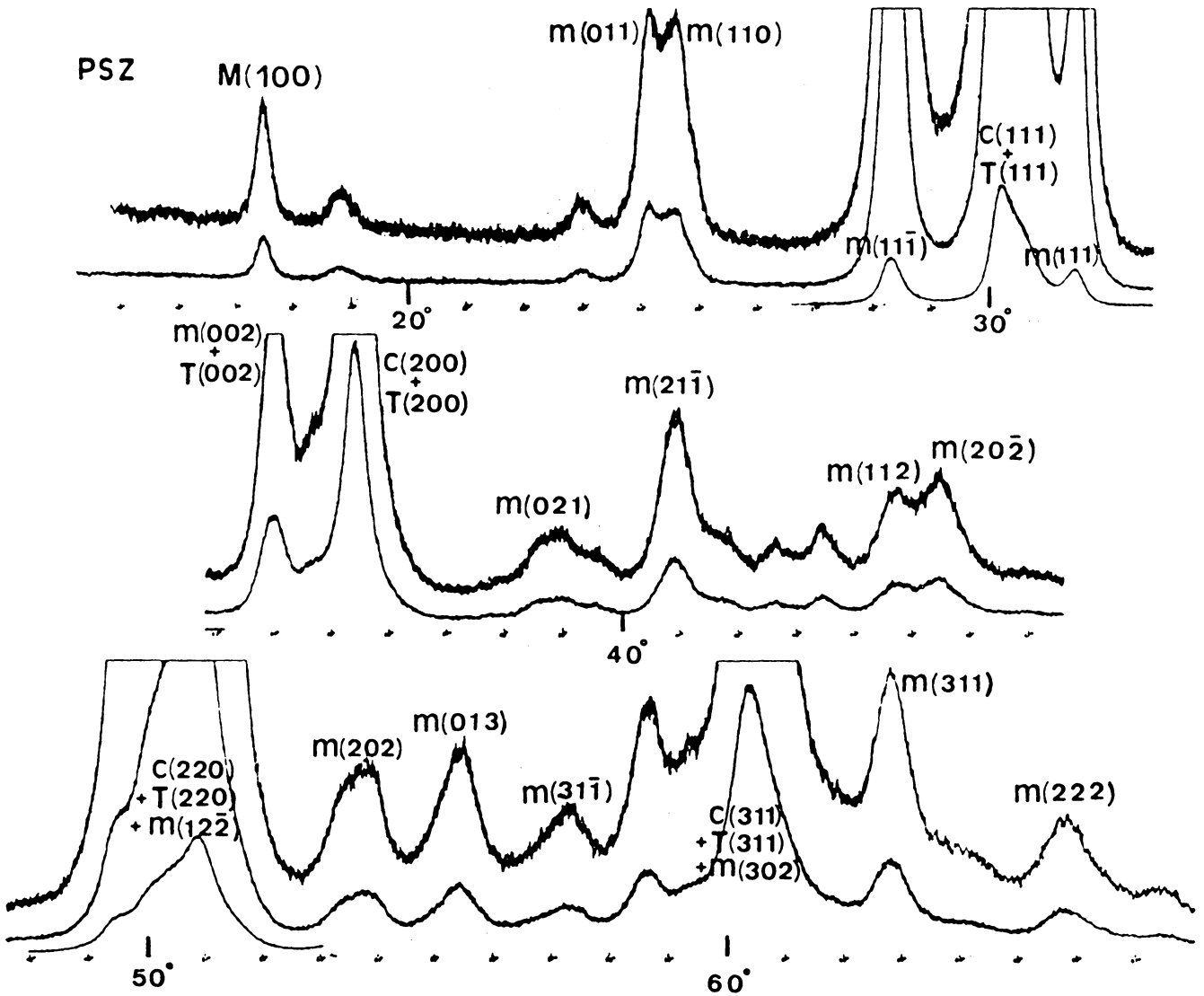

Figure 54. The XRD pattern of the ground, lapped PSZ cube (Cu Kα radiation).

Table 10. (a) Peak Positions ($2\theta°$) of the Monoclinic Phase of PSZ (Cu Kα Radiation).

Plane	Observed on current sample	Calculation based on Pearson	Calculation based on Taylor & Kagle	Calculation based on current lattice parameters*	Deviation from observed values
(100)	47.49	47.38	47.46	47.44	-0.05
(011)	24.17	23.96	24.09	24.19	+0.02
(11$\bar{1}$)	28.32	28.09	28.23	28.35	+0.03
(111)	31.49	31.33	31.49	31.52	+0.03
(21$\bar{1}$)	40.92	40.59	40.79	40.89	-0.03
(112)	44.78	44.61	44.86	44.72	-0.06
(20$\bar{2}$)	45.48	45.36	45.61	45.51	+0.03
(202)	53.81	53.82	54.12	53.83	+0.02
(31$\bar{1}$)	57.32	56.96	57.25	57.32	0.00
(222)	65.81	65.38	65.74	65.82	+0.01

*See Table 10(b).

Table 10(b) Lattice Parameters (Å) and Interaxial Angles (°) of Monoclinic Zirconia

Lattice Parameters	Data from Pearson	Data from Taylor & Kagle	Values Cauculated from Current Sample
a	5.169	5.1454	5.1484
b	5.232	5.2075	5.1314
c	5.341	5.3107	5.3442
α	90	90	90
β	99.15	99.23	98.99
γ	90	90	90

are listed in the second column of Table 10(a). The lattice parameters and interaxial angles calculated by the "lattice" program based on these reflections are listed in Table 10(b) along with the data from (1) Pearson's[19] and (2) Taylor and Kagle's[20] handbooks. The calculated length of the cell edge along the b axis deviates somewhat from the corresponding values given by the handbooks. This is no surprise because different investigators used materials from different sources. The calculated lattice parameters and interaxial angles based on the observed XRD pattern are used as input in the "powder" program to calculate the 2θ positions of previous reflections. The results are listed in 5th column of Table 10(a). Their deviations from the observed values are listed in the last column of Table 10(a). Shown in 3rd and 4th columns of Table 10(a) are the 2θ positions calculated from the lattice parameters and interaxial angles given by the handbooks. The three sets of 2θ positions listed in Table 10(a) have slight differences among one another because of the differences in the lattice parameters and interaxial angles.

Besides the monoclinic phase, the tetragonal and cubic phases are also present in the ground and lapped sample. However, the peaks of the tetragonal and cubic phases are overlapping and can not be distinguished in the XRD pattern (see Fig. 54). The overlapping between the tetragonal and cubic phases is most clearly seen in the 2θ range from 27° to 32° where three peaks are present. The peaks on the low and high angle sides are the $(11\bar{1})$ and (111) reflections of the monoclinic phase. The broad, asymmetrical peak in the center consists of the overlapped (111) reflections from the tetragonal and cubic phases. Compared to other 2θ regions with reflections from all three phases, this region has the strongest intensity and the pattern is relatively simple. Therefore, this region is most suitable for peak separation and subsequent quantitative analysis. A highly accurate XRD pattern covering the (111) reflections of all three phases was obtained by using Cu $K\alpha_1$ radiation and point counting. This is shown in Figure 55. The result of peak separation is also shown in Fig. 55 where each individual peak is fitted by a Pearson-VII function. The parameters in each individual Pearson-VII function were adjusted by trial and error until the summation of all Pearson-VII functions matched the experimental pattern. The intensities of these separated peaks are listed in Table 11 along with their reflectivities. The data in Table 11 is then used to calculate

the volume fractions of all three phases (see Section **2.5**). The result shows that the volume fractions of the monoclinic, tetragonal and cubic phases are 0.43, 0.43 and 0.15, respectively.

Similarly to the case of the monoclinic phase, the calculation of the lattice parameters and 2θ positions is also carried out for the cubic phase. The results are listed in Tables 12(a) and 12(b), where good agreement among different sets of data are observed. The intensity of the tetragonal phase is weak due to its relatively low volume fraction. No "lattice" or "powder" calculation was made for the tetragonal phase because of the difficulty to separate its peaks from the dominant cubic peaks.

(2) As-received MS and TS grade PSZ plates

The Nilsen PSZ samples can be TS or MS grade. A straightforward way of identifying the grade of a unknown PSZ sample is to compare the XRD pattern of the unknown sample with the XRD patterns of both known TS and MS grade samples. The XRD patterns of an as-received MS grade sample and an as-received TS grade sample were obtained with Cu $K\alpha$ radiation. These are shown in Figures 56 and 57, respectively. Differences between these two patterns are observed in the 2θ ranges around 30°, 35°, 50° and 60°. According to the previous simulations shown in Tables 9, 10(a) and 12(a), each of these four regions contains reflections from all three phases. Despite the difficulty in distinguishing the individual peaks in these regions, the overall features of these patterns are sufficient to identify the grade of a unknown PSZ sample. As a matter of fact, the following sample, a PSZ cam, is identified as Ms grade because its XRD pattern matches with that shown in Fig. 56.

(3)PSZ cam

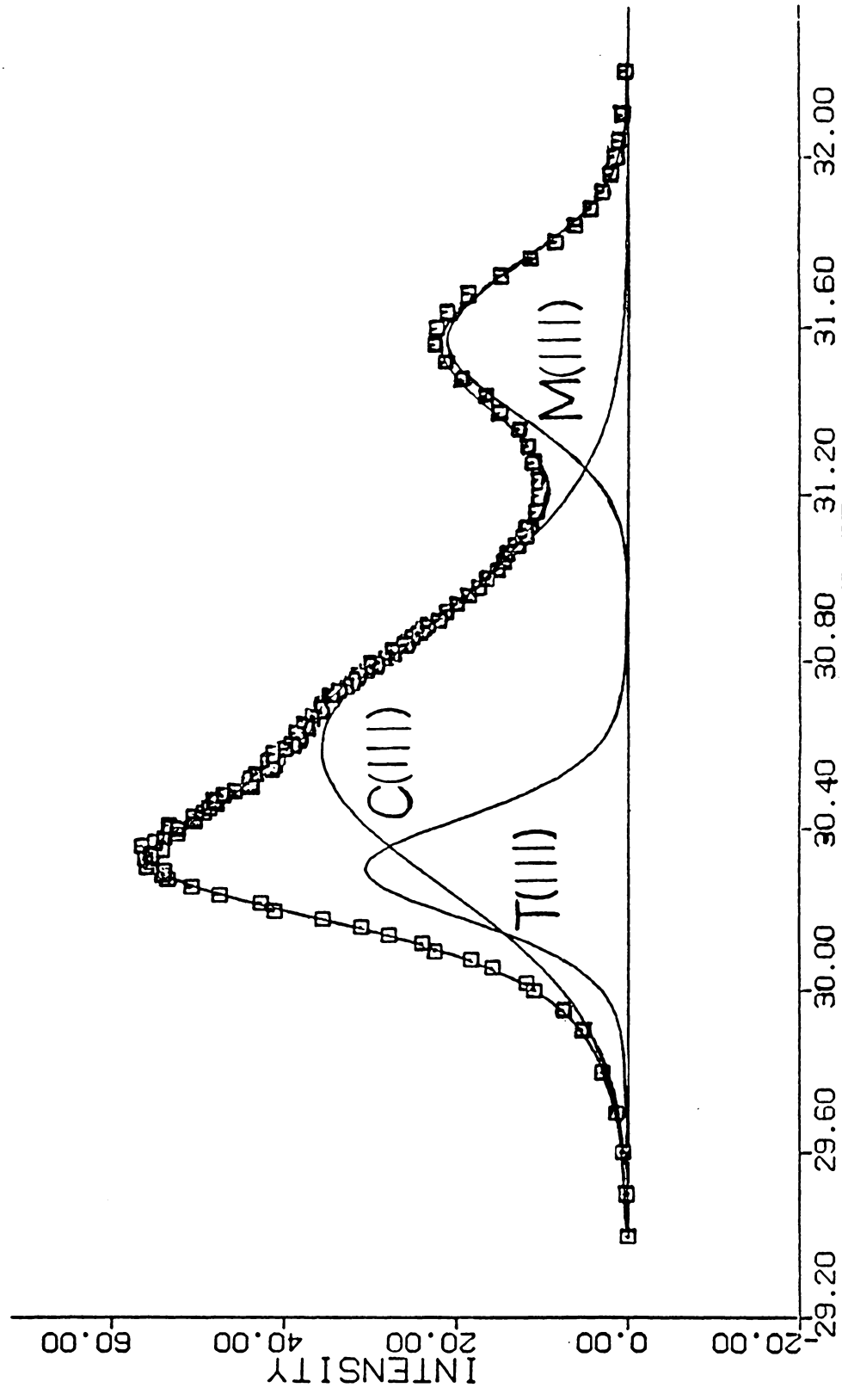

Figure 55. The XRD pattern of the ground, lapped PSZ cube (Cu Kα radiation, point counting).

Table 11. Q and Measured Intensities (Relative Units) of PSZ (Cu Kα radiation).

	M(111)	T(111)	C(111)
Q	116	364	376
I	9.4	10.5	30.3

Table 12. (a) Peak Positions (2θ°) of the Cubic Phase of the Ground, Lapped PSZ Cube (Cu Kα Radiation).

Plane	Observed on current sample	Calculation based on Pearson	Calculation based on Taylor & Kagle	Calculation based on current lattice parameters*	Deviation from observed values
(200)	35.37	35.27	35.41	35.33	-0.04
(220)	50.88	50.73	50.94	50.87	-0.01
(311)	60.39	60.31	60.57	60.43	+0.04

*See Table 12(b).

Table 12(b) Lattice Parameters of Cubic Zirconia (Å)

Lattice Parameters	Data from Pearson	Data from Taylor & Kagle	Values Cauculated from Current Sample
a=b=c=	5.0900	5.07	5.0804

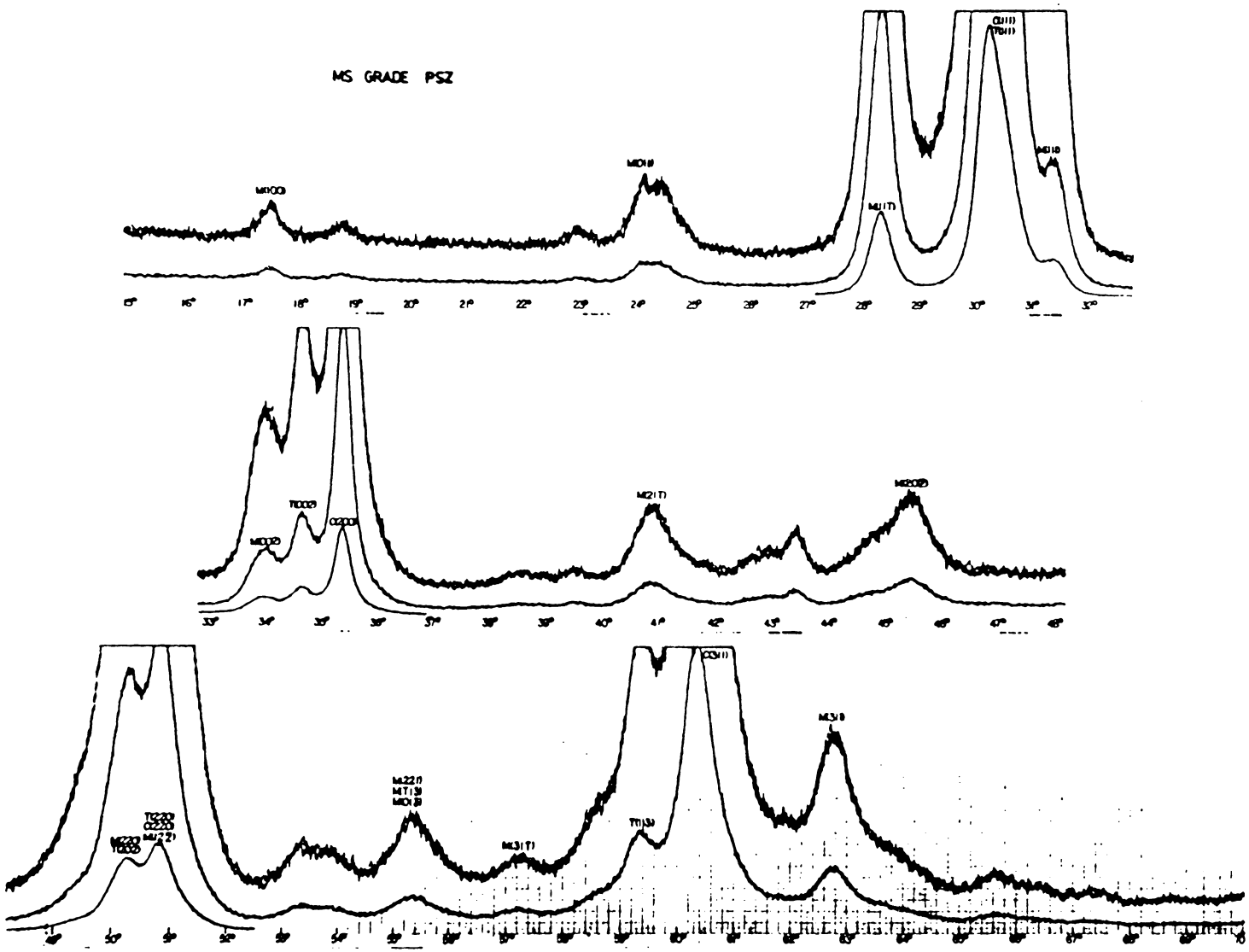

Figure 56. The XRD pattern of the as-received MS grade PSZ plate (Cu Kα radiation).

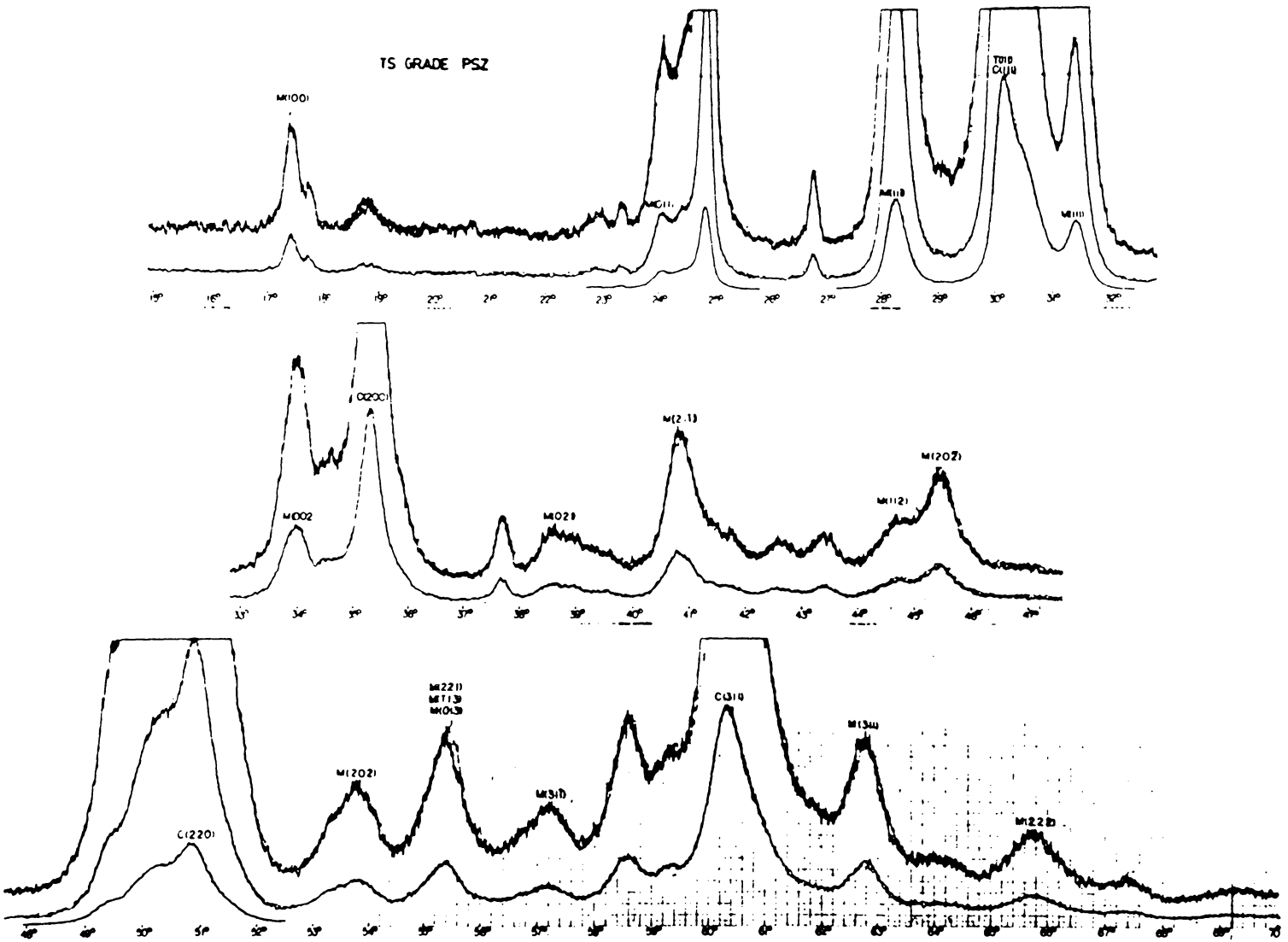

Figure 57. The XRD pattern of the as-received TS grade PSZ plate (Cu Kα radiation).

The XRD patterns with Cu Kα radiation for both the worn and unworn sides of a PSZ cam are shown in Figures 58 and 59. By comparing these patterns with the patterns of the MS and TS grade PSZ shown in Figs. 56 and 57, it is found that the cam is made of MS grade material. The patterns from the worn and unworn sides of the cam are slightly different in the 2θ regions with overlapping reflections mentioned above. Because any structure change introduced by the wear process is expected to happen in the near surface region, the less penetrating Cr *Kα* radiation is used to obtain the XRD patterns in the 2θ region of strong (111) reflections. The resulting XRD patterns from both the worn and unworn sides are shown in Figures 60 and 61. A comparison of these patterns reveals that the intensity of the monoclinic phase relative to that of the cubic and tetragonal phases was reduced after wear. A similar change is observed in the XRD patterns of the as-received and ground, lapped TS grade PSZ samples obtained with Cr *Kα* radiation (see Figures 62, 63). These suggest that a phase transformation favoring the high temperature phases has been introduced by wear or grinding and lapping. This is possible because the friction at localized contacting asperities could produce a sufficiently high temperature[31] to facilitate the phase transformation. This transformation to the high temperature phase will be further confirmed in the following analysis of wear debris.

(4) Debris collected from a pin on disk test

A pin-on-disk test was performed at Advanced Mechanical Technology, Inc. with both the pin and disk made of Nelsen TS grade PSZ. The debris were collected during the wear test and then examined using x-ray diffraction in this work. The very small amount of debris made it essential to devise an optimum holder. The optimum dimensions for the cross-section were established as the irradiated beam size at the lowest reflection angle with Cu *Kα* radiation. By etching with HCl for 5 hours, a square indentation of 1 cm × 0.7 cm × 0.08 cm was formed on a small piece of glass. This served as the sample holder for the PSZ debris. 0.0269 grams of Vaseline was added to 0.1567 grams of debris and stirred sufficiently to make a homogeneous mixture, which was then

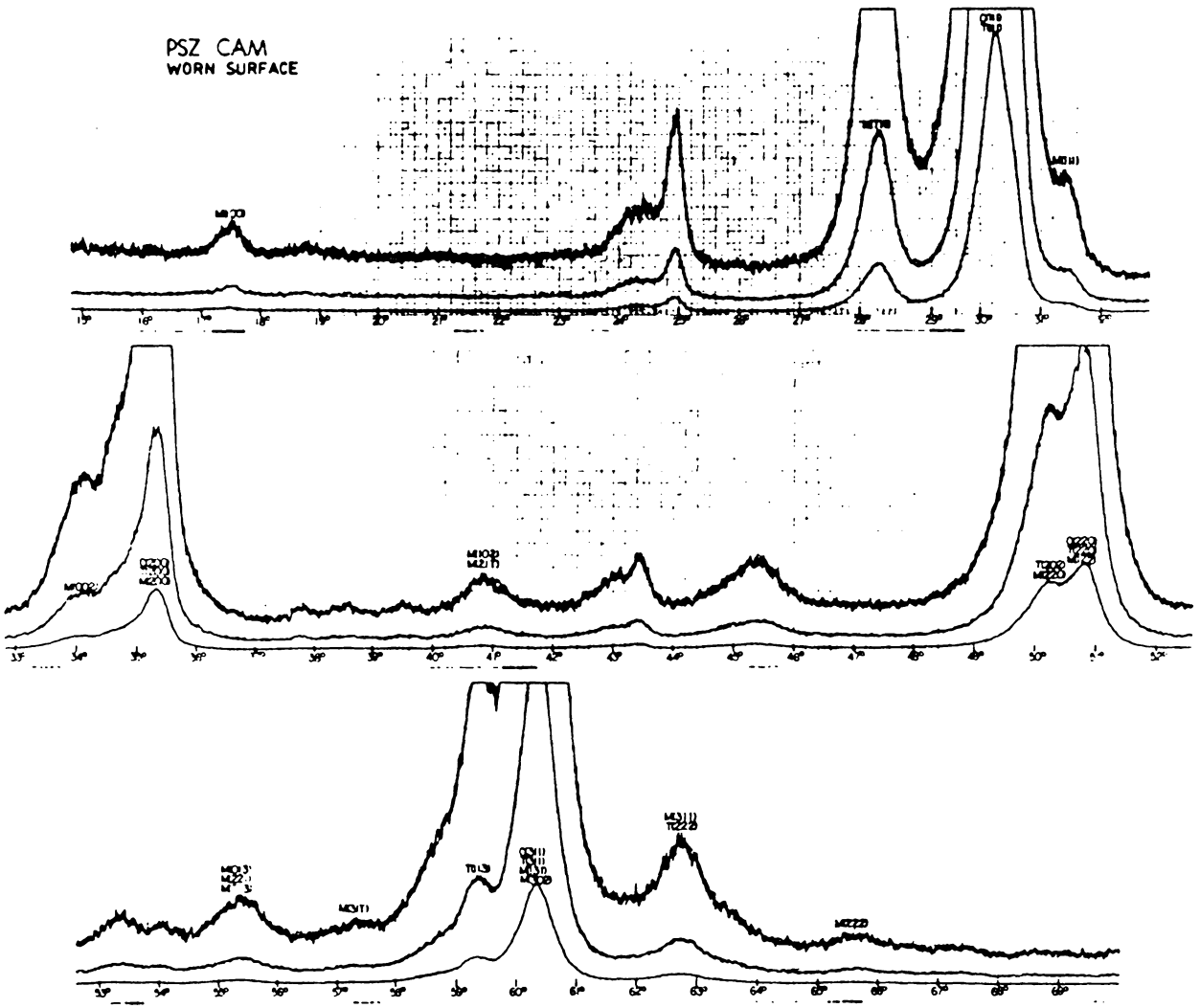

Figure 58. The XRD pattern of the PSZ cam (worn side, Cu Kα radiation).

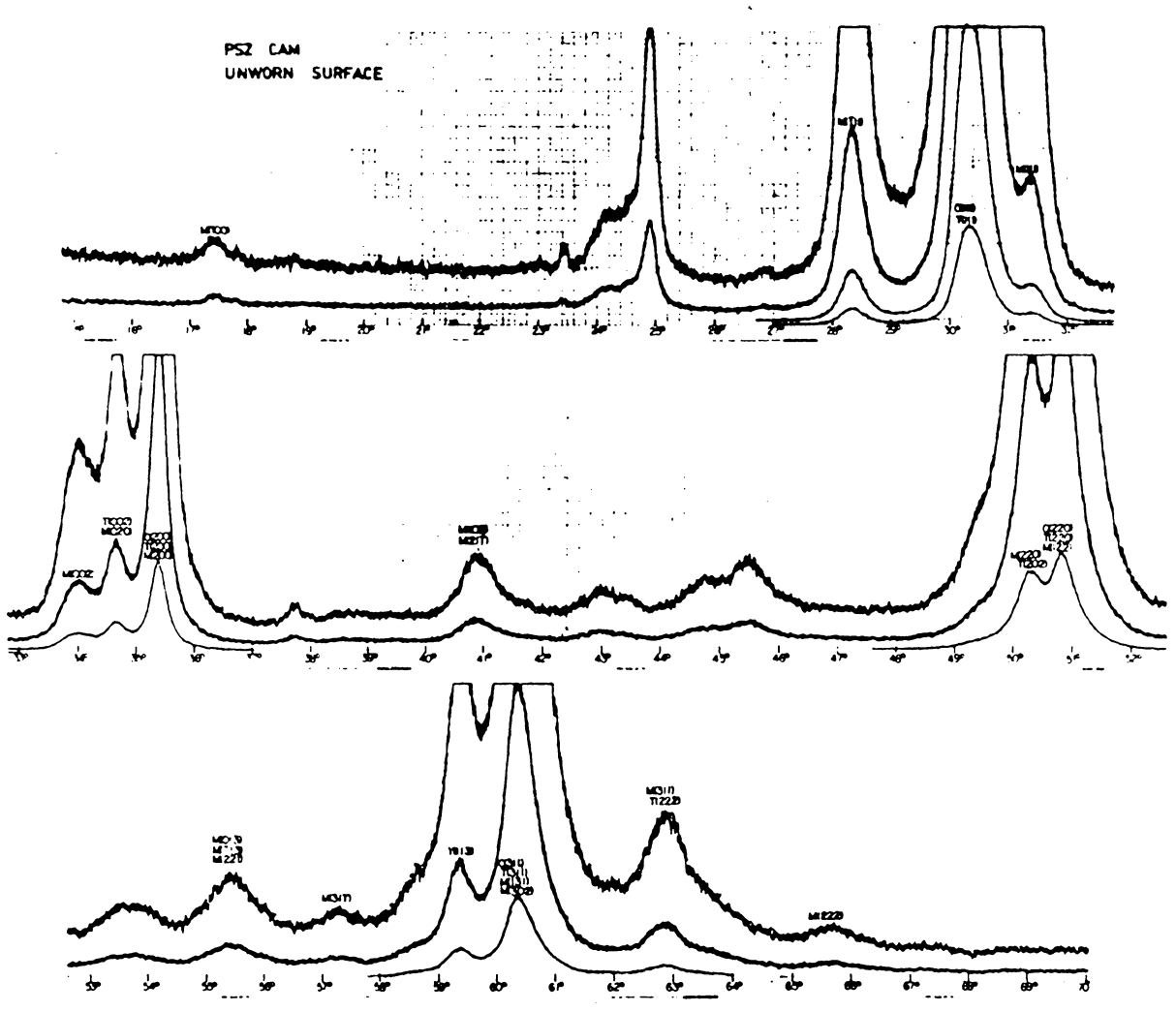

Figure 59. The XRD pattern of the PSZ cam (unworn side, Cu Kα radiation).

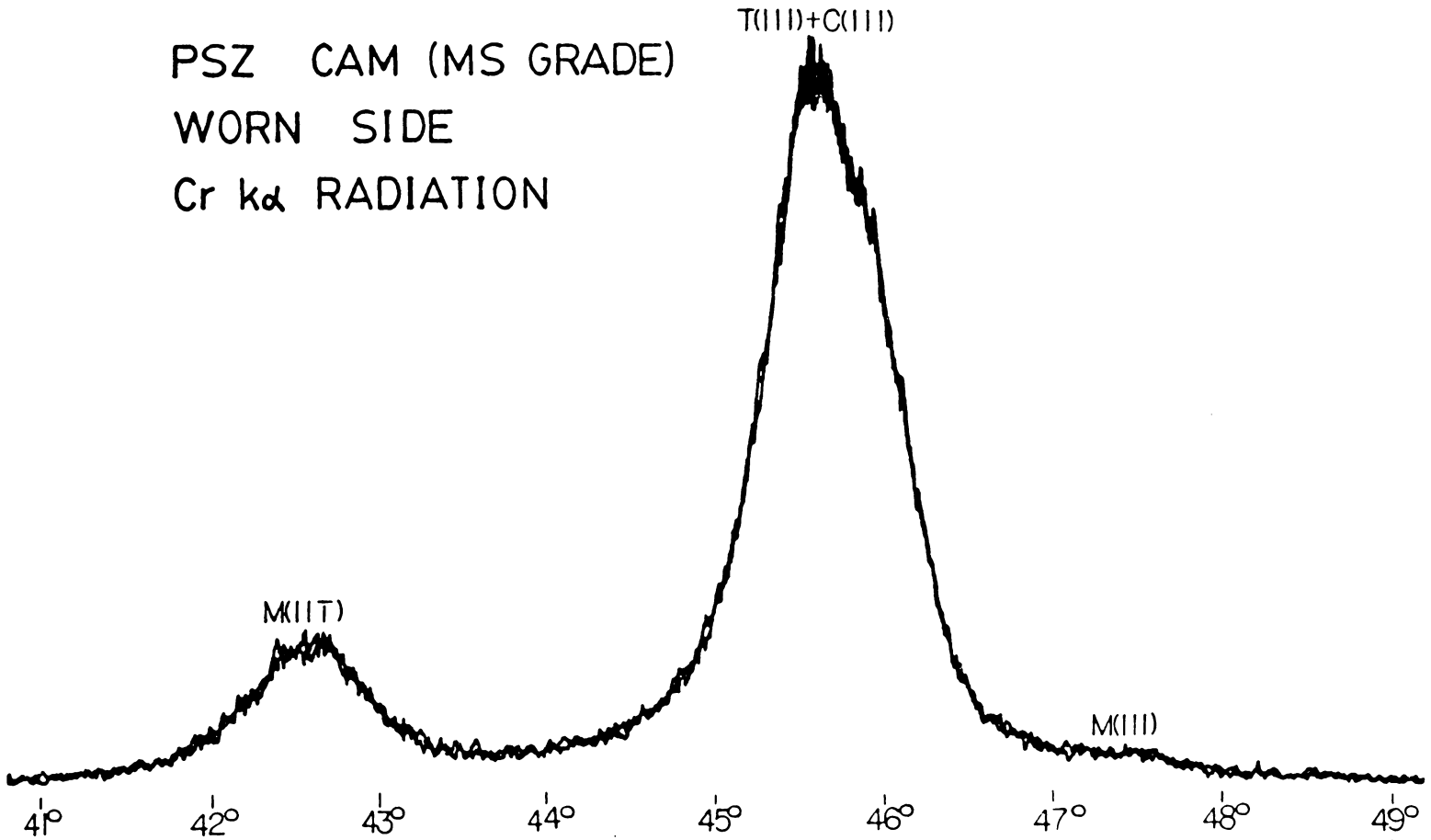

Figure 60. The XRD pattern of the PSZ cam (worn side, Cr Kα radiation).

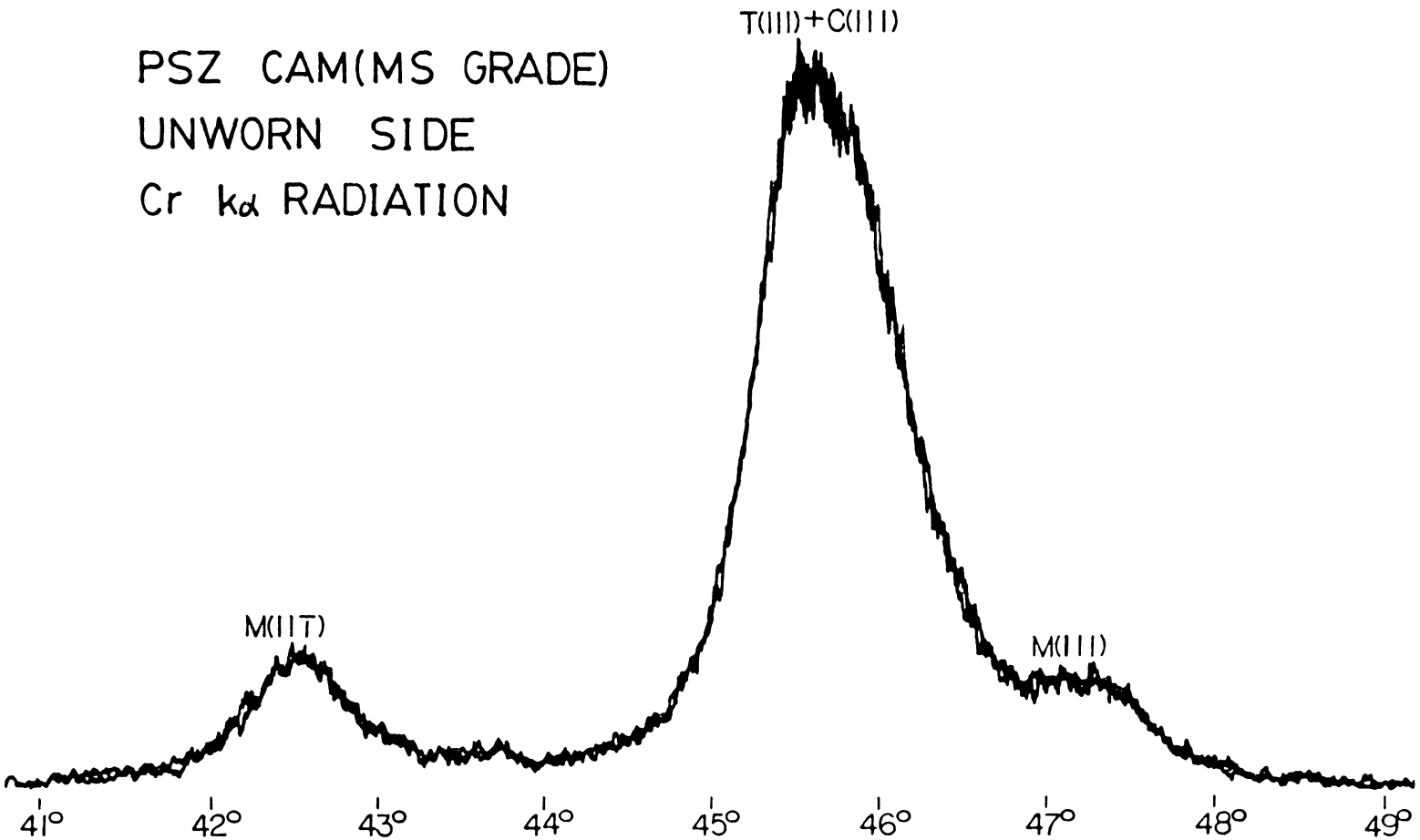

Figure 61. The XRD pattern of the PSZ cam (unworn side, Cr Kα radiation).

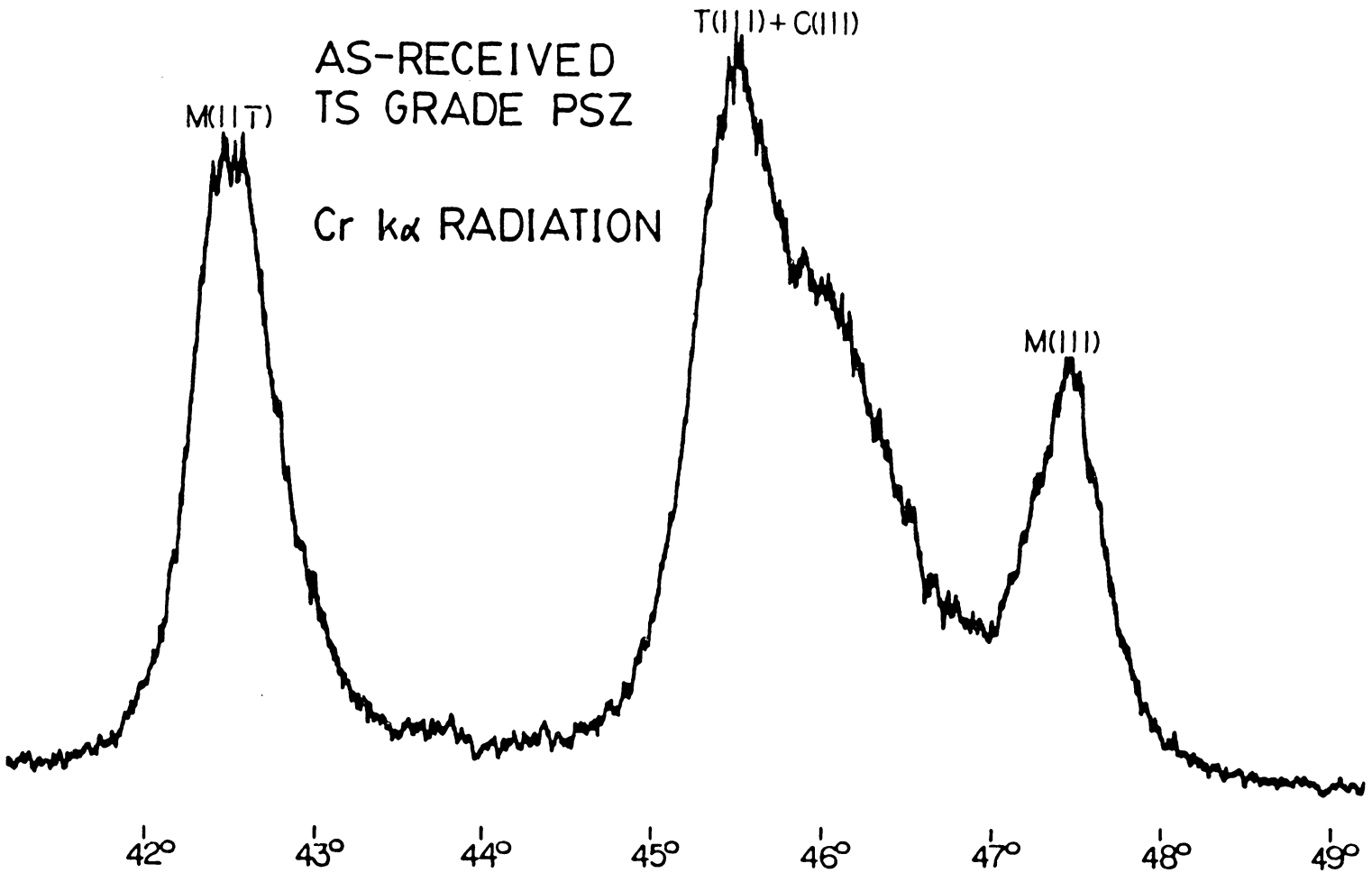

Figure 62. The XRD pattern of the as-received PSZ plate (TS grade, Cr Kα radiation).

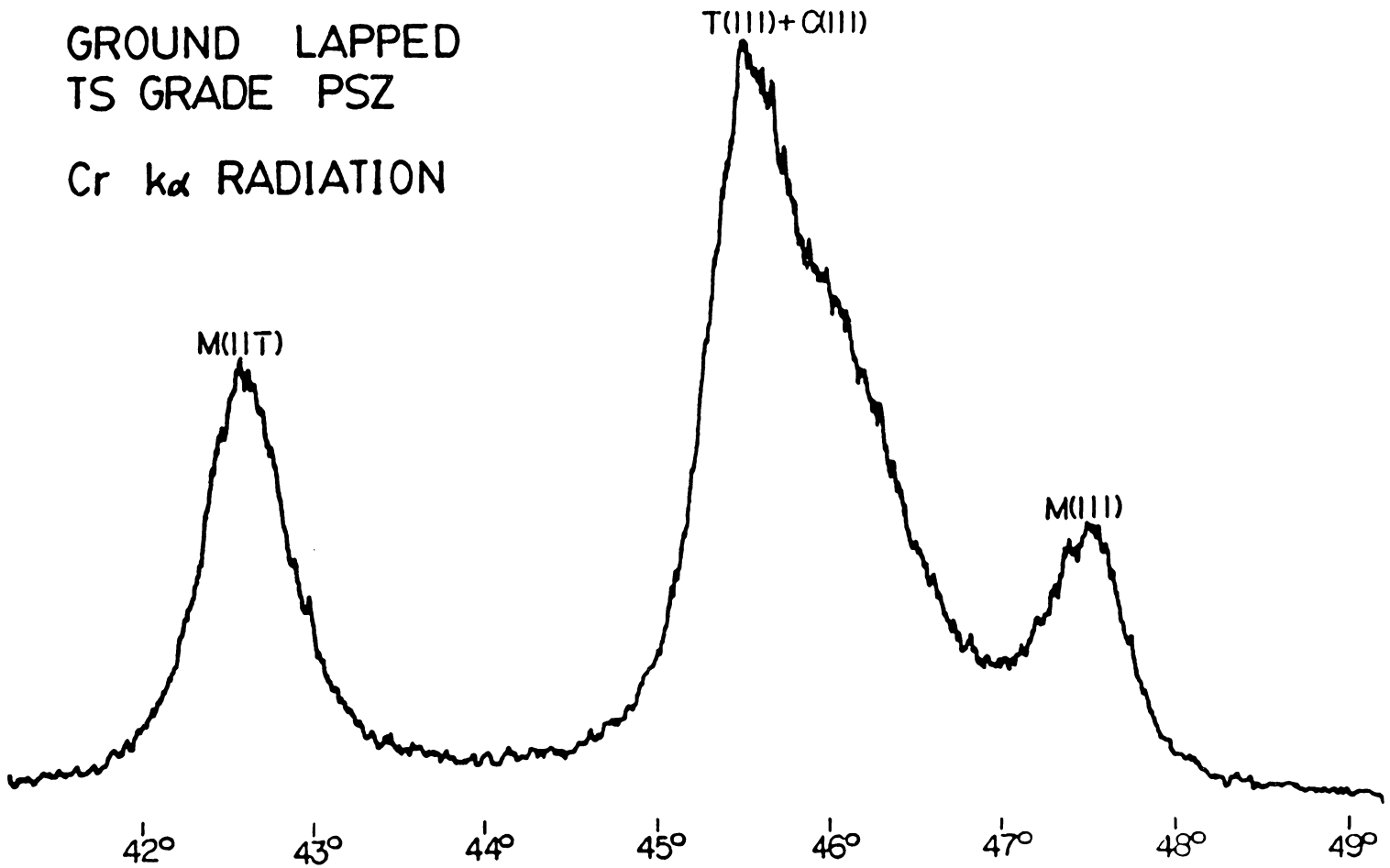

Figure 63. The XRD pattern of the ground, lapped PSZ cube (TS grade, Cr Kα radiation).

poured into the indentation of the sample holder. Finally, a razor blade was passed over the indentation to make the surface as flat as possible. The XRD pattern of pure Vaseline was also obtained to prove its amorphism.

The XRD pattern using Cu $K\alpha$ radiation from the debris is shown in Figure 64. It is surprising that only the reflections from the cubic phase are observed in the pattern. This fact strongly supports the previous conclusion that the tranformation to the high temperature phase happens in the contacting asperities because the debris, coming from the contacting asperities, consist exclusively of cubic phase.

Highly accurate profiles of the (200) and (400) peaks of the debris are obtained by using Cu $K\alpha_1$ radiation and point counting (see Figure 65). A subsequent analysis of the peak shapes was carried out by Rao[32]. These results show that the average linear size of the subgrains defined by the dislocation network is 86 Å. The variation coefficient of the size distribution of the subgrains is 0.51. If the geometrical arrangement of the dislocations is assumed to be statistically spherical, a variation coefficient of 0.51 indicates that the subgrains are not uinform in size. A nonuniform root mean square strain component, $(\bar{\varepsilon}_{1D}^2)^{1/2}$ is also determined to be 0.022. This strain component is derived from the relative displacement between neighboring unit cells which can be attributed to dislocation fields. The magnitude of this strain component is surprisingly close to that found in heavily cold worked metals and metal films, indicating a very high density of dislocations in PSZ wear debris.

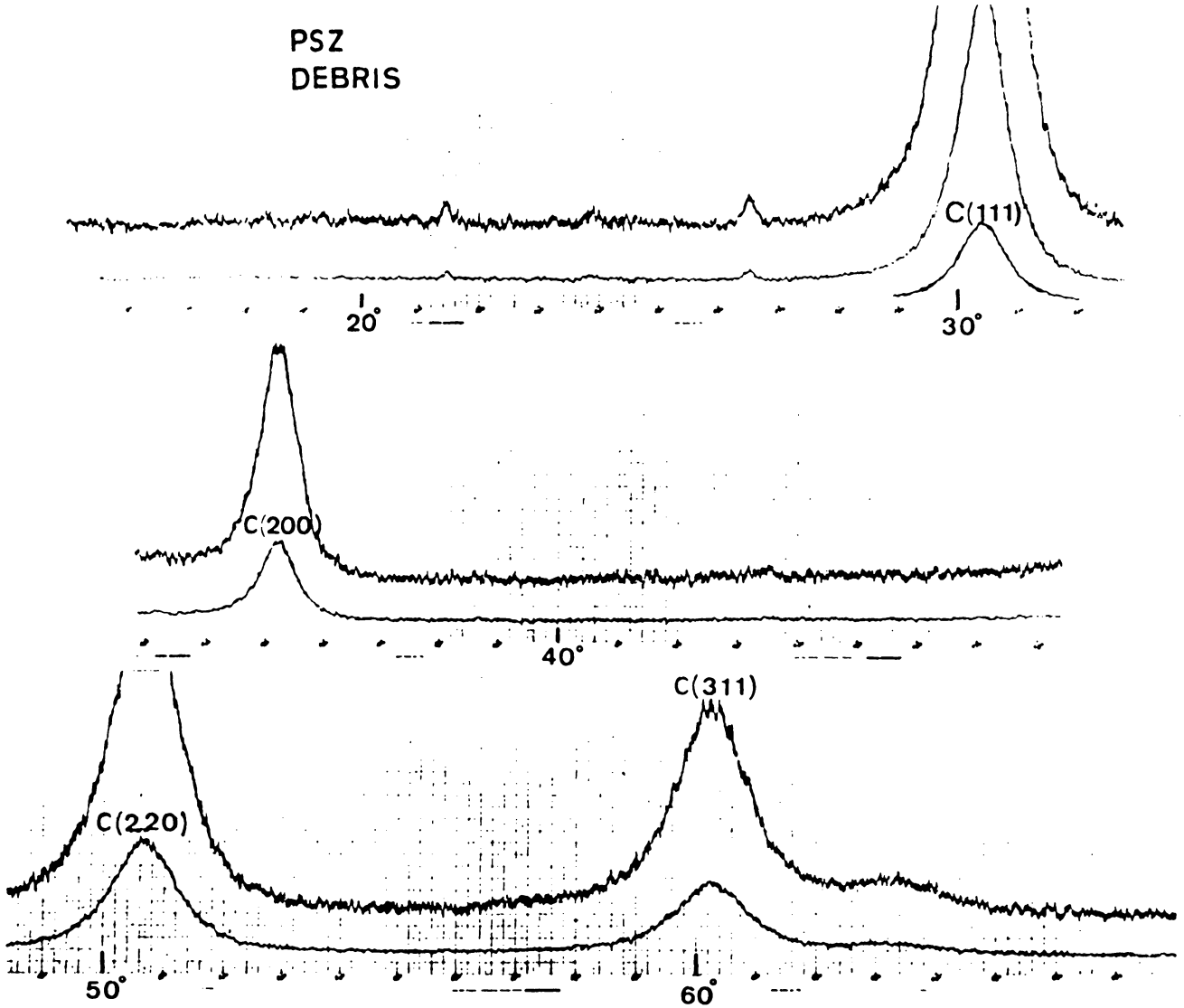

Figure 64. The XRD pattern of the PSZ wear debris (Cu Kα radiation).

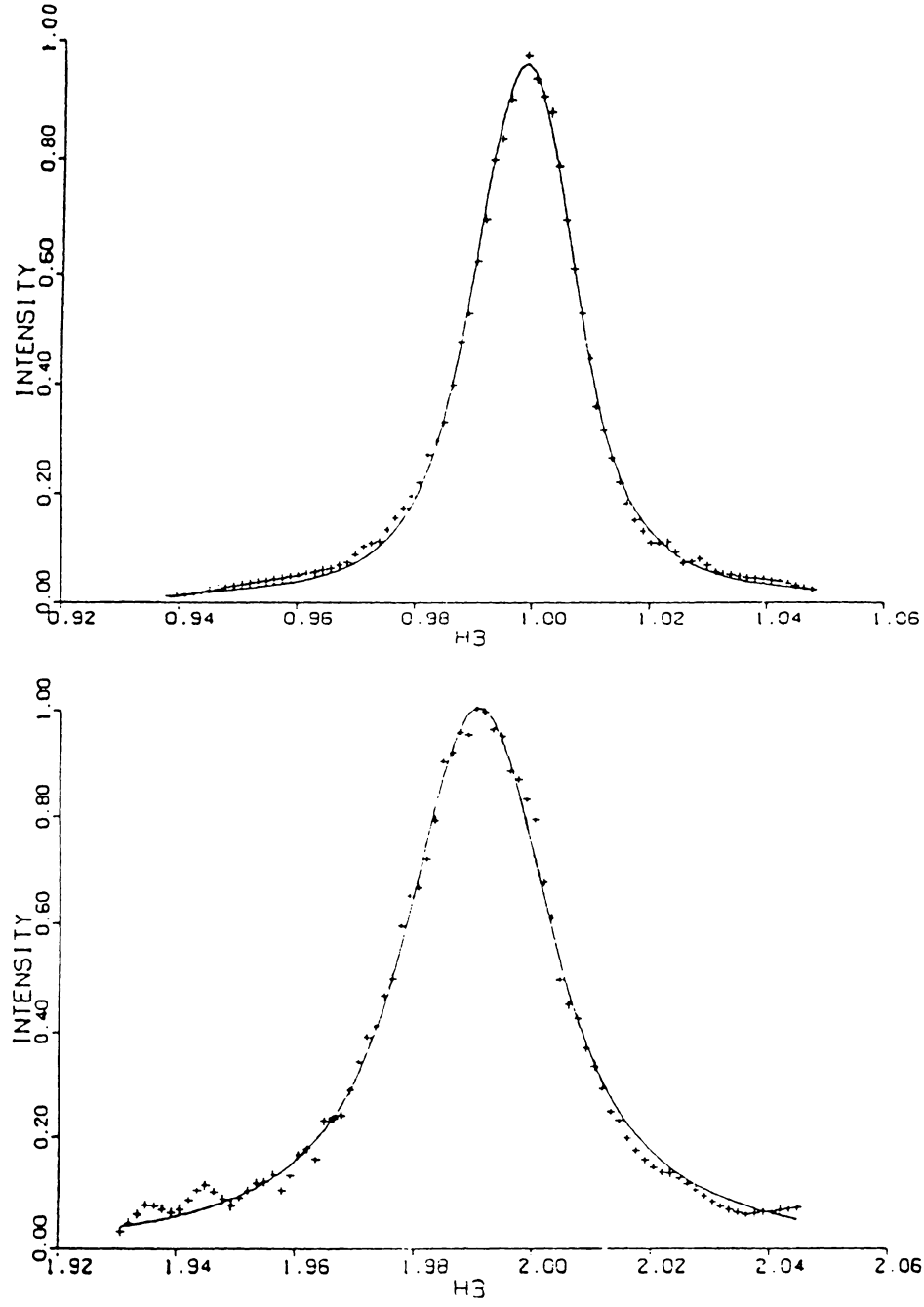

Figure 65. **Line profiles of (200) (upper) and (400) (lower) reflections from PSZ wear debris:** Cu Kα radiation, point counting.

Chapter 9

X-RAY ANALYSIS OF THE NEAR SURFACE PHASE DISTRIBUTION APPLIED TO WEAR ON A PSZ DISK

The distributions of the individual phases of a multiphase sample are often depth dependent instead of homogeneous. This depth gradient causes the diffracted intensity to vary as the penetration depth of the incident beam varies. For example, the intensity from a phase which is highly concentrated in the near surface region will be larger when a shallower probe depth is used. The intensity from the same phase will become smaller and smaller when deeper and deeper probe depths are used. By examining the variation of diffracted intensity as a function of the probe depth, one can in principle determine the distribution of the individual phases.

An XRD technique using two different wavelengths was first proposed by Swain et al. to determine the transformation zones for some fractured PSZ samples.[33] The transformation zone was described by a step function. In another experimental work, a linear or exponential distribution was

found.[34] However, this was not incorporated into the x-ray calculation. The two-wavelength technique is extended in this chapter to cover all three distributions, namely, step, linear and exponential functions. Another XRD technique using the symmetrical and asymmetrical diffraction geometries to obtain two probe depths is also described in this chapter. The theoretical derivation is based on an ideal powder sample. Nonhomogeneous powder samples with unknown depth-dependent preferred orientations are not considered. The method is demonstrated using the symmetrical and asymmetrical diffraction geometries and a PSZ sample subjected to a pin on disk wear testing.

9.1 Theory

For a specific phase j, the three depth distribution functions used in this chapter can be expressed as:

(a) linear distribution

$$H_j(Z) = \begin{cases} k_j + a_j(1 + \frac{Z}{b_j}) & -b_j \le Z \le 0 \\ k_j & Z < b_j \end{cases} \qquad (9-1)$$

(b) exponential distribution

$$H_j(Z) = k_j + a_j e^{\frac{Z}{b_j}} \quad Z \le 0 \qquad (9-2)$$

(c) step distribution

$$H_j(Z) = \begin{cases} k_j + a_j & -b_j \le Z \le 0 \\ k_j & Z < -b_j \end{cases} \qquad (9-3)$$

where $H_j(Z)$ is the area fraction of phase j at a depth $|Z|$. Note that Z is defined as a negative distance below the surface. For a thin layer of thickness dZ, the area fraction can be be treated as a volume fraction. All three functions decrease from a value of "$k_j + a_j$" at the surface to "k_j" in the bulk. Because all three distributions decrease monotonically as a function of depth, at least one of the phases must have monotonically increasing distributions to make the total volume fraction unity. These monotonically increasing functions are assumed to be the complementary functions of Eqs. (9-1), (9-2) and (9-3) (i.e. $1 - H_j(Z)$) in this work. Each depth distribution is determined by two parameters "a_j" and "b_j", giving a total of 2n parameters required to describe the depth distributions in a sample containing n phases. Because the sum of the volume fractions of n phases is unity, only 2(n-1) parameters are required to completely determine the depth distributions in an n phase sample. By using either two wavelengths or two beam paths, one can obtain two probe depths. This allows one to relate the gradient parameters to the measured intensities. The reduced intensity from a reflection i and phase j for an ideal powder is given by:[6]

$$I'_{i,j,\lambda,\omega} = \frac{I_{i,j,\lambda,\omega}}{I_0 Q_{i,j,\lambda}} = V_{i,j,\lambda,\omega} \qquad (9-4)$$

where

λ = wavelength

ω = tilt angle of the sample normal toward the incident beam (seeFig. 66).

I_0 = incident intensity

$$Q_{i,J,\lambda} = costant \times \frac{\lambda^3}{v_c^2} \times \frac{1 + \cos^2 2\theta \cos^2 2\theta'}{\sin\theta \sin 2\theta} \times pF^2 \qquad (9-5)$$

v_c = the volume of a unit cell.

2θ = the Bragg angle

$2\theta'$ = the Bragg angle for the diffracted beam monochromator

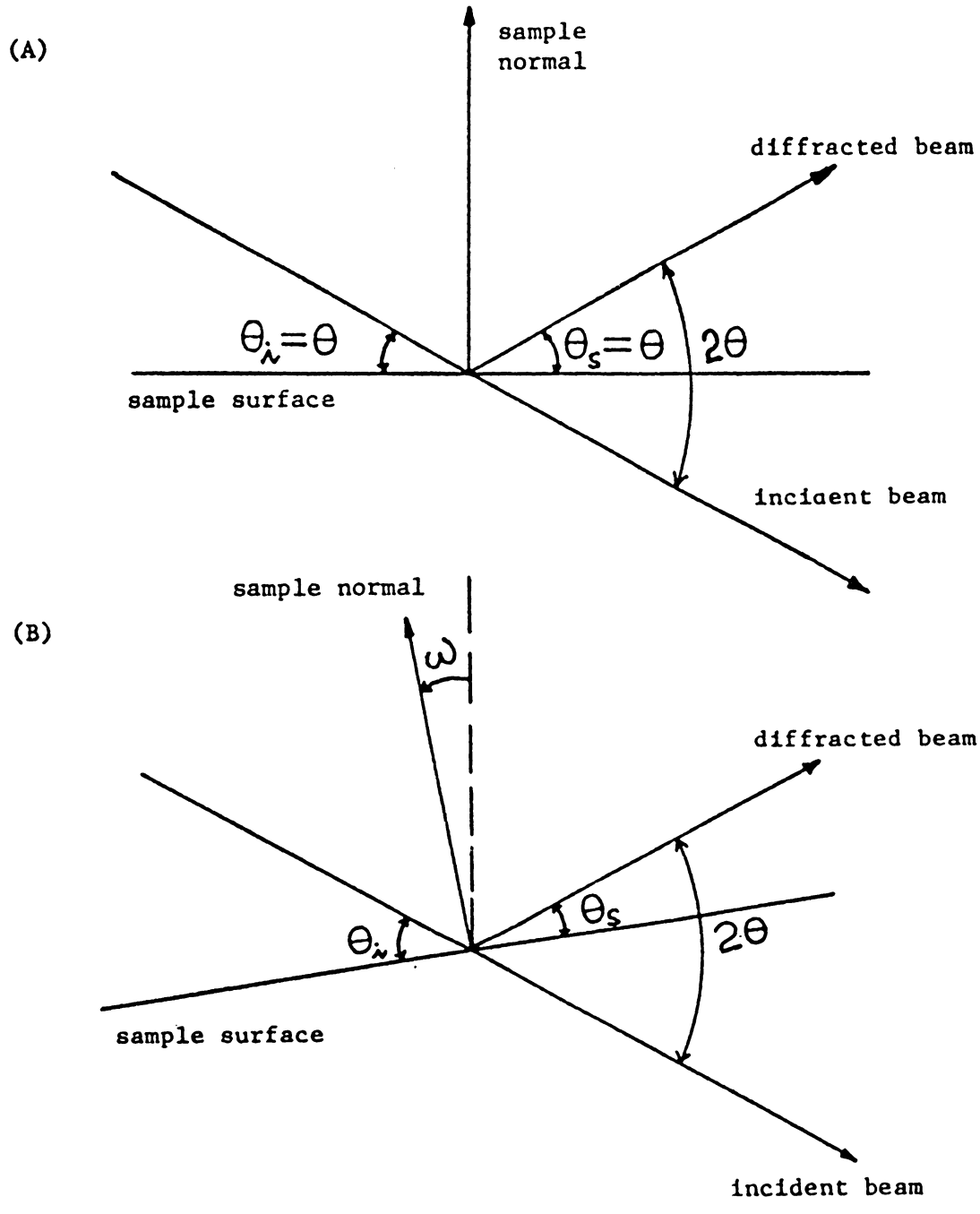

Figure 66. (a) Symmetric (b) Asymmetric optics of a diffractometer.

p = multiplicity

F = structure factor

The effective volume $V_{ij,\lambda,\omega}$ is

$$V_{ij,\lambda,\omega} = \frac{A_0}{\sin(\theta + \omega)_{ij,\lambda}} \int_{-\infty}^{0} H_j(Z)\, e^{<\mu>_\lambda Z(\frac{1}{\sin(\theta+\omega)_{ij,\lambda}} + \frac{1}{\sin(\theta-\omega)_{ij,\lambda}})}\, dZ \qquad (9-6)$$

A_0 = cross sectional area of the incident beam

$<\mu>_\lambda$ = the linear absorption coefficient (averaged over all phases)

Note that the thermal term has been omitted with the assumption that $e^{-2M_j} = 1$ in Eq. (9-5). The ratio of the reduced intensity (or volume) of one phase to another is

$$R_{\lambda,\omega} = \frac{\sum_i I'_{ij,\lambda,\omega}}{\sum_{i'} I'_{i',j',\lambda,\omega}} = \frac{\sum_i V_{ij,\lambda,\omega}}{\sum_{i'} V_{i',j',\lambda,\omega}} \qquad (9-7)$$

Note that j, j′ are any two phases in the sample with n phases. The summations over i and i′ indicate that one or more than one reflections can be selected from the corresponding phases. Because j, j′ may be any two of the n phases, Eq.(9-7) represents a set containing up to (n-1) independent intensity ratios for a fixed λ and a fixed ω. In the two-wavelength technique, one use $\omega = 0°$ and $\lambda = \lambda_1, \lambda_2$ in Eq. (9-7) to get 2(n-1) intensity ratios in terms of n effective volumes. With the intensity ratios measured from the XRD patterns of λ_1, and λ_2, the unknown parameters contained in the effective volumes can be determined. Similarly, with two diffraction geometries, one can use a fixed λ and $\omega = \omega_1, \omega_2$ in Eq. (9-7) to obtain 2(n-1) intensity ratios in terms of n effective volumes. The unknown parameters, located in the effective volumes, can be obtained from the measured intensities and other data normally available. The effective volumes obtained from Eq. (9-6) are:

(a) linear distribution

$$V_{ij,\lambda,\omega} = \frac{A_0}{\sin(\theta + \omega)_{ij,\lambda} < \mu >_\lambda S_{ij,\lambda,\omega}} \left\{ k_j + a_j \left[1 - \frac{1 - e^{- < \mu >_\lambda b_j S_{ij,\lambda,\omega}}}{< \mu >_\lambda b_j S_{i,j,\lambda,\omega}} \right] \right\} \quad (9-8)$$

(b) exponential distribution

$$V_{ij,\lambda,\omega} = \frac{A_0}{\sin(\theta + \omega)_{ij,\lambda} < \mu >_\lambda S_{ij,\lambda,\omega}} \{ k_j + \frac{a_j}{1 + \frac{1}{b_j < \mu >_\lambda S_{,ij,}\lambda,\omega}} \} \quad (9-9)$$

(c) step interface

$$V_{ij,\lambda,\omega} = \frac{A_0}{\sin(\theta + \omega)_{ij,\lambda} < \mu >_\lambda S_{ij,\lambda,\omega}} \left\{ k_j + a_j [1 - e^{- < \mu >_\lambda b_j S_{ij,\lambda,\omega}}] \right\} \quad (9-10)$$

where

$$S_{ij,\lambda,\omega} = \frac{1}{\sin(\theta + \omega)_{i,j,\lambda}} + \frac{1}{\sin(\theta - \omega)_{i,j,\lambda}} \quad (9-11)$$

The effective volumes for the complementary linear, exponential and step distributions can be obtained from Eqs.(9-8), (9-9) and (9-10) with "k_j" and "a_j" replaced by "$1 - k_j$" and "$-a_j$", respectively. The two beam path approach is applied to a PSZ disk in the next section.

9.2 *Phase Distribution for A PSZ Disk*

The determination of the phase distributions for a PSZ disk after a pin on disk wear testing was carried out for both the worn track and an unworn region. The wear testing was carried out at an ambient temperature of 400° F, within an atmosphere of prepurified nitrogen. A 1/4" diameter pin was loaded to 2.8 pounds against a disk traveling at 1 ft./sec. at the point of contact. The

total time of testing was 61 hours. XRD patterns from both the worn track and the back side of the disk were obtained with synchrotron radiation ($\lambda = 2.4797$ Å) using the Oak Ridge National Laboratory beamline at the National Synchrotron Light Source. Two paths were obtained using a typical symmetrical arrangement ($\omega = 0°$) and an asymmetrical arrangement having the sample normal tilted toward the incident beam. Here the sample was at a 6° angle with the diffracted beam. The XRD patterns include the (111) and ($11\bar{1}$) reflections of the monoclinic phase (M(111), M($11\bar{1}$)) and the overlapping (111) reflections of the cubic and the tetragonal phases (C(111), T(111)). These XRD patterns are shown in Figures 67, 68, 69 and 70. A peak separation using the Pearson-VII function[9] was then carried out for each pattern to unscramble the profiles. the region where the C(111) and T(111) reflections are expected appears to be symmetrical for the unworn sample and could be fitted by only one peak. The same region of the patters of the worn track is asymmetric and requires a fitting with two peaks. The peak separation is also shown in the XRD patterns. The peak area of T(111) in Fig. 69 or Fig. 70 is about 25% of the total area for all reflections. Because the small separation between the T(111) and C(111), a level lower than 25% is not expected to produce perceptible asymmetry and a separation cannot be justified. Although wear testing introduces a detectable amount of the tetragonal phase, The combined intensity of C(111) and T(111) and the intensities of the M(111) and M($11\bar{1}$) are measured and listed in Table 13. These will be used later to determine the phase distributions of the combined cubic and tetragonal phases because of quantitative uncertainty in the unscrambling procedure for closely spaced peaks. the combibed C(111) and T(111) reflections is denoted by CT(111) and its intensity is given by

$$I_{CT(111),\omega} = I_0 Q_{C(111)} V_{C(111),\omega} + I_0 Q_{T(111)} V_{T(111),\omega} \qquad (9-12)$$

Note that the subscript λ is dropped in Eq. (9-12) because λ is fixed in this approach. $Q_{C(111)}$ and $Q_{T(111)}$ are very close and are replaced by the averaged value $\bar{Q}_{CT(111)}$, i.e.

$$I_{CT(111),\omega} = I_0 \bar{Q}_{CT(111)} (V_{C(111),\omega} + V_{T(111),\omega}) = I_0 \bar{Q}_{CT(111)} V_{CT(111),\omega} \qquad (9-13)$$

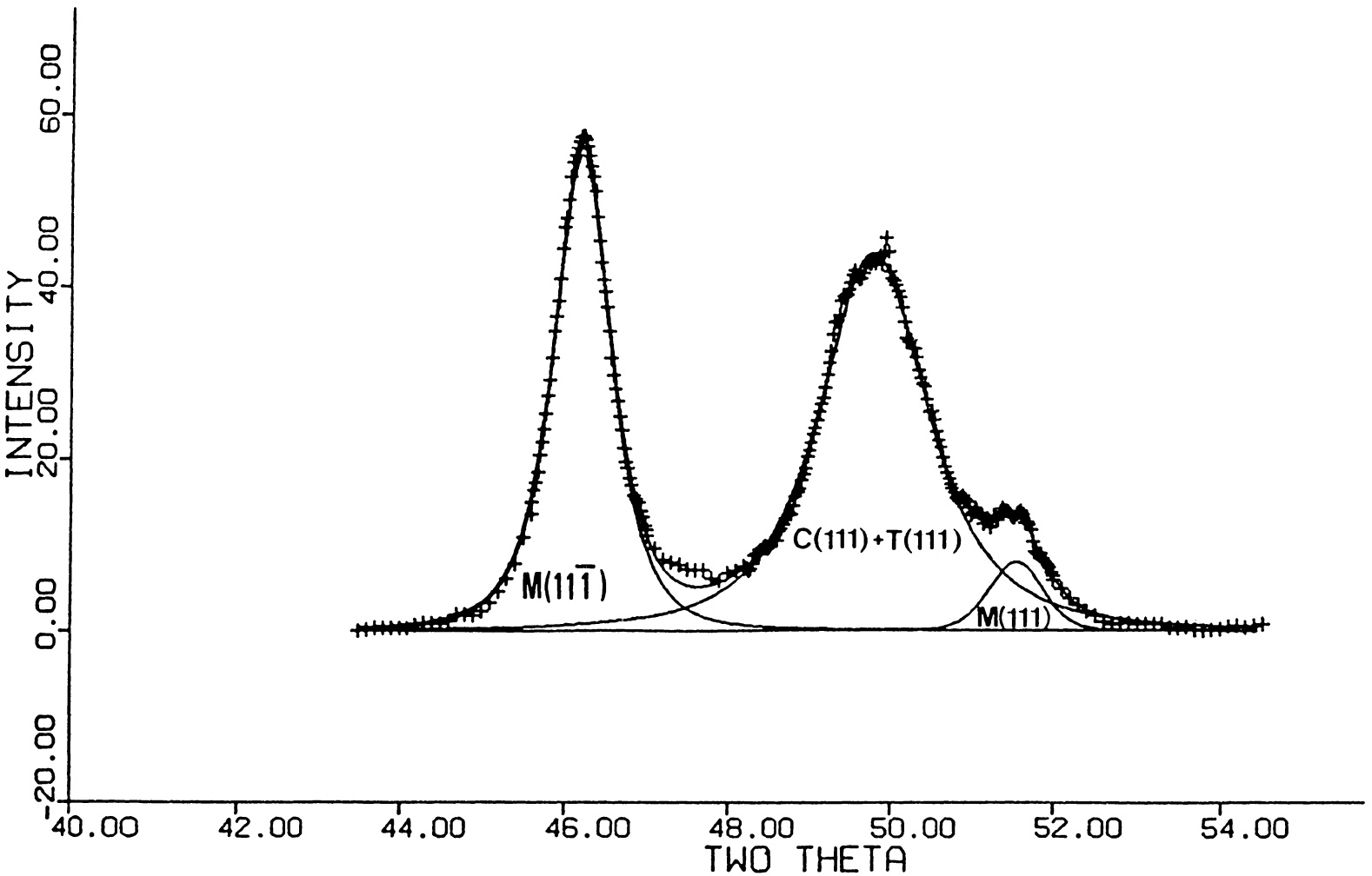

Figure 67. The XRD pattern of the back side of the PSZ disk (symmetrical diffraction optics, λ = 2.4797 A).

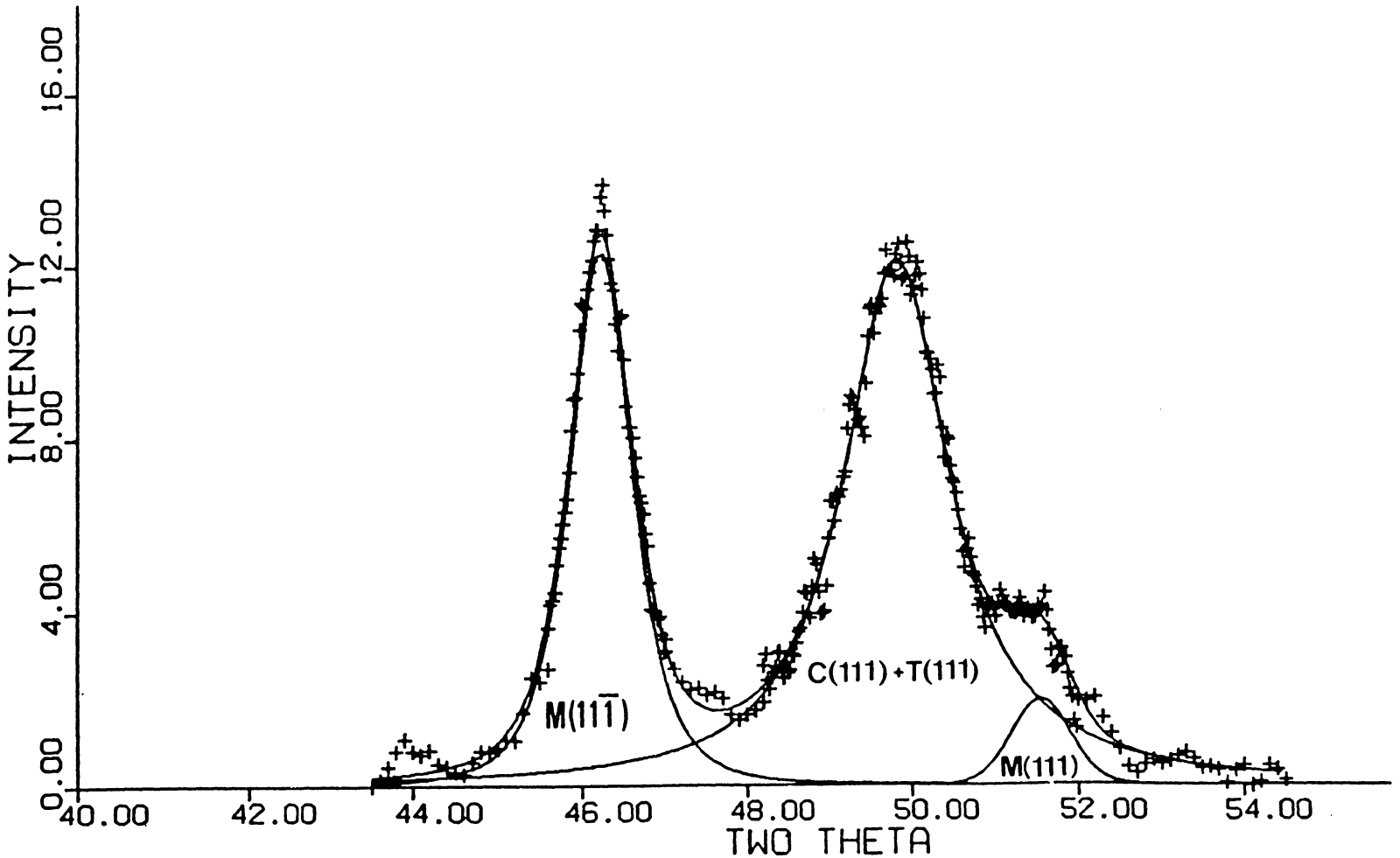

Figure 68. The XRD pattern of the back side of the PSZ disk (asymmetrical diffraction optics, λ = 2.4797 A).

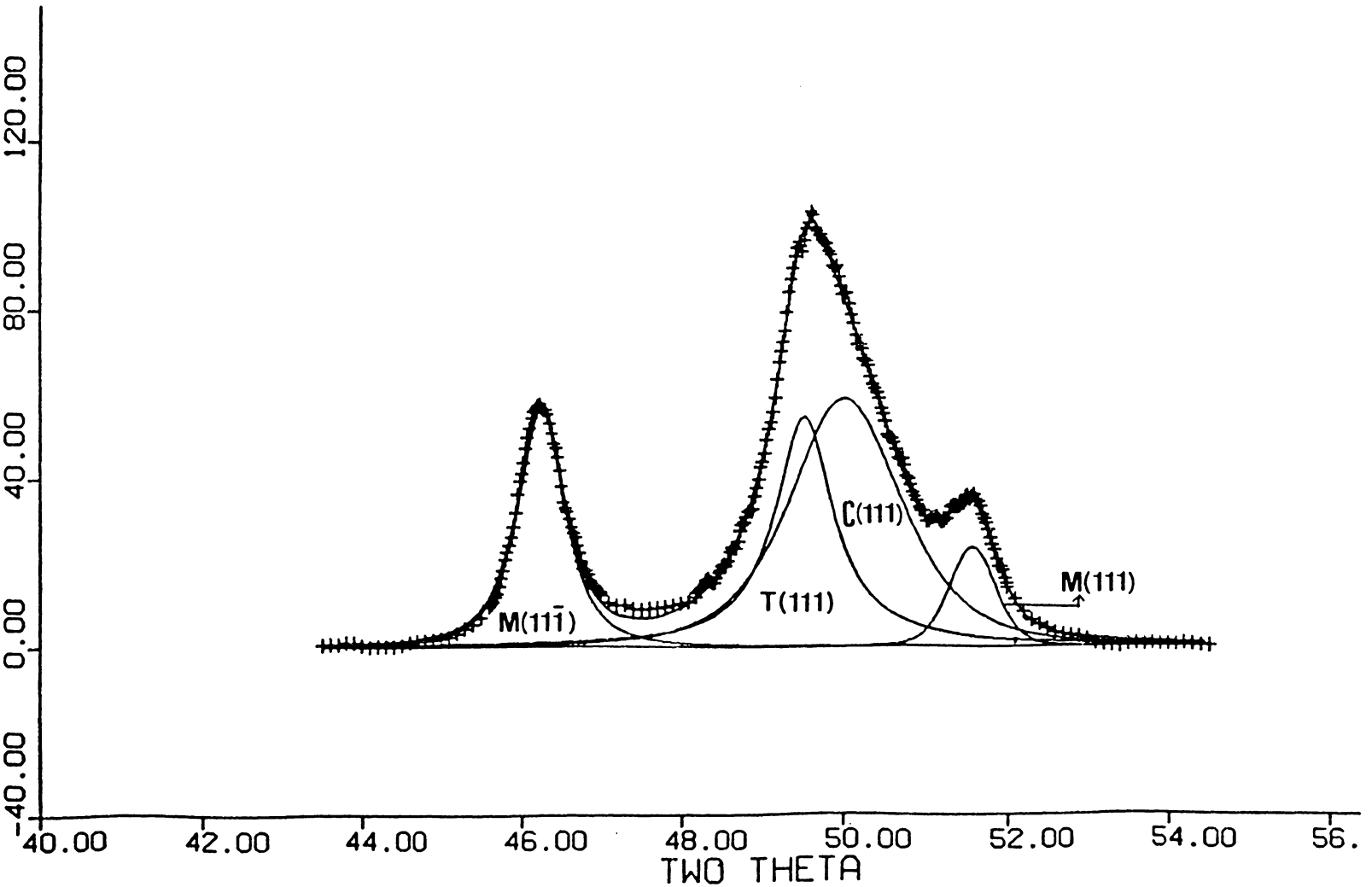

Figure 69. The XRD pattern of the worn track of the PSZ disk (symmetrical diffraction optics, $\lambda =$ 2.4797 A).

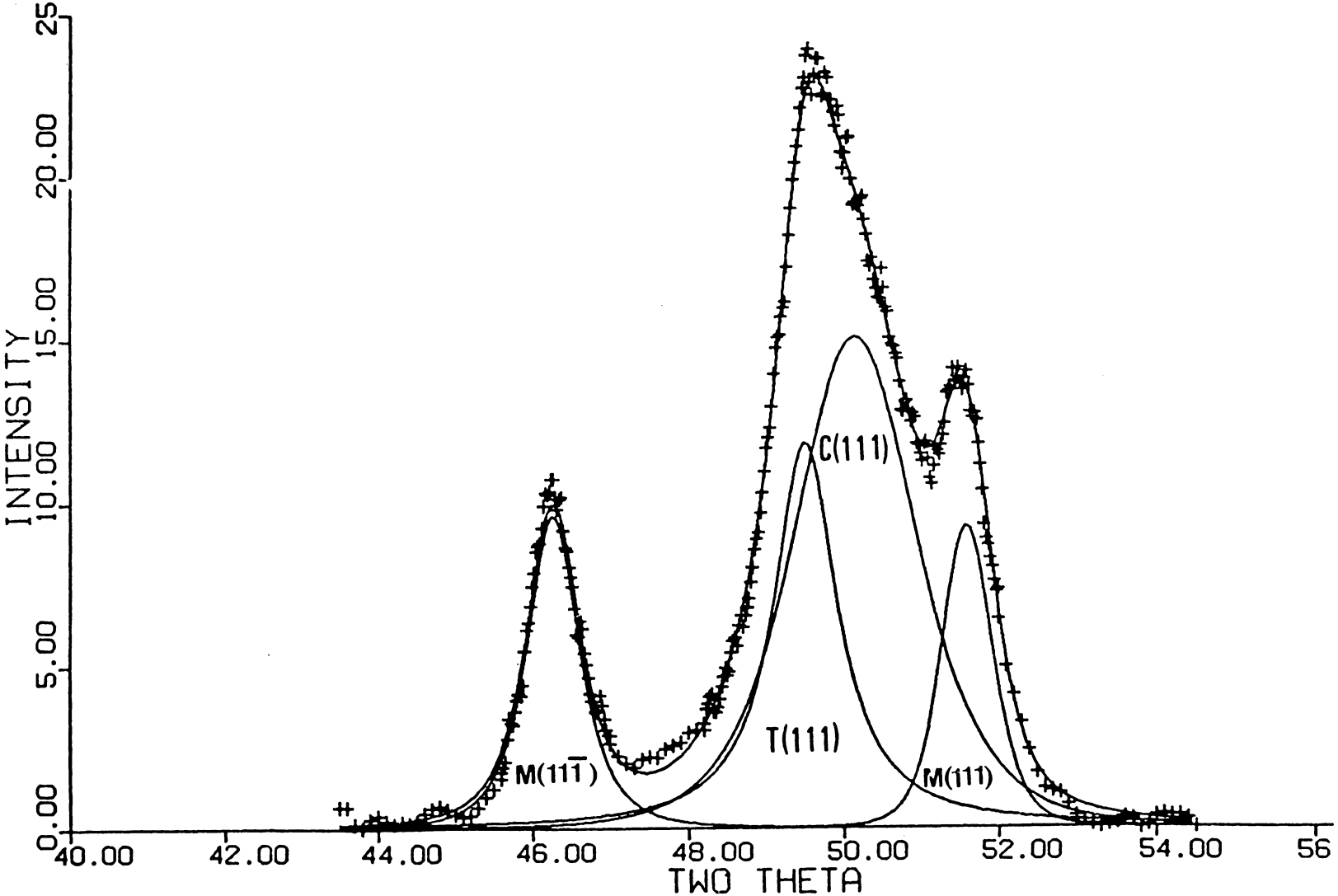

Figure 70. The XRD pattern of the worn track of the PSZ disk (asymmetrical diffraction optics, λ = 2.4797 A).

Table 13. The Relative Intensities Measured from the XRD Patterns of the PSZ Disk with λ = 2.4797 A.

		M(11$\bar{1}$)	M(111)	CT(111)
worn	$\omega = 0°$	51.3	17.3	192.6
track	$\omega \neq 0°$	9.8	8.0	52.4
back	$\omega = 0°$	58.1	6.5	88.1
side	$\omega \neq 0°$	14.0	1.8	25.9

This allows one to treat the cubic and tetragonal phases collectively with a theoretical ratio of (see Eq.(9-7))

$$R_\omega = \frac{I'_{CT(111),\,\omega}}{I'_{M(111),\,\omega} + I'_{M(11\bar{1}),\,\omega}} = \frac{V_{CT(111),\,\omega}}{V_{M(111),\,\omega} + V_{M(11\bar{1}),\,\omega}} \qquad (9-14)$$

It is believed that the volume fraction of the high temperature cubic and tetragonal phases is due to the development of highly localized temperature rises. This produces a distribution of localized temperature gradients and cooling rates with each rotation of the disk during a wear test. If distribution models (a), (b) and (c) are considered, an exponential distribution best approximates the thermal factors that shape the phase distribution. Therefore, only the exponential distribution is considered in this example. By using Eq. (9-14) and treat the cubic and tetragonal phases collectively, one can obtain

$$\frac{V_{CT(111),\,\omega}}{V_{M(111),\,\omega} + V_{M(11\bar{1}),\,\omega}} = \frac{\dfrac{1}{\sin(\theta+\omega)_{CT(111)} <\mu> S_{CT(111),\,\omega}}\left\{k + \dfrac{a}{1 + \dfrac{1}{b} <\mu> S_{CT(111),\,\omega}}\right\}}{\displaystyle\sum_i \frac{1}{\sin(\theta+\omega)_{ij} <\mu> S_{ij,\,\omega}}\left\{1 - k - \frac{a}{1 + \dfrac{1}{b <\mu> S_{i,j,\,\omega}}}\right\}} \qquad (9-15)$$

i = (111) and $(11\bar{1})$, j = monoclinic phase

which is equal to the following reduced intensities:

$$\frac{I'_{CT(111),\,\omega}}{I'_{M(111),\,\omega} + I'_{M(11\bar{1}),\,\omega}} = \frac{I_{CT(111),\,\omega}/\bar{Q}_{CT(111)}}{I_{M(111),\,\omega}/Q_{M(111)} + I_{M(11\bar{1}),\,\omega}/Q_{M(11\bar{1})}} \qquad (9-16)$$

Measured intensities are listed in Table 13. Values for θ, ω, and Q are given in Table 14. The constant volume fraction of the undisturbed bulk region were obtained from XRD intensities obtained from the back side of the PSZ disk with Cu $K\alpha_1$ radiation and symmetrical diffraction ge-

ometry. The linear absorption coefficient for PSZ with Cu $K\alpha_1$ radiation is about 1/4 of that for the λ obtained with synchrotron radiation. This results in a correspondinly deeper penetration of the x-ray beam. Under these conditions, the XRD pattern better represents the phase distribution in the bulk material. These intensities gave an upper limit of 0.445 for the constant "k".[10] This value and the data in Tables 13 and 14 were used in Eqs. (9-14), (9-15), and (9-16) to solve for "a" and "b" in H_{CT}. H_{CT} for both the worn track and the back side of the disk are shown in Figure 71.

9.3 Discussions

Because the thermal conductivity of PSZ is two orders of magnitude larger than that of the surrounding nitrogen atmosphere, a high temperature region beneath the asperities is developed after prolonged wear testing. Although a high temperature in this region favors the tetragonal and cubic phases, the volume fraction of these phases is finally determinated by the local cooling rates. Radiation at the free surface gives a maximum cooling rate and this decreases gradually at greater depths within the disk. High cooling rates increase the retention of the high temperature phases.

The polishing process, which the back side was subjected to, produces the similar conditions of localized heating and cooling. However, the surface conditions are much milder and not prolonged.

The results in Fig. 71 show that the high temperature phases are first increased by the preliminary polishing and then enhanced by the prolonged wear. Phase transformations and their retention introduced by the polishing is localized to within 2 μm from the surface. The corresponding zone introduced by the wear testing is much larger. Because of high beam absorption in the sample, our data is not sensitive to the depth distribution of phases beyond a distance of a few μm. There-

Table 14. The Q values from Eq.(9-5), Bragg Angles (2θ), Incident Angles and Signal Angles for PSZ Reflections with λ = 2.4797 A.

	2θ(°)	$\theta_i = \theta + \omega$ (°)		$\theta_s = \theta - \omega$ (°)		Q (relative unit)
		$\omega = 0^\circ$	$\omega \neq 0^\circ$	$\omega = 0^\circ$	$\omega \neq 0^\circ$	
C(111)	49.83	24.92	43.83	24.92	6	725
T(111)						704
M(111)	51.60	25.80	45.60	25.80	6	228
M(11$\bar{1}$)	46.27	23.14	40.27	23.14	6	304

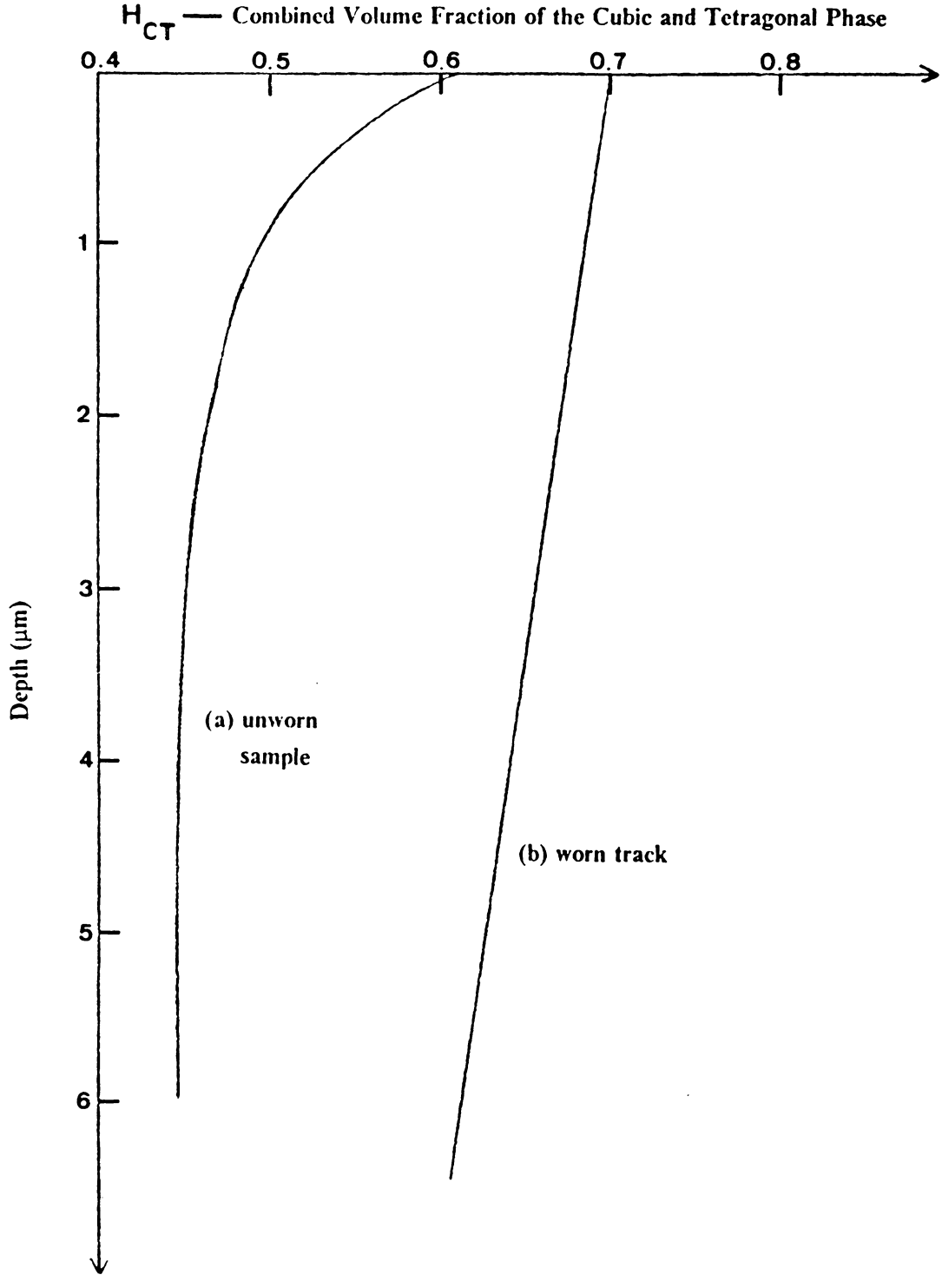

Figure 71. The phase distributions in the PSZ disk: (a) unworn sample (b) worn track

fore, the phase distribution under the wear track (see Fig. 71) should be considered as only semi-quantitative beyond the depth of about 4 μm.

Chapter 10

CONCLUSIONS

10.1 General Picture of the Wear Process for Ceramics

In a wear process, two components are put under relative motion with their surfaces making dynamic contact. The resistance to tangential motion is called friction. The externally applied energy is consumed in mechanically deforming the contacting surfaces and in frictionnal heat. Microscopically, any surface has asperities and appears to consist of mountains and valleys. The highest mountains make initial contacts and first experience a sequence of elastic deformation, plastic deformation, and fracture which produces debris. Then the second highest mountains become the highest mountains and experience the same deformation sequence. Some of the produced debris are sandwiched between the contacting surfaces and interact with both surfaces in the following deformation process. The repeated, localized, dynamic deformation tends to smear the surfaces and change their features. The change of the surface morphology is best observed by the scanning electron microscope (SEM).

The amount of the frictional heat produced in a wear process depends on the speed of the relative motion and the magnitude of the external load. When a lubricant is present, most of the frictional heat is carried away by the lubricant. When no lubricant is used, the frictional heat is partially dissipated in the ambient atmosphere and partially absorbed by the contacting components. Because the frictional heat is localized at the contacting asperities, a local high temperature may be reached to introduce thermal effects like oxidation or phase transformation.

The examinations of PSZ and FSZ samples in this work leads one to the following picture of the wear process in ceramic components:

At first, two surfaces with various sizes and populations of asperities are brought together, then the relative motion of the two contacting surfaces changes their morphologies. Because of the general low thermal conductivity of the ceramic materials, the temperature developed at the contacting asperities due to friction heat is often high enough to introduce both localized segregation and phase transformations. Hot spots with temperature as high as 2703° C were observed by Winer et al.[31] in the wear test of a silicon nitride pin against a sapphire disk. Debris coming off the asperities can retain the high temperature structures because of the fast cooling rate provided by radiation into the ambient environment. The high temperature phases within the near surface regions of the contacting components may or may not be retained depending on the post-wear cooling rate. Due to the direct exposure to the ambient atmosphere, the cooling rate is maximum at the surface and smaller at greater depths. This gradient of the thermal conditions can cause a depth gradient of the phase distributions. The breakage of debris from the contacting asperities are preceded by elastic and plastic deformations. Large locally elastic nonuniform residual strains are observed in both the debris and the contacting components. Residual strains are compressive in a zone near surface and range from a few tenths of a μm to a few μm, depending on the severity of the wear process. This general picture is illustrated schematically in Figure 72.

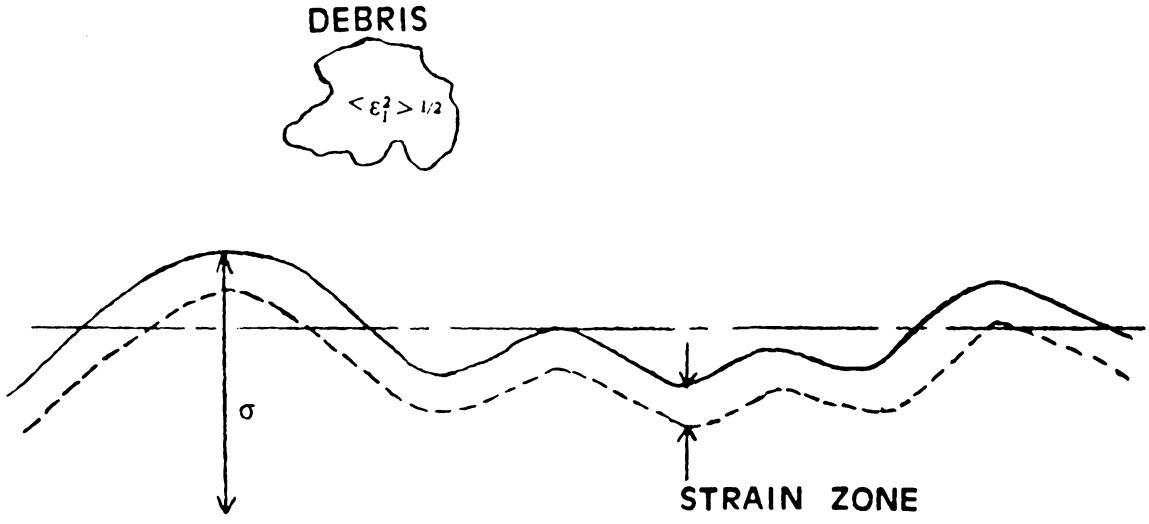

Figure 72. Schematic picture of the wear process.

10.2 X-ray Techniques for the Study of Wear Structure

The x-ray techniques illustrated in this work for wear structure study include phase analysis, strain profile determination , and line shape analysis. Each technique requires some specific experimental conditions to study a specific feature of a sample. This is reviewed as follows.

10.2.1 Quantitative phase analysis

For a homogeneous sample, the intensities of at least one reflection from each phase is needed to carry out the quantitative phase analysis. These intensities are usually measured with a symmetrical diffraction geometry and a fixed wavelength. No second wavelength or diffraction geometry is needed. If the phase distributions are not homogeneous but depth dependent, two probe depths are needed to measure the intensitites of at least one reflection from each phase. The two probe depths can be obtained by using either two wavelengths or two diffraction geometries. A synchrotron radiation source can conveniently provide two or more probe depths.

10.2.2 Strain gradient determination

The presence of strain gradient in the near surface region can be revealed by comparing the peak profile of a well separated reflection with the corresponding profile of a annealed standard. If a strain gradient exists, the peak will be broadened and appear as an intensity band. As illustated in Chapter 7, the intensity band can be fitted by a proper d-spacing profile by a trial and error procedure. An accurate peak profile is required. Also, the selected peak must be well separated from other reflections to eliminate uncertainties of the shape caused by peak overlapping. The degree of overlapping can be greatly reduced by using synchrotron radiation becaue that no $K\alpha_2$ component is

involved,and the intrinsic collimation produces a much smaller instrumental broadening. Although the peak profile is usually measured with symmetrical diffraction geometry, one can use the asymmetrical diffraction geometry and a longer wavelength to obtain a small penetration depth for the measurement of a thin strained zone. These conditions are best satisfied with single phase, high symmetry crystal structures when polycrystalline ceramic materials are studied. Single crystals would be required if samples are of low symmetry.

10.2.3 Line shape analysis

One can obtain the information of subgrain size and the average nonuniform strain in a sample by carrying out the line shape analysis. The detailed theoretical derivation can be found in references 35 and 36. An analysis for the PSZ debris can be found in reference 32. This technique requires accurate peak profiles including two orders of a reflection from the sample being studied and two reflections from an annealed standard. The peaks from the standard serve as strain-free references, and should be selected from the same 2θ regions. Peak profiles are usually obtained with symmetrical diffraction and point counting. The accurate peak profiles needed in Sections **10.2.2** and **10.2.3** require a prolonged measurement in a conventional system. A system with synchrotron radiation can greatly reduce the measurement time because of the tremendous large intensity. The experimental conditions of the x-ray techniques mentioned in Sections **10.2.1, 10.2.2** and **10.2.3** are summarized in Table 15.

10.2.4 Quantitative analysis of chemical composition

A depth gradient of chemical composition can be developed by segregation during a wear process. As shown in Chapter 7, this depth gradient can be studied by XPS measurement and ion milling. A nondestructive x-ray technique using fluorescent signal can also be used to determine

Table 15. Summary of the Applications of X-ray Techniques.

	samples	minimum reflections	standard	wavelength and diffraction optics
phase analysis	multiphase homogeneous	one line each phase	none	1 wavelength sym. diff. optics
	multiphase with depth gradient	one line each phase (2 or 3 probe depths)	none	2 wavelengths or 2 diff. optics
strain gradient	single phase or homogeneous multiphase	1 separated line from a selected phase	annealed sample	1 wavelength sym. or asym. diffraction optics
line shape analysis	single phase or multiphase	one line (two orders)	2 lines from annealed sample	1 wavelength sym. optics

the depth gradient of chemical composition. This technique is similar to the XRD technique presented in Chapter 9 for the analysis of phase distributions using two probe depths. The theoretical derivation is exactly the same except that integrated intensities of fluorescent signal are calculated instead of the diffraction signal. As shown in Chapter 2 (see Eqs. (2-2), (2-3), (2-4)), the calculation of the integrated intensity for the fluorescent signal is simialr to that for the diffraction signal except that (1) two different linear absorption coefficients corresponding to the incident and fluorescent radiation are used for the incident and signal rays. (2) Q_f is used instead of Q_d. Because the fluorescent signal is not restricted by Bragg's law, a fluorescence intensity can be measured at any arbitrarily chosen 2θ position. A fluorescent signal is normally much weaker than a diffraction signal. Synchrotron radiation can be used to increase the intensity and shorten the measurement time. For each element, the emitted fluorescent radiation includes several characteristic lines. A characteristic line strongly absorbed by the sample should be selected when a surface phenomenon is studied. For example, to show the intensity correction due to the surface roughness, a radiation strongly absorbed by the sample will give a maximum correction. For an FSZ sample, the most suitable radiation is Zr $L\alpha_1$. The linear absorption coefficient of FSZ for Zr $L\alpha_1$ radiation is 4625 cm^{-1} comparing to the value of 110 cm^{-1} for the $K\alpha_1$ radiation. To reduce the extra absorption of the fluorescent signal in air and the beryllium window, a vacuum path and thin windows are needed. These, however, are not currently available at ORNL beamline in NSLS.

10.3 A Complete Procedure of Wear Structure Study

Knowing the general picture of the wear process and the capabilities of the x-ray techniques, a complete procedure of wear structure study is designed as follows. First, both pins and disks are prepared. Both should have several duplicates so that different measurements can be made at different stages and preserved. A complete information of these samples including grain size, preparation history, anneal process...should be prescribed. The next step is the preliminary XRD

examination of the pin and disk. A survey scan will show how many phases are present in the sample. If the sample has more than one phase, the XRD patterns with two probe depths should be obtained to check if the phase distribution is homogeneous. An accurate peak profile from a well separated reflection is also needed as a reference for future analysis of strain profile. These scans from the annealed samples before wear test are to be compared with the corresponding scans following the wear test for phase identification, quantitative phase anaysis and determination of the depth gradients of phases or strain. Following the preliminary x-ray examination is the SEM examination. The results are to be compared with the corresponding results obtained after the wear test to see the change of morphology of the contacting surfaces. A profilometer measurement follows the SEM examination to obtain various roughness parameters such as σ(standard deviation of the excursion height), τ_c (correlation distance) and p(Z) (probability density of the excursion height). The results are to be compared with the corresponding results measured after the wear test. Continuous measurements of the frictional forces and the temperature at the contacting surface is made during the pin on disk test. The measured temperature can show if the frictional force is large enough to cause phase transformation. The wear debris are also collected during the test for XRD examination. The complete procedure of the wear structure study is shown in the flow chart of Table 16.

The comparison of the XRD results before and after the wear test can give the following information:

1. Which phases are present before and after the wear test ? Which phases were added or lost after wear test ? What are the corresponding phase transformations ?

2. Are intensity bands developed by wear process ? If the intensity bands developed, what is the strain profile in the near surface region ?

Table 16. The Flow Chart of Wear Test and Characterization.

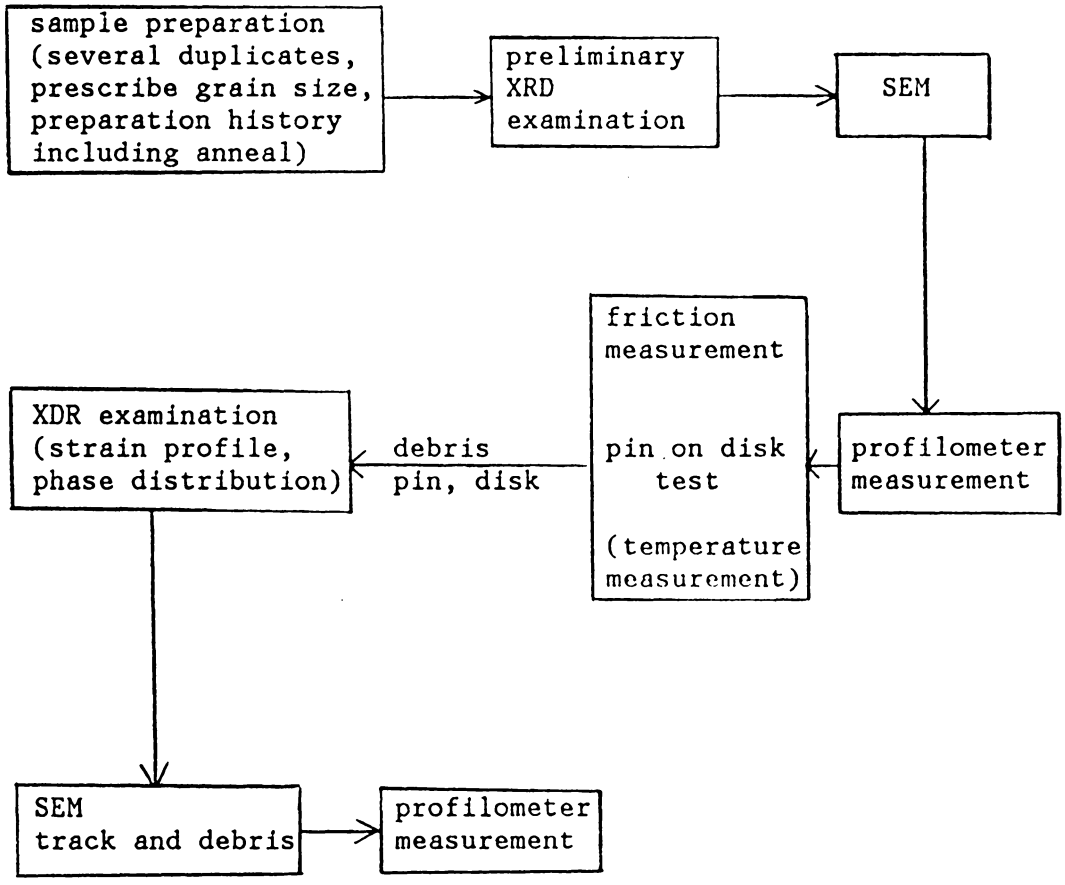

3. For a multiphase sample, is it homogeneous or inhomogeneous before and after the wear test ? For homogeneous samples, what are the volume fractions for each phase ? For inhomogeneous samples, What are the depth distributions for each phase ?

The flow charts of the XRD examinations are shown in Tables 17, 18 and 19. The tables shown in this chapter can serve as a quick guide for designing the experimental procedure of XRD examination and wear study.

As a final point, all the x-ray techniques developed in this work are equally applicable to both metals and ceramics. However, for ceramics materials, very little residual strain work has been carried out using XRD technique. The capabilities demonstrated in this work should provide a basis for continued applications by ceramists.

Table 17. The Flow Chart of the Preliminary XRD Examination.

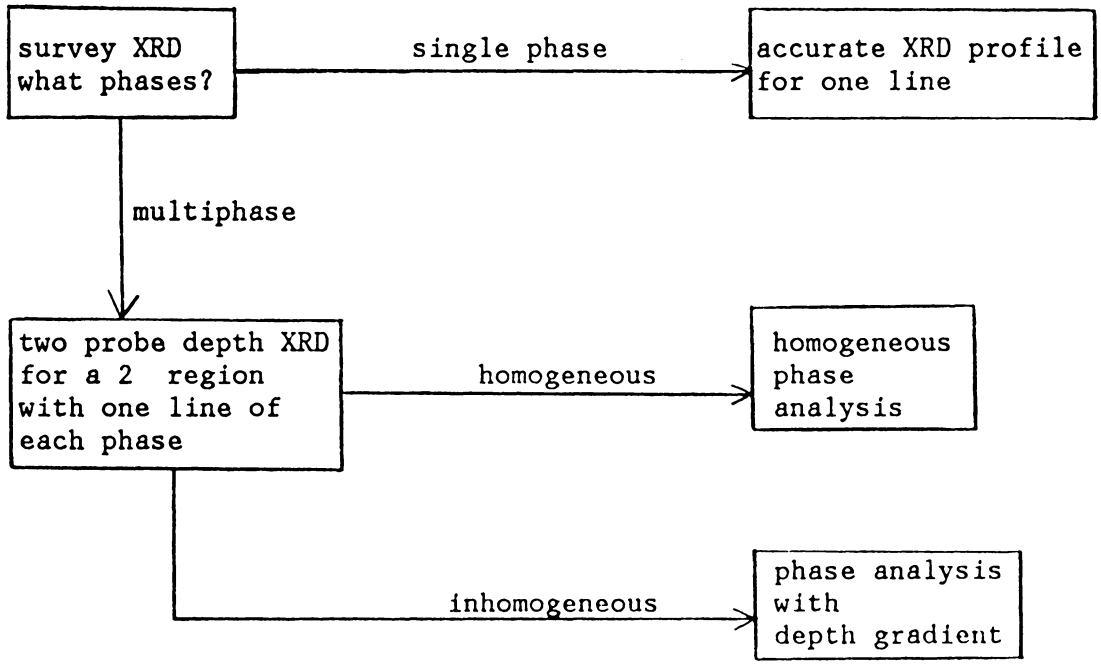

Table 18. The Flow Chart of the XRD Examination after the Pin on Disk Test.

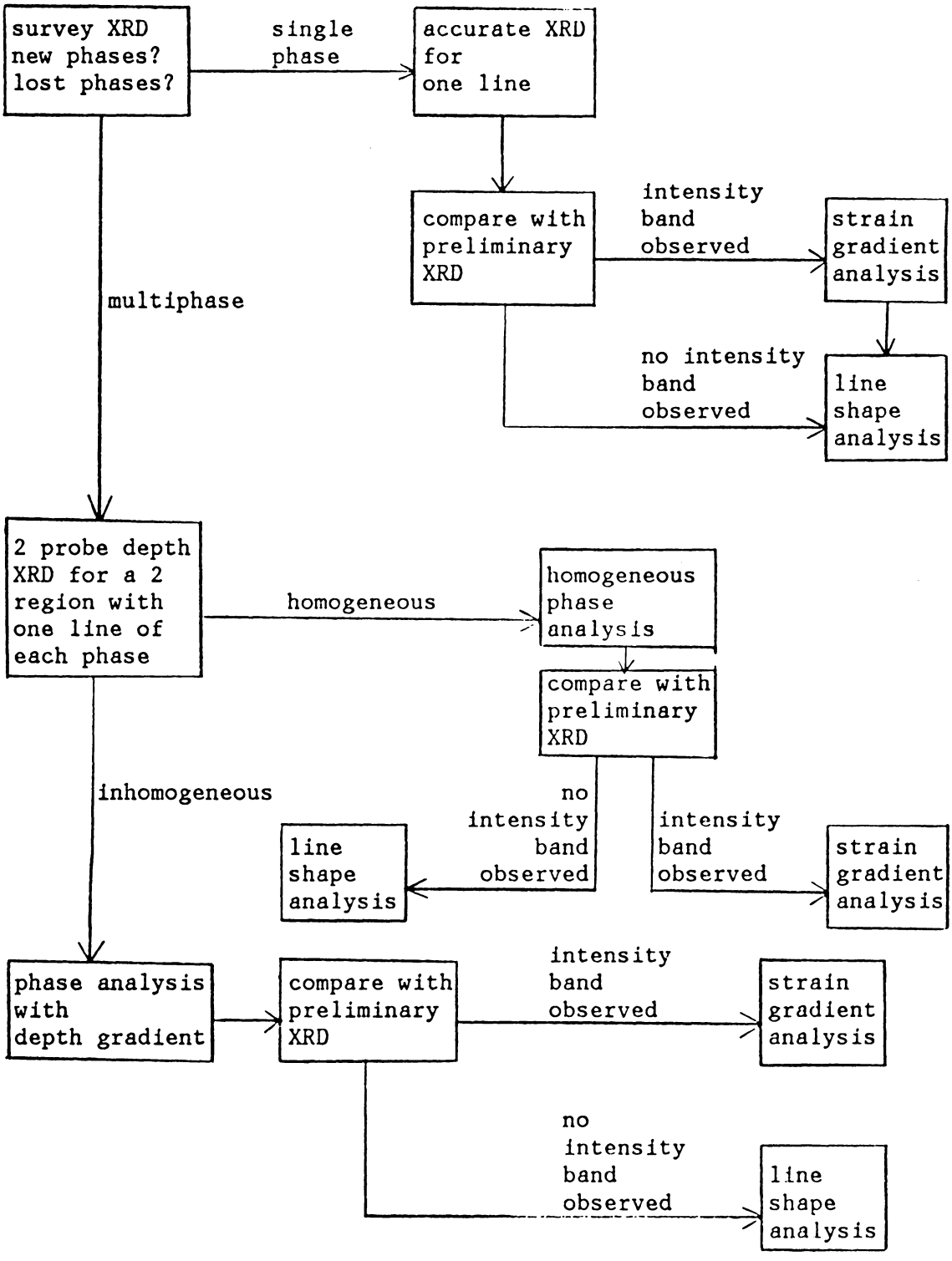

Table 19. The Flow Chart of the XRD Examination for Debris.

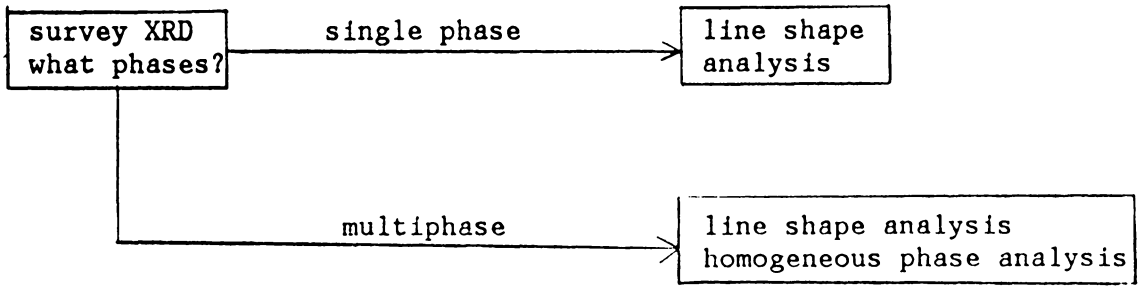

Chapter 11

BIBLIOGRAPHY

1. T. R. Thomas, "Rough Surfaces", Longman, London (1982).

2. R. J. Harrison and A. Paskin, Acta. Crystallography, **17**, 325 (1964).

3. C. R. Houska, unpublished work.

4. B. S. Borie, J. Appl. Cryst., **14**, 219-222 (1981).

5. H. Winick and S. Doniach, Eds., "Synchrotron Radiation Research", Plenum, N.Y., (1980), See C. T. Sparks, p459.

6. C. R. Houska, Area Ciencia De Los Materials I, ANO XII, Julio, **55**, 38-43 (1982).

7. Argonne National Laboratory, Applied Mathematics Division, Program Library, B106.

8. Karl Wiedemann, "A Computer Program for the Simulation of X-Ray Powder Diffraction Pattern", College of Engineering, VPI and SU, Blacksburg, VA 24061 (1983).

9. S. V. N. Naidu and C. R. Houska, J. Appl. Cryst., **15**, 190-198 (1982).

10. B. D. Cullity, "Elements of X-ray Diffraction", Addison-Wesley, Reading, Mass. (1978).

11. J. Unnam, D. R. Tenney, J. A. Carpenter and C. R. Houska, "A Computer Program for the Simulation of X-Ray Diffraction Intensity Bands", College of Engineering, VPI and SU, Blacksburg, VA 24061, February (1976).

12. J. S. Bendat, "Principles and Applications of Random Noise Theory", Wiley, N.Y. (1958).

13. J. S. Bendat and A. G. Piersol, "Measurement and Analysis of Random Data", John Wiley and Sons, (1966).

14. R. S. Sayles and T. R. Thomas, Nature, **271**, 431-434 (1978).

15. R. S. Sayles and T. R. Thomas, Trans. Am. Soc. Mech. Engrs. J. Lub. Tech. **101F**, 409-418 (1979).

16. J. B. Williamson, J. Pullen and R. T. Hunt, 'The shape of solid surface', in F. F. Ling (ed.), Surface Mechanics (ASME, NY), 24-35 (1969).

17. F. D. Bloss, "Crystallography and Crystal Chemistry", Holt, Rinehart and Winston, N.Y. (1971).

18. D. Briggs and M. P. Seah, Wiley and Sons, N. Y. (1983).

19. W. B. Pearson, "A Handbook of Lattice Spacings and Structures of Metals and Alloys",Vol. 2, Pergamon Press, N.Y. (1967).

20. A. Taylor and B.J. Kagle, "Crystallographic Data on Metals and Alloy Structures", Dover, N.Y. (1963).

21. "Science and Technology of Zirconia", Advances in Ceramics, Vol. 3, The American Cermiac society, Edited by A. H. Heuer and L. W. Hobbs. (1981).

22. G. M. Wolten, J. Am. Ceram. Soc., **46**[9], 418-422 (1963).

23. R. F. Geller and P. J. Yavorsky, J. Res. Natl. Bur. Stand., **35**[1], 87-110 (1945).

24. B. C. Weber, "Zirconia - An Annotated Bibliography", Aerospace Res. Lab. Rept., ARL 64-205 (1964).

25. O. J. Whittemore, Jr., and N. N. Ault, J. Am. Cerm. Soc., **39**[12], 434-44 (1956). [C

26. V. S. Stubican, pp25-36, Reference 21.

27. R. E. Jaeger and R. E. Nickell, pp163-84 in Ceramics in Severe Environments, "Matterials Science Research", Vol. 5, Plenum Press, N.Y. (1971).

28. O. Ruff and F. Ebert, Z. Anorg. Allg. Chem. **180**[1], 19-41 (1929).

29. G. Taufer, Acta Cryst. **15**, 1187 (1962).

30. T. F. J. Quinn and W. O. Winer, Quarterly Progress Report, Tribology Project, Jan.-March, 1985, pp37-52. ECUT Program of DOE.

31. S. Rao and C. R. Houska, Acta Cryst., **A42**, 14-19 (1986).

32. R. C. Garvie, R. J. Hannink and M. V. Swain, J. Mat. Lett. **1**, 437-440 (1982).

33. R. T. Pascoe and R. C. Garvie, "Ceramic Microstructure 1976", edited by R. M. Fulrath and J. A. Pask, Westview Press, Boulder (1977).

34. T. Adler and C. R. Houska, J. Appl. Phys., **50**(5), 3282-3287 (1979).

35. C. R. Houska and T. M. Smith, J. Appl. Phys., **52**(2), 748-754 (1981).

Appendix A

The Computer Program for Intensity Calculation of A Rough Sample

```
C  THIS IS A FORTRAN PROGRAM TO CALCULATE THE INTENSITY RATIO
C  BETWEEN THE ROUGH SAMPLE AND THE FLAT SAMPLE.
C
C  THE CALCULATION IS VALID FOR BOTH THE DIFFRACTION SIGNAL AND
C  THE FLUORESCENCE SIGNAL.
C
C  THE INCIDENT AND SIGNAL BEAMS CAN BE SYMMETRICAL OR ASYMME-
C  trical WITH RESPECT TO THE SAMPLE NORMAL.
C
C  THIS PROGRAM USES 12 POINTS GAUSSIAN-LEGENDRE QUADRATURE IN-
C  TEGRATION TO CALCULATE EQUATION (5-29) IN THIS THESIS.
C
```

```
      DIMENSION X(12),W(12)
      COMMON X,W,SIGMA,TC,TCS,UI,US,THETAI,THETAS
      CALL ERRSET(208,256,-1)
C
CCCCCCCCCCCCCVC BEGINING OF INPUT DATACCCCCCCCCCCCCCCCCCCCC
C
C **SIGMA = THE STANDARD DEVIATION OF THE HEIGHT OH THE SURFACE
C PROFILE RELATIVE TO THE MEAN SURFACE. THIS VALUE IS OBTAINED
C FROM THE PROFILOMETER MEASUREMENT (UNIT:CM)
C **TC = THE AUTOCORRELATION DISTANCE OBTAINED FROM THE PROFI-
C LOMETER MEASUREMENT  (UNIT:CM),  TCS IS THE SCALED VALUE OF
C TC WITH THE SCALING FACTOR = (SQURE ROOT OF 2)*SIGMA.
C **UI =  THE LINEAR ABSORPTION COEFFICIENT FOR INCIDENT BEAM (UNIT:
C 1/CM).
C **US =  THE LINEAR ABSORPTION  COEFFICIENT FOR SIGNAL BEAM  (UNIT:
C 1/CM).
C **THETAI =  INCIDENT ANGLE (UNIT:DEGREE).
C **THETAS =  SIGNAL ANGLE (UNIT:DEGREE).
C THE PARAMETER VALUES GIVEN BELOW SERVE AS AN EXAMPLE, THE
C CORRESPOINDING OUTPUT FOLLOWS THIS PROGRAM.
      SIGMA = 6.2/10000.
      TC = 82./10000.
      UI = 650.
      US = 650.
      THETAI = 45.
      THETAS = 45.
C
CCCCCCCCCCCCCCC END OF THE INPUT DATA CCCCCCCCCCCCCCCCCCCCC
```

```
C
C  X(1)....X(12) GIVEN BELOW ARE THE 12 SCALED VALUES  BETWEEN -1
C  AND  + 1 ALONG THE ABSCISSA WHERE THE FUNCTIONAL VALUES NEED TO
C  BE CALCULATED
      X(6) = -0.12523
      X(5) = -0.36783
      X(4) = -0.587318
      X(3) = -0.76990
      X(2) = -0.904117
      X(1) = -0.98156
      X(7) = -X(6)
      X(8) = -X(5)
      X(9) = -X(4)
      X(10) = -X(3)
      X(11) = -X(2)
      X(12) = -X(1)
C  W(1).....W(12) GIVEN BELOW ARE THE CORRESPONDING WEIGHTING FA-
C  CTORS FOR THE FUNCTION VALUES EVALUATED AT X(1)... X(12).
      W(1) = 0.047175
      W(2) = 0.10694
      W(3) = 0.160078
      W(4) = 0.203167
      W(5) = 0.23349
      W(6) = 0.249147
      W(7) = W(6)
      W(8) = W(5)
      W(9) = W(4)
      W(10) = W(3)
```

```
      W(11) = W(2)
      W(12) = W(1)
      TCS = TC/SQRT(2.)/SIGMA
      ANGLEI = THETAI/180.*ARCOS(-1.)
      ANGLES = THETAS/180.*ARCOS(-1.)
      ZS = -3.
      DOWN = ZS
      UP = DOWN + 3.
      F1S = 0.
C 100 AND 101 LOOPS ARE USED TO CALCULATE THE OUTER INTEGRAL IN EQ.
C (5-29).
      DO 101 N = 1,2
      F1 = 0.
      DO 100 I = 1,12
      X1 = ((UP-DOWN)*X(I) + UP + DOWN)/2.
      DN2 = X1
      DT = (3.5-DN2)/2.
      IF(DT .LE. 1.) NN = 1
      IF(DT .LE. 1.) DT = 3.5-DN2
      UP2 = DN2 + DT
      F2S = 0.
C  200 AND 201 LOOPS ARE USED TO CALCULATED THE MIDDLE INTEGRAL
C  IN EQ. (5-29).
      DO 201 N2 = 1,2
      F2 = 0.
      DO 200 J = 1,12
      X2 = ((UP2-DN2)*X(J) + UP2 + DN2)/2.
      CALL SUBRZ(X1,X2,Y2)
```

```
200 F2=F2+(UP2-DN2)/2.*W(J)*Y2*EXP(-X2*X2)
    UP2=UP2+DT
    DN2=DN2+DT
201 F2S=F2S+F2
202 Y1=F2S
100 F1=F1+(UP-DOWN)/2.*W(I)*Y1
    DOWN=DOWN+3.
    UP=UP+3.
101 F1S=F1S+F1
    Q=UI/SIN(ANGLEI)+US/SIN(ANGLES)
    R1=F1S*SQRT(2.)*SIGMA/SQRT(ARCOS(-1.))*Q
    R=R1+EXP(-3.*SQRT(2.)*Q*SIGMA)
    WRITE(6,22)SIGMA,TC,UI,US
 22 FORMAT(' SIGMA=',E12.5,'  TC=',E12.5,'  UI=',
   1E12.5,'  US=',E12.5)
    WRITE (6,23) THETAI, THETAS, R
 23 FORMAT (' THETAI=', F5.1, '   THETAS=', F5.1, '  R=', E15.8)
 24 CONTINUE
    STOP
    END


C  THIS SUBROUTINE IS USED TO CALCULATE THE ABSORPTION ATTENUATION
C  FACTOR FOR A SIGNAL GENERATING GROUP.  ALL DATA COME FROM THE
C  MAIN PROGRAM, NO EXTRA INPUT IS NEEDED.
    SUBROUTINE SUBRZ(ZS,Z0S,S2)
    DIMENSION X(12),W(12),Z1S(12)
    COMMON  X,W,SIGMA,TC,TCS,UI,US,THETAI,THETAS
```

```
      CALL ERRSET(208,256,-1)
      ANGLEI = THETAI/180.*ARCOS(-1.)
      ANGLES = THETAS/180.*ARCOS(-1.)
      DOWN = ZS
      UP = DOWN + 1.0
      S2I = 0.
      S2S = 0.
      DO 201 JSS = 1,300
      F2I = 0.
      F2S = 0.
      DO 200 JS = 1,12
      Z1S(JS) = ((UP-DOWN)*X(JS) + UP + DOWN)/2.
      Y0I = EXP(-(Z1S(JS)-ZS)/TAN(ANGLEI)/TCS)
      Y0S = EXP(-(Z1S(JS)-ZS)/TAN(ANGLES)/TCS)
      Y1I = EXP(-(Z1S(JS)-Y0I*Z0S)*(Z1S(JS)-Y0I*Z0S)/(1.-Y0I*Y0I))
      Y1S = EXP(-(Z1S(JS)-Y0S*Z0S)*(Z1S(JS)-Y0S*Z0S)/(1.-Y0S*Y0S))
      UTI = 1./SQRT(1.-Y0I*Y0I)-(Y0I*Y0I*Z1S(JS)-Y0I*Z0S)/TCS/TAN
     1(ANGLEI)/(1.-Y0I*Y0I)**1.5
      UTS = 1./SQRT(1.-Y0S*Y0S)-(Y0S*Y0S*Z1S(JS)-Y0S*Z0S)/TCS/TAN
     1(ANGLES)/(1.-Y0S*Y0S)**1.5
      Y1I = Y1I*UTI/SQRT(ARCOS(-1.))
      Y1S = Y1S*UTS/SQRT(ARCOS(-1.))
      Y2I = Y1I*EXP(-SQRT(2.)*SIGMA*UI*(Z1S(JS)-ZS)/SIN(ANGLEI))
      Y2S = Y1S*EXP(-SQRT(2.)*SIGMA*US*(Z1S(JS)-ZS)/SIN(ANGLES))
      F2I = F2I + (UP-DOWN)/2.*W(JS)*Y2I
  200 F2S = F2S + (UP-DOWN)/2.*W(JS)*Y2S
      IF (DOWN .GE. 4.1) GO TO 202
      DOWN = UP
```

```
      UP = DOWN + 1.0
      S2I = S2I + F2I
  201 S2S = S2S + F2S
  202 CONTINUE
      S2 = S2I*S2S
      RETURN
      END
```

```
CCCCCCCCCCC THIS IS A SAMPLE OUTPUT OF LAST PROGRAM CCCCCCCCCC
 SIGMA = 0.62000E-03  TC = 0.82000E-02  UI = 0.65000E + 03  US = 0.65000E + 03
 THETAI =  45.0   THETAS =  45.0  R =  0.94047058E + 00
```

Appendix B

The Computer Program for intensity band simulation

```
C  THIS FORTRAN PROGRAM SIMULATES AN XRD INTENSITY BAND BASED
C  ON A GIVEN D-SPACING PROFILE. BOTH THE SIMULATED AND THE
C  EXPERIMENTAL INTENSITY BANDS ARE PLOTTED USING THE GRAPHICS
C  SOFTWARE AVAILABLE AT THE LIBRARY OF VIRGINIA TECH. COMPUTER
C  CENTER. THE WHOLE SIMULATION AND PLOTTING CAN BE RUN INTER-
C  ACTIVELY WITH A GRAPHICS TERMINAL.
C
C  THE SIMULATION CAN BE CARRIED OUT FOR A SYMMETRICAL OR AN
C  ASYMMETRIC DIFFRACTION OPTICS FOR A FLAT OR A ROUGH SAMPLE.
C
      DIMENSION
     1 P(3000),AINTENB(100),T2VB(100),Y2B(100),X2B(100),
     1 TG(3000),Y2(300),X2(300),T2V(300),X(2),W(12)
     1 AINTEN(300),DIST(3000),D(3000)
      COMMON X,W,SIGMA,TC,TCS,U,U.THETAI,THETAS
```

```
      CALL ERRSET(208,256,-1)
C
CCCCCCCCCCCC BEGINING OF INPUT PARAMTERS CCCCCCCCCCCCCCCCCC
C  ALAMDA = WAVELENGTH IN ANGSTROM
C  D0 = THE D-SPACING IN THE BULK (ANGSTROM)
C  U = LINEAR ABSORPTION COEFFICIENT IN 1/CM
C  OS = OPTION FOR SAMPLE, OS = 1 = FLAT SAMPLE, OS = 2 = ROUGH SAMPLE
C  SIGMA = THE STANDARD DEVIATION OF THE HEIGHT OF THE SURFACE
C  PROFILE (UNIT: CM, NEEDED ONLY WHEN OS = 2).
C  TC = THE AUTOCORRELATION DISTANCE OF THE SURFACE PROFILE IN CM
C  (NEEDED ONLY WHEN OS = 2).
C  OO = OPTION OF OPTICS, OO = 1:SYMMETRICAL OPTICS, OO = 2:ASYMMETRIC
C  OPTICS.
C  THETAI = THE FIXED INCIDENT ANGLE IN DEGREES (NEEDED ONLY WHEN
C  OO = 2).
C  NY = THE TOTAL NUMBER OF DIGITIZED POINTS FROM THE D-SPACING
C  PROFILE.
C  NE = THE TOTAL NUMBER OF THE INTENSITY VS. TWO THETA PAIRS TO BE
C  READ FROM THE EXPERIMENTAL INTENSITY BAND.
C  NEB = THE NUMBER OF THE INTENSITY DATA OF THE EXPERIMENTAL
C  BAND TO BE BOOSTED BY 10 TIMES TO SHOW THE FITTING DETAILS.
C  NS = THE TOTAL NUMBER OF THE INTENSITY VS. TWO THETA PAIRS TO BE
C  SIMULATED BY THIS PROGRAM.
C  FINAL = THE TWO THETA VALUE (IN DEGREES) OF THE HIGH ANGLE END
C  OF THE INTENSITY BAND TO BE SIMULATED.
C  START = THE TWO THETA VALUE (IN DEGREES) OF THE LOW ANGLE END
C  OF THE INTENSITY BAND TO BE SIMULATED.
C  NSB = THE NUMBER OF THE INTENSITY DATA OF THE SIMULATED BAND
```

```
C  TO BE BOOSTED BY 10 TIMES TO SHOW THE FITTING DETAILS.
C  B1 = THE 'A' PARAMETER IN PEARSON-VII  FUNCTION TO BE  USED FOR
C  THE BROADENING IN THE LOW ANGLE PORTION OF THE INTENSITY BAND.
C  B2 = THE 'M' PARAMETER IN PEARSON-VII  FUNCTION TO BE  USED FOR
C  THE BROADENING IN THE LOW ANGLE PORTION OF THE INTENSITY BAND.
C  B3 = THE 'A' PARAMETER IN PEARSON-VII  FUNCTION TO BE  USED FOR
C  THE BROADENING IN THE HIGH ANGLE PORTION OF THE INTENSITY BAND.
C  B4 = THE 'M' PARAMETER IN PEARSON-VII  FUNCTION TO BE  USED FOR
C  THE BROADENING IN THE HIGH ANGLE PORTION OF THE INTENSITY BAND.
C  RTT = THE TWO THETA VALUE (IN DEGREES) SEPARATING THE HIGH AND
C  LOW ANGLE PORTIONS OF THE INTENSITY BAND.
C
C  THE VALUES ASSIGNED FOR THE FOLLOWING PARAMETERS SERVE AS AN
C  EXAMPLE. THESE VALUES, ALONG WITH THE INPUT DATA FILES FO-
C  LLOWING THIS PROGRAM,  GIVE THE INTENSITY  BANDS SHOWN IN
C  FIGURE 34 OF THIS THESIS.
      ALAMDA = 1.540562
      D0 = 2.9646
      U = 630.
      OS = 1
      OO = 1
      NY = 431
      NE = 124
      NEB = 60
      NS = 200
      FINAL = 32.
      START = 28.
      NSB = 88
```

```
      B1 = 0.032
      B2 = 1.8
      B3 = 0.032
      B4 = 1.8
C  THE FOLLOWING TWO STATEMENTS READ THE DIGITIZED D-SPACING PRO-
C  FILE AND THE MEASURED INTENSITY VS. TWO THETA PAIRS OF THE IN-
C  TENSITY BAND.
C  D = D-SPACING IN ANGSTROM
C  DIST = DEPTH MEASURED FROM THE FREE SURFACE IN CM.  DIST(1) = 0.
C  CORRESPONDS TO THE SAMPLE SURFACE.
C  TG = THE TWO THETA VALUE  RELATED TO THE D-SPACING  BY BRAGG'S
C  LAW.
C  X2 = THE TWO THETA VALUES OF THE EXPERIMENTAL INTENSITY BAND.
C  Y2 = THE INTENSITY VALUES OF THE EXPERIMENTAL INTENSITY BAND.
      READ(5,*)((D(J),DIST(J),TG(J)),J = 1,NY)
      READ(5,*)((X2(I),Y2(I)), I = 1,NE)
CCCCCCCCCCCCCCCCCC END OF INPUT CCCCCCCCCCCCCCCCCCCCCCCCCC
      CVOL = ALAMDA/8./D0/U
      IID2 = NY + 20
      DO 50 J = NY,IID2
      DIST(J) = DIST(NY) + FLOAT(J-NY)*CVOL
      D(J) = D0
   50 TG(J) = 2.*ASIN(ALAMDA/2./D(J))*180./ACOS(-1.)
CCCCCCC BEGINING: CAUCULATION OF THE INTENSITY CCCCCCCCCCCCC
CCCCCCCCCC FOR EACH LAYER OF A ROUGH SAMPLE CCCCCCCCCCCCCCCC
      IF(OS .EQ. 1) GO TO 223
      X(6) = -0.12523
      X(5) = -0.36783
```

```
X(4) = -0.587318
X(3) = -0.76990
X(2) = -0.904117
X(1) = -0.98156
X(7) = -X(6)
X(8) = -X(5)
X(9) = -X(4)
X(10) = -X(3)
X(11) = -X(2)
X(12) = -X(1)
W(1) = 0.047175
W(2) = 0.10694
W(3) = 0.160078
W(4) = 0.203167
W(5) = 0.23349
W(6) = 0.249147
W(7) = W(6)
W(8) = W(5)
W(9) = W(4)
W(10) = W(3)
W(11) = W(2)
W(12) = W(1)
TCS = TC/SQRT(2.)/SIGMA
LAST = IID2-1
DO 221 J = 1,LAST
YS = (DIST(J + 1) + DIST(J))/2./SQRT(2.)/SIGMA
IF (OO .EQ. 1) THETAI = TG(J)/2.
THETAS = TG(J)-THETAI
```

```
      ANGLEI = THETAI/180.*ACOS(-1.)
      ANGLES = THETAS/180.*ACOS(-1.)
      ZS = -3.
      DOWN = ZS
      UP = DOWN + 3.
      F1S = 0.
      DO 101 N = 1,2
      F1 = 0.
      DO 100 I = 1,12
      XX1 = ((UP-DOWN)*X(I) + UP + DOWN)/2.
      XX2 = XX1 + YS
      CALL SUBRZ(XX1,XX2,S2)
      YY1 = EXP(-(XX1 + YS)*(XX1 + YS))*S2
  100 F1 = F1 + (UP-DOWN)/2.*W(I)*YY1
      DOWN = DOWN + 3.
      UP = UP + 3.
  101 F1S = F1S + F1
      UT = SQRT(2.)*SIGMA*(U/SIN(ANGLEI) + U/SIN(ANGLES))
      F1S = F1S + SQRT(ACOS(-1.))/2.*EXP(UT*UT/4.-YS*UT)*(1. + ERF(YS-3.
     1-UT/2.))
  221 P(J) = F1S/SQRT(ACOS(-1.))/SIN(ANGLEI)*(DIST(J + 1)-DIST(J))
CCCCCCCCCCCCCC END: CAUCULATION OF THE INTENSITY CCCCCCCCCCC
CCCCCCCCCCCCCC FOR EACH LAYER IN A ROUGH SAMPLE  CCCCCCCCCCC
      GO TO 225
CCCCCCCC BEGINING: CALCULATION OF THE INTENSITY CCCCCCCCCCCC
CCCCCCCCC FOR EACH LAYER IN A FLAT SAMPLE CCCCCCCCCCCCCCCCCC
  223 LAST = IID2-1
      DO 224 J = 1,LAST
```

```
      IF (OO .EQ. 1) THETAI=  TG(J)/2.
      THETAS = TG(J)-THETAI
      ANGLEI = THETAI/180.*ACOS(-1.)
      ANGLES = THETAS/180.*ACOS(-1.)
      P(J) = (DIST(J + 1)-DIST(J))/SIN(ANGLEI)*EXP(-(U/SIN(ANGLEI) +
     1U/SIN(ANGLES))*(DIST(J) + DIST(J + 1))/2.)
  224 CONTINUE
CCCCCCCCCCCC END: CALCULATION OF THE INTENSITY BAND CCCCCCCCC
CCCCCCCCCCCCCCC FOR EACH LAYER IN A FLAT SAMPLE CCCCCCCCCCCCC
  225 DO 61 I = 1,NS
   61 AINTEN(I) = 0.
      T2INC = (FINAL-START)/NS
C T2V  =  THE TWO THETA POSITIONS  WHERE THE INTENSITIES ARE TO BE
C  SIMULATED.
C  AINTEN  =  THE SIMULATED INTENSITY AT T2V
      DO 324 I = 1,NS
  324 T2V(I) = START + T2INC*(I-1)
C  301 LOOP CALCULATES THE INTENSITY FOR EACH POINT OF THE INTEN-
C  SITY BAND BEING SIMULATED.
      DO 301 K = 1,NS
      IF(K.EQ.1.OR.K.EQ.NS) GO TO 16
      ALI = (T2V(K) + T2V(K-1))/2.
      ULI = (T2V(K) + T2V(K + 1))/2.
C LOOP 489 BROADENS THE  CALCULATED INTENSITY OF EACH LAYER USING
C THE PEARSON-VII FUNCTION, THEN SUPERIMPOSES THEM TO GET THE SI-
C MULATED INTENSITIY.
   16 DO 489 J = 1,LAST
      TTJ = (TG(J) + TG(J + 1))/2.
```

```
      XZ = T2V(K)-TTJ
      IF(TTJ .LT. RTT) B1P = B1
      IF(TTJ .LT. RTT) B2P = B2
      IF(TTJ .GE. RTT) B1P = B3
      IF(TTJ .GE. RTT) B2P = B4
      YNORM = 1./SQRT(B2P*ACOS(-1.))/B1P*GAMMA(B2P)/GAMMA(B2P-0.5)
      BR = 1./(1. + (XZ**2)/(B2P*B1P**2))**B2P*YNORM
      IF(K .EQ. 1.OR.K .EQ. NS)GO TO 489
  489 AINTEN(K) = AINTEN(K) + P(J)*BR
  301 CONTINUE
C  814 LOOP PERFORMS THE BACKGROUND CORRECTION FOR THE
C  MEASURED INTENSITY BAND.
      DO 814 I = 1,NE
      Y2(I) = Y2(I)-(Y2(1) + (X2(I)-X2(1))*(Y2(NE)-Y2(1))/(X2(NE)-X2(1
     V)))
      IF(Y2(I) .LT. 0.)Y2(I) = 0.
  814 CONTINUE
C  LOOPS 815, 816 AND 817 RESCALE THE INTENSITY FOR THE SIMULATED
C  BAND SO THAT THE MAXIMUM INTENSITIES OF BOTH THE SIMULATED AND
C  THE MEASURED BANDS ARE EQUAL.
      PR = 0.
      PR3 = 0.
      DO 815 I = 1,NS
  815 PR = AMAX1(PR,AINTEN(I))
      DO 816 I = 1,NE
  816 PR3 = AMAX1(PR3,Y2(I))
      DO 817 I = 1,NS
```

```
  817 AINTEN(I) = AINTEN(I)*PR3/PR
CCCCCCCCCCCCCCC BEGINING OF PLOTTING CCCCCCCCCCCCCCCCCCCCC
      CALL PLOTS(0,0,50)
      CALL PLOT(1.,1.,-3)
      CALL SCALE(T2V,4.5,NS,1)
      CALL SCALE(AINTEN,6.5,NS,1)
      CALL NEWPEN(3)
      CALL AXIS(0.,0.0,'TWO THETA',-9,4.5,0.,T2V(NS + 1),T2V(NS + 2))
      CALL AXIS(0.,0.0,'INTENSITY',7,6.5,90.,AINTEN(NS + 1),AINTEN(
     1NS + 2))
      CALL LINE(T2V,AINTEN,NS,1,0,0)
C  AINTENB = THE BOOSTED SIMULATED INTENSITY
      DO 818 I = 1,NSB
      T2VB(I) = T2V(I)
  818 AINTENB(I) = AINTEN(I)*10.
      T2VB(NSB + 1) = T2V(NS + 1)
      T2VB(NSB + 2) = T2V(NS + 2)
      AINTENB(NSB + 1) = AINTEN(NS + 1)
      AINTENB(NSB + 2) = AINTEN(NS + 2)
      CALL PLOT(0.0,0.0,-3)
      CALL NEWPEN(3)
      CALL LINE(T2VB,AINTENB,NSB,1,0,0)
      CALL PLOT(0.,0.,-3)
      X2(NE + 1) = T2V(NS + 1)
      X2(NE + 2) = T2V(NS + 2)
      CALL SCALE(Y2,6.5,NE,1)
      CALL NEWPEN(3)
```

```
      CALL LINE(X2,Y2,NE,1,-1,2)
C  Y2B  =  THE BOOSTED MEASURED INTENSITY.
      DO 819 I = 1,NEB
      X2B(I) = X2(I)
  819 Y2B(I) = Y2(I)*10.
      X2B(NEB + 1) = X2(NE + 1)
      X2B(NEB + 2) = X2(NE + 2)
      Y2B(NEB + 1) = Y2(NE + 1)
      Y2B(NEB + 2) = Y2(NE + 2)
      CALL PLOT(0.0,0.0,-3)
      CALL NEWPEN(3)
      CALL LINE(X2B,Y2B,NEB,1,-1,2)
      CALL PLOT(12.0,0.0,999)
CCCCCCCCCCCCCCCCCC END OF PLOTTING CCCCCCCCCCCCCCCCCCCCCC
      STOP
      END

C  THE FOLLOWING SUBROUTINE CALCULATES THE ABSORPTION ATTENUA-
C  TION FACTOR FOR A SIGNAL GENERATING GROUP IN A ROUGH SAMPLE.
      SUBROUTINE SUBRZ(ZS,Z0S,S2)
      DIMENSION X(12),W(12),Z1S(12)
      COMMON  X,W,SIGMA,TC,TCS,U,THETAI,THETAS
      CALL ERRSET(208,256,-1)
      ANGLEI = THETAI/180.*ACOS(-1.)
      ANGLES = THETAS/180.*ACOS(-1.)
      DOWN = ZS
      Z0D = Z0S-0.2
      Z0U = Z0S + 0.1
```

```
      Z0DD = Z0D-1.0
      DT = 1.0
      IF(DOWN .GT. Z0DD .AND. DOWN .LT. Z0D) DT = Z0D-DOWN
      IF(DOWN .GE. Z0D .AND. DOWN .LE. Z0U) DT = 0.1
      UP = DOWN + DT
      S2I = 0.
      S2S = 0.
      DO 201 JSS = 1,300
      F2I = 0.
      F2S = 0.
      DO 200 JS = 1,12
      Z1S(JS) = ((UP-DOWN)*X(JS) + UP + DOWN)/2.
      Y0I = EXP(-(Z1S(JS)-ZS)/TAN(ANGLEI)/TCS)
      Y0S = EXP(-(Z1S(JS)-ZS)/TAN(ANGLES)/TCS)
      Y1I = EXP(-(Z1S(JS)-Y0I*Z0S)*(Z1S(JS)-Y0I*Z0S)/(1.-Y0I*Y0I))
      Y1S = EXP(-(Z1S(JS)-Y0S*Z0S)*(Z1S(JS)-Y0S*Z0S)/(1.-Y0S*Y0S))
      UTI = 1./SQRT(1.-Y0I*Y0I)-(Y0I*Y0I*Z1S(JS)-Y0I*Z0S)/TCS/TAN
     1(ANGLEI)/(1.-Y0I*Y0I)**1.5
      UTS = 1./SQRT(1.-Y0S*Y0S)-(Y0S*Y0S*Z1S(JS)-Y0S*Z0S)/TCS/TAN
     1(ANGLES)/(1.-Y0S*Y0S)**1.5
      Y1I = Y1I*UTI/SQRT(ARCOS(-1.))
      Y1S = Y1S*UTS/SQRT(ARCOS(-1.))
      Y2I = Y1I*EXP(-SQRT(2.)*SIGMA*U*(Z1S(JS)-ZS)/SIN(ANGLEI))
      Y2S = Y1S*EXP(-SQRT(2.)*SIGMA*U*(Z1S(JS)-ZS)/SIN(ANGLES))
      F2I = F2I + (UP-DOWN)/2.*W(JS)*Y2I
  200 F2S = F2S + (UP-DOWN)/2.*W(JS)*Y2S
      IF(DOWN .GE. 4.1) GO TO 202
      DOWN = UP
```

```
      DT = 1.0
      IF(DOWN .GT. Z0DD .AND. DOWN .LT. Z0D) DT = Z0D-DOWN
      IF (DOWN .GE. Z0D .AND. DOWN .LE. Z0U) DT = 0.1
      UP = DOWN + DT
      S2I = S2I + F2I
  201 S2S = S2S + F2S
  202 CONTINUE
      S2 = S2I*S2S
      RETURN
      END
```

```
C  THE FOLLOWING IS A SAMPLE INPUT FILE, THE FIRST 431  ROWS ARE
C  DATA FOR THE D-SPACING  PROFILE, THE FIRST, SECOND AND THIRD
C  ENTRY IN EACH ROW ARE D-SPACING (ANGSTROM), DEPTH (CM) AND TWO
C  THETA (DEGREES), RESPECTIVELY. THE NEXT 124 ROWS ARE DATA OF
C  THE EXPERIMEMTAL INTENSITY BAND. THE FIRST AND SECOND ENTRY IN
C  EACH ROW ARE TWO THETA (DEGREES) AND INTENSITY, RESPECTIVELY.
   3.11460 0.0             28.63713
   3.11367 0.99999973E-08  28.64586
   3.11275 0.19999998E-07  28.65448
   3.11185 0.29999995E-07  28.66298
   3.11096 0.40000000E-07  28.67137
   3.11008 0.49999983E-07  28.67966
   3.10921 0.59999991E-07  28.68784
   3.10835 0.69999942E-07  28.69591
   3.10751 0.79999950E-07  28.70387
   3.10667 0.89999958E-07  28.71176
```

3.10585 0.99999966E-07 28.71951

3.10504 0.10999997E-06 28.72719

3.10423 0.11999998E-06 28.73477

3.10344 0.12999993E-06 28.74226

3.10266 0.13999994E-06 28.74966

3.10189 0.14999995E-06 28.75697

3.10113 0.15999996E-06 28.76418

3.10038 0.16999996E-06 28.77130

3.09963 0.17999997E-06 28.77835

3.09890 0.18999998E-06 28.78529

3.09818 0.19999999E-06 28.79218

3.09746 0.20999994E-06 28.79898

3.09676 0.21999995E-06 28.80566

3.09606 0.22999996E-06 28.81230

3.09537 0.23999996E-06 28.81886

3.09469 0.24999997E-06 28.82535

3.09401 0.25999998E-06 28.83174

3.09335 0.26999999E-06 28.83809

3.09269 0.27999999E-06 28.84435

3.09204 0.28999995E-06 28.85052

3.09140 0.29999995E-06 28.85663

3.09077 0.30999996E-06 28.86269

3.09014 0.31999997E-06 28.86867

3.08952 0.32999998E-06 28.87460

3.08891 0.33999999E-06 28.88045

3.08830 0.34999999E-06 28.88623

3.08770 0.36000000E-06 28.89195

3.08711 0.36999995E-06 28.89763

3.08653 0.37999996E-06 28.90323

3.08595 0.38999997E-06 28.90875

3.08537 0.39999969E-06 28.91425

3.08481 0.40999981E-06 28.91966

3.08425 0.41999965E-06 28.92503

3.08369 0.42999977E-06 28.93036

3.08314 0.43999995E-06 28.93561

3.08260 0.44999979E-06 28.94081

3.08206 0.45999991E-06 28.94597

3.08153 0.46999975E-06 28.95107

3.08101 0.47999993E-06 28.95613

3.08049 0.48999971E-06 28.96112

3.07997 0.49999989E-06 28.96608

3.07946 0.50999967E-06 28.97096

3.07896 0.51999984E-06 28.97583

3.07846 0.52999962E-06 28.98062

3.07796 0.53999980E-06 28.98540

3.07747 0.54999998E-06 28.99011

3.07699 0.55999976E-06 28.99478

3.07651 0.56999994E-06 28.99940

3.07603 0.57999972E-06 29.00400

3.07556 0.58999990E-06 29.00853

3.07509 0.59999968E-06 29.01303

3.07463 0.60999986E-06 29.01749

3.07417 0.61999964E-06 29.02190

3.07372 0.62999982E-06 29.02629

3.07327 0.64000000E-06 29.03062

3.07283 0.64999978E-06 29.03491

3.07238 0.65999996E-06 29.03918

3.07195 0.66999979E-06 29.04341

3.07151 0.67999991E-06 29.04759

3.07108 0.68999975E-06 29.05176

3.07066 0.69999987E-06 29.05586

3.07024 0.70999971E-06 29.05995

3.06982 0.71999989E-06 29.06400

3.06940 0.72999967E-06 29.06801

3.06899 0.73999985E-06 29.07199

3.06858 0.75000003E-06 29.07594

3.06818 0.75999981E-06 29.07986

3.06778 0.76999999E-06 29.08374

3.06738 0.77999977E-06 29.08759

3.06699 0.78999994E-06 29.09142

3.06660 0.79999973E-06 29.09518

3.06621 0.80999990E-06 29.09897

3.06582 0.81999968E-06 29.10269

3.06544 0.82999986E-06 29.10640

3.06506 0.83999964E-06 29.11008

3.06469 0.84999982E-06 29.11372

3.06431 0.86000000E-06 29.11736

3.06394 0.86999978E-06 29.12094

3.06358 0.87999996E-06 29.12450

3.06321 0.88999974E-06 29.12804

3.06285 0.89999992E-06 29.13156

3.06249 0.90999976E-06 29.13504

3.06214 0.91999988E-06 29.13850

3.06178 0.92999971E-06 29.14195

3.06143 0.93999989E-06 29.14534

3.06108 0.94999967E-06 29.14874

3.06074 0.95999985E-06 29.15213

3.06039 0.96999975E-06 29.15546

3.06005 0.97999964E-06 29.15877

3.05972 0.98999953E-06 29.16208

3.05938 0.99999943E-06 29.16534

3.05614 0.10999993E-05 29.19693

3.05311 0.11999991E-05 29.22661

3.05025 0.12999999E-05 29.25462

3.04754 0.13999997E-05 29.28117

3.04497 0.14999996E-05 29.30643

3.04252 0.15999995E-05 29.33054

3.04018 0.16999993E-05 29.35361

3.03794 0.17999992E-05 29.37576

3.03579 0.18999990E-05 29.39708

3.03372 0.19999998E-05 29.41762

3.03172 0.20999996E-05 29.43745

3.02978 0.21999995E-05 29.45665

3.02791 0.22999993E-05 29.47525

3.02610 0.23999992E-05 29.49330

3.02435 0.24999990E-05 29.51082

3.02264 0.25999998E-05 29.52786

3.02098 0.26999996E-05 29.54449

3.01935 0.27999995E-05 29.56071

3.01777 0.28999993E-05 29.57655

3.01623 0.29999992E-05 29.59206

3.01471 0.30999990E-05 29.60727

3.01323 0.31999989E-05 29.62218

3.01177 0.32999997E-05 29.63689

3.01033 0.33999995E-05 29.65137

3.00891 0.34999994E-05 29.66570

3.00750 0.35999992E-05 29.67987

3.00611 0.36999991E-05 29.69395

3.00472 0.37999998E-05 29.70798

3.00334 0.38999997E-05 29.72195

3.00196 0.39999995E-05 29.73596

3.00058 0.40999994E-05 29.74998

2.99919 0.41999992E-05 29.76405

2.99779 0.42999991E-05 29.77826

2.99638 0.43999989E-05 29.79254

2.99497 0.44999997E-05 29.80698

2.99354 0.45999996E-05 29.82155

2.99209 0.46999994E-05 29.83630

2.99063 0.47999993E-05 29.85120

2.98916 0.48999991E-05 29.86626

2.98767 0.49999990E-05 29.88144

2.98618 0.50999988E-05 29.89674

2.98468 0.51999996E-05 29.91216

2.98317 0.52999994E-05 29.92758

2.98167 0.53999993E-05 29.94302

2.98017 0.54999991E-05 29.95840

2.97869 0.55999990E-05 29.97363

2.97723 0.56999988E-05 29.98868

2.97580 0.57999996E-05 30.00346

2.97440 0.58999995E-05 30.01787

2.97305 0.59999993E-05 30.03185

2.97175 0.60999992E-05 30.04529

2.97051 0.61999990E-05 30.05811

2.96934 0.62999961E-05 30.07024

2.96825 0.63999951E-05 30.08156

2.96724 0.64999995E-05 30.09207

2.96632 0.65999984E-05 30.10164

2.96549 0.66999964E-05 30.11024

2.96476 0.67999954E-05 30.11781

2.96413 0.68999943E-05 30.12434

2.96361 0.69999987E-05 30.12982

2.96315 0.70999977E-05 30.13455

2.96273 0.71999966E-05 30.13895

2.96235 0.72999946E-05 30.14294

2.96199 0.73999936E-05 30.14661

2.96168 0.74999925E-05 30.14992

2.96139 0.75999969E-05 30.15289

2.96114 0.76999959E-05 30.15553

2.96092 0.77999948E-05 30.15784

2.96073 0.78999929E-05 30.15981

2.96057 0.79999982E-05 30.16150

2.96043 0.80999962E-05 30.16289

2.96033 0.81999951E-05 30.16399

2.96025 0.82999941E-05 30.16479

2.96019 0.83999930E-05 30.16537

2.96016 0.84999974E-05 30.16570

2.96016 0.85999964E-05 30.16576

2.96017 0.86999944E-05 30.16562

2.96021 0.87999933E-05 30.16525

2.96026 0.88999923E-05 30.16470

2.96033 0.89999967E-05 30.16396

2.96042 0.90999956E-05 30.16306

2.96052 0.91999946E-05 30.16197

2.96064 0.92999935E-05 30.16077

2.96076 0.93999979E-05 30.15942

2.96091 0.94999968E-05 30.15796

2.96105 0.95999949E-05 30.15642

2.96121 0.96999938E-05 30.15475

2.96138 0.97999928E-05 30.15303

2.96155 0.98999972E-05 30.15125

2.96173 0.99999961E-05 30.14940

2.96191 0.10099995E-04 30.14751

2.96209 0.10199993E-04 30.14560

2.96228 0.10299992E-04 30.14363

2.96247 0.10399996E-04 30.14169

2.96266 0.10499995E-04 30.13972

2.96284 0.10599994E-04 30.13779

2.96303 0.10699993E-04 30.13583

2.96321 0.10799998E-04 30.13393

2.96339 0.10899997E-04 30.13203

2.96357 0.10999995E-04 30.13019

2.96375 0.11099994E-04 30.12839

2.96391 0.11199993E-04 30.12662

2.96408 0.11299997E-04 30.12492

2.96424 0.11399996E-04 30.12326

2.96439 0.11499995E-04 30.12166

2.96454 0.11599993E-04 30.12013

2.96468 0.11699992E-04 30.11865

2.96481 0.11799997E-04 30.11725

2.96494 0.11899995E-04 30.11592

2.96506 0.11999994E-04 30.11465

2.96518 0.12099993E-04 30.11345

2.96529 0.12199997E-04 30.11234

2.96539 0.12299996E-04 30.11128

2.96548 0.12399995E-04 30.11031

2.96557 0.12499993E-04 30.10938

2.96565 0.12599992E-04 30.10854

2.96573 0.12699997E-04 30.10777

2.96579 0.12799996E-04 30.10707

2.96586 0.12899995E-04 30.10641

2.96591 0.12999993E-04 30.10582

2.96596 0.13099992E-04 30.10530

2.96601 0.13199997E-04 30.10484

2.96605 0.13299995E-04 30.10443

2.96608 0.13399994E-04 30.10408

2.96611 0.13499993E-04 30.10378

2.96614 0.13599997E-04 30.10352

2.96616 0.13699996E-04 30.10332

2.96617 0.13799995E-04 30.10315

2.96618 0.13899993E-04 30.10301

2.96619 0.13999992E-04 30.10294

2.96620 0.14099996E-04 30.10289

2.96620 0.14199995E-04 30.10289

2.96620 0.14299994E-04 30.10291

2.96619 0.14399993E-04 30.10294

2.96618 0.14499998E-04 30.10303

2.96617 0.14599997E-04 30.10312

2.96616 0.14699996E-04 30.10324

2.96615 0.14799994E-04 30.10339

2.96613 0.14899992E-04 30.10355

2.96612 0.14999997E-04 30.10373

2.96610 0.15099996E-04 30.10393

2.96608 0.15199995E-04 30.10414

2.96605 0.15299986E-04 30.10435

2.96603 0.15399986E-04 30.10458

2.96601 0.15499987E-04 30.10483

2.96599 0.15599988E-04 30.10509

2.96596 0.15699989E-04 30.10533

2.96594 0.15799989E-04 30.10559

2.96591 0.15899990E-04 30.10587

2.96589 0.15999991E-04 30.10612

2.96586 0.16099992E-04 30.10638

2.96583 0.16199992E-04 30.10666

2.96581 0.16299979E-04 30.10693

2.96578 0.16399994E-04 30.10721

2.96575 0.16499995E-04 30.10748

2.96573 0.16599981E-04 30.10776

2.96570 0.16699982E-04 30.10803

2.96568 0.16799982E-04 30.10829

2.96565 0.16899983E-04 30.10857

2.96563 0.16999984E-04 30.10881

2.96560 0.17099985E-04 30.10909

2.96558 0.17199985E-04 30.10933

2.96555 0.17299986E-04 30.10957

2.96553 0.17399987E-04 30.10982

2.96550 0.17499988E-04 30.11008

2.96548 0.17599988E-04 30.11031

2.96546 0.17699989E-04 30.11053

2.96544 0.17799990E-04 30.11078

2.96542 0.17899991E-04 30.11101

2.96539 0.17999992E-04 30.11122

2.96537 0.18099992E-04 30.11143

2.96535 0.18199979E-04 30.11165

2.96533 0.18299994E-04 30.11185

2.96531 0.18399995E-04 30.11206

2.96530 0.18499981E-04 30.11224

2.96528 0.18599982E-04 30.11244

2.96526 0.18699997E-04 30.11263

2.96524 0.18799983E-04 30.11281

2.96523 0.18899984E-04 30.11299

2.96521 0.18999985E-04 30.11316

2.96519 0.19099985E-04 30.11333

2.96518 0.19199986E-04 30.11349

2.96516 0.19299987E-04 30.11366

2.96515 0.19399988E-04 30.11382

2.96513 0.19499988E-04 30.11398

2.96512 0.19599989E-04 30.11411

2.96510 0.19699990E-04 30.11426

2.96509 0.19799991E-04 30.11441

2.96507 0.19899991E-04 30.11455

2.96506 0.19999992E-04 30.11469

2.96505 0.20099993E-04 30.11481

2.96504 0.20199994E-04 30.11493

2.96503 0.20299995E-04 30.11505

2.96501 0.20399981E-04 30.11519

2.96500 0.20499981E-04 30.11530

2.96499 0.20599997E-04 30.11542

2.96498 0.20699983E-04 30.11552

2.96497 0.20799984E-04 30.11563

2.96496 0.20899985E-04 30.11574

2.96495 0.20999985E-04 30.11584

2.96494 0.21099986E-04 30.11594

2.96493 0.21199987E-04 30.11604

2.96492 0.21299988E-04 30.11612

2.96491 0.21399988E-04 30.11621

2.96491 0.21499989E-04 30.11629

2.96490 0.21599990E-04 30.11639

2.96489 0.21699991E-04 30.11647

2.96488 0.21799991E-04 30.11656

2.96487 0.21899992E-04 30.11664

2.96487 0.21999993E-04 30.11671

2.96486 0.22099994E-04 30.11679

2.96485 0.22199980E-04 30.11687

2.96485 0.22299981E-04 30.11693

2.96484 0.22399981E-04 30.11700

2.96483 0.22499982E-04 30.11707

2.96483 0.22599983E-04 30.11714

2.96482 0.22699984E-04 30.11720

2.96481 0.22799984E-04 30.11725

2.96481 0.22899985E-04 30.11732

2.96480 0.22999986E-04 30.11739

2.96480 0.23099987E-04 30.11745

2.96479 0.23199987E-04 30.11749

2.96479 0.23299988E-04 30.11755

2.96478 0.23399989E-04 30.11760

2.96478 0.23499990E-04 30.11766

2.96477 0.23599991E-04 30.11769

2.96477 0.23699991E-04 30.11774

2.96476 0.23799977E-04 30.11780

2.96476 0.23899993E-04 30.11784

2.96475 0.23999994E-04 30.11789

2.96475 0.24099980E-04 30.11794

2.96475 0.24199981E-04 30.11798

2.96474 0.24299996E-04 30.11801

2.96474 0.24399982E-04 30.11806

2.96473 0.24499983E-04 30.11810

2.96473 0.24599984E-04 30.11813

2.96473 0.24699984E-04 30.11818

2.96472 0.24799985E-04 30.11821

2.96472 0.24899986E-04 30.11824

2.96472 0.24999987E-04 30.11829

2.96471 0.25099987E-04 30.11830

2.96471 0.25199988E-04 30.11833

2.96471 0.25299989E-04 30.11836

2.96470 0.25399990E-04 30.11841

2.96470 0.25499990E-04 30.11844

2.96470 0.25599991E-04 30.11847

2.96469 0.25699992E-04 30.11850

2.96469 0.25799993E-04 30.11852

2.96469 0.25899993E-04 30.11853

2.96469 0.25999980E-04 30.11856

2.96469 0.26099980E-04 30.11861

2.96468 0.26199996E-04 30.11862

2.96468 0.26299982E-04 30.11864

2.96468 0.26399983E-04 30.11867

2.96468 0.26499984E-04 30.11870

2.96467 0.26599984E-04 30.11870

2.96467 0.26699985E-04 30.11873

2.96467 0.26799986E-04 30.11876

2.96467 0.26899987E-04 30.11876

2.96467 0.26999987E-04 30.11880

2.96466 0.27099988E-04 30.11882

2.96466 0.27199989E-04 30.11884

2.96466 0.27299990E-04 30.11885

2.96466 0.27399990E-04 30.11887

2.96466 0.27499991E-04 30.11888

2.96466 0.27599992E-04 30.11890

2.96465 0.27699993E-04 30.11891

2.96465 0.27799993E-04 30.11893

2.96465 0.27899980E-04 30.11896

2.96465 0.27999995E-04 30.11896

2.96465 0.28099996E-04 30.11897

2.96465 0.28199982E-04 30.11899

2.96465 0.28299983E-04 30.11900

2.96465 0.28399983E-04 30.11902

2.96464 0.28499984E-04 30.11903

2.96464 0.28599985E-04 30.11905

2.96464 0.28699986E-04 30.11905

2.96464 0.28799986E-04 30.11906

2.96464 0.28899987E-04 30.11906

2.96464 0.28999988E-04 30.11909

2.96464 0.29099989E-04 30.11909

2.96464 0.29199990E-04 30.11911

2.96463 0.29299990E-04 30.11913

2.96463 0.29399991E-04 30.11913

2.96463 0.29499992E-04 30.11914

2.96463 0.29599993E-04 30.11916

2.96463 0.29699979E-04 30.11917

2.96463 0.29799980E-04 30.11917

2.96463 0.29899995E-04 30.11919

2.96463 0.29999981E-04 30.11919

2.96463 0.30099982E-04 30.11919

2.96463 0.30199983E-04 30.11920

2.96463 0.30299983E-04 30.11922

2.96463 0.30399984E-04 30.11922

2.96463 0.30499985E-04 30.11922

2.96462 0.30599986E-04 30.11925

2.96462 0.30699986E-04 30.11925

2.96462 0.30799987E-04 30.11925

2.96462 0.30899988E-04 30.11925

2.96462 0.30999989E-04 30.11926

2.96462 0.31099989E-04 30.11928

2.96462 0.31199990E-04 30.11928

2.96462 0.31299991E-04 30.11928

2.96462 0.31399992E-04 30.11928

2.96462 0.31499992E-04 30.11929

2.96462 0.31599979E-04 30.11929

2.96462 0.31699979E-04 30.11929

2.96462 0.31799995E-04 30.11931

2.96462 0.31899981E-04 30.11931

2.96462 0.31999982E-04 30.11931

2.96461 0.32099982E-04 30.11932

2.96461 0.32199983E-04 30.11932

2.96461 0.32299984E-04 30.11932

2.96461 0.32399985E-04 30.11932

2.96461 0.32499986E-04 30.11934

2.96461 0.32599986E-04 30.11934

2.96461 0.32699987E-04 30.11935

2.96461 0.32799988E-04 30.11937

2.96461 0.32899989E-04 30.11937

2.96461 0.32999989E-04 30.11937

2.96461 0.33099990E-04 30.11937

2.96461 0.33199991E-04 30.11937

2.96461 0.33299992E-04 30.11937

2.96461 0.33399992E-04 30.11938

2.96461 0.33499979E-04 30.11938

2.96461 0.33599994E-04 30.11938

2.96461 0.33699995E-04 30.11938

2.96461 0.33799981E-04 30.11938

2.96461 0.33899982E-04 30.11938

2.96461 0.33999982E-04 30.11938

28.00 1.079

28.02 0.979

28.04 1.146

28.06 1.012

28.08 1.056

28.12 1.046

28.16 1.069

28.20 1.042

28.24 1.091

28.28 1.095

28.32 1.059

28.36 1.180

28.38 1.198

28.40 1.099

28.44 1.146

28.48 1.206

28.52 1.257

28.56 1.311

28.60 1.313

28.64 1.338

28.68 1.363

28.72 1.429

28.74 1.555

28.76 1.617

28.78 1.597

28.80 1.595

28.82 1.784

28.84	1.833
28.88	1.957
28.92	2.104
28.96	2.344
29.00	2.601
29.04	2.734
29.08	3.031
29.10	3.100
29.12	3.107
29.14	3.178
29.16	3.364
29.20	3.574
29.24	3.722
29.28	3.753
29.32	3.809
29.34	3.984
29.36	4.046
29.38	4.089
29.40	4.090
29.42	4.139
29.44	4.300
29.46	4.085
29.48	4.109
29.50	4.170
29.52	4.082
29.54	4.205
29.56	4.310
29.58	4.271

29.60 4.347

29.62 4.470

29.64 4.542

29.68 4.672

29.72 5.020

29.76 5.439

29.80 5.915

29.84 6.573

29.88 7.800

29.92 9.758

29.96 15.764

29.98 25.957

30.00 38.760

30.02 74.766

30.03 108.696

30.04 142.349

30.05 206.718

30.06 284.698

30.07 398.010

30.08 503.145

30.09 720.721

30.10 938.967

30.11 1025.641

30.12 1047.120

30.13 963.855

30.14 732.601

30.15 522.876

30.16 329.218

30.17 219.178

30.18 152.091

30.19 104.712

30.20 83.682

30.22 39.235

30.24 22.384

30.26 11.992

30.28 8.080

30.32 4.438

30.36 3.232

30.40 2.680

30.44 2.131

30.48 1.867

30.52 1.586

30.56 1.519

30.60 1.386

30.64 1.333

30.68 1.314

30.72 1.244

30.76 1.232

30.80 1.205

30.84 1.219

30.88 1.127

30.92 1.095

30.96 1.115

31.00 1.121

31.04 1.038

31.08 1.150

31.12	1.034
31.16	1.021
31.20	1.049
31.24	1.006
31.28	0.984
31.32	0.972
31.36	0.960
31.40	0.925
31.44	1.010
31.48	0.952
31.52	1.002
31.56	0.959
31.60	0.966

The vita has been removed from the scanned document